Durham E-Theses

The Role of Environment in Galaxy Formation

TANKARD-EVANS, TAMSYN,AMY

How to cite:

Use policy

The Role of Environment in Galaxy Formation

Tamsyn Amy Tankard-Evans

A Thesis presented for the degree of
Doctor of Philosophy

Extragalactic Astronomy and Cosmology Group
and
Institute for Computational Cosmology
Department of Physics
Durham University
UK

October 2015

The Role of Environment in Galaxy Formation

Tamsyn A. Tankard-Evans

Abstract

In this thesis we investigate the influence that environment has on the formation and evolution of galaxies in the Galaxy And Mass Assembly (GAMA) survey. The highly complete equatorial regions of GAMA cover $180\,\mathrm{deg}^2$ of the sky, providing spectroscopic redshifts for 180,000 galaxies brighter than $m_r = 19.8$. GAMA is the largest multi-wavelength spectroscopic survey of its kind to date, designed to study aspects of galaxy formation on scales of $< 1\,\mathrm{Mpc}$.

The dependence of the galaxy luminosity function (LF) on local environment is well described by linear relations with overdensity. The faint end slope of the LF is largely independent of environment but steepens in void regions. The environmental dependence shows little evolution over the last 3 Gyrs, and can again be parameterised by a linear relation when split by colour. The dependence of the LF on the cosmic web classification can be predicted from its dependence on overdensity and the distribution of overdensities within each cosmic web structure.

Observations from the GAMA survey can be theoretically interpreted by comparing to predictions made by the semi-analytic galaxy formation model of GAL-FORM through lightcone mock catalogues, which exhibit the same selection criteria as GAMA. Galaxy groups trace the underlying distribution of dark matter haloes in the Universe, and the use of galaxy group properties to infer the properties of dark matter, such as halo mass, is explored. Measurements of the galaxy density profile in galaxy groups in the GAMA survey and in the lightcone mocks suggest that the GALFORM model predicts the galaxy density profile to be too centrally concentrated. Comparisons to galaxy surveys such as GAMA lead to a bright future for the studies of galaxy formation.

Declaration

The work in this thesis is based on research carried out by the author between 2011 and 2015 while the author was a research student under the supervision of Dr. Peder Norberg, Prof. Cedric Lacey and Prof. Carlton Baugh in the Department of Physics, Durham University. No part of this thesis has been submitted elsewhere for any other degree or qualification.

Chapter 4 has been published in the form of a paper:

- *Galaxy And Mass Assembly (GAMA): the dependence of the galaxy luminosity function on environment, redshift and colour*, McNaught-Roberts, Tamsyn; Norberg, Peder; Baugh, Carlton; Lacey, Cedric; Loveday, J.; Peacock, J.; Baldry, I.; Bland-Hawthorn, J.; Brough, S.; Driver, Simon P.; Robotham, A. S. G.; Vázquez-Mata, J. A., MNRAS 445, 2125–2145 (2014).

The implementation of the method to classify structures in the cosmic web, as presented in section 5.2, was performed by Elizabeth Eardley (University of Edinburgh). Portions of Chapter 5 have been published in the form of a paper:

- *Galaxy And Mass Assembly (GAMA): the galaxy luminosity function within the cosmic web*, Eardley, E.; Peacock, J. A.; McNaught-Roberts, T.; Heymans, C.; Norberg, P.; Alpaslan, M.; Baldry, I.; Bland-Hawthorn, J.; Brough, S.; Cluver, M. E.; Driver, S. P.; Farrow, D. J.; Liske, J.; Loveday, J.; Robotham, A. S. G., MNRAS 448, 3554-3678 (2015).

Chapter 5 highlights the areas most contributed to by the author.

Acknowledgements

First of all I'd like to thank Peder Norberg for his supervision and continual support over the last few years, as well as Carlton Baugh and Cedric Lacey for their valuable contributions in all my scientific endeavours. I have been very fortunate in having had the fantastic opportunity to work in such a scientifically stimulating environment as the Durham extragalactic astronomy group and to be involved in such an enthusiastic team as the GAMA team.

The past and present residents of 327, Alex I, Claudia, Michelle, Flora, Matthieu, Alex II and Jascha, have created an unforgettable office environment which I am privileged to have been a part of. Special mention should be made of those long gone but never forgotten, the likes of Ben, Rachel, Danny, Rob and Rachael, and those who made my time in Durham momentous, including Charles, Peter, Will, Emma, Violeta, Helen, Sownak, Wojtek and many others.

Additionally, many thanks to Roisin Boadle and James Whitburn for putting up with my rants and rambling over the years, and I would be lost without the inspirational pillars that are Emily McCabe and Bronwynn Neumann.

Thanks also to family members far and wide across the globe who have influenced me greatly or accommodated me during my various astronomical adventures. I would never be where I am now without the support of my close family, Mandy, Noel and Cian Evans.

Contents

List of Figures

List of Tables

Chapter 1

Introduction

Galaxies are beacons in the Universe, paving out an observable map of the distribution of matter. With such maps of the Universe, we can begin to understand the physical processes governing the formation and evolution of galaxies. To constrain these processes, questions can be asked, such as: How does galaxy environment affect galaxy evolution? Does the scale on which environment is defined matter? Since dark matter is thought to be the dominant matter component in the Universe, how well do galaxies trace the underlying dark matter distribution? How efficiently do they form in dark matter haloes with different masses? Is their evolution affected by the mass of their host dark matter halo?

This thesis addresses these questions by investigating how galaxy properties vary with environment in the Galaxy And Mass Assembly (GAMA) redshift survey (Driver et al., 2011; Liske et al., 2015). Environment is measured both locally, characterised by the galaxy number overdensity over scales of 8 Mpc, and on larger scales, by classifying the geometric structure of voids and filaments in the cosmic web. The galaxy density profile in galaxy groups is also investigated to study how well galaxies trace the underlying dark matter distribution.

In this thesis, an intrinsic, observable statistical property of galaxies, the galaxy luminosity function, is measured and parameterised for galaxies in GAMA in different environments, to determine how the environment affects the distribution of galaxy luminosities. Galaxy colour is related to the star formation history of galaxies, and the GAMA galaxy sample is large enough to be split by colour while still

providing statistically useful subsamples. Investigating the effect of environment on the luminosity function for different populations provides insight into how galaxies of different types populate the Universe.

By comparing observational measurements to the predictions of simulations, galaxies can be used to trace the underlying dark matter. The way in which galaxies populate dark matter haloes provides valuable information about how galaxies form and evolve within their dark matter environment, and tells us the effect that the dark matter halo mass has on galaxy properties.

Galaxy formation models such as GALFORM (Cole et al., 2000) can be used to construct mock galaxy catalogues for comparison to galaxy survey catalogues like GAMA. The ability of such mock catalogues to reproduce the observed trends in galaxy properties with environment indicates how well the physical processes involved in galaxy formation are modelled and provides a tool with which an understanding of the formation and evolution of galaxies can be developed.

1.1 The Geometry and Properties of the Universe

The present day Universe is comprised of a visible cosmic web of matter within which galaxies reside. The formation of the web structure is largely linked to the geometry and dynamics of the Universe, gravity and the constituents of the Universe. In order to understand how this structure was formed, we provide a brief background.

Hubble (1929) first found evidence that the Universe was expanding, stating that the recessional velocities, v, of galaxies are proportional to their distance from us, d:

$$v = H_0 \, d, \tag{1.1}$$

where the Hubble constant, H_0, is related to the rate of expansion of the Universe at the present day.

The scale factor, $a(t)$, is defined as the ratio of a distance scale in the Universe, $D(t)$, at time t, to a distance scale now, D_0, therefore describing the relative increase in proper distance due to the expansion of the Universe:

$$D(t) = a(t) \, D_0. \tag{1.2}$$

The rate of expansion of the Universe is given by $\dot{a}(t)$, and the acceleration of the expansion by $\ddot{a}(t)$.

Following equation 1.1, the Hubble parameter at time t is defined as:

$$H = \frac{\dot{a}(t)}{a(t)}, \tag{1.3}$$

and, assuming the Universe is homogeneous and isotropic, the geometry and dynamics of the Universe are given by the Freidmann equation:

$$H^2 = \left(\frac{\dot{a}}{a}\right)^2 = \frac{8\pi G}{3}\rho - \frac{k}{a^2} + \frac{\Lambda}{3}, \tag{1.4}$$

with gravitational constant G, matter density ρ, curvature k, and cosmological constant Λ, which acts as a vacuum energy with negative pressure.

The evolution of the Hubble parameter is determined by the density contributions from the constituents of the Universe, Ω_{x}, namely the matter density Ω_{M}, radiation density Ω_{R}, curvature density Ω_{K} and dark energy density Ω_{Λ}. The density of each component, ρ_{x}, is expressed relative to the critical density of the Universe,

$$\Omega_{\mathrm{x}} = \frac{\rho_{\mathrm{x}}}{\rho_{\mathrm{crit}}}, \tag{1.5}$$

where the critical density, ρ_{crit}, depends on the Hubble parameter as:

$$\rho_{\mathrm{crit}} = \frac{3\,H^2}{8\pi\,G}. \tag{1.6}$$

The change in the relative contribution from each of these constituents with the expansion of the Universe fully describes the evolution of the geometry of the Universe:

$$H(t) = H_0 \sqrt{\Omega_{\mathrm{R},0}\, a(t)^{-4} + \Omega_{\mathrm{M},0}\, a(t)^{-3} + \Omega_{\mathrm{K},0}\, a(t)^{-2} + \Omega_{\Lambda,0}}. \tag{1.7}$$

Since the radiation density is negligible at recent times and the Universe is roughly flat ($\Omega_{\mathrm{K}} = 0$), equation 1.7 can be simplified to $H(t) = E(t)H_0$, where:

$$E(t) = \sqrt{\Omega_{\mathrm{M},0}\, a(t)^{-3} + \Omega_{\Lambda,0}}. \tag{1.8}$$

The velocity of galaxies caused solely by the expansion of the Universe is referred to as the Hubble flow, such that galaxies following the Hubble flow always appear

to be moving away from us. The shift of a galaxy's spectrum towards redder wavelengths for a galaxy following the Hubble flow is characterised by the term *redshift*, z, which is related to the scale factor as:

$$a(t) = \frac{1}{1 + z}.$$ (1.9)

For a flat Universe the evolution of ρ_{crit} is described by:

$$\rho_{\mathrm{crit}}(z) = \rho_{\mathrm{crit},0} \left[\Omega_{\mathrm{M},0} (1 + z)^3 + \Omega_{\Lambda,0} \right]$$ (1.10)

and the mean density of the Universe is $\rho_{\mathrm{mean}} = \rho_{\mathrm{crit},0} \Omega_{\mathrm{M},0} (1 + z)^3$ at all times.

It is useful to describe the Universe in terms of comoving units, to compare different epochs. The evolution of ρ_{crit} with redshift in comparison to ρ_{mean}, the mean density of the Universe, is given in Fig. 1.1 for various combinations of $\Omega_{\mathrm{M},0}$ and $\Omega_{\Lambda,0}$ relevant to this thesis. At $z = \infty$, $\rho_{\mathrm{crit}} = \rho_{\mathrm{mean}}$.

1.1.1 Cosmological Redshift

A photon emitted with wavelength, λ_{em}, from a galaxy following the Hubble flow, will be observed with a longer wavelength, λ_{obs}, caused by the recession velocity, v, of the galaxy. The effect of stretching the wavelength of a photon through expanding space causes an apparent reddening of the photon, or redshift, z.

For objects with low recessional velocities, such that $v \ll c$, the effect of general relativity is negligible, and the change in wavelength of the photon defines the redshift as:

$$z \equiv \frac{\lambda_{\mathrm{obs}} - \lambda_{\mathrm{em}}}{\lambda_{\mathrm{em}}} = \frac{v}{c}.$$ (1.11)

and is also related to the scale factor $a(t)$ through equation 1.9.

Cosmological redshift effectively acts as a measure of the proper distance, r, to a galaxy, the recessional velocity due to Hubble flow, v, and the scale factor of the Universe at the epoch of the galaxy, $a(t)$.

1.1.2 Peculiar Velocities

In reality the observed redshift is a combination of the cosmological redshift, z_{cos}, and the *peculiar* velocity of the galaxy, caused by the dynamics of galaxies within
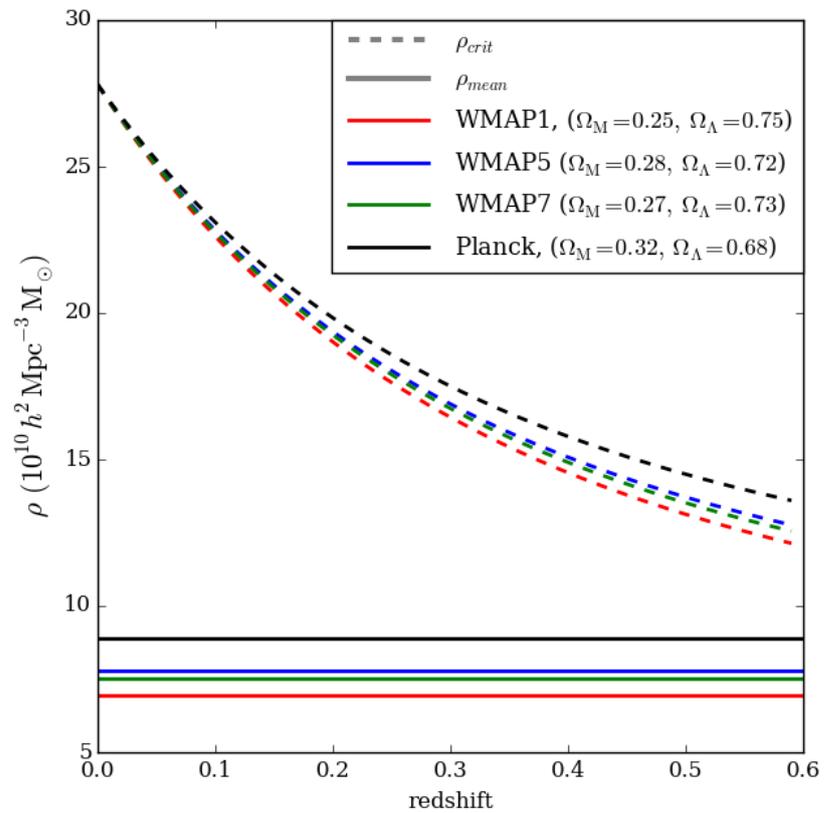
Figure 1.1: The mean (solid) and critical (dashed) density of the Universe (in comoving units) as a function of redshift for different cosmologies (see key).

the dark matter halo, and can be of the order of a few $100\,\mathrm{km\,s^{-1}}$. The line of sight component of the peculiar velocity, v_p, causes a Doppler effect in the frequency of photons emitted from the galaxy, ν, such that the observed frequency is ν':

$$\frac{\nu}{\nu'} = 1 + \frac{v_p}{c}, \tag{1.12}$$

which is indistinguishable from the cosmological redshift, z_{cos}. The effect of the peculiar velocity is a change in observed redshift to z_{obs}:

$$z_{\mathrm{obs}} = (1 + z_{\mathrm{cos}})(1 + \frac{v_p}{c}) - 1 \tag{1.13}$$

The peculiar velocities of galaxies lead to an apparent elongation of the positions of galaxies within groups, commonly called the "Finger-of-God" effect.

1.1.3 Observational Measures in Cosmology

When measuring distances in the Universe it is useful to factor out the expansion of the Universe and use *comoving* distances. Comoving distance takes into account the change in the expansion of the Universe with redshift and is calculated as:

$$D_{\mathrm{C}}(z) = \frac{c}{H_0} \int_0^z \frac{dz'}{E(z')}, \tag{1.14}$$

where $E(z)$ is given in equation 1.8 (for a flat Universe).

Distances to objects (standard candles) in the Universe can be determined by their intrinsic luminosity and the flux received by the observer. The observed bolometric flux, f, of an object with bolometric luminosity, L, at a luminosity distance D_{L} is:

$$f = \frac{L}{4\pi D_{\mathrm{L}}^2}. \tag{1.15}$$

Due to the reduction in surface brightness of an object with redshift, D_{L} is related to the comoving distance, D_{C}, of the galaxy in a flat Universe through:

$$D_{\mathrm{L}} = (1 + z)D_{\mathrm{C}}. \tag{1.16}$$

Usually flux will be measured for a specific frequency range, ν, in which case the difference between the observed and emitted frequency must be taken into account through a *k-correction* (Hogg et al., 2002).

1.1.4 Evidence for Dark Matter

Measurements of the cosmological density parameters indicate that while matter constitutes ∼25% of the Universe, the observable matter, baryonic matter, (Ω_b) only accounts for ∼4%. The remaining matter is not directly observable and is therefore termed "dark matter", but is inferred by its effects on the luminous component of the Universe through the motion of luminous matter within galaxies, the dynamics of galaxies in clusters, and by gravitational lensing. Although the nature of dark matter is as yet unknown, evidence of its existence through its gravitational effects on baryons has been observed for decades.

The existence of missing matter was first noted by Zwicky (1933) when analysing the radial velocities of galaxies in the Coma cluster and discovering the galaxies only contributed to a small fraction of the total gravitating mass of the cluster.

The rotational velocity of stars and interstellar gas on circular orbits within galaxies is expected to decrease at large radii as the observed mass, $M(r)$, decreases:

$$V_{\mathrm{circ}}(r) = \sqrt{\frac{GM(r)}{r}}, \tag{1.17}$$

This is not found when analyzing the rotation curves of spiral galaxies. Rather they retain a fairly constant velocity out to large radii. Such a rotation curve can be explained by a system contained within a larger, more extended mass, namely a dark matter halo (e.g. Rubin & Ford, 1970; Persic et al., 1996).

The mass of a dark matter halo, can be measured by measuring its gravitational lensing effect on luminous background objects (i.e. other galaxies). The light from the distant object is distorted by the gravitational field of the foreground halo, which can result in multiple images of the background object, or distorted shapes or arcs. The density field of the invisible "lensing" mass is measured by modelling the mass expected to produce such a distortion assuming general relativity. While individual strong lensing studies focus on the mass distributions within specific galaxy clusters (e.g. Smail et al., 1994), wide-field lensing surveys such as the Canada-France-Hawaii Telescope Lensing Survey (CFHTLenS) (e.g. Gillis et al., 2013) map the dark matter mass distribution over a large scale in the universe using weak gravitational lensing, which produces a subtle change in the appearance of the background galaxies.
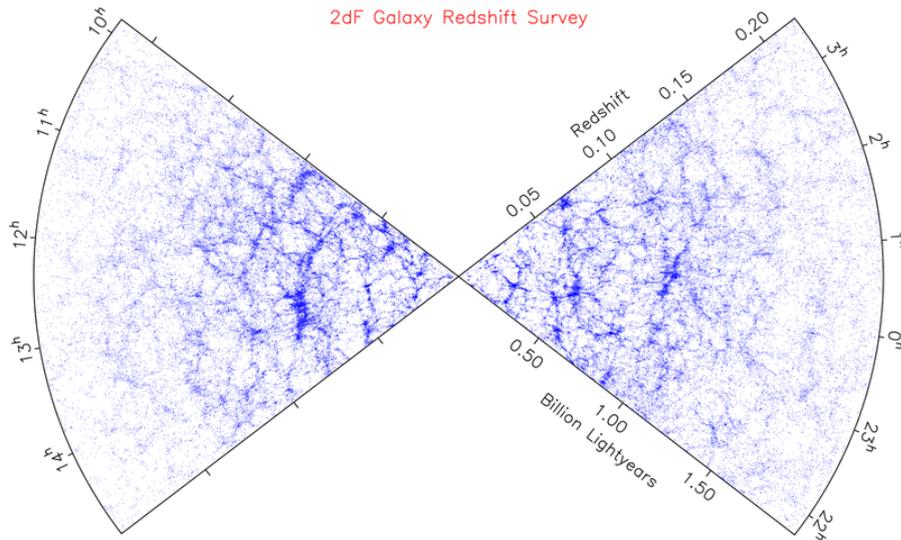
Figure 1.2: Map of the distribution of galaxies in the 2dF Galaxy Redshift survey. Image from Colless et al. (2003).

1.1.5 Structure formation

The Universe is approximately homogeneous and isotropic on scales larger than $\sim 100 \, \text{Mpc}$. On smaller scales gravity plays the dominant role in the formation of the intricate cosmic web of structure seen in the visible Universe (e.g. Fig. 1.2).

The observed large-scale structure is the result of the growth of tiny perturbations in an otherwise smooth density field, which grew in amplitude with the expansion of the Universe and collapsed through gravitational instability to form the network of structure seen today.

These deviations are essentially linear density perturbations on a smooth background, for $\delta \ll 1$, but the growth of the perturbations is no longer well approximated by linear theory for higher overdensities, and non-linear effects start to dominate. The non-linear growth of such perturbations lead to the formation of voids, sheets, filaments and knots, manifestions of the large scale structure visible in the Universe, like that seen in Fig. 1.2.

1.1.6 Constraining Cosmological Parameters

In order to investigate aspects of the large-scale structure of the Universe, cosmological parameters must first be set to provide a description of the geometry and

expansion history of the Universe.

Constraining the density parameters, $\Omega_{M,0}$ and $\Omega_{\Lambda,0}$, is a non-trivial task due to the degeneracies between them. Type Ia supernovae have a standardizable value for their peak luminosity (Arnett, 1969), making them useful standard candles (Sandage & Tammann, 1982) covering a large range of redshifts. Distances to Type Ia supernovae therefore allow measurements of the expansion of the Universe (Perlmutter et al., 1999; Riess et al., 1998) to be made, suggesting a non-zero cosmological constant and leading to the discovery of dark energy.

Modern constraints have been introduced by measurements of the anisotropies in the temperature and polarisation of the cosmic microwave background (CMB). The small temperature fluctuations in the CMB provide an angular power spectrum, the shape of which can be modelled and is sensitive to $\Omega_{M,0}$ and $\Omega_{\Lambda,0}$.

1.2 Galaxy Redshift Surveys

The redshift of an object provides a measure of its radial distance from us. Therefore a 3D map of the observable Universe can be obtained by mapping the redshifts of detected galaxies over a region of the sky, as shown in Fig. 1.2. Tracing the structure of matter by analysing galaxy groups and clusters helps to provide constraints on the effect of the structure on galaxy properties.

Using galaxy spectra, the spectroscopic redshift of the galaxy is measured by comparing the wavelengths of emission and absorption lines to template spectra. The speed of obtaining such spectra and the quality of galaxy redshifts has improved over time and consequently galaxy redshift surveys have become larger and more complete.

With the increasing availability of large galaxy surveys (e.g. GAMA; Driver et al., 2011), the properties of galaxy such as colour, morphology, luminosity, stellar mass, and their dependence on both the local and large scale environments can be explored and compared to predictions from galaxy formation models. Increasing survey depth also provides a means to study the evolution of galaxy properties and their dependence on environment, paving way to a more thorough understanding of

galaxy evolution.

1.2.1   Characterising the galaxy population

Galaxy number counts are a simple statistical tool adopted in the analysis of early galaxy surveys, and quantify the number of galaxies per solid angle for a given magnitude (e.g. Ferguson et al., 2000), providing a useful tool to test models describing galaxy populations (e.g. Driver et al., 1998).

Another commonly used statistical tool is the galaxy luminosity function (Schechter, 1976; Efstathiou et al., 1988; Loveday et al., 2012; Blanton et al., 2003b) which characterises the distribution of luminosity for a sample of galaxies, and is expressed as the number of galaxies per unit volume for a given luminosity, $\phi(L)$. The luminosity function, $\phi(L)$, can be estimated by simply summing the number of galaxies in a luminosity bin, weighted by the inverse of the maximum volume over which the galaxy can be seen in the survey, $V_{\max}$ (e.g. Schmidt, 1968; Eales, 1993), taking into account the survey selection. While this approach does not require a parameteric shape for the luminosity function, a uniform distribution of galaxies is assumed and the resulting estimate of the luminosity function is therefore sensitive to large-scale structure. Alternatively, the luminosity function can be estimated using the non-parametric step-wise maximum likelihood (SWML) approach of Efstathiou et al. (1988). A Schechter (Schechter, 1976) function, with a power-law slope at the faint end and an exponential decline in abundance at the brightest luminosities, is generally found to be a good description of the shape of the luminosity function.

Galaxy colours provide an indication of some of the processes a galaxy has undergone during its evolution. Red galaxies suggest the presence of older and redder stellar populations, more metals, and more dust extinction, while blue galaxies indicate populations of bright, young stars. Galaxies can also be classified morphologically, for example using the Hubble tuning fork. Historically, elliptical and lenticular galaxies are commonly referred to as *early-types*, while spiral and irregular galaxies are *late-types*. However, these terms bear no implications for the epoch at which these galaxies formed.

1.3 Outline of Thesis

The work presented in this thesis explores the relationship between the distribution of galaxies and their properties in the Galaxy and Mass Assembly (GAMA) survey, and provides comparisons to predictions from the galaxy formation model GALFORM. The environment in which a galaxy resides can shape its evolution, and subsequently the observable properties of the galaxy, such as luminosity and colour. A measure of environment as traced by the spatial distributions of galaxies can provide useful information about the underlying dark matter halo in which the galaxies reside, and the impact of the properties of the underlying halo (e.g. mass) can be investigated.

The outline of this thesis is as follows. The galaxy sample and technical survey details of the GAMA survey, and previous scientific results relevent to this work, are summarised in Chapter 2.

The models of galaxy formation used to provide predictions for the GAMA survey are discussed in Chapter 3, along with the method for constructing lightcone mock catalogues for direct comparison with GAMA observations.

Chapter 4 explores the relationship between the galaxy luminosity function and the local galaxy environment, as traced by the galaxy overdensity within spheres of $8\,h^{-1}\mathrm{Mpc}$, parametrising the change in shape of the luminosity with overdensity. The evolution of the luminosity function, and its dependence on galaxy colour within each environment is explored.

Chapter 5 extends the work presented in Chapter 4 to larger scales and a different means of quantifying the environment, investigating the dependence of the luminosity function on a geometric classification of the cosmic web.

Chapter 6 presents a pipeline for measuring the properties of dark matter haloes, as constructed in the Millennium N-body simulation, which was used as a baseline for the implementation of the GALFORM model and the construction of lightcone mocks.

The galaxy density profile in GAMA groups is measured in Chapter 7, again comparing to GALFORM. This work utilises the calculation of dark matter halo properties to constrain estimates of radius and mass as traced by galaxies, also providing a comparison of the galaxy denisty profile to the dark matter density

profile in GAMA.

A summary of the work presented in this thesis is given in Chapter 8, along with possible directions for future work.

Chapter 2

The Galaxy and Mass Assembly (GAMA) Survey

This thesis focuses on the analysis of the Galaxy And Mass Assembly (GAMA) survey to constrain theoretical models of galaxy formation and evolution. Galaxy spectra were collected at the Anglo-Australian Telescope (AAT), providing reliable spectroscopic reshifts for 238,000 objects over 5 regions of the sky. With photometry from ultraviolet to far-infrared, GAMA is a truly multi-wavelength redshift survey.

This chapter gives a brief overview of galaxy surveys and describes the details of the GAMA survey which are relevent to the work presented in this thesis.

2.1 Galaxy redshift surveys

Galaxy redshift surveys allow us to probe the large-scale structure of the Universe and the formation and evolution of galaxies. The latter is quantified by measuring statistics like the galaxy luminosity function, the stellar mass function and the two-point galaxy correlation function, as well as their evolution. A deep survey such as GAMA allows better constraints to be placed on the evolution of galaxies than has been possible using earlier shallower surveys.

One of the earliest galaxy redshift survey, the CfA Redshift Survey (Huchra et al., 1983), began in 1977 and measured 2,401 galaxy redshifts over 5 years. Galaxy spectra were obtained on a galaxy by galaxy basis, and obtaining galaxy redshifts

was a slow process. Later the CfA2 survey (Falco et al., 1999) increased the number of redshifts to 13,700.

The ability to explore the physical aspects of galaxy formation was greatly extended with the improved number statistics and depth of modern spectroscopic redshift surveys. In particular, the 2dF Galaxy Redshift Survey (2dFGRS; Colless et al., 2003), obtained 245,591 galaxy spectra, limited to a b_J band magnitude of 19.45, with a median redshift of $z{\simeq}0.1$ and covering an area of the sky of about $\sim$1500 deg^2. The Sloan Digital Sky Survey (SDSS; York et al., 2000) saw first light in 1998, obtaining imaging in five passbands, u, g, r, i, z, providing a million galaxy redshifts by 2007 down to a depth of $m_r = 17.77$, also corresponding to a median redshift of $z{\simeq}0.1$ and allowing the large-scale structure of the Universe to be measured over more than 7000 deg^2 on the sky.

Building on local surveys such as 2dFGRS and SDSS, deeper redshift surveys provide a valuable tool to constrain galaxy evolution. For example, the Canada-France Redshift Survey (CFRS; Lilly et al., 1995) was designed to have a median redshift of 0.6, measuring 700 redshifts down to $m_I \leq 22.5$. More recently, $\sim$10,000 galaxy redshifts were obtained with the zCosmos bright survey (Lilly et al., 2007, 2009), covering 1.7 deg^2 on the sky, down to an I-band apparent magnitude limit of $m_I = 22.5$, observing $0.1{<}z{<}1.2$. The DEEP2 Galaxy Redshift survey (Newman et al., 2013), consisting of 38,000 reliable redshifts over the range $0{<}z{<}1.4$, provides a particularly dense galaxy sample, covering 2.8 deg^2 split into 4 regions on the sky, to an r-band limit of $m_r = 24.1$.

The large area and depth of such surveys provides a large volume within which galaxy formation models can be tested. Future galaxy redshift surveys aim to increase the observed volume by simultaneously increasing both survey area and depth. For example the Bright Galaxy Survey (BGS) which will be carried out with the Dark Energy Spectroscopic Instrument (DESI) (Levi et al., 2013) will provide redshifts for galaxies down to $m_r = 19.5$, a similar depth to GAMA, but over an area of 14,000 deg^2, thus probing a volume 50 times larger than GAMA. The 4MOST WAVES-Deep and WAVES-Wide surveys (Driver et al., 2015) will build on the success of the GAMA survey, providing redshifts for $\sim$2 million galaxies down to

$m_r = 22$, extending the statistical power of previous galaxy surveys to $z\sim1$.

A comparison of the area and on-sky number density of galaxy spectra for various galaxy surveys is given in Fig. 2.1. GAMA is a multi-wavelength, highly complete spectroscopic redshift survey which allows the large-scale structure in the galaxy distribution to be measured to a depth $z < 0.51$, over a large area of the sky ($286 \deg^2$), and represents a compromise between area and on-sky spectra number density in comparison to surveys with a similar depth. The ability of GAMA to probe galaxies 2 magnitudes fainter than SDSS provides a large increase in the volume of the Universe probed for a fixed solid angle. The median redshift of GAMA ($z\sim0.25$) is subsequently more than twice that of SDSS ($z\sim0.1$).

2.2 Science Goals of GAMA

One of the main science goals of GAMA is to study structure formation in the Universe. In particular, measurements of the halo mass function provide a direct test of the CDM model in the observable Universe. The halo mass function is dependent on the values of the cosmological parameters, gravity and the velocity dispersion of the dark matter particle, with only a small dependence on baryons at high and intermediate halo masses (Springel et al., 2005), and therefore depends only weakly on galaxy formation. While previous surveys have allowed measurements of the halo mass function (e.g. Eke et al., 2004), only halo masses greater than $10^{14}\,\mathrm{M_\odot}$ have been probed for redshifts $z < 0.12$. The motivation for deeper surveys, such as GAMA, is to provide constraints on the halo mass function down to lower halo masses, $10^{12}\,\mathrm{M_\odot}$ (the mass at which the efficiency of galaxy formation is thought to peak), with the ability to observe lower mass haloes to higher redshifts. The solid angle of GAMA also provides a reasonable number of massive haloes at low redshifts.

Other studies of structure formation which can be undertaken with GAMA include constraining models for redshift-space distortions, describing the line-of sight dynamics of galaxies in clusters and measuring the growth of structure at different epochs in the Universe. The ability of deep surveys like GAMA to probe lower mass
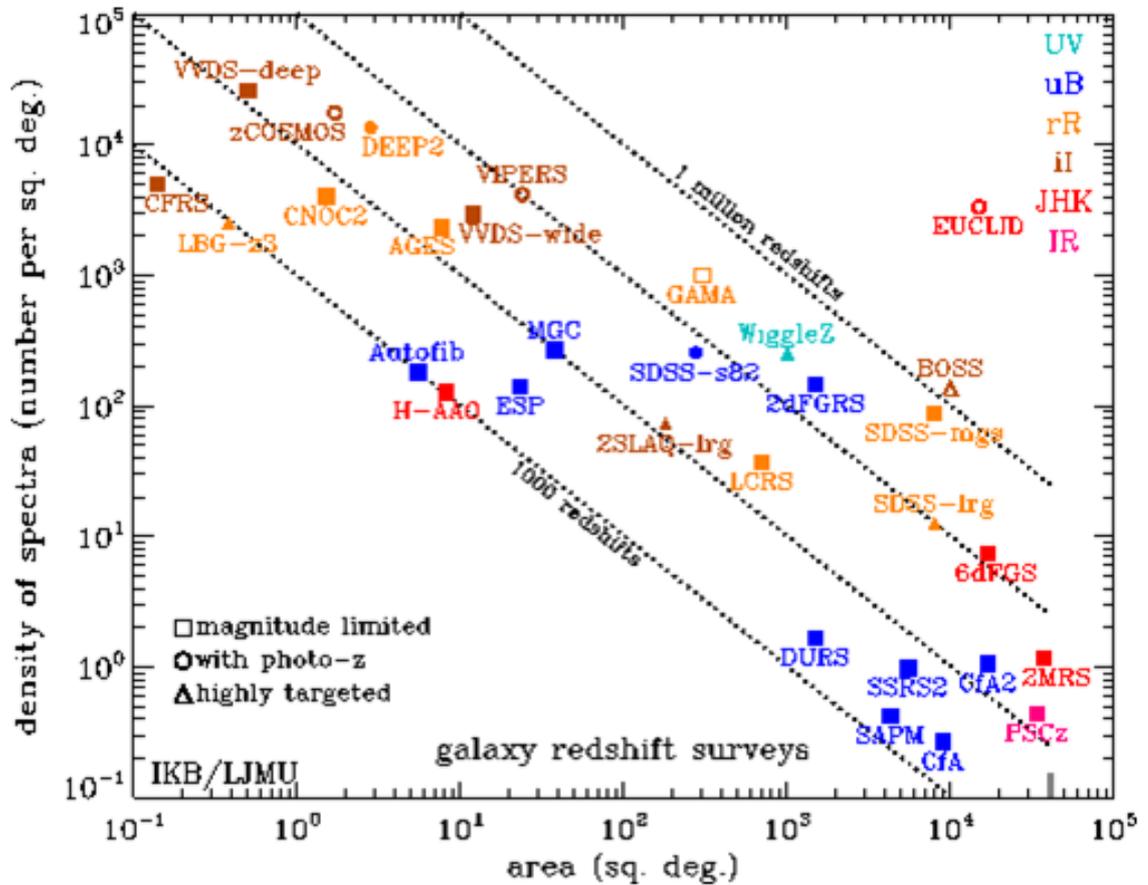
Figure 2.1: Number density of spectra against area on the sky for a selection of galaxy surveys. Squares indicate surveys which are magnitude limited, circles show surveys with colour cuts for photometric redshift selection, and triangles show surveys which are targeted to observe specific samples (e.g. luminous red galaxies). Colours indicate the selection wavelength of each survey (see labels). The GAMA survey makes a compromise between area and depth, allowing accurate measurements of the statistical properties of galaxies and their evolution. Image credit: Ivan Baldry (`http://www.astro.ljmu.ac.uk/~ikb/research/galaxy-redshift-surveys.html`).

haloes also allows the variation of star formation with halo mass to be probed down to less massive galaxy groups than previously possible.

On smaller scales, another motivation for GAMA is to develop a better understanding of the moderation of star formation in galaxies. Feedback mechanisms in galaxies and the regulation of gas fuelling star formation are not yet fully understood (Hopkins et al., 2008; Schaye et al., 2015, ; Lacey et al. *in prep*).

Environment is thought to play a significant role in galaxy evolution. On small scales close pairs and mergers have an impact on the star formation in galaxies and hence their evolution. On larger scales, theoretical models link galaxy properties to the mass of the host halo in which they reside.

2.3   GAMA Survey Details

The galaxy sample used in this thesis consists of the equatorial fields of the GAMA-II survey, described in Liske et al. (2015), which cover a total of $180\,\mathrm{deg}^2$ over three regions of the sky, centred on 9^h (G09), 12^h (G12) and 15^h (G15). Each region covers $5 \times 12\,\mathrm{deg}^2$, around a declination of $\delta \simeq 0°$, and down to a Petrosian (Petrosian, 1976) r-band apparent magnitude of $m_r = 19.8$. Reliable spectroscopic redshifts were obtained for 178,579 galaxies, corresponding to a spectroscopic completeness of 98.48% and providing a median redshift of $z = 0.25$. Galaxy colours are measured using SDSS model magnitudes in 5 photometric bands (u,g,r,i,z), and stellar mass estimates are derived from aperture magnitudes (Hill et al., 2011).

2.3.1   Technical Survey Details

Observations for GAMA were made using the 3.9m Anglo-Australian Telescope (AAT). Galaxy light is fed through fibres positioned by the 2 degree Field (2dF) fibre positioner, split into two dispersed beams and analysed using the AAOmega multi-fibre benchmounted spectrograph (Sharp et al., 2006) to obtain galaxy spectra. The 2dF allows the simultaneous analysis of up to 392 galaxy spectra over a two degree field of view, with $2''$ fibres. Taking into account fibres which are broken and therefore unusable for galaxy targets, on average only 342.5 fibres were available

per field (Liske et al., 2015).

Tiling Algorithm

Since each 2dF observation covers 2 degrees in diameter on the sky, a tiling algorithm (Robotham et al., 2010) was implemented to efficiently cover the entire area of each region. Fig. 2.2 shows the distribution of observed fields for each GAMA region. Since the 2dF instrument was designed to make the shallower 2dF Galaxy Redshift Survey, the number of fibres per square degree (at most $124 \, \mathrm{deg}^{-2}$) is significantly less than the on-sky number density of galaxies in GAMA ($\sim 1000 \, \mathrm{deg}^{-2}$). GAMA regions must therefore be visited multiple times in order to obtain spectra for all targetted galaxies. For the regions relevant to this thesis, G09, G12 and G15, each position within the region is visited on average >10 times, so in total more than 200 fields are observed in each region.

The algorithm for tiling the GAMA regions is chosen to optimise both the quality and quantity of the galaxy spectra observed. The chosen approach is described in Robotham et al. (2010), and efficiently samples the high density of galaxies on the sky due to the depth of the survey. The tiling algorithm prioritises particularly dense regions, and galaxies with unsuccessful redshift measurements are observed again. In order to investigate close pairs of galaxies, one of the main science goals of GAMA, fields with close pairs are re-visited, prioritising fibre placement for each of the pair to avoid fibre collisions.

With the use of an optimal tiling algorithm, GAMA has very high spatial completeness, particularly on small scales as is highly desirable for finding galaxy groups and determining group properties.

Input Catalogue

The GAMA equatorial regions were selected in the region of the sky previously observed by SDSS. Dust maps (e.g. Schlegel et al., 1998) indicate that for the GAMA regions the Galactic dust extinction in the r-band is less than $0.25 \, \mathrm{mag}$. The angular width of the GAMA fields is motivated by the requirement to probe a larger volume for group finding, allowing a measurement of the halo mass function at low redshift.
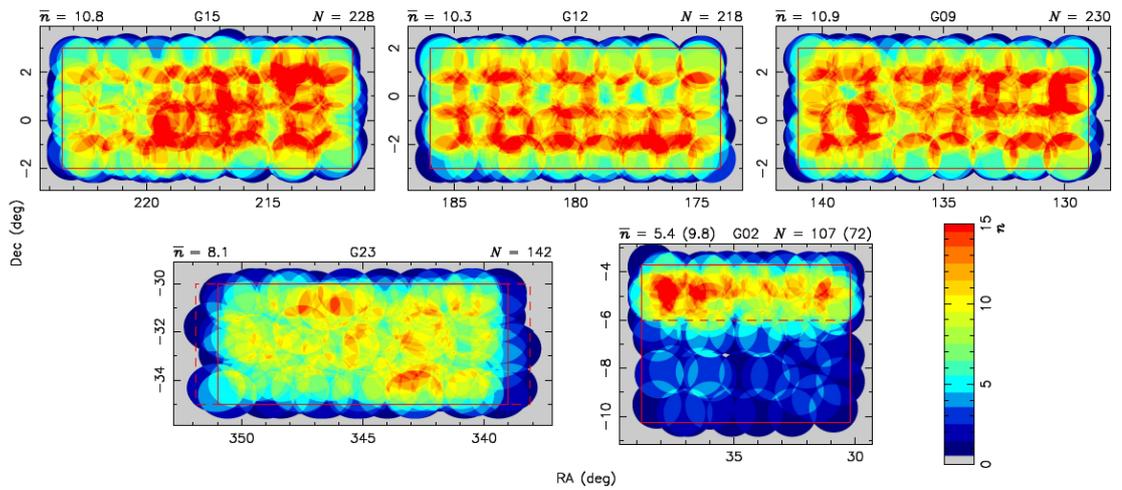
Figure 2.2: Tiling of each of the GAMA regions, indicated as the area within the solid red rectangles. The colour coding shows the number of times each position has been observed by a 2dF/AAOmega field, n, while the average number of times a position is visited, $\bar{n}$, is given at the top left for each region. The total number of 2dF/AAOmega fields, N, is indicated on the top right for each region. While the fields of interest for this thesis are the top three (G15, G12 and G09), the tiling of an additonal two southern fields, G23 and G02, are also shown. Figure from Liske et al. (2015).
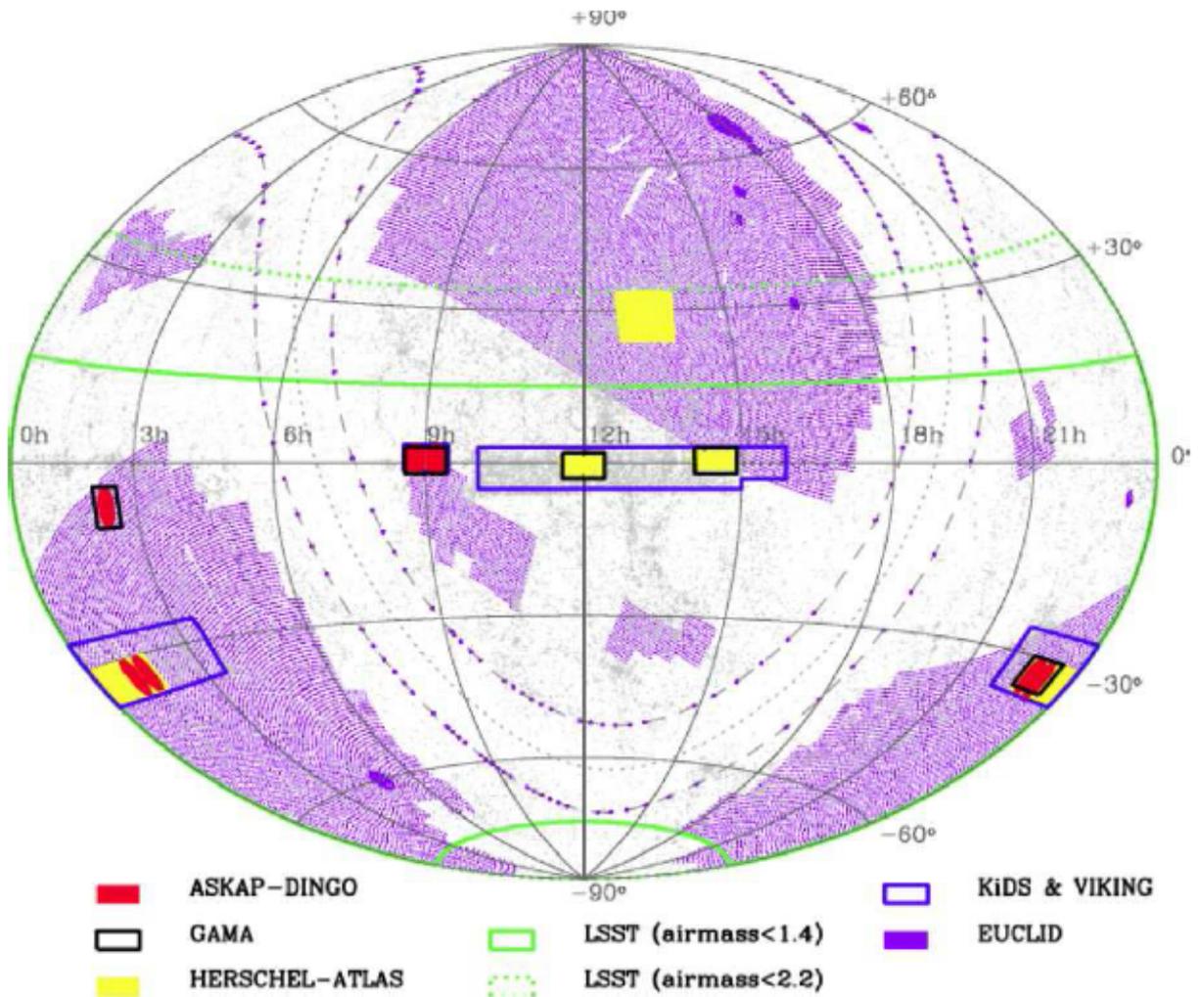
Figure 2.3: GAMA-II regions (black boundaries) shown in comparison to other on-going (e.g. Herschel-ATLAS and VST KiDS) and future surveys (e.g. Euclid, LSST). Figure from Driver (2015).

The survey targets for GAMA-I were selected from SDSS DR6 imaging, and for GAMA-II, were updated to DR7 imaging. The positions of the GAMA regions are motivated by the positions of photometric samples from comparable redshifts surveys, with which photometry from UV to far-IR can be obtained for galaxies in GAMA. Fig. 2.3 shows the positions of the GAMA regions (black rectangles) in comparison to the Herschel-ATLAS (Eales et al., 2010) which complements the GAMA survey, providing far-infrared photometry, as well as future surveys such as Euclid (Laureijs et al., 2011).

Photometry

Photometry is available for all galaxies in the GAMA equatorial sample in the
ugrizYJHK bands, with imaging data from SDSS (Abazajian et al., 2009) and
UKIDSS (Lawrence et al., 2007). The galaxy sample is selected in the Petrosian
r-band (Petrosian, 1976) and galaxy colours are calculated using SDSS model mag-
nitudes [1]. While the Petrosian magnitude of an object is measured by fitting a
circular aperture around the object, with the aim of capturing a large fraction of the
total light, the SDSS model magnitudes depend on the model (i.e. a de Vaucouleurs
profile or an exponential profile) which best describes the light profile. Details of the
fitting processes involved in photometry for GAMA are given in Hill et al. (2011).
While magnitudes are re-calculated for galaxies in GAMA, the Petrosian and Model
magnitudes used in this work are the original SDSS magnitudes.

In addition galaxy surveys which overlap with GAMA provide complementary
photometry in 21 bands from the far-UV (e.g. Martin et al., 2005, Galex) to the
mid-infrared (e.g. Cluver et al., 2014, WISE) and far-infrared (e.g. Eales et al., 2010,
Herchel-ATLAS).

Magnitudes in GAMA are also corrected for the effect of dust in the Milky Way
which absorbs and scatters extragalactic light, making galaxies appear redder than
their intrinsic colour (Schlegel et al., 1998).

Spectroscopic redshifts

The observed wavelengths of emission and absorption lines in a galaxy spectrum
are used to estimate its spectroscopic redshift. Previously, GAMA redshifts were
determined using the code RUNZ (see e.g. Driver et al., 2011), which is similar to
that used for 2dFGRS (Colless et al., 2001). For each spectrum the redshift is
verified by the user and a quality, nQ, from 1 (bad) to 4 (good) is assigned. An
automated code, AUTOZ, described in Baldry et al. (2014), was designed to improve
the reliability of redshift measurements by cross correlating the galaxy spectra with
extensive emission and absorption line template spectra. The median redshift error

---

[1]`http://classic.sdss.org/dr7/algorithms/photometry.html`
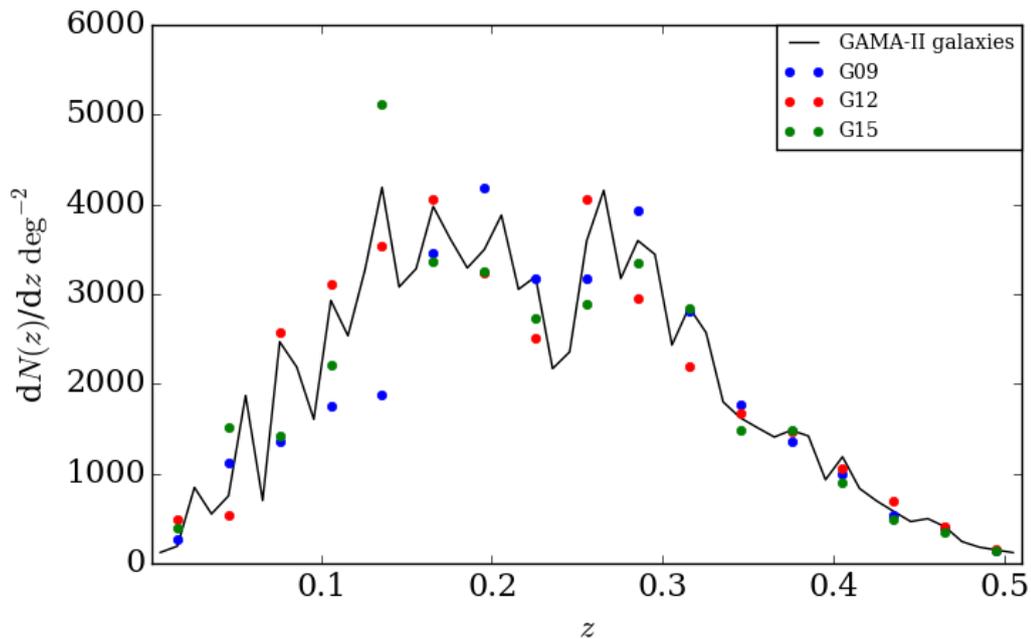
Figure 2.4: Redshift distribution, $N(z)$ per solid angle, for galaxies in GAMA-II (black line) and in each equatorial region (dots, see key). Sample variance due to structure is clear in each region, particularly for low redshifts where the survey volume is small.

when using AUTOZ is $33\,\mathrm{km\,s^{-1}}$, which is much smaller than that obtained with RUNZ (see Fig. 19 of Liske et al. 2015). Lower redshift errors improve the estimates of the dynamical properties of galaxy groups.

To use galaxy redshift as a reliable measure of cosmological distance, the measured heliocentric redshifts are converted to the rest frame of the cosmic microwave background (CMB) (Baldry et al., 2012), providing an estimate of the cosmological redshift (but including the effects of peculiar velocities). For low redshifts ($z<0.03$) the effect of local velocity flows are also accounted for using the flow model described by Tonry et al. (2000).

The distribution of redshifts in each of the equatorial regions in GAMA is shown in Fig. 2.4. The effect of structure on the redshift distribution is clearly seen in each region, causing significant variations in the $N(z)$. This is less significant at higher redshifts where the survey volume is larger and sample variance is smaller.

Survey completeness mask

Reliable redshifts are obtained for more than 98% of galaxies in the GAMA equatorial regions. The combination of imaging completeness (of the input catalogue), target completeness (targets for which spectra are available) and spectroscopic completeness (the success rate of obtaining spectroscopic redshifts) affects mostly the observation of the lowest surface brightness galaxies (Loveday et al., 2012). When analysing statistical properties requiring spatial information (e.g. galaxy clustering studies), a completeness mask is used to take into account the completeness of the survey in a given region of the sky.

k-corrections

To account for the difference between the wavelength range over which flux is observed within a given passband and the wavelength range over which the flux was emitted in the galaxy's rest frame, the observed magnitude of an object is *k-corrected* (Hogg et al., 2002). Magnitudes of galaxies in GAMA are k-corrected using the KCORRECT algorithm (Blanton et al., 2003a). The algorithm requires the passband used and the galaxy's redshift, an estimate of the spectral energy distribution (SED) and a reference redshift. Knowledge of the k-correction of a galaxy at a different redshift is sometimes required (e.g. to measure the maximum redshift out to which a galaxy can be seen at the survey apparent magnitude limit when constructing a volume limited sample). A polynomial of the form:

$$K(z) = \sum_{i=0}^{4} a_i (z - z_{\text{ref}})^i,$$ (2.1)

with reference redshift z_{ref}, and polynomial coefficients a_i, is adopted to describe the k-correction of a galaxy as a function of redshift. The polynomials for each galaxy in GAMA are provided in a k-correction DMU (Data management unit) (Loveday et al., 2012). In Chapter 4 a further refinement of the k-correction is introduced, making use of the dependence of $K(z)$ on galaxy colour.

To compare galaxy populations across time, it is common to correct for the evolution of the characteristic galaxy luminosity and number density (e.g. Lin et al.,

1999; Loveday et al., 2012). Luminosity evolution is parameterised using a linear dependence on redshift and a scaling parameter Q, such that the characteristic magnitude of the luminosity function at a given redshift, $M^*(z)$, is corrected to:

$$M^*(z) = M^*(z_{\rm ref}) - Q(z - z_{\rm ref}).$$ (2.2)

The density evolution is parameterised using a power law dependence on redshift and a scaling parameter P, correcting the normalisation of the luminosity function for a given redshift, $\phi^*(z)$, as:

$$\phi^*(z) = \phi^*(z_{\rm ref})10^{0.4\,P(z-z_{\rm ref})},$$ (2.3)

for a reference redshift, $z_{\rm ref}$. There are strong degeneracies between P and Q, making the precise measurements of each difficult (Loveday et al., 2015).

In this work magnitudes are k-corrected and luminosity is evolution corrected to $z_{\rm ref} = 0$.

2.4 Applications of the GAMA survey

The GAMA survey has provided new insights into the formation and evolution of galaxies in the Universe, helping to constrain models of galaxy formation.

The aim of the work presented in this thesis is to build on and extend previous studies of the dependence of galaxy properties on environment, thereby better understanding how galaxies form and evolve with respect to their local and large-scale environments.

2.4.1 The galaxy luminosity function

The galaxy luminosity function is a primary constraint on galaxy formation models, and provides information about galaxy evolution if the luminosity function can be measured at various epochs. A survey such as GAMA provides not only the volume to supply a large sample of galaxies which can be used to reliably measure the luminosity function at low redshifts, but also the depth over which the evolution of

the luminosity function can be quantified. In particular, the shape of the faint end of the luminosity function at low redshift is yet to be precisely constrained due to the inability to observe the lowest luminosity galaxies in previous surveys as a result of their shallow depth compared to GAMA.

Loveday et al. (2012) measured the GAMA galaxy luminosity function in 5 photometric bands, u,g,r,i,z, and characterised the shape of the galaxy luminosity function as a function of colour. They find that for $z < 0.1$, while the luminosity function of blue galaxies is well fitted by a simple Schechter function (Schechter, 1976) in all photometric bands, whereas the luminosity function of red galaxies and consequently the full sample require a double power-law Schechter function to fit the upturn in galaxy abundance towards the faintest luminosities. The steepness at the faint end for red galaxies is thought to be partly due to the reddening of edge-on disc galaxies caused by dust. Blue and red galaxy populations exhibit different luminosity evolution, with stronger evolution seen for red galaxies such that the characteristic luminosity is brighter at higher redshifts. As expected from theories of galaxy evolution, the galaxy density increases with redshift for blue galaxies, while decreasing with redshift for red galaxies.

The degeneracy between the luminosity and density evolution parameters, Q and P, is further explored in Loveday et al. (2015) for GAMA-II data, by constraining the galaxy luminosity function using a joint stepwise maximum likelihood method (Cole, 2011), which simultaneously provides an estimate of the luminosity function and the luminosity density evolution. Degeneracies in P and Q are found such that $Q = 1.4 - 0.4P$. Again blue galaxies are found to exhibit a stronger luminosity density evolution than red galaxies.

2.4.2   Galaxy environment

The role of environment on the formation and evolution of galaxies is still unclear. While it has been long established that red, passive galaxies predominantly reside in dense environments (e.g. Dressler, 1980), the physical processes causing this dependence on environment are not well understood. Large, complete surveys such as GAMA allow us to measure galaxy environment, locally and on larger scales,

hence helping to understand how environment influences the evolution of a galaxy population. Using the GAMA survey, various measures of environment have been investigated. Most significantly these are local environments, as measured by the nth nearest neighbour technique (e.g. Wijesinghe et al., 2012) or by the overdensity within spheres (Chapter 4, McNaught-Roberts et al., 2014), and galaxy groups (Robotham et al., 2011). Galaxy groups can be used to investigate the properties of galaxies in filaments and voids in the larger scale cosmic web environment (Alpaslan et al., 2014). Alternatively, a larger scale environment can be characterised using a geometric definition of environment (Chapter 5, Eardley et al., 2015).

The 3D local galaxy overdensity, estimated within spheres of a given radius, is implemented in Chapter 4 to investigate the dependence of the galaxy luminosity function and colour distribution on local environment. This analysis is then extended in Chapter 5 to also take into account the geometric environment within the cosmic web.

Galaxy groups provide a measure of environment that is motivated to be analogous to dark matter haloes. The high completeness of GAMA allows a more accurate determination of galaxy groups than has been possible using previous surveys (e.g. 2dFGRS, Eke et al. 2004; SDSS, Yang et al. 2007). Details of the group catalogue for GAMA (produced in Robotham et al. 2011) are given in Chapter 7 of this thesis. The group finding algorithm requires constraints on parameters through the use of mock catalogues, which are introduced in Chapter 3, to optimise the recovery of the underlying dark matter haloes. The distribution of GAMA galaxies which are in groups is shown in Fig. 2.5, for $z < 0.213$. The work presented in Chapter 7 investigates how the radial distribution of galaxies traces the radial distribution of the dark matter, by measuring the galaxy density profile in haloes in the mock catalogues and in GAMA groups.

The high completeness and depth of the GAMA survey allows us to test a variety of environment definitions and investigate the dependence of galaxy properties on environment. By constructing mock catalogues which imitate the selection effects of the GAMA survey (Chapter 3), the physical processes involved in galaxy formation can be further constrained.
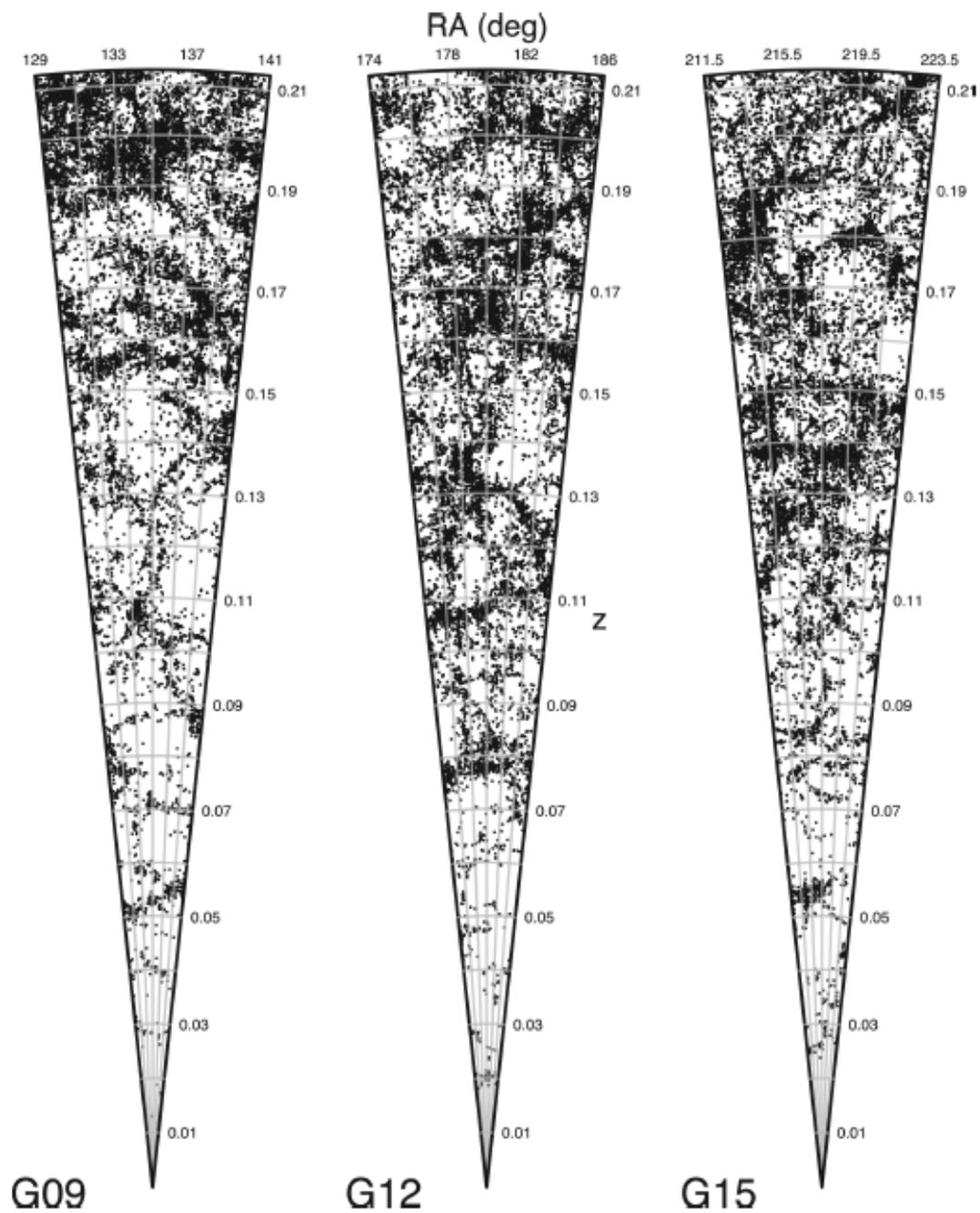
Figure 2.5: Galaxies which reside in groups with two or more members in the GAMA-II equatorial regions, which are volume limited to $z = 0.213$. Figure from Alpaslan et al. (2014).

Chapter 3

Theoretical infrastructure for the GAMA lightcone mocks

Galaxy surveys such as GAMA can provide valuable constraints on models of galaxy formation. Galaxy formation models provide predictions for the distribution of galaxy luminosities, colours, sizes, morphologies, spatial clustering, and how these properties relate to the underlying dark matter in the Universe. The ability to create mock catalogues to imitate the observable Universe is a valuable tool not only to test the models, but also to assess the effects of selection criteria on the ability to measure statistical properties of galaxies in the Universe from surveys of real galaxies.

This chapter describes the process through which such mock galaxy catalogues are generated for comparison to the GAMA survey, starting with a dark matter N-body simulation used to model the underlying matter distribution in §3.1. The physical prescriptions implemented in the galaxy formation model, GALFORM, populating dark matter haloes with galaxies, are outlined in §3.2. Finally, §3.3 describes the method used to generate lightcone mock catalogues from the simulation volume populated with galaxies, imitating the selection criteria of the GAMA galaxy survey.

3.1 Dark Matter framework

Observations of the dynamics of galaxies suggest galaxies form in dense regions of dark matter, therefore galaxy formation models first require a dark matter framework to be defined. The standard cosmological model adopted for simulating the structure formation in dark matter is the ΛCDM paradigm, for a Universe dominated by a cosmological constant, Λ, and with a matter component dominated by cold dark matter (CDM).

3.1.1 N-body simulations

The formation and hierarchical build-up of structure is calculated through numerical simulations (e.g. Davis et al., 1985; Springel et al., 2005; Boylan-Kolchin et al., 2009), where dark matter particles are assumed to be collisionless point particles which interact only through gravitation. Such *N-body* simulations require the assumption of a cosmology and theory of gravity. The adopted cosmology is determined by recent observations, such as those from the Wilkinson Microwave Anisotropy Probe (WMAP, Spergel et al., 2003), or more recently the Planck satellite (Planck Collaboration et al., 2014) while gravity is generally assumed to be Newtonian. The size of the computational box used in the simulations is chosen to be sufficiently large to depict a reasonable cosmological volume within which galaxy formation models can be tested, sampling a range of environments, while also probing the smallest scales within dark matter substructures.

The simulations adopted here are the Millennium Simulation (Springel et al., 2005) and MS-W7 (e.g. Guo et al., 2013), a list of parameters for which can be found in Table 3.1. The Millennium-II simulation (Boylan-Kolchin et al., 2009) is designed to have a higher mass resolution with the same number of particles, therefore covering a smaller volume.

The positions and velocities of dark matter particles are output at *snapshots*, corresponding to specific redshifts, the time between which is sufficiently small to allow dark matter halo merger trees to be constructed.

Simulation	Cosmology	L	$m_{\rm p}$	$N_{\rm p}$
	$(\Omega_0,\ \Lambda_0,\ \sigma_8)$	$(\,h^{-1}{\rm Mpc})$	$(h^{-1}{\rm M}_\odot)$	
Millennium	WMAP1 (0.25, 0.75, 0.9)	500	8.61×10^8	2160^3
Millennium-II	WMAP1 (0.25, 0.75, 0.9)	100	6.88×10^6	2160^3
MS-W7	WMAP7 (0.272, 0.728, 0.81)	500	9.31×10^8	2160^3

Table 3.1: Dark matter simulations and the corresponding cosmology, box length (L), particle mass ($m_{\rm p}$), and number of particles ($N_{\rm p}$) in the simulation.

3.1.2   Identifying haloes

Dark matter haloes are generally defined by using algorithms which group particles, linking those which are close together, such as the friends-of-friends (FoF) algorithm (Davis et al., 1985), or by locating an overdensity maxima with a halo extent determined by setting a minimum density enclosed within the halo (e.g. Press & Schechter, 1974).

The method for finding haloes adopted here is as follows. Particles at each snapshot are grouped together by a FoF algorithm with a linking length of $b = 0.2$ (in units of mean particle separation). Particles belonging to FoF haloes are shown in the left side of Fig. 3.1. Self-bound, locally overdense subhaloes within each FoF halo are found using the algorithm, SUBFIND (Springel et al., 2001), with the resulting subhaloes indicated in the right of Fig. 3.1 by coloured circles. SUBFIND identifies local overdensity maxima within the parent FoF halo to define subhaloes containing only gravitationally bound particles. Particles not belonging to a subhalo contribute to the background particle "fuzz".

Halo finders generally define haloes based on a FoF algorithm (e.g. ROCKSTAR Behroozi et al., 2012), or by locating local overdensities within the dark matter density field (e.g. AHF Knollmann & Knebe, 2009). Knebe et al. (2011) compares a wide range of halo finding codes, such as ROCKSTAR, AHF and SUBFIND, finding a broad agreement in the resulting halo properties and mass functions. A well behaved halo finder is essential when tracking haloes through snapshots, since the loss of mass in subhaloes accumulates through time, resulting in a lower subhalo mass function (Han et al., 2012).

FoF halo   **Subhalos within FoF halo**
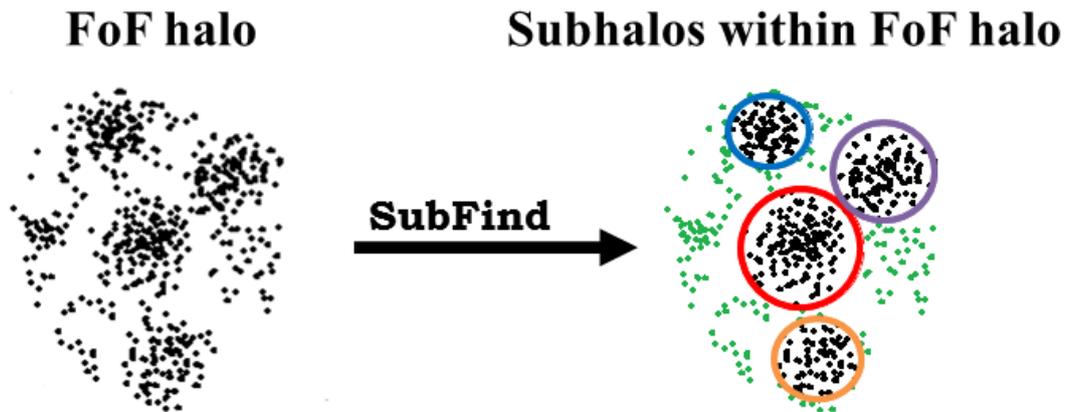
SubFind →

Figure 3.1: Schematic describing the identification of subhaloes. *Left*: Particles are grouped into a FoF halo. *Right*: Within the FoF halo, SUBFIND determines self-bound, locally overdense subhaloes (coloured circles). Particles not belonging to a subhalo (green) contribute to the particle "fuzz" in the halo.

3.1.3   Dhalo merger trees

Galaxy formation models require knowledge of how haloes grow through mergers. A *merger tree* connects haloes between snapshots, resulting in branches defining sets of *progenitor* haloes that have merged together, and are identified at a later time as *descendants*.

The process of creating Dhalo merger trees, as adopted by the galaxy formation model used in this thesis, is described in detail in Jiang et al. (2014). To summarise, merger trees follow the descendants of haloes through time to link together subhaloes into a "Dhalo". Once a subhalo falls into a larger halo, is within twice the half mass radius of the larger halo, and loses more than 25% of its mass, it becomes part of the Dhalo. It will then always be considered part of the Dhalo at later times, even if the radius condition is no longer satisfied. An example of this is shown in Fig. 3.2, where haloes B and C, originally belonging to their own Dhaloes, fall into halo A, becoming satellites of the larger parent halo A. After B and C fall in, they belong to the Dhalo at all later times, regardless of whether or not they remain in the vicinity of the halo. In this example halo C becomes unresolved and merges with A, while B remains as a subhalo within A.
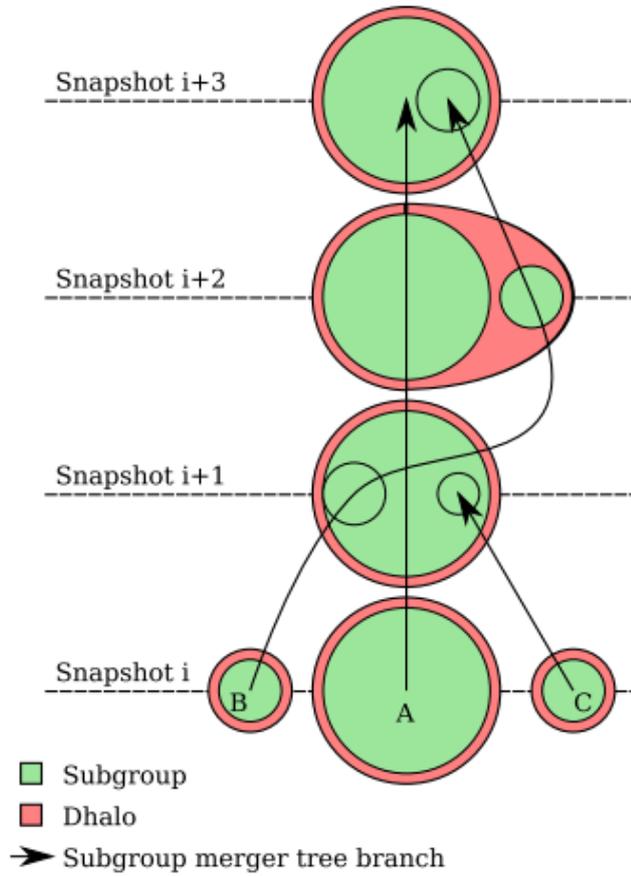
Figure 3.2: Schematic showing an example of a Dhalo merger. At snapshot i, haloes A, B and C are distinct and belong to their own individual Dhaloes. Subhaloes B and C fall into A by snapshot $i + 1$, then although B is no longer residing within A at snapshot $i + 2$, it still belongs to the Dhalo, and always will at later times. At snapshot $i + 3$, B has rejoined A. Figure from Jiang et al. (2014).

Subhaloes are followed between snapshots by identifying the descendant containing the most bound 10% of the subhalo's mass (or the 10 most bound particles if this is a larger mass). If a subhalo within a Dhalo is not recovered in a snapshot, it can still be considered part of the Dhalo if recovered up to 5 snapshots later. This is to ensure subhaloes are not lost if they are temporarily unresolved when passing through a region of higher density. The central subhalo is defined as the most massive subhalo within a host Dhalo.

The mass of a Dhalo at any time is defined as the sum of all particle masses in subhaloes of the Dhalo. Since particles within a subhalo can be stripped and lost, the mass of a subhalo can change, and the lost particles contribute to the main subhalo. In the case of heirarchical galaxy formation models such as GALFORM where haloes are assumed to monotonically increase in mass over time, the loss of mass is undesirable, and so in GALFORM, Dhalo merger trees are restricted to never lose mass.

The main advantage of using Dhaloes rather than FoF haloes is the ability to separate substructures linked by tenuous low density bridges of material in FoF haloes. Dhalo masses are found to be more indicative of the virial mass of a halo than FoF halo masses (Jiang et al., 2014), and are therefore more relevant for the work presented in this thesis (specifically Chapters 6 and 7).

3.2 Implementation of galaxy formation models

With the framework of the underlying dark matter density laid out, models describing how galaxies form in dark matter haloes can be formulated.

Populating dark matter haloes with galaxies can be done empirically through halo occupation distribution (HOD) modelling, where the number of galaxies occupying a halo depends on the halo mass (Berlind & Weinberg, 2002).

Two more physically motivated approaches to populating dark matter haloes with galaxies are described as *semi-analytic* models and *hydrodynamical* simulations.

In the case of semi-analytics (e.g. GALFORM, Cole et al. 2000; LGALAXIES, Springel et al. 2001; GALACTICUS, Benson 2012), prescriptions for the physical pro-

cesses governing galaxy formation are analytically modelled in the form of a set of differential equations. Although uncertain, the parameters describing such processes are constrained to match observable properties (e.g. the present day galaxy luminosity function). The ability to change prescriptions by altering these parameters allows the impact of various physical processes on galaxy formation to be explored. Hydrodynamical simulations track the flow of baryonic matter, numerically solving the hydrodynamical equations which govern the evolution of baryons. Physical processes which affect baryons on smaller scales than are directly resolved (e.g. supernova and AGN feedback) are dubbed "sub-grid" physics, and are treated similarly to semi-analytic prescriptions.

While hydrodynamical simulations can probe much smaller scales than semi-analytics, they are computationally expensive and cannot provide the large cosmological volume on the scale of galaxy surveys. For this reason semi-analytical models are ideal for comparison to the Universe observed by galaxy surveys, and to test the impact of imposed selection functions on the observed distribution of galaxies.

3.2.1 GALFORM, a physical model of galaxy formation

The semi-analytical model, GALFORM, is adopted in this thesis to determine how galaxies populate dark matter haloes. GALFORM, introduced by Cole et al. (2000), implements some prescriptions for the physical processes governing the formation of galaxies, briefly summarised as the following.

- Gas falls into a potential well of a virialised dark matter halo and is shock heated to create a hot gas halo. Further gravitational collapse of the gas is prevented by thermal pressure, with a temperature, T, which depends on the halo mass. This temperature determines the ionisation state, chemical composition and density of the gas, and determines the rate of radiative cooling. Cooled gas then falls into the centre of the halo over the dynamical timescale of the halo, forming a rotationally supported disk at the centre (Efstathiou & Fall, 1984).

- Star formation in galaxies is determined by the rate at which gas cools from

the halo, which is further moderated by energy feedback processes preventing the hot gas from cooling or ejecting cold gas from galaxies. Forms of feedback include supernovae, which heat up the cold gas forming bubbles which flow into the hot gas halo.

- An empirical relation based on observations between the star formation rate and the surface density of molecular hydrogen was introduced to the model by Lagos et al. (2012), implementing a star formation law which depends on the amount of H_2 rather than the total cold gas mass.

- A stellar initial mass function (IMF) specifies the distribution of stellar masses produced when star formation occurs in galaxies. The IMF adopted in the models considered here is that proposed by Kennicutt (1983), which is consistent with the solar neighbourhood IMF.

- To stop the formation of more bright galaxies than are observed, a prescription for AGN feedback is implemented. For galaxies residing in the massive haloes, material is accreted onto the central black hole, resulting in large amounts of energy being injected into the hot gas halo. The cooling of gas is suppressed if the energy released exceeds that which would be released by cooling. This process is described and implemented in Bower et al. (2006), and is only effective for galaxies undergoing quasi-hydrostatic cooling in the model.

In GALFORM galaxies evolve differently depending on whether they are central or satellite galaxies. A galaxy is placed at the centre of its host subhalo, unless the subhalo becomes unresolved, in which case it is instead tagged to the most bound particle which belonged to the subhalo. The galaxy residing in the most massive subhalo of a Dhalo is treated as the central galaxy in the halo, otherwise it is a satellite. If a central galaxy falls into a larger halo, it becomes a satellite of the larger halo.

Examples of possible merging senarios for galaxies and haloes are depicted in Fig. 3.3 over a period of a few snapshots. Originally at snapshot $S1$ both galaxies are centrals in their own distinct subhaloes. At snapshot $S2$, the galaxy in the
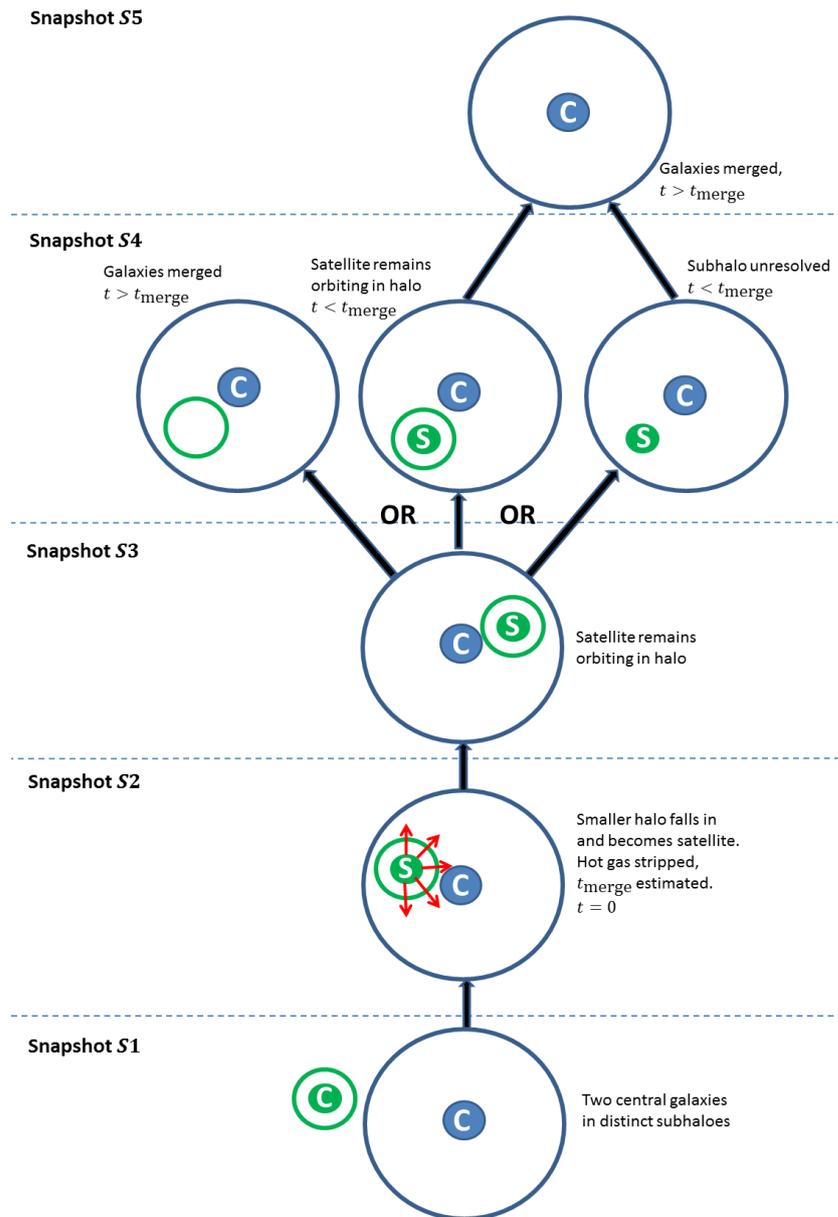
Figure 3.3: Schematic depicting the treatment of galaxy mergers in the GALFORM models considered in this thesis, from the infall of the satellite subhalo, over 5 snapshots, for cases ending with the two galaxies merging. The merger timescale is determined analytically at infall. The calculated timescale can result in the satellite subhalo being far from the centre of the halo after the satellite galaxy has merged (*left option* at snapshot 4). Typically the satellite and its host subhalo will remain orbiting in the host halo for some time (*middle option*). Sometimes the satellite halo might become unresolved within the parent halo and the satellite galaxy which has not yet merged is instead located on to the most bound particle from the lost subhalo (*right option*). More than one snapshot may exist between each stage pictured here.

smaller halo falls into the larger halo, and becomes a satellite within the larger halo. Due to ram pressure stripping, the hot gas halo is immediately stripped from the new satellite to join the main hot gas halo, and star formation can only continue while there is cold gas remaining in the disk, and so star formation is rapidly quenched in the satellite. At the moment of infall, $t = 0$, a dynamical friction timescale for the satellite galaxy to merge with the central galaxy is calculated, t_{merge}, based on the initial energy and angular momentum of the satellite's orbit, the mass of the satellite and the mass of the host halo (see §4.3.1 of Cole et al. 2000). However, since the evolution of the subhalo's orbit is not taken into account, the estimation of t_{merge} may be inaccurate. The system remains as a satellite galaxy residing in its subhalo orbiting within the host halo at snapshot $S3$. If the merging timescale t_{merge} is small, the satellite galaxy will be considered to have merged with the central galaxy early on, and the satellite subhalo may remain resolved but without a galaxy in the larger halo. This is shown by the left branch of snapshot $S4$. The middle branch shows a typical case where $t < t_{\mathrm{merge}}$ and the satellite galaxy has not yet merged with the central, and still has a resolved subhalo. Alternatively, for cases where $t < t_{\mathrm{merge}}$, the branch on the right of snapshot $S4$ shows the case where the subhalo of the satellite galaxy becomes unresolved, since the dark matter density of the subhalo is not sufficiently larger than the background density of the parent halo. The subhalo will be considered to have merged with the host halo. If t_{merge} is large, the time for the satellite to merge with the central galaxy may be unrealistically large. At this point the satellite is likely to reside close to the centre of the halo and its subhalo is likely to be unresolved, since the density at the centre of the parent halo is high. Once the merger timescale has passed, the galaxies are considered merged (snapshot $S5$). If the host halo becomes a subhalo of a larger system at a time before galaxies have merged, t_{merge} is recalculated based on the new parent halo.

The effects of the assumption that hot gas is immediately lost from satellite galaxies at the moment of infall into their host haloes is investigated in Font et al. (2008), who implement a model for gradual ram pressure stripping following the work of McCarthy et al. (2008). The most massive satellite galaxies retain some of their hot gas halo such that the cold star-forming gas in the disk can be replenished

allowing further star formation, reproducing the observed fraction of blue satellite galaxies. This prescription is not implemented in the model of GALFORM adopted here, but one of the possible extentions that could be done to the models considered in this work.

3.3 Lightcone mock catalogues

To compare the output of simulations with observations of the real Universe, catalogues of model galaxies are created from the simulations, imitating those observed in galaxy surverys. These mock catalogues not only take into account the geometry of the galaxy survey but also limitations on the galaxy sample caused by the survey selection criteria. As well as the ability to directly test the physics implemented in the models against observations, the mocks provide a means to test statistical analysis methods and to understand how galaxies relate to the underlying dark matter haloes, for example interpreting the properties of galaxy groups in redshift surveys. While mock catalogues can be required to simply reproduce current observations in order to make predictions for future galaxy surveys (Orsi et al., 2010), or make use of Halo Occupation Distribution (HOD) modelling to populate dark matter haloes with galaxies to model clustering in galaxy surveys (e.g. LasDamas, McBride et al., 2009), the mock catalogues described here can be utilised for a broad range of applications.

The algorithm used to generate the lightcone mocks is presented in Merson et al. (2013), and briefly summarised here.

3.3.1 Lightcone geometry

The construction of the lightcone first requires a simulation box to be defined, containing dark matter haloes populated with galaxies through a galaxy formation model. For the purposes of this work, the lightcone is constructed within the Millennium (Chapter 4) or MS-W7 (Chapters 6, 7) simulation box (see Table. 3.1), populated with galaxies from the Bower et al. (2006) (Chapter 4) or the Gonzalez-Perez et al. (2014) (Chapters 6,7) GALFORM model. The observer is placed at a

random location within the simulation box, with a randomly chosen orientation. A sphere centred on the observer is constructed, with a comoving radius, r_{max}, corresponding to the maximum redshift observed in the real survey. The sphere is then cut into wedges to create a solid angle covering the same fraction of the sky as the galaxy survey. If the survey contains multiple fields, the wedges keep the separation of the fields on the sky.

Fig. 3.4 gives a 2D representation of the geometry of a lightcone, with the observer "O", placed at the centre of the simulation box (highlighted by the outer square). The outer circle indicates the maximum distance from the observer observed in the survey, corresponding to a maximum redshift, and the survey fields are indicated by the shaded wedges.

An ideal case is shown in Fig. 3.4, where the simulation box is large enough to enclose the cosmic volume covered by the galaxy survey. However, the simulation box will usually not be large enough (the $500\,h^{-1}\mathrm{Mpc}$ box in the Millennium simulation corresponds to a redshift of $z \sim 0.17$). In this case the simulation box is then replicated around the original box multiple times to provide the volume required. For reasonably small or narrow surveys the repetition of structure is unlikely, since the observer can usually be placed with an orientation such that the same region of the box is not seen by the lightcone more than once. For the simulations considered here, if structure is sampled more than once, it will be at different epochs within the lightcone. Multiple lightcone mock catalogues can be provided for one survey by placing the observer at different positions with different orientations within the survey box.

With the lightcone geometry in place, a galaxy's cosmological redshift is directly calculated from the comoving distance between the galaxy and the observer. The concentric circles seen in Fig. 3.4 show different snapshots corresponding to the redshift at that distance from the observer. The specific redshift of the galaxy is found by its position within the simulation box and hence may correspond to a time between snapshots. The galaxy's position in the lightcone is then found by interpolating between snapshots.
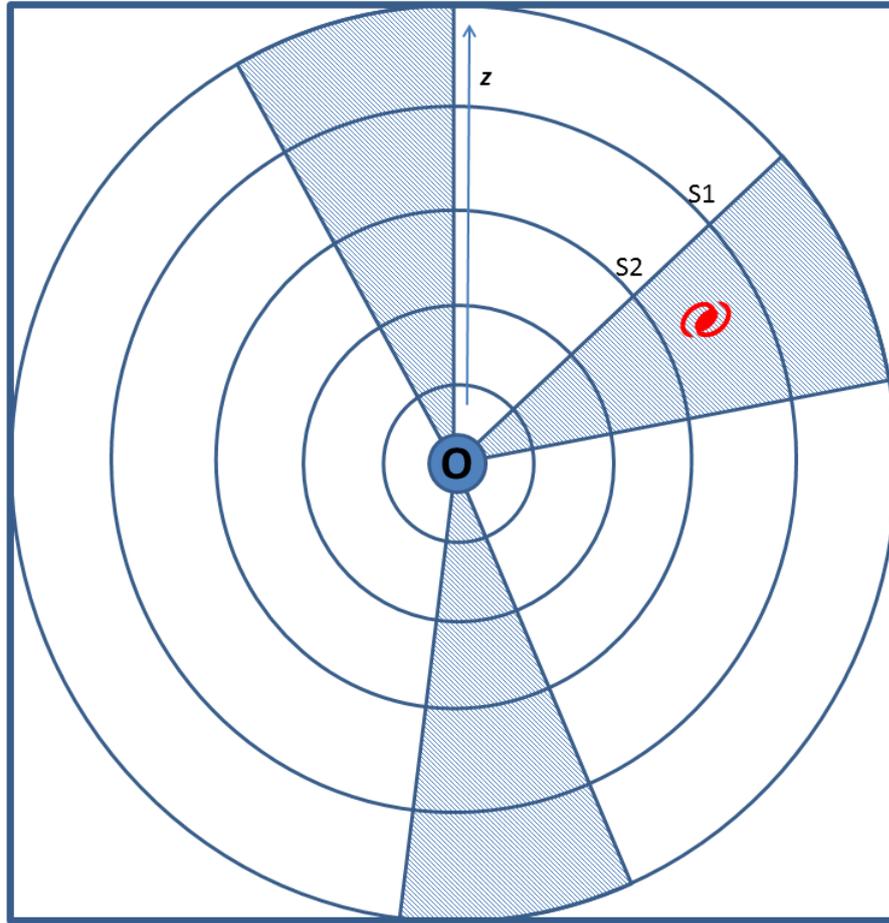
Figure 3.4: A 2D representation of the construction of a lightcone, assuming the simulation box is large enough to simulate a galaxy survey. In this case the observer ('O') is placed at the centre of the simulation box (outlined by the square), and 3 fields imitating the geometry of the survey are constructed (shown here by shaded wedges). Concentric circles indicate snapshots determined by the redshift at a given distance from the observer. Properties of a galaxy are taken to be those at the snapshot with the highest redshift closest to that of the galaxy, (e.g. S1 for the red galaxy here). The galaxy's position is determined by interpolating between snapshot S1 and S2.

3.3.2   Lightcone galaxy properties

Once the galaxies in the lightcone have been assigned positions and cosmological redshifts, galaxy properties can be determined. Since galaxy properties are only output at specific redshifts corresponding to snapshots in the simulation, it is not possible to infer what has happened to the galaxy between snapshots. Therefore galaxy properties cannot be inferred for a specific redshift, and the intrinsic properties, such as rest-frame luminosity and stellar mass, assigned to a galaxy are those taken from a snapshot with a redshift previous to that of the galaxy. For example the galaxy shown in red in Fig. 3.4 is assigned properties from the output corresponding to the first concentric circle enclosing the galaxy, labelled as S1.

The positions and intrinsic properties of galaxies allow for observable properties to be estimated. To reproduce the selection effects of galaxy surveys, the apparent magnitude or flux in given photometric bands must be calculated for each galaxy. The luminosity is determined for a photometric band by a filter response, R, defined at the redshift corresponding to an output snapshot. The absolute magnitude of a galaxy in a given photometric band therefore corresponds to the total luminosity emitted over the frequency range with the filter response of the band.

Given the observer frame absolute magnitude, M, of a galaxy at snapshot redshift z (and corresponding luminosity distance, d_{L}), the apparent magnitude m is determined as:

$$m = M + 5 \log_{10} \frac{d_{\mathrm{L}}(z)}{10 Mpc} - 2.5 \log_{10}(1 + z), \tag{3.1}$$

where the last term accounts for the variation in the filter bandwidth with redshift.

The addition of the line of sight peculiar velocity v_{r}, to the cosmological redshift z_{cos} of a galaxy, provides an observed redshift, z_{obs}, given by:

$$z_{\mathrm{obs}} = (1 + z_{\mathrm{cos}}) \left(1 + \frac{v_{\mathrm{r}}}{c}\right) - 1. \tag{3.2}$$

The availability of both cosmological and observed redshifts allow tests of how peculiar velocities affect the measurements of cosmological distances in galaxy surveys, and are essential for studying the dynamics of galaxies in groups.

With a complete catalogue of galaxies defined by their positions, redshifts and

intrinsic and observed properties, the lightcone catalogues can be made survey specific by applying the survey selection criteria. Galaxies which have an observed flux fainter than the specified flux limits of the survey are rejected from the catalogue. The survey incompleteness is not considered in the lightcone generation. However, this does not significantly affect comparisons with surveys such as GAMA for which the redshift completeness is very high ($> 98\%$).

In practice, lightcones can be generated from any GALFORM model, and are a very effective way of determining how different prescriptions of physics in galaxy formation present themselves in galaxy surveys.

3.3.3   GAMA lightcone mocks

The lightcone mock catalogues generated for the use of the work presented in this thesis are created to imitate the GAMA survey. The specifics of the survey selection criteria are discussed in Chapter 2, but in short consist of 5 fields (3 of which are used here), each covering an angle on the sky of $5 \times 12 \, \mathrm{deg}^2$, with an apparent magnitude limit in the r-band of $m_r < 21$. This faint apparent magnitude limit is deeper than in GAMA, and the effect of applying different selection criteria can be tested. 26 mock catalogues are produced by placing the observer at different positions with different orientations as discussed previously. Such a large number of realisations of the mocks increase the number statistics with which to test the model, but structure repetition due to use of a periodic simulation box can become large.

The distributions of galaxy redshifts and r-band apparent magnitudes in GAMA and in the lightcones (constructed using the Gonzalez-Perez et al. (2014) model of GALFORM) are given in Fig. 3.5. The number of faint galaxies in the lightcones is slightly lower than observed in GAMA. To ensure the number density of galaxies is comparable in the GAMA survey and lightcones, a faint apparent magnitude limit of $m_{\mathrm{r}} = 19.9$ is imposed on the lightcone mocks. With this faint magnitude limit imposed, the redshift distribution of mock galaxies closely follows that of GAMA galaxies. Similarly, the r-band galaxy luminosity function in the GAMA lightcones (shown in Fig. 3.6), which is not tuned to match the observed luminosity function, is a remarkably good match to the luminosity function of galaxies in the GAMA
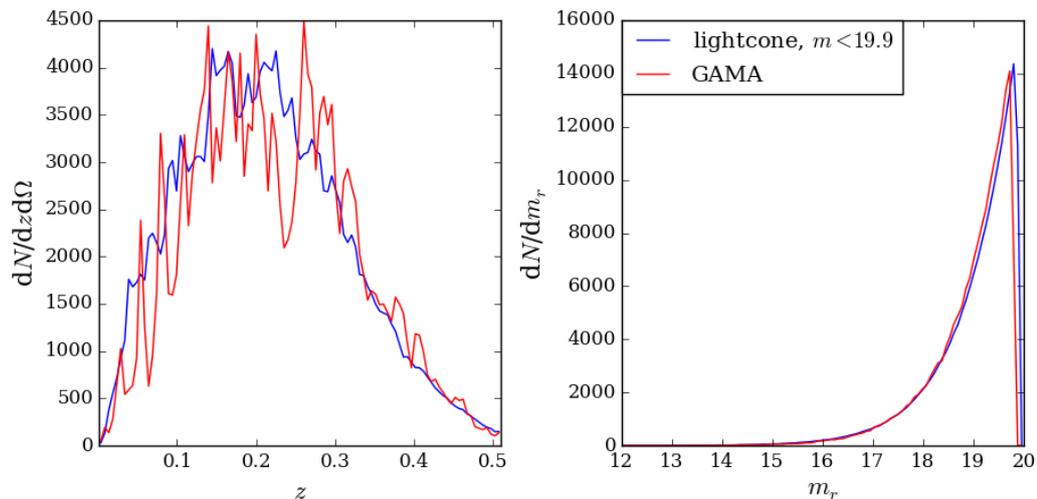
Figure 3.5: Redshift distribution (*left*) and distribution of r-band apparent magnitudes (*right*) for galaxies in the GAMA survey (red) and in the lightcone mocks (blue). The distributions for the mock galaxies are averaged over the 26 lightcone mocks, and limited to include galaxies with $m_r < 19.9$ ($m_r < 19.8$ for galaxies in the GAMA survey).

survey, particularly at the bright end.

Halo lightcone mock catalogues are also generated, for the purpose of assessing the properties of dark matter haloes in the mocks. These halo mock catalogues contain all dark matter Dhaloes that would have been included in a survey with no magnitude limit (and hence contain at least one galaxy), and which fall within the redshift range and angular boundary of the survey. This also helps to test the effects of applying magnitude limits to galaxy surveys. The halo mocks do not depend on the galaxy formation model used, so long as the haloes considered are massive enough to host a galaxy in any of the models, regardless of the galaxy formation physics prescribed.

The lightcone mocks adopted in Chapter 4 (and to optimise the GAMA group finder discussed in Chapter 7) are constructed using the GALFORM model described in Bower et al. (2006), using a cosmology based on WMAP1 observations. The GALFORM model used to construct the lightcone mocks adopted in Chapters 6 and 7 is described in Gonzalez-Perez et al. (2014), instead using a cosmology based on the more recent WMAP7 observations. To account for the different cosmology, some parameters of the model (e.g. feedback efficiencies) are altered between these two
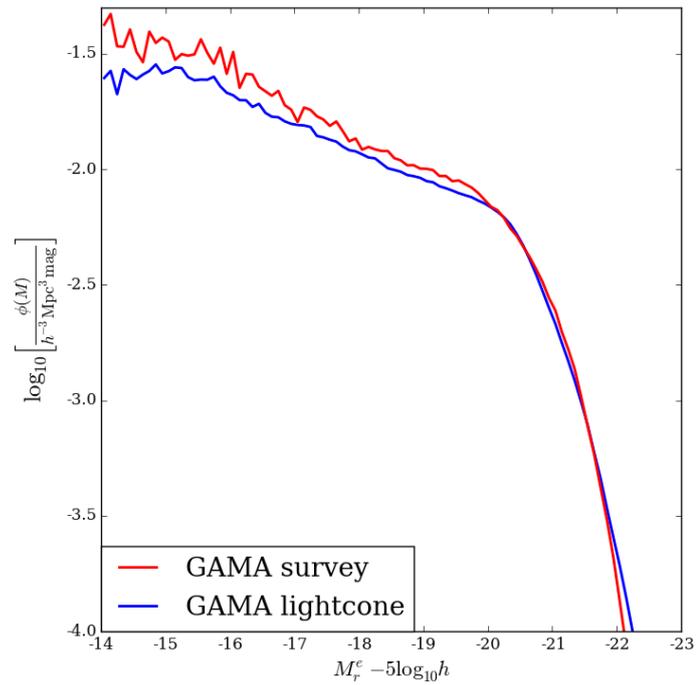
Figure 3.6: r-band galaxy luminosity function in the GAMA survey (red) and the GAMA lightcones (blue). The lightcone galaxy luminosity function is averaged over 10 lightcone mocks and limited to include galaxies with $m_r < 19.9$ ($m_r < 19.8$ for galaxies in the GAMA survey).

models to reproduce the observed optical luminosity function at $z = 0$.

3.4 Summary

This chapter has provided an overview of the generation of GAMA lightcone mock catalogues, for comparison with the GAMA survey, details of which are provided in Chapter 2. The simulations providing the dark matter framework are first introduced, along with the application of the halo finder, SUBFIND, and the Dhalo merger tree, to identify dark matter haloes and trace their merger histories. The physical prescriptions relevent to this thesis, which are implemented in the semi-analytical model GALFORM are then listed, and the treatment of central and satellite galaxies in haloes is discussed. With the underlying dark matter simulation and galaxy formation model laid out, the lightcone geometry is constructed from the simulation box, and galaxies are assigned properties in the lightcone mock catalogues. By applying the selection effects and geometry of the GAMA survey, the lightcone mocks become theoretical representations of the GAMA survey, readily available to use as a tool for testing the physical prescriptions implemented in the galaxy formation model and to assess the impact that selection effects have on galaxy surveys such as GAMA.

Chapter 4

The Dependence of the Galaxy Luminosity function on Local Environment

We use 80922 galaxies in the Galaxy And Mass Assembly (GAMA) survey to measure the galaxy luminosity function (LF) in different environments over the redshift range $0.04 < z < 0.26$. The depth and size of GAMA allows us to define samples split by colour and redshift to measure the dependence of the LF on environment, redshift and colour. We find that the LF varies smoothly with overdensity, consistent with previous results, with little environmental dependent evolution over the last 3 Gyrs. The modified GALFORM model predictions agree remarkably well with our LFs split by environment, particularly in the most overdense environments. The LFs predicted by the model for both blue and red galaxies are consistent with GAMA for the environments and luminosities at which such galaxies dominate. Discrepancies between the model and the data seen in the faint end of the LF suggest too many faint red galaxies are predicted, which is likely to be due to the over-quenching of satellite galaxies. The excess of bright blue galaxies predicted in underdense regions could be due to the implementation of AGN feedback not being sufficiently effective in the lower mass haloes.

4.1 Introduction

The galaxy luminosity function (LF) is a fundamental tool for probing the distribution of galaxies in the observable Universe. Measuring how the LF varies with environment and other galaxy properties can help us to constrain the environmental processes involved in galaxy formation and evolution.

Large galaxy redshift surveys have allowed accurate measurements of the LF over a large area and depth (e.g. Lin et al. 1996; Norberg et al. 2002b; Blanton et al. 2003b; Loveday et al. 2012), with samples big enough to split by redshift and galaxy property. These large surveys have allowed the measurement of the LF in voids (Hoyle et al., 2005) and over a large range of environments (Bromley et al., 1998; Hütsi et al., 2002; Croton et al., 2005; Tempel et al., 2011). Splitting these samples by different galaxy properties also allows an accurate analysis of how galaxies behave in these environments (e.g. Dressler 1980).

Historical studies of the dependence of the LF on environment have been restricted to the comparison of cluster and field galaxies, due to the small number of galaxies observed. It has been well established that the LF in clusters is significantly different from that of field galaxies. For example, De Propris et al. (2003) found that the LF in clusters in the 2dF Galaxy Redshift Survey (2dFGRS, Colless et al. 2003) differs from the field LF (Madgwick et al., 2002). The cluster LF has a characteristic magnitude (M^*) that is 0.3 magnitudes brighter, and a faint-end slope (α) that is steeper by 0.1 than the field LF. To measure the LF over a larger range of environments, and to include galaxies in voids, deep and highly complete galaxy surveys are needed.

Croton et al. (2005) measured the b_J-band LF for a range of environments in the 2dFGRS, finding no significant variation of the faint-end slope with environment. However, M^* varies smoothly with environment being brighter in denser regions. When further splitting samples by spectral type, faint, late-type galaxies dominate void regions, and clusters contain an excess of bright early-types. This dependence of galaxy properties such as colour on environment has previously been found to be stronger than the morphology-density relation described in Dressler (1980) (see Blanton et al., 2005). A comparable analysis by Tempel et al. (2011), using Sloan

Digital Sky Survey (SDSS) (Abazajian et al., 2009), reached a similar conclusion, namely that the faint-end slope depends only weakly on environment. Splitting the SDSS sample by morphological type, Tempel et al. (2011) concluded the environmental dependence is strong for elliptical galaxies, but the LF of spirals is almost independent of environment. They also found that the brightest galaxies are absent from void regions, which instead are mainly populated by spirals. These dominate the faint end of the LF, whereas the bright end is dominated by ellipticals.

Alternatively, the environmental dependence of the LF can be investigated by considering the properties of groups in which galaxies reside. Robotham et al. (2006) measured the LF for galaxies in the 2PIGG group catalogue (Eke et al., 2004) for different group luminosities, finding the faint-end slope steepens and M^* brightens with increasing group luminosity, but these trends flatten for very rich clusters. This trend is visible for the entire population as well as when split by colour. Following on from this work, Robotham et al. (2010) investigate how the LF varies as a function of virial mass and group multiplicity. Both the 2PIGG and the Yang et al. (2005) (SDSS) group catalogues show similar variations of the galaxy LF with these properties.

The measure of density used determines the underlying environment that can be probed, thus helping to identify the key physical processes that shape galaxy formation. Friends-of-friends algorithms (e.g. Davis & Huchra 1982; Eke et al. 2004; Robotham et al. 2011) are a good probe of the scales internal to a dark matter halo, whereas fixed sized apertures are a better measure of the large scale environment, essentially tracing the underlying dark matter distribution (Muldrew et al., 2012). Brough et al. (2013) and Wijesinghe et al. (2012) both defined local environment as the 5th nearest neighbour surface density when measuring the dependence of the star formation rate on environment in GAMA. The GAMA Group catalogue is constructed by Robotham et al. (2011) using a friends-of-friends algorithm, to measure how galaxy properties depend on the underlying matter distribution. This is used by Alpaslan et al. (2014) to construct a catalogue of filaments, probing the large scale structure of the Universe, and by Vázquez-Mata et al., (in prep) to determine how the LF varies with various group properties.

Galaxy formation models have been used to determine the underlying physical processes that shape the LF (Benson et al., 2003a), particularly the faint end, and to predict how the LF changes with environment (Benson et al., 2003b; Mo et al., 2004). In particular, the influence of halo mass and the physics of galaxy formation in voids have been investigated in some detail (Peebles, 2001; Mathis & White, 2002; Benson et al., 2003c). Mathis & White (2002) predict that the faint-end slope of the LF steepens in underdense environments. In contrast, Hoyle et al. (2005) measured the LF of galaxies in voids in the SDSS and found that the faint-end slope is much shallower than is predicted by galaxy formation models, suggesting a deficit of dwarf galaxies in these extremely underdense regions.

In this analysis the Galaxy And Mass Assembly (GAMA) survey (Driver et al., 2011) is used to investigate how the galaxy LF varies with environment, cosmic time and colour. GAMA is a highly complete survey down to $m_r = 19.8$. Our work extends the analysis of Croton et al. to higher redshifts and much higher sampling and takes advantage of the more extensive photometry of GAMA to further split the galaxy sample by colour. Another novel feature of our analysis is that we use simulated galaxy data to create lightcone mock galaxy catalogues to test our approach. The availability of mock catalogues also allows us to compare our measurements from GAMA against the predictions from theoretical models on an equal footing.

The data and mock catalogues used in this analysis are described in §4.2.1, and §4.2.2. The methods adopted for measuring local environment, determining splits in colour, and measuring the luminosity function are given in §4.2.3 to §4.2.5. Our LFs split by environment, redshift and colour are presented in §4.3 and discussed in §4.4. We summarize our findings in §4.5.

We adopt a standard ΛCDM cosmology with $\Omega_M = 0.25$, $\Omega_\Lambda = 0.75$ and $H_0 = 100h\,\mathrm{kms^{-1}Mpc^{-1}}$, the same cosmology as is used when constructing the mock catalogues.

4.2 Method

In this section we describe the data and mock catalogues used, along with the k- and evolution corrections to galaxy magnitudes. This is followed by a discussion of the methods implemented to measure galaxy overdensity, colour and the galaxy luminosity function.

4.2.1 GAMA DATA

The details of the Galaxy And Mass Assembly (GAMA) survey are laid out in Chapter 2. To briefly summarise the data used here, GAMA is a multi-wavelength spectroscopic data set, with input catalogue defined in Baldry et al. (2010), tiling strategy explained in Robotham et al. (2010), GAMA survey output for DR1 and DR2 in Driver et al. (2011) and Liske et al. (2015) respectively, while the spectroscopic pipeline is described in Hopkins et al. (2013). The GAMA Equatorial regions, G09, G12 and G15, are centered on 9h, 12h and 14.5h in right ascension respectively, each covering 5 x 12 deg^2 of sky, totaling $\sim$180 deg^2. The data set used is from GAMA-II, defined by SDSS DR7 Petrosian magnitudes, limited to $r_{\mathrm{petro}} \leq 19.8$, a redshift completeness of $\sim 98\%$. We use 80922 galaxies ($z \leq 0.26$), with good quality redshifts ($NQ \geq 3$; Driver et al. 2011; Liske et al. 2015).

k-corrections

Petrosian magnitudes are k-corrected to account for band shifting when estimating luminosities. This process is described in §2.3.1 and Loveday et al. (2012), and involves fitting an SED to each galaxy using template spectra and SDSS model magnitudes in each of the *ugriz* bands (Blanton et al., 2003a; Blanton & Roweis, 2007). The redshift dependent k-correction to a reference redshift $z = 0$ for each galaxy, $k(z)$, is characterised by a fourth-order polynomial of the form

$$k(z) = \sum_{i=0}^{4} a_i(z)^{4-i}. \tag{4.1}$$

To speed up the k-correction calculation, and to account for galaxies with $k(z)$ tracks that differ significantly from the median, thereby over- or underestimating
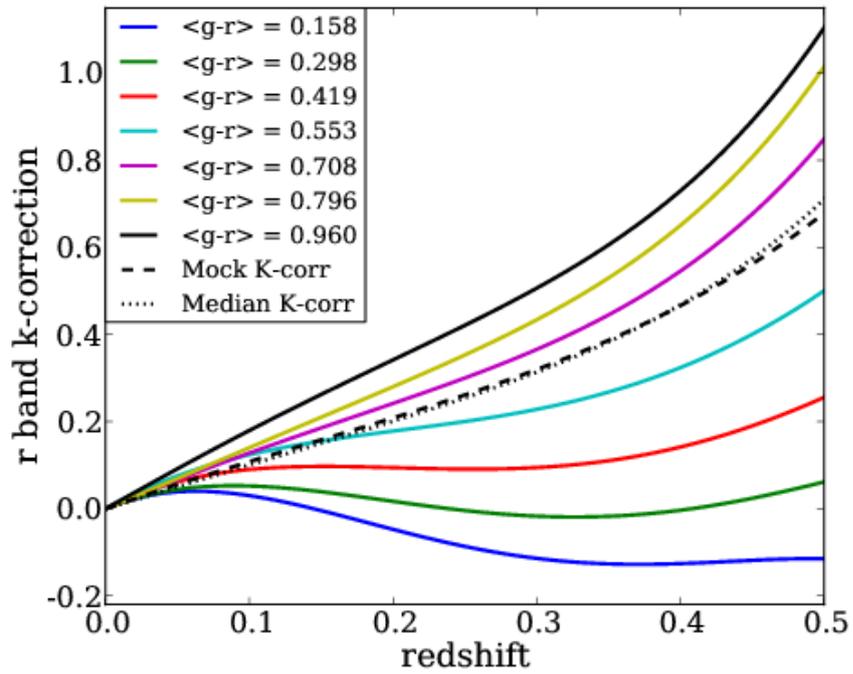
Figure 4.1: Median k-correction tracks to $z_{\mathrm{ref}} = 0$ for different rest-frame $(g - r)_0$ colours as a function of redshift. The dashed and dotted lines show the k-correction track used for mock galaxies and the median k-correction track of the data. The global k-correction used in the mock catalogues is almost identical to the measured median k-correction for GAMA.

$(g-r)_0$	$a_{0,col}$	$a_{1,col}$	$a_{2,col}$	$a_{3,col}$	$a_{4,col}$
0.158	-31.36	38.63	-14.79	1.427	0.001301
0.298	-17.77	25.50	-10.79	1.366	0.006235
0.419	-12.94	21.44	-9.826	1.683	-0.001972
0.553	-6.299	14.76	-7.473	1.847	-0.006801
0.708	9.017	-1.390	-0.9145	1.376	-0.004724
0.796	14.78	-6.592	0.9443	1.357	-0.005131
0.960	15.09	-5.730	-0.2097	1.859	-0.01250

Table 4.1: median colour, $(g-r)_0$, in the seven colour bins and coefficients ($a_{i,col}$ for $i = 0, 1, 2, 3, 4$) for $k_{col}(z)$ polynomials of the form given in Eqn. 4.1, as shown in Fig. 4.1.

the k-correction of a galaxy at a given redshift, we bin the individual galaxy $k(z)$ into seven bins of uniform width in rest-frame colour $(g-r)_0$. Firstly the $(g-r)_0$ colour is measured for each galaxy using SDSS g- and r-band model magnitudes in the observer frame, and individual SED fitted k-corrections for each galaxy. The median $k(z)$ within each $(g-r)_0$ bin is then calculated ($k_{col}(z)$), and this can be used as an approximate k-correction for all galaxies associated with that bin and at any redshift. The coefficients of the seven colour dependent tracks used in this paper are listed in Table 4.1 and are shown in Fig. 4.1, together with the median k-correction of the mock catalogues (Robotham et al., 2011).

Luminosity evolution

The luminosity evolution (indicated by Q_0) of the sample is taken into account to ensure the sample selection is comparable over a range of redshifts. Luminosity evolution, $E(z)$, is calculated as

$$E(z) = -Q_0(z - z_{ref}), \tag{4.2}$$

where the reference redshift, z_{ref}, is the redshift relative to which luminosity evolution is defined ($z_{ref} = 0$).

To quantify luminosity evolution in the galaxy population, the GAMA-II dataset is split into 3 redshift bins: $0.01 < z < 0.21$, $0.21 < z < 0.31$, $0.31 < z < 0.51$.

The luminosity function (§4.2.5) is measured for each of these ranges, originally assuming no luminosity evolution ($Q_0 = 0$). When fitting a Schechter function to the LFs at higher redshifts, the faint-end slope, α, is not well constrained. Similarly we cannot reliably measure evolution in ϕ^* using this method. Therefore, for the higher redshifts, α and ϕ^* are fixed to the values found for the lowest redshift bin. Jackknife errors are used to determine uncertainties on the LF. The value of Q_0 can then be estimated by measuring the increase in M^* with redshift. Again the uncertainty on M^* is found using jackknife errors. The new value for Q_0 is used to again measure the LFs in the 3 redshift bins, and repeat the process iterating on Q_0 until the difference between subsequent values of Q_0 is less than 0.01.

This process is carried out for red and blue galaxies in order to determine luminosity evolution for the different populations. $Q_{0,\mathrm{red}}$ and $Q_{0,\mathrm{blue}}$ are used when measuring LFs.

For all galaxies, we find $Q_{0,\mathrm{all}} = 0.97 \pm 0.15$, and when split into red and blue samples (where colour, $(g-r)_0$, is as defined in §4.2.4), we find $Q_{0,\mathrm{blue}} = 2.12 \pm 0.22$ and $Q_{0,\mathrm{red}} = 0.80 \pm 0.26$.[1])

The values found for $Q_{0,\mathrm{red}}$ and $Q_{0,\mathrm{blue}}$ are significantly different from those found in Loveday et al. (2015), mostly due to our assumption of no density evolution, $P_0 = 0$. Density and luminosity evolution are highly degenerate (see Loveday et al., 2012; Loveday et al., 2015), and therefore not allowing ϕ^* to vary with redshift allows much different values for Q_0. However, the redshift range used in this analysis is not large enough to allow for a small change in Q_0 to significantly affect the shape of the LF.

Absolute magnitudes

Petrosian magnitudes (r_{petro}) are used to calculate r-band absolute magnitudes, as GAMA is selected on r_{petro}. The k-corrected and luminosity evolution corrected absolute r-band magnitude (M_r^e at $z = 0$) is given by:

---

[1]The corresponding Q_0 values for mock galaxies are found to be $Q_{0,\mathrm{all}} = 0.89 \pm 0.09$, $Q_{0,\mathrm{blue}} = 1.71 \pm 0.16$ and $Q_{0,\mathrm{red}} = 0.63 \pm 0.07$.

$$M_{\rm r}^e - 5\log_{10}h = r_{\rm petro} - 5\log_{10}\left(\frac{d_{\rm L}(z)}{h^{-1}{\rm Mpc}}\right) - 25 - k_{col}(z) - E(z) \qquad (4.3)$$

with $E(z)$ as given in Eqn. 4.2, $k_{col}(z)$ depending on galaxy colour and given by
Eqn. 4.1, and luminosity distance is given by $d_{\rm L}(z)$. $Q_{0,\rm all}$ is used when defining a
volume limited sample (see §4.2.3), while LFs are measured using the specific $Q_{0,\rm red}$
or $Q_{0,\rm blue}$ corresponding to the colour of a galaxy.

4.2.2   GAMA Mock Catalogues

To illustrate how our results can be used to test models of galaxy formation, we
perform the same analysis on mock galaxy catalogues. These mock catalogues,
as described fully in Chapter 3, have the same faint apparent magnitude limit as
GAMA, and cover the same area on the sky, allowing a more direct comparison of the
properties of the data and the models. To summarise, the lightcone mock catalogues
are constructed from the Millennium dark matter N-body simulation (Springel et al.,
2005), and are populated with galaxies using the Bower et al. (2006) GALFORM semi-
analytic galaxy formation model. For further details of the construction of the mock
catalogues, see Chapter 3 and Merson et al. (2013), while a more comprehensive
description of the limitations of the GAMA mock catalogues is given in Robotham
et al. (2011). The r-band magnitudes are modified such that the redshift dependent
luminosity and selection functions of the mock catalogues match those of GAMA
(e.g. Loveday et al. 2012), while the colours and the ranking of galaxies in luminosity
remain unchanged. The k-correction track used for mock galaxies is given by Eqn.
8 in Robotham et al. (2011) and is shown by the dashed black line in Fig. 4.1, very
similar to the median track in GAMA (dotted black line). For historical reasons
these mock catalogues contain a bright apparent magnitude limit of $m_{\rm r} = 15.0$,
restricting the faint luminosity limit of the galaxy LF and the redshift limit over
which densities are measured.

The combined mock galaxy catalogue gives better statistics and allows a smoother,
more accurate measurement of the galaxy LF. Realistic errors based on the sample
variance between the 9 mock catalogues are used to provide error estimates for the

mock galaxy LFs.

4.2.3   Environment Measure

Environment is defined in terms of galaxy number density smoothed over a localised kernel using a density defining population of galaxies that is introduced below. We then explain how the local density of a galaxy is defined.

Density Defining Population (DDP)

A density defining population (DDP) of galaxies is used as a tracer of environment, following Croton et al. (2005). This galaxy sample is volume limited given a range of absolute magnitudes (M_r^e), and the apparent magnitude limits of the survey, that define a limiting redshift range. A galaxy is included as a DDP galaxy if it falls within the absolute magnitude limits of the DDP, and can be seen over the whole redshift range defined by these absolute magnitude limits.

It is expected that brighter galaxies will reside in denser environments. A brighter DDP sample will therefore cover a larger dynamic range of density in over-dense regions, whereas a fainter DDP sample will better sample environments corresponding to underdense regions (i.e. voids). Ideally a DDP sample should cover a large absolute magnitude range, to better sample all environments. However, with a magnitude limited survey, the larger the absolute magnitude range the smaller the range in redshift, and therefore the volume over which overdensities can be measured is reduced. To mitigate sample variance and to enable evolutionary studies, we prefer to use a DDP that covers a reasonably large redshift range, while preserving a high sampling rate.

Different DDP samples corresponding to different ranges in absolute magnitude and redshift are shown by the coloured rectangles in Fig. 4.2, and described in Table 4.2. The number of galaxies and subsequently the number density of DDP galaxies is smaller in each of the GAMA DDP samples than in the mock galaxy DDP samples due to redshift incompleteness in GAMA which is not modelled in the mock catalogues, and the bright apparent magnitude limit in the mock catalogues, which is fainter in the mock catalogues than in the data, limiting the volume over
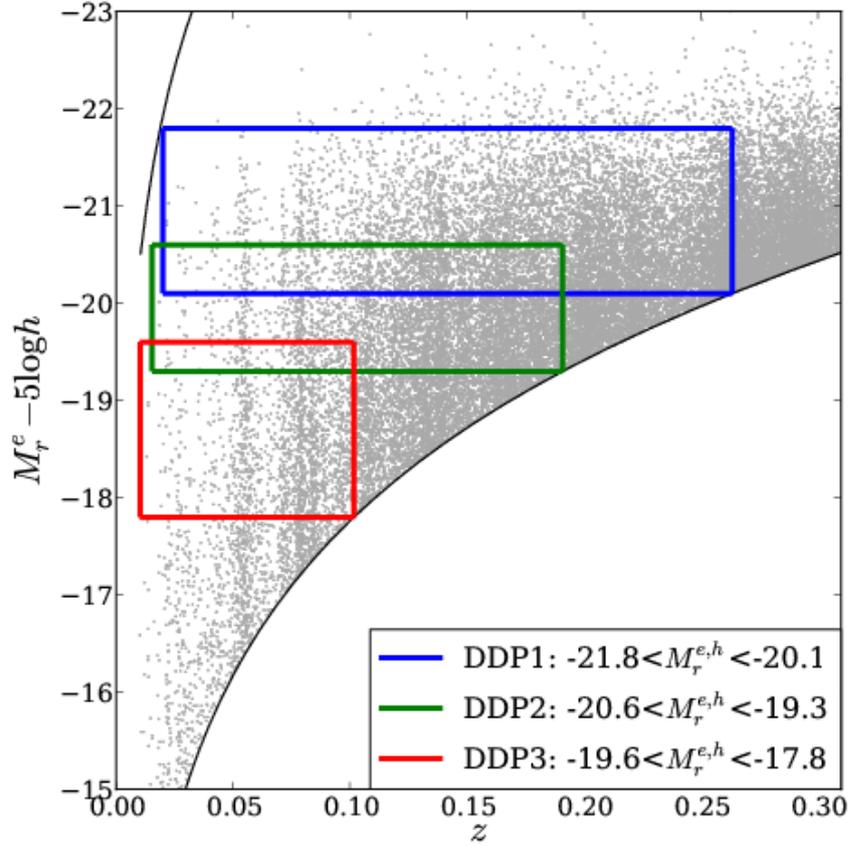
Figure 4.2: Absolute magnitude against redshift for all GAMA data with DDP samples enclosed by different coloured rectangles. Upper and lower black lines show bright and faint apparent magnitude limits of $r = 12$ and $r = 19.8$ respectively. To define DDP samples a global k-correction is used (see Fig. 4.1). See key for DDP samples, where $M_r^{e,h}$ is defined as $M_r^e - 5\log_{10} h$. DDP1 spans the redshift range $0.04 < z < 0.26$.

DDP	$M_\mathrm{r}^e - 5\log_{10} h$		z_min	z_max	$V_\mathrm{DDP}/(10^6 h^{-3}\mathrm{Mpc}^3)$		$\rho_\mathrm{DDP}/(10^{-3} h^3\mathrm{Mpc}^{-3})$	
	faint	bright			GAMA	$\langle\mathrm{Mock}\rangle$	GAMA	$\langle\mathrm{Mock}\rangle$
1	-20.1	-21.8	0.039	0.263	6.75	6.45 ± 0.02	5.35	6.38 ± 0.18
2	-19.3	-20.6	0.015	0.191	2.52	2.42 ± 0.06	8.99	9.47 ± 0.66
3	-17.8	-19.6	0.010	0.102	0.32	0.31 ± 0.05	12.7	18.1 ± 6.8

Table 4.2: Properties of DDP samples. Columns 2-3 list the r-band absolute magnitude range and columns 4-5 list the GAMA redshift ranges. Subsequent columns list the number of galaxies that fall within the DDP redshift limits, the effective co-moving volume of the DDP sample, and the number density of DDP galaxies. For each of these the values for GAMA and the mock catalogues are given, with the latter indicating the mean and scatter from the 9 mock catalogues.

which densities can be measured. The blue rectangle in Fig. 4.2, DDP1, is used to determine the local galaxy environment. It provides a large volume over which environment can be measured and enables evolution with redshift to be investigated. The other DDP samples shown in Fig. 4.2 and described in Table 4.2 are used to investigate how robust this measure of environment is, by comparing how the different DDP samples probe the underlying density field.

Once the DDP sample has been defined, all galaxies lying within the redshift limits of the DDP sample can have a local overdensity measured (i.e. including galaxies outside the absolute magnitude range of the DDP).

Overdensity

Once a DDP sample has been defined, the local environment around a galaxy is measured by counting the number of DDP galaxies (N_s) that lie within a sphere of a given radius around the galaxy. For this analysis we use a radius of $r_\mathrm{s} = 8\,h^{-1}\mathrm{Mpc}$ (co-moving). Different sphere sizes are discussed in Appendix B of Croton et al. (2005), who conclude that smaller spheres ($4\,h^{-1}\mathrm{Mpc}$) are a better probe of denser environments. However, sphere sizes that are too small are more likely to be sensitive to redshift-space distortions and shot noise and hence provide less reliable estimates of the density than larger sphere sizes. In agreement with Croton et al. (2005) we

find $8\,h^{-1}\mathrm{Mpc}$ radius spheres to be a good probe of both underdense and overdense regions, since larger sphere sizes tend to probe void regions well.

Muldrew et al. (2012) investigate how various measures of environment relate to the underlying dark matter distribution, finding that environment measures using apertures are a better probe of the halo as a whole compared to those using nearest neighbour methods, such that larger density measures more accurately reflect larger halo masses. Larger apertures (e.g. $8\,h^{-1}\mathrm{Mpc}$ as used here) correlate well with underlying dark matter environments over large ($5\,h^{-1}\mathrm{Mpc}$) scales. However, Blanton & Berlind (2007) compare galaxy properties within the group environment (defined using a friends-of-friends algorithm) to those within a density field over scales ranging from $0.1\,h^{-1}\mathrm{Mpc}$ to $10\,h^{-1}\mathrm{Mpc}$, determining that galaxy properties do not depend on surrounding environment over scales of $> 1\,h^{-1}\mathrm{Mpc}$ any more than the environment within the group.

If a galaxy is close to the edge of the survey, N_s will be underestimated, as the sphere will sample a volume outside of the survey. This is accounted for by correcting the measured density for the fraction of the sphere volume that falls outside the survey. For an unclustered data set this correction is exact, while for a clustered data set the correction is likely to be less accurate. Spectroscopic completeness is also corrected for in the same way using the GAMA masks.

To ensure robust results, a completeness threshold is set to discard galaxies for which the completeness correction is large. Fig. 4.3 shows how the fraction of the volume of galaxies kept in the sample decreases as a function of the completeness threshold chosen, for the 3 different DDP samples shown in Fig. 4.2. The denser (and hence fainter) the DDP sample is, the smaller the redshift range is and hence the larger the volume correction becomes with the completeness threshold applied. A completeness threshold of 80% is adopted such that less complete spheres (taking into account redshift and volume completeness) are not included in the analysis. 77% of the volume of the sample defined by DDP1 is retained.

The local galaxy density, defined within a sphere of radius r_s, accounting for volume completeness (C_v) and redshift completeness (C_z) is given by
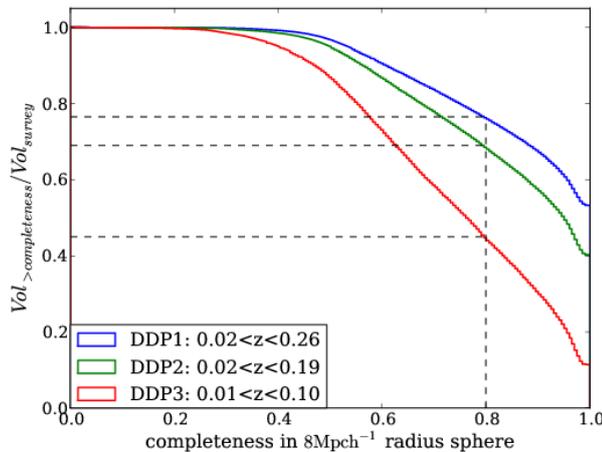
Figure 4.3: Fraction of volume retained in the sample as a function of spectroscopic and masking completeness threshold. A completeness threshold of 80% retains 77% of DDP1, but only 45% of DDP3. If a $4\,h^{-1}$Mpc radius sphere was used rather than $8\,h^{-1}$Mpc, 89% of DDP1 would be retained for the same completeness threshold.

$$\rho = \frac{N_{\mathrm{s}}}{\frac{4}{3}\pi r_{\mathrm{s}}^3}\frac{1}{C_{\mathrm{v}}}\frac{1}{C_{\mathrm{z}}}, \tag{4.4}$$

for which an overdensity can be calculated for the case $r_{\mathrm{s}} = 8\,h^{-1}$Mpc

$$\delta_8 = \frac{\rho - \overline{\rho}}{\overline{\rho}}, \tag{4.5}$$

where $\overline{\rho}$ is the effective mean density of DDP galaxies in the volume.

Each sample is split into overdensity bins, the basic properties of which are listed in Table 4.3 for DDP1. The bins are chosen such that they cover a large range of environments, including extreme underdense and overdense regions where statistics such as the LF may be changing more rapidly. The galaxy LF is measured for all density bins, but for clarity we focus on d1, d4, d6, and d9 from Table 4.3, sampling a variety of environments, from voids (d1) to clusters (d9).

Fig. 4.4 shows where galaxies lie in overdensity and absolute magnitude for DDP1, and hence which density bin they fall in (given by solid horizontal lines). Galaxies are coloured according to the density bin they occupy before their local density is corrected for redshift and volume completeness. This shows that there are no significant jumps in density classification: only adjacent bins are affected by the
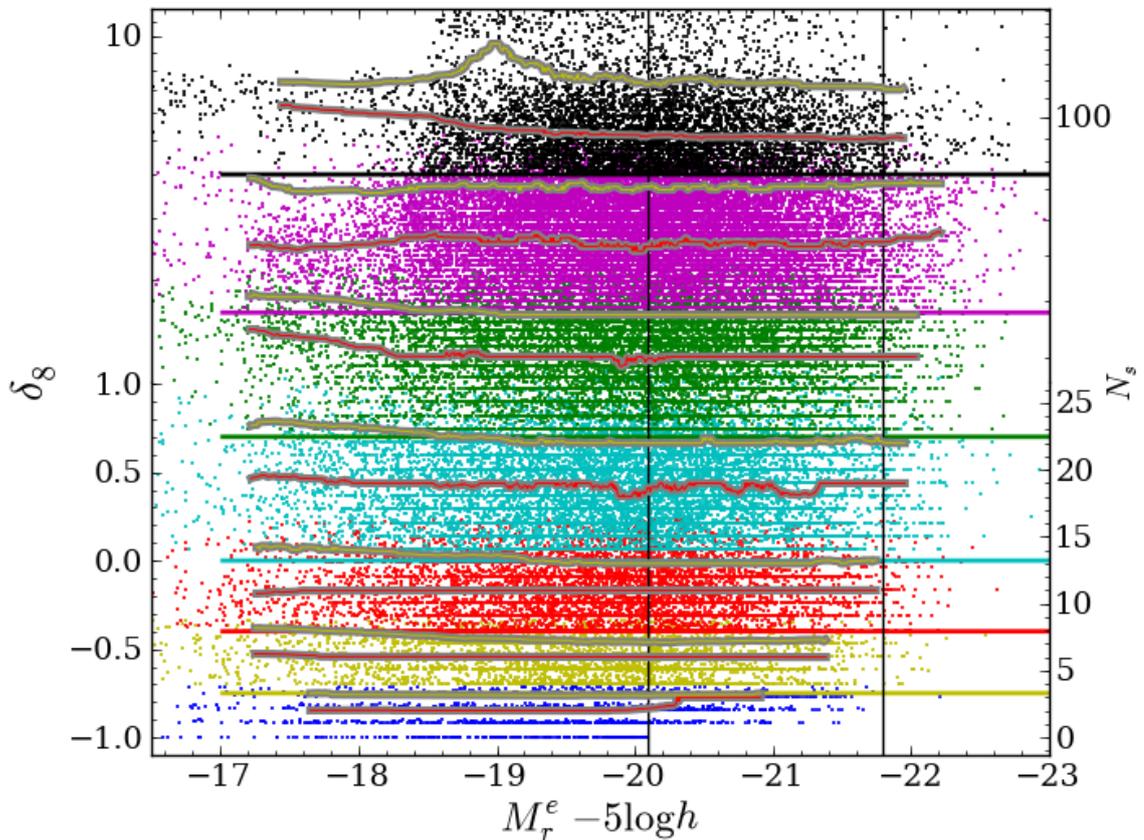
Figure 4.4: Overdensity against absolute magnitude for GAMA data. Black vertical lines show the absolute magnitude limits of the DDP1 sample, solid horizontal lines indicate the lower density limits of our density bins, coloured according to overdensity bin. Each point is coloured according to the overdensity bin it belongs to before completeness corrections are applied. The right side of the y-axis gives the corresponding number of DDP galaxies within an $8\,h^{-1}$Mpc radius sphere (see §4.2.3 for discussion). The darker solid lines (red on top of grey) show the running median overdensity (over 1000 galaxies) as a function of absolute magnitude, and the lighter solid lines (yellow on top of grey) show the 90th percentiles. For clarity d2 and d3 are combined here to form the yellow overdensity bin, likewise d7 and d8 are combined to form the magenta overdensity bin. Fainter than $M_{\rm r}^e - 5\log_{10} h = -18$, the range over which the running median is calculated is broad (~ 1 mag). The y-axis is linear until $\delta_8 = 1$ and logarithmic (base 10) thereafter.

completeness corrections when the threshold of 80% completeness is imposed. The discrete lines of overdensity (visible especially in the lower density bins) are due to the integer numbers of DDP galaxies within a sphere, corresponding to a specific value of δ_8. The mean number of DDP galaxies within a $8\,h^{-1}$Mpc radius sphere is 13.2. Galaxies falling between these discrete lines have had their overdensity corrected for incompleteness.

Since a DDP galaxy will always have at least one galaxy in its overdensity measurement (the DDP galaxy itself is included in N_{DDP}), there are no galaxies with $\delta_8 = -1$ in the magnitude range of the DDP sample (shown by black vertical lines). This effect becomes apparent in the shape of the LF if the lowest density bin considered is chosen to be significantly underdense. To correct for this, the LF estimator in the DDP absolute magnitude range (e.g. between the dashed vertical lines in Fig. 4.8) takes into account the effective volume of the DDP sample in each overdensity bin (see §4.2.5 for details). In the most underdense density bins this volume is much lower for DDP galaxies than for non-DDP galaxies and so not correcting for it would result in an incorrect LF estimate. An alternative approach would be to subtract one from the DDP count when measuring overdensity for a DDP galaxy. However this method implies that the definition of overdensity measured at a position infinitely close to a DDP galaxy is different to that measured at any other position. In order to produce an overdensity measurement which is consistent for all galaxies we use the method described above. This different treatment of DDP galaxies only has significant effect when dealing with small numbers of galaxies in an $8\,h^{-1}$Mpc radius sphere. As Fig. 4.4 shows, this is only the case in the lowest density bin, where the correction to the LF as described above is most significant.

The apparent absence of galaxies at faint magnitudes in the highest overdensity bin plotted in Fig. 4.4 is due to this bin being affected by one large cluster in G15 at $z \simeq 0.14$. Given the faint apparent magnitude limit of GAMA and the redshift of the cluster, it is not possible to pick up galaxies fainter than $M_{\mathrm{r}}^e - 5\log_{10} h = -18.5$. Most galaxies in this overdensity belong to the largest group recovered in the GAMA group catalogue (Robotham et al., 2011).

The spatial distribution of galaxies in these density bins is shown in Fig. 4.5
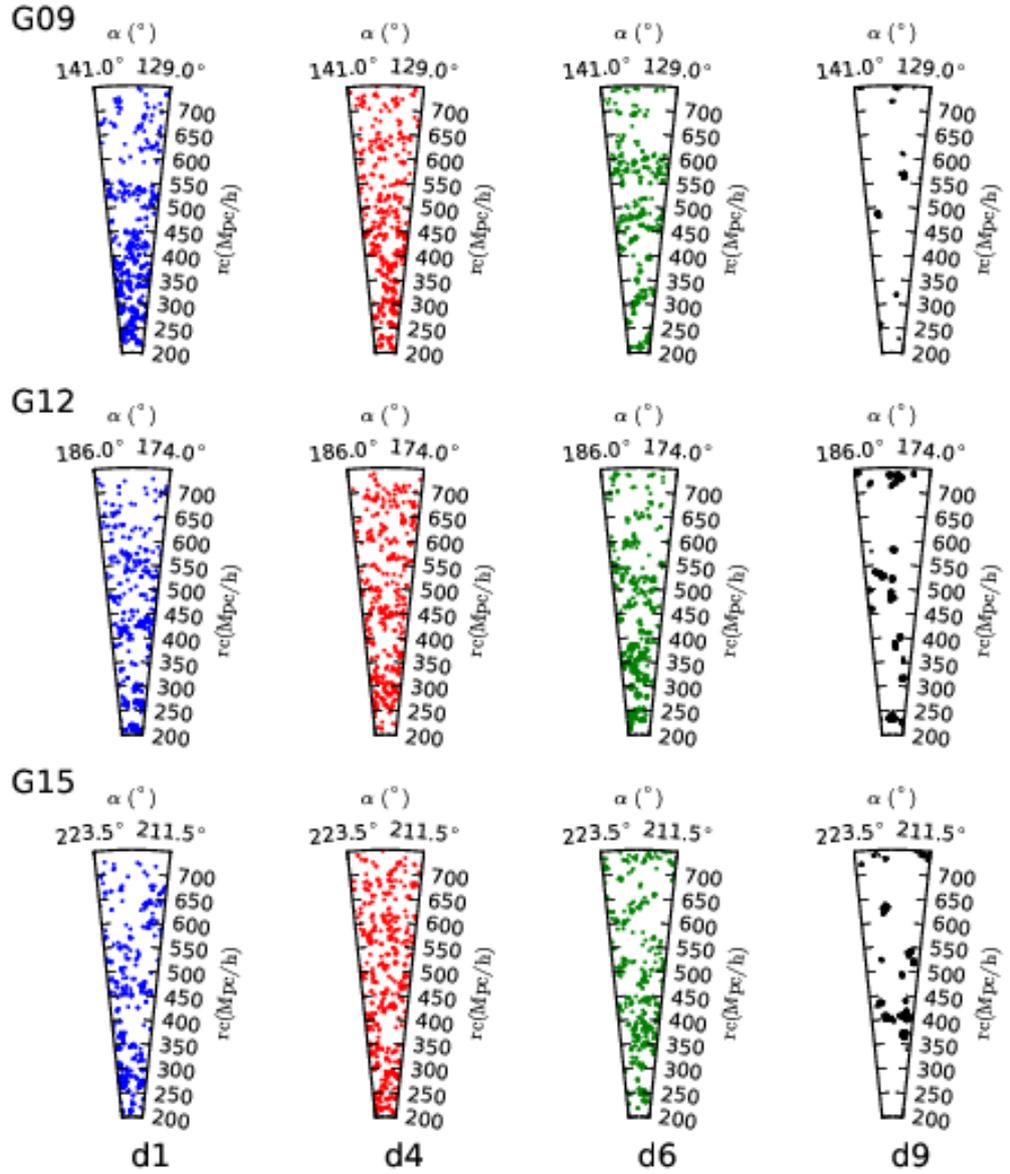
Figure 4.5: The spatial distribution of galaxies for different overdensities (left = most underdense to right = most overdense) in GAMA fields G09, G12, and G15 (top to bottom), over a constant projection thickness of $18.1\,h^{-1}$Mpc. Points are coloured according to overdensity bin and are plotted such that a random selection of galaxies totalling the same number in each overdensity bin is shown. Sample variance between the 3 GAMA fields is easily visible, so LFs are estimated using all 3 fields combined.
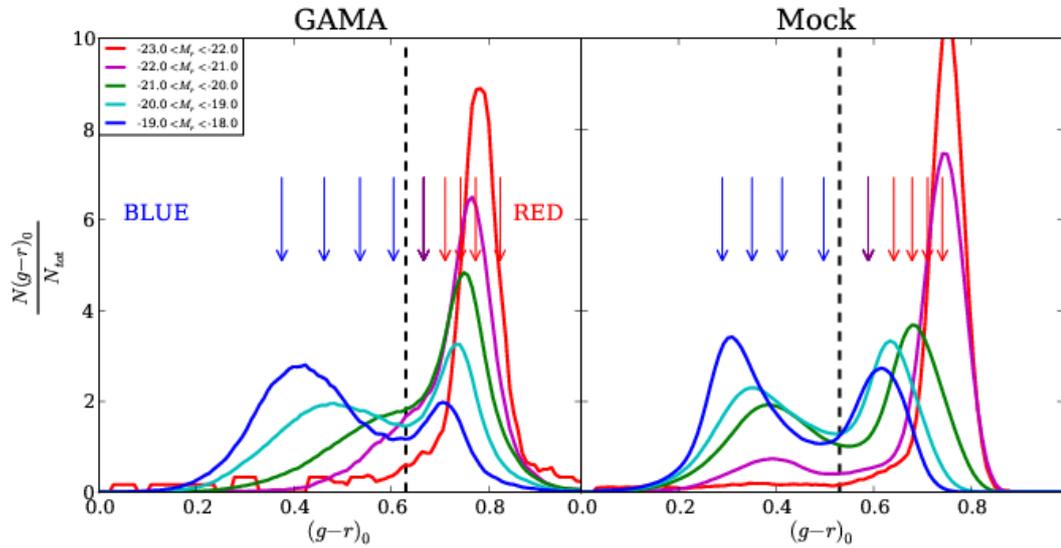
Figure 4.6: Distribution of rest-frame $(g - r)_0$ colour for 5 different ranges of r-band absolute magnitude for GAMA (*left*) and the mock catalogues (*right*). The vertical dashed black lines show the splits in colour used for GAMA and the mock catalogues. The colour split for the mock catalogues is chosen to keep the same fraction of galaxies in each colour sample as for GAMA, whilst ensuring the bimodality in the distribution is still clearly apparent. The arrows correspond to every 10th percentile in global $(g - r)_0$ distribution (see Fig. 4.15 for results using these splits).

Label	δ_8		f_δ	f_δ	$N_{\delta,\mathrm{DDP1}}/10^3$	
	min	max	GAMA	Mock	GAMA	Mock
d1	**−1.00**	**−0.75**	**0.259**	**0.226 ± 0.011**	**2.18**	**1.88 ± 0.13**
d2	−0.75	−0.55	0.109	0.149 ± 0.012	2.31	3.30 ± 0.32
d3	−0.55	−0.40	0.087	0.101 ± 0.016	2.72	3.52 ± 0.55
d4	**−0.40**	**0.00**	**0.189**	**0.175 ± 0.004**	**9.48**	**9.77 ± 0.29**
d5	0.00	0.70	0.168	0.169 ± 0.008	16.1	16.7 ± 1.02
d6	**0.70**	**1.60**	**0.106**	**0.099 ± 0.003**	**17.3**	**16.9 ± 0.80**
d7	1.60	2.90	0.057	0.053 ± 0.002	16.2	15.5 ± 1.05
d8	2.90	4.00	0.016	0.016 ± 0.001	7.21	7.49 ± 0.55
d9	**4.00**	**∞**	**0.010**	**0.012 ± 0.001**	**7.57**	**9.34 ± 0.72**

Table 4.3: Table of DDP1 overdensity bins, listing overdensity limits, effective volume fraction (f_δ) of each bin (Eqn. 4.8), and number of galaxies in DDP1 redshift range for GAMA and the mock catalogues, where the scatter is calculated as the variation between the individual mock catalogues. Overdensity bins used for comparison of LFs are d1, d4, d6 and d9 (in bold). A visual representation of these is shown in Fig. 4.5.

for each of the GAMA regions (G09, G12 and G15). A random sample of galaxies is plotted such that there is an equal number of points in each density bin, and within a constant thickness of $18.1\,h^{-1}\mathrm{Mpc}$, therefore giving a clearer view of how the galaxies are distributed according to overdensity.

Comparison of overdensities measured by different DDPs

The precise definition used for the density classification could potentially have a quantitative effect on the results obtained. Here we address whether or not there is a qualitative effect that needs to be accounted for.

Brighter galaxies tend to live in more overdense regions (and higher mass haloes, e.g. Einasto et al. 2005), whereas underdense regions (lower mass haloes) are populated with fainter galaxies (e.g. Hamilton 1988; Zandivarez et al. 2006). Due to this strong correlation between absolute magnitude and environment, it is possible that a DDP sample containing bright galaxies would be biased towards overdense
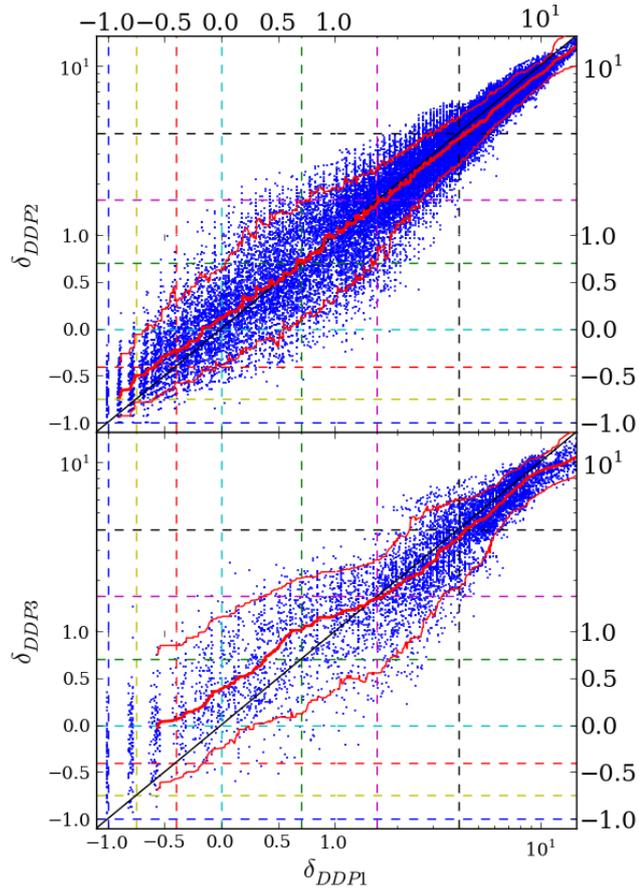
Figure 4.7: Comparison of overdensities measured by different DDP samples. Top panel compares DDP2 overdensities to DDP1 overdensities, for galaxies in the common redshift range to both DDP samples. The running median, 10th and 90th percentiles are shown by the solid and dashed thick, red lines. The lower panel shows a similar comparison, but for DDP3 and DDP1. The chosen overdensity bin limits are shown by the coloured dashed lines (using the same colour coding as in Fig. 4.4).

environments (Zehavi et al., 2011), thereby sampling a particularly large dynamic range of overdense environments compared to an unbiased sample of galaxy tracers and a smaller range in underdense environments.

Fig. 4.7 shows how the overdensity depends on the DDP sample used. The top panel shows galaxies in the redshift range covered by both DDP1 and DDP2 ($0.04 < z < 0.19$), with overdensities measured by DDP1 and DDP2 on the x-axis and y-axis respectively. Both DDPs measure extremely similar overdensities, shown by the median of the galaxies as a function of DDP2 (thick red line), with the 10th and 90th percentiles (dashed red line) showing the scatter does not typically extend to more than an overdensity bin (where overdensity bins are shown by coloured dashed lines). The lower panel compares δ_{DDP3} with δ_{DDP1} over their common redshift range ($0.04 < z < 0.10$). The median shows the overdensities measured are very similar. However, below $\delta_8 = 1$ (lower left of the figure), DDP3 tracers seem to measure higher overdensities than DDP1, and above $\delta_8 = 1$ (upper right), DDP3 traces slightly underestimate overdensities in comparison to DDP1.

Therefore when measuring overdensities for galaxies, it is important to note that the sample used to trace density can have an impact on which galaxies fall into the most underdense density bins.

The shape of the LF also does not vary significantly depending on which DDP sample is used to measure overdensity, suggesting DDP tracers allow for a robust measure of overdensity.

4.2.4 Colour

Observed galaxy colour is a strong indication of star formation history (Mahajan & Raychaudhury, 2009; Maller et al., 2009; Wetzel et al., 2012), but also depends on properties such as metallicity and gas content. In agreement with Fig. 2 of Mahajan & Raychaudhury (2009), we find there is a clear correlation between colour as defined here, and specific star formation rate (as measured by Gunawardhana et al. (2013) using H_α flux). However, significant scatter in the correlation suggests our measure of colour cannot be used as a direct indication of star formation. The correlation and scatter are consistent over all overdensities, and we therefore do not expect a

colour definition that is more indicative of star-formation to have any significant qualitative impact on our results.

The galaxy sample is split by colour to test for any further environmental dependence of the LF. Galaxies colours are defined by the $g-r$ rest frame colour, that depends only on the r-band and g-band apparent magnitudes, and the individual k-corrections in the r- and g-bands.

Galaxies are assumed to have no difference in luminosity evolution between the r- and g-bands when rest frame colours are calculated. SDSS model magnitudes are used as apparent magnitudes when calculating colours, following the procedure of Loveday et al. (2012). The sample is split between blue and red at $(g-r)_0 = 0.63$, resulting in a mean colour of $\langle g - r \rangle = 0.47(0.74)$ for blue(red) galaxies. The left panel of Fig. 4.6 shows this divide in colour (dashed vertical line) and how it splits up the sample of galaxies in $(g-r)_0$ for different ranges of $M_r^e - 5\log_{10} h$. The chosen splits in colour are motivated by the clear bimodality seen in Fig. 4.6. Any luminosity dependent bimodality is small enough to be ignored for this analysis. The sample is also divided into 10 colour bins, defined by every 10th percentile of the DDP1 galaxy sample, to determine how the LF changes with environment for narrow splits in colour.

The colour split in the mock catalogues is set by preserving the same fraction of red and blue galaxies as in GAMA. This cut is consistent with a cut based on the bimodality of the colour distribution in the mock catalogues, but is about 0.10 mag bluer than the corresponding cut in GAMA. This is a known limitation of the colour distribution in the Bower et al. model, however it is encouraging that despite this colour offset, the colour distributions are similar, barring a much stronger bimodality in the mock catalogues.

4.2.5 Luminosity Function

The galaxy LF is measured for the galaxies in each overdensity bin. Here we use the step-wise maximum likelihood (SWML) estimator (Efstathiou et al., 1988), that does not require the assumption of a functional form for the LF. The probability, p, that a galaxy, i, will be seen with an absolute magnitude, M_i, given its redshift, z_i

is calculated as:

$$p(M_i|z_i) = \phi(M_i) / \int_{M(z_{\mathrm{min}})}^{M(z_{\mathrm{max}})} \phi(M) \, \mathrm{d}M, \tag{4.6}$$

and the likelihood, the product of the probabilities, is maximised.

The LF, $\phi(M) \, \mathrm{d}M$, estimated using this method is normalised using the number of galaxies (N) within the volume defined by the redshift limits (z_1 and z_2) of the galaxy sample, and the solid angle of the survey (Ω):

$$N = \Omega \int_{z_1}^{z_2} \mathrm{d}z \frac{\mathrm{d}V}{\mathrm{d}z \mathrm{d}\Omega} \int_{M_{\mathrm{faint}(z)}}^{M_{\mathrm{bright}(z)}} \phi(M) \, \mathrm{d}M \; . \tag{4.7}$$

To take into account the effective volume populated by an overdensity bin, the overdensity is measured as in §4.2.3 but at positions distributed uniformly within the volume. The corresponding effective volume fraction is estimated as the fraction of points within overdensity bin δ:

$$f_\delta = \frac{N_{\mathrm{r},\delta}}{N_{\mathrm{r}}}, \tag{4.8}$$

where $N_{\mathrm{r},\delta}$ is the number of randoms with a specific overdensity, including those with completeness greater than the threshold defined above, and N_{r} is the total number of randoms spanning the entire DDP volume. Galaxies are weighted by $1/f_\delta$ when measuring the LF to estimate their abundance. As discussed in §4.2.3, due to the definition of overdensity, DDP galaxies from a given density bin will, in effect, cover a slightly smaller volume of the survey than non-DDP galaxies. DDP galaxies are weighted by $1/f_{\delta,\mathrm{DDP}}$, with

$$f_{\delta,\mathrm{DDP}} = \frac{N_{\mathrm{r},\delta,\mathrm{DDP}}}{N_{\mathrm{r}}}, \tag{4.9}$$

where $N_{\mathrm{r},\delta,\mathrm{DDP}}$ is the number of randoms, treated as DDP galaxies (and therefore having adding one to their DDP count), within a given overdensity bin δ. This chosen normalisation of the LF in each environment is such that the total LF is obtained by a weighted sum over each environment, with the weight inversely proportional to the volume fraction covered by that environment.

We do not correct the GAMA data for any global imaging incompleteness. We assume that the main effect is to globally change the normalisation in all density

bins. See Loveday et al. (2012) for more information.

Schechter function fits

The LF is often well described by a Schechter (1976) function, that expressed in units of absolute magnitude is given by:

$$\phi(M) = \frac{\ln 10}{2.5} \phi^* 10^{0.4(M^*-M)(1+\alpha)} \exp(-10^{0.4(M^*-M)}), \tag{4.10}$$

The Schechter function is specified by α, M^* and ϕ^* describing, respectively, the power law slope of the faint end, the magnitude at which there is a break from the power law (the 'knee' of the LF), and the normalisation of the LF. The values of these parameters that best fit the LF are found by minimising χ^2 over a grid of values of α, M^* and ϕ^*, using the errors described in §4.2.5. Due to the shape of the Schechter function, there are known degeneracies between M^*, α and ϕ^* (Fig.4.10).

LF errors

Errors for the GAMA LFs are estimated using jackknife errors from 9 samples, obtained by splitting each of the GAMA regions into a further 3 samples. Errors estimated from the scatter between the mock catalogues provide a reliable estimate accounting for sample variance. Despite the advantage of using the variation between mock catalogue as errors, we use jackknife errors for the data for the following reasons. When measuring the LF for samples split by a property for which the mock catalogues and GAMA do not agree (e.g. colour, see Fig. 4.6), the variation in the mock catalogues does not faithfully describe the constraints on the GAMA LF. The mock catalogues do not probe the full range of apparent magnitudes provided by GAMA (due to an imposed bright limit of $m_r = 15.0$). Nevertheless, comparing jackknife errors within a mock catalogue with the variation between mock catalogues, we find they are compatible to the level required in this work. The errors used for the mock galaxy LFs are calculated as the standard deviation from the combined mock catalogue. If fewer than 5 galaxies contribute to a LF bin (shown by an open circle), errors on it cannot be estimated reliably and it is ignored when fitting a Schechter function.

Similarly, the variation of the best fitting Schechter function parameters between the mock catalogues or jackknife samples provides reliable errors with which we can constrain scaling relations for the parameters with overdensity, and subsequently assess the significance of these scaling relations.

4.3 Results

We present LFs split by density in §4.3.1, by redshift in §4.3.2 and by colour in §4.3.3, to better understand any environmental, evolutionary and colour dependent trends.

4.3.1 Environmental dependence of the LF

Overdensities are measured for all galaxies within the redshift limits of the DDP1 sample ($0.04 < z < 0.26$). Overdensity bins are listed in Table 4.3 for which galaxy LFs are measured. The top panel of Fig. 4.8 shows the LFs and best fitting Schechter function for 4 of these overdensity bins, from the most underdense (d1) to the most overdense bin (d9), with jackknife errors. As expected, these errors are smallest around the knee of the LF which is best constrained.

Defining a *reference* Schechter function allows us to compare how the shape of the LF varies with environment. Our reference Schechter function is based on the best fitting one to the LF of the full sample over all environments within the volume defined by the DDP1 sample ($\phi_{\rm tot}$), and is described by $\alpha_{\rm tot} = -1.25$, $M_{\rm tot}^* - 5\log_{10} h = -20.89$ and $\log_{10} \phi_{\rm tot}^*/h^3{\rm Mpc}^{-3} = -2.01$ for GAMA.[2] These values are slightly different to those quoted in Loveday et al. (2012). These differences are not of too much concern for this study, the reference function is derived using the same data and volume as that used here, thereby minimising any systematic effects introduced using slightly different data, volume or method of estimating the LF.

Assuming ϕ^* scales approximately with overdensity as $(1+\langle\delta_8\rangle)$ (hereafter $1+\langle\delta_8\rangle$

---

[2]The reference Schechter function for the mock galaxies is described by $\alpha_{\rm tot} = -1.13$, $M_{\rm tot}^* - 5\log_{10} h = -20.84$ and $\log_{10} \phi_{\rm tot}^*/h^3{\rm Mpc}^{-3} = -1.90$.
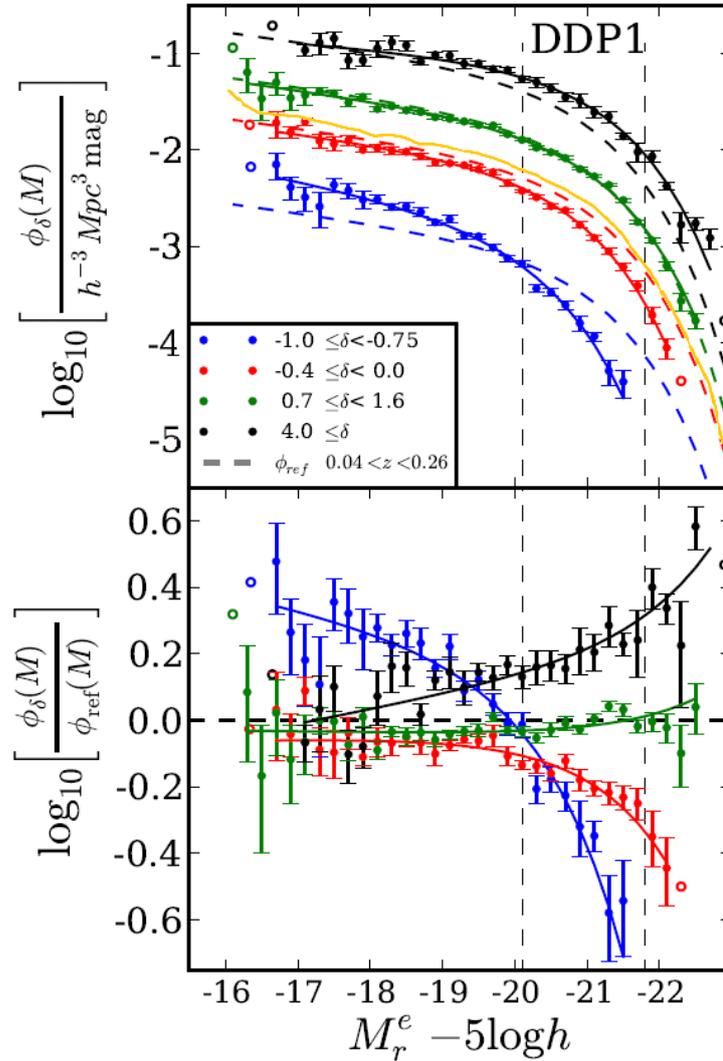
Figure 4.8: *Top panel*: GAMA galaxy luminosity functions coloured according to environment (see key). The best fitting Schechter functions are shown by coloured solid lines, and the reference Schechter functions (ϕ_{ref}, see §4.3.1) are given by dashed coloured lines (Eqn. 4.11). For comparison, the total luminosity function is given by the yellow line. *Bottom panel*: ratio of the LF to the reference Schechter function, emphasizing the differences in shape between the LFs in different environments and the global LF. Errors in each panel are jackknife errors. Open circles are shown for LF bins where errors cannot be reliably estimated, these are not used when fitting a Schechter function. The dashed vertical lines show the absolute magnitude limits of the DDP sample.
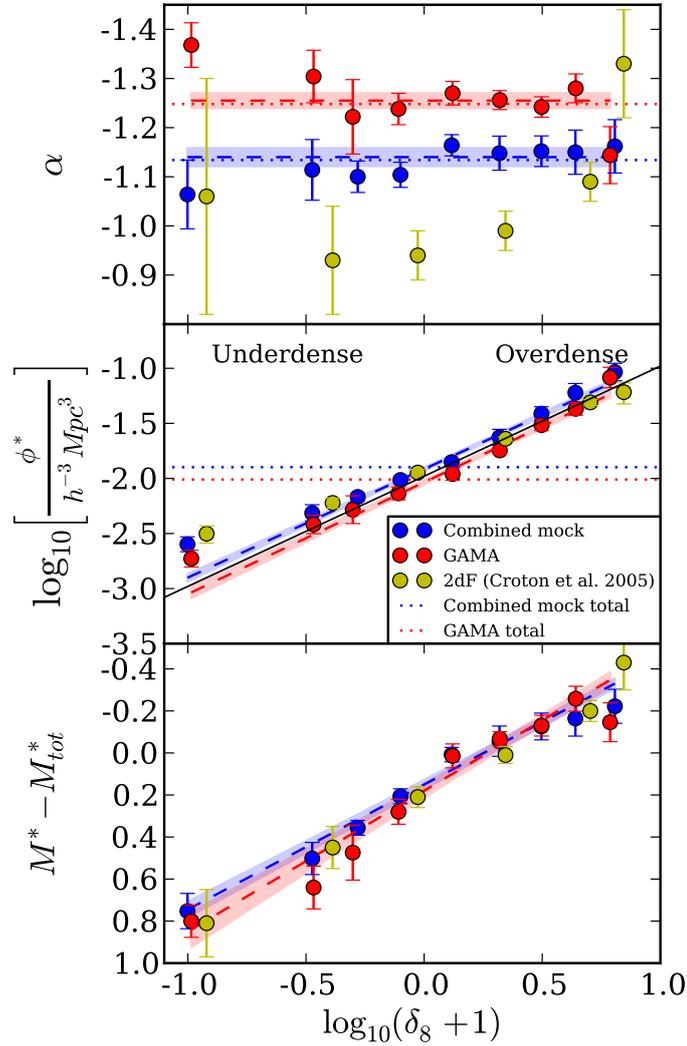
Figure 4.9: Schechter function parameters α (*top*), ϕ^* (*middle*), and M^* (*bottom*) as a function of environment for GAMA data (red) and simulated galaxy data (blue). M^* is plotted relative to M^*_{tot}, a reference value to compare different samples. α_{tot} and ϕ^*_{tot}, given by the reference Schechter function, are indicated by horizontal dotted lines for GAMA and the mock catalogues. Yellow points show the results of Croton et al. (2005) from the 2dFGRS. Dashed lines show the best fitting relation as a function of overdensity, with the shaded regions indicating the uncertainty in the relations. M^* and $\log_{10}(\phi^*)$ vary linearly with $\log_{10}(1 + \delta_8)$ (the black solid line in the second panel indicates a gradient of unity), while α seems to be broadly independent of overdensity.

is noted as $1 + \delta_8$), we scale our reference Schechter function for each density bin as

$$\phi_{\text{ref}} = \frac{1 + \delta_8}{(1 + \delta_{\text{tot}})} \phi_{\text{tot}} \qquad (4.11)$$

where ϕ_{tot} is the Schechter function described above, and δ_{tot} is the mean overdensity of the sample over the whole DDP volume, found to be $\delta_{\text{tot}} = 0.007$.

The dashed coloured lines in the top panel of Fig. 4.8 show the scaled reference Schechter function for each overdensity bin. We notice that our assumed scaling with $(1 + \delta_8)$ is a very good description of how ϕ^* scales with overdensity in all but the most extreme bins in overdensity. The deviation of the LFs in different environments from the scaled global LF is seen more distinctly in the lower panel of Fig. 4.8. The variation seen at faint magnitudes indicates differences in the faint-end slope of the LF in different environments and those at bright magnitudes reflect a dependence of the characteristic luminosity on environment.

Fig. 4.9 shows how the best fitting Schechter function parameters vary with δ_8 for GAMA and the mock catalogues. M^* is shown as $M^* - M^*_{\text{tot}}$ with M^*_{tot} set by the reference Schechter function. Hence the variation of M^* with environment can be measured and compared to the b_{J}-band results of Croton et al. (2005) from 2dFGRS. We note that the best fitting Schechter function for the total GAMA sample within the DDP redshift limits (defined above) is in very good agreement with that found in the mock catalogues.

The uncertainty on the Schechter parameters correlates strongly with sample size (Table 4.3). This mostly explains the observed bin to bin variations of the errors. The strong correlations between α, M^* and ϕ^* also have an effect on the inferred errors. These degeneracies make it difficult to determine whether or not an apparent trend in any of these parameters with overdensity is true. Fig. 4.10 shows 1σ contours for the 9 jackknife samples within each density bin. A brightening of M^* by 0.1 mag corresponds to a steepening of α by ~ 0.07. The offset of the contours confirms our result that the parameters vary strongly with environment. Although a full covariance matrix analysis would be required in order to statistically constrain these correlations, this clear variation of the M^* - α degeneracy with environment (also shown in Fig. 6 of Croton et al. (2005)) can rule out the trends with overdensity
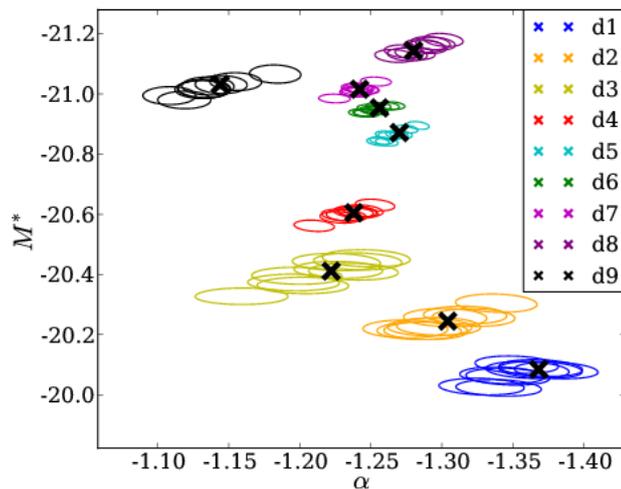
Figure 4.10: 1σ contours in the M^*-α plane for each jackknife sample for all 9 density bins in GAMA, coloured by density bin. The best fit value for the total sample is shown by the black crosses in each density bin. The degeneracies between α and M^* are obvious within a given density bin.

being a result of the degeneracy.

The coloured dashed lines in Fig. 4.9 show how the Schechter function parameters scale with overdensity. The variation in the scaling relations due to sample variance (as indicated by the shaded regions) is found by calculating the scatter between the best fitting lines for each jackknife sample or mock catalogue. Table 4.4 gives parameters for the linear fits, shown by the dashed lines. α does not show any specific trend with environment and we therefore fit it as a constant. M^* and ϕ^* vary significantly with environment. This is expected for ϕ^*, since the most overdense regions have the highest number density of galaxies.

M^* brightens linearly with $\log_{10}(1 + \delta_8)$, at very similar rates for GAMA and the mock catalogues. This is characterised by a negative slope, given in Table 4.4.

The bottom panels of Fig. 4.11 show how the LFs for the GAMA and the combined mock catalogue compare in the most underdense bin (d1), an overdense bin (d8) and for the total sample. The GAMA and mock galaxy LFs are very similar in the two extreme environments.

The results found from GAMA are mostly in good agreement with those from Croton et al. (2005), although the values of α in different environments seem somewhat

inconsistent, as discussed further in §4.4.1.

4.3.2   Evolution of the LF dependence on environment

To determine whether or not the dependence of the LF on environment evolves with redshift, we measure the LF for the same environments given above, but for 3 separate redshift slices of equal volume: $0.04 < z < 0.18$, $0.18 < z < 0.23$ and $0.23 < z < 0.26$. The highest redshift sample only probes galaxies brighter than $M_r^e - 5 \log_{10} h = -19.8$, resulting in the faint end of the LF being poorly constrained. Therefore, when fitting Schechter functions in the two higher redshift slices, α is fixed to the best fitting value of the lowest redshift slice in each environment, and only M^* and ϕ^* are treated as free parameters. This value of α is highly consistent with that measured over the whole redshift range, only deviating by at most ± 0.02. To constrain any evolution in α, a deeper survey is necessary, allowing the LF to be constrained down to lower luminosities at higher redshifts. The resulting LFs are shown in Fig. 4.12.

Fig. 4.12 shows a small offset in the LFs between different redshifts for underdense environments. These offsets can be accounted for by a small density evolution, that has not been taken into account in this analysis, and/or an additional luminosity evolution (see §4.2.1). These are very degenerate and cannot be constrained well enough through this analysis due to the sample size considered, but since this trend is visible in all 3 GAMA regions, it is evident that there is some small density and/or additional luminosity evolution in the LF, especially in underdense environments. Fig. 4.13 however shows that sample variance within GAMA is larger than this offset.

The best fitting values for M^* and ϕ^* as a function of overdensity are shown in Fig. 4.13 for GAMA and the mock catalogues (left and right panels respectively). The dashed coloured lines show the linear fits to the total samples split by overdensity, as shown in Fig. 4.9. The best fitting values for ϕ^* and M^* for different redshifts mostly follow the scaling relation with overdensity of the total sample, the degeneracies in ϕ^* and M^* are likely to affect these results such that a value for M^* that is measured to be "too faint" according to the scaling, can have a good fit
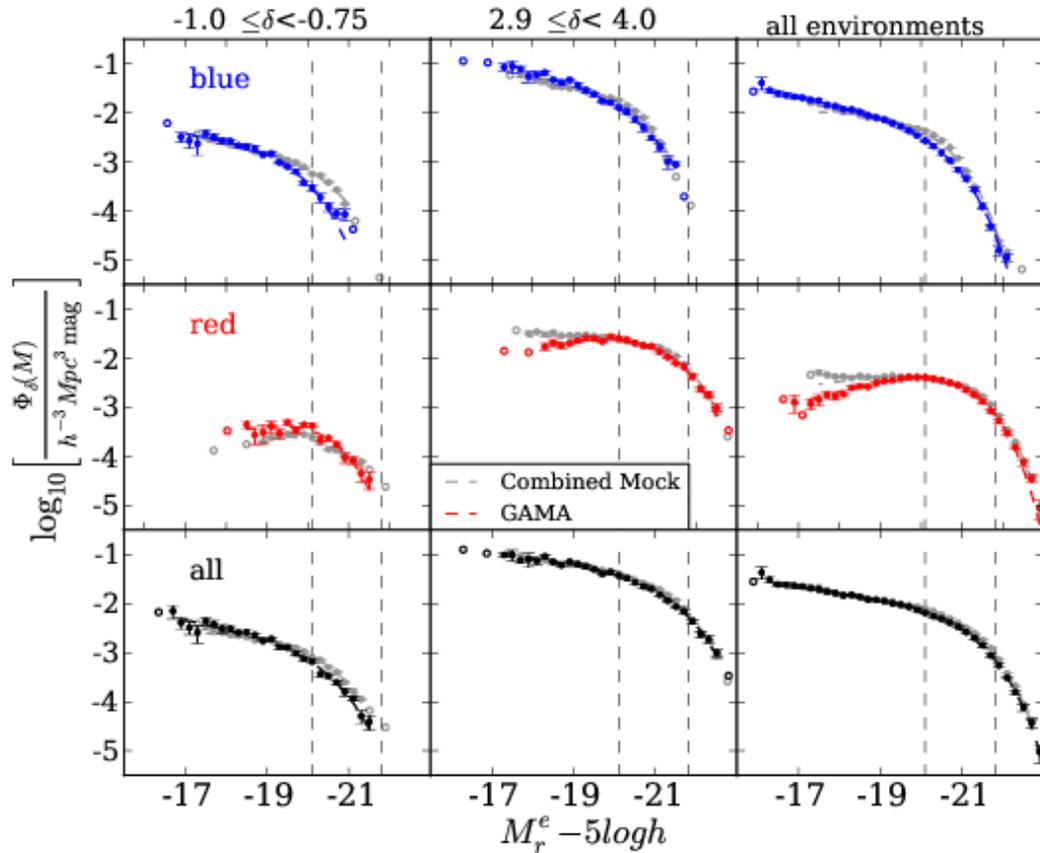
Figure 4.11: Luminosity functions for mock galaxies (grey) compared to GAMA galaxies, for different splits in colour (top to bottom) and overdensity (left to right). From left to right: LFs in the most underdense environment, an overdense environment and the global LFs (i.e. not split by density). Top to bottom: LFs for blue, red and all galaxies. Open circles are shown for LF bins where errors cannot be reliably estimated, these are not used when fitting a Schechter function. The LFs are remarkably similar between the mock catalogues and GAMA, given that only the total LF (bottom right) has been constrained in the mock catalogues. The more significant discrepancies between GAMA and the mock catalogues are at the bright end of the blue LFs, and the faint end of the red LFs (see §4.4.2 for further discussion).
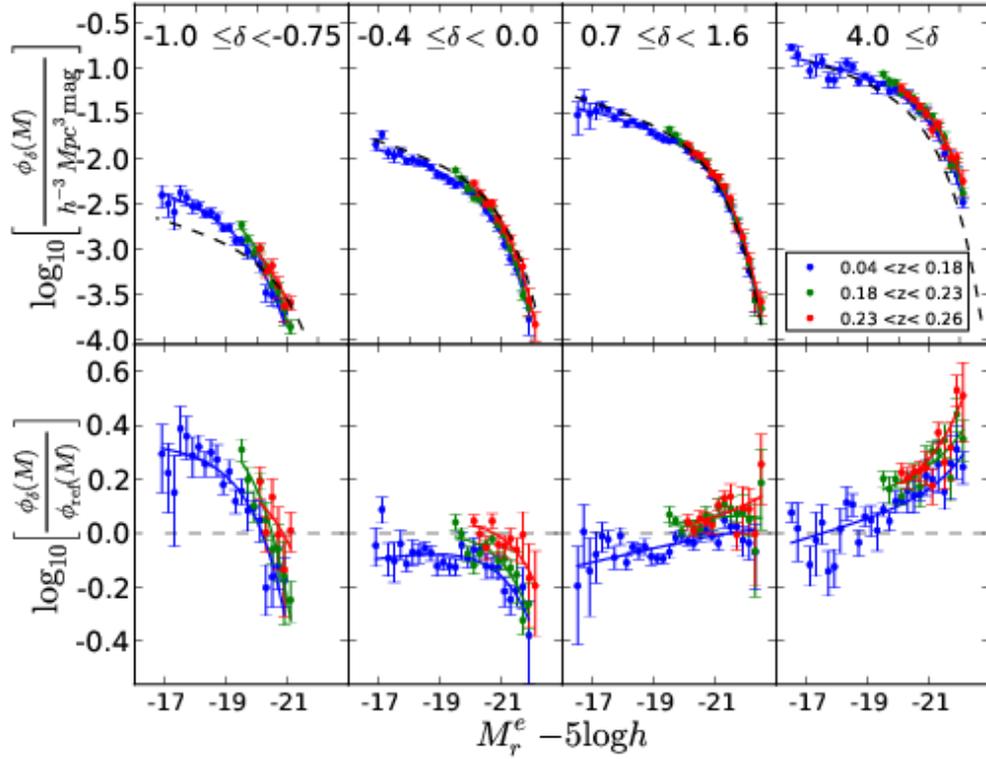
Figure 4.12: *Top panel*: GAMA LFs for 4 different overdensity bins (same as in Fig. 4.8), from most underdense (left) to most overdense (right), split by redshift (see key). The solid coloured curves show the best fitting Schechter functions, and the black dashed curves show the reference Schechter function (ϕ_{ref}, see §4.3.1) for the whole redshift range (as in Fig. 4.8. *Bottom panel*: ratio of the LFs to the reference Schechter function. Errors in each panel are jackknife errors.
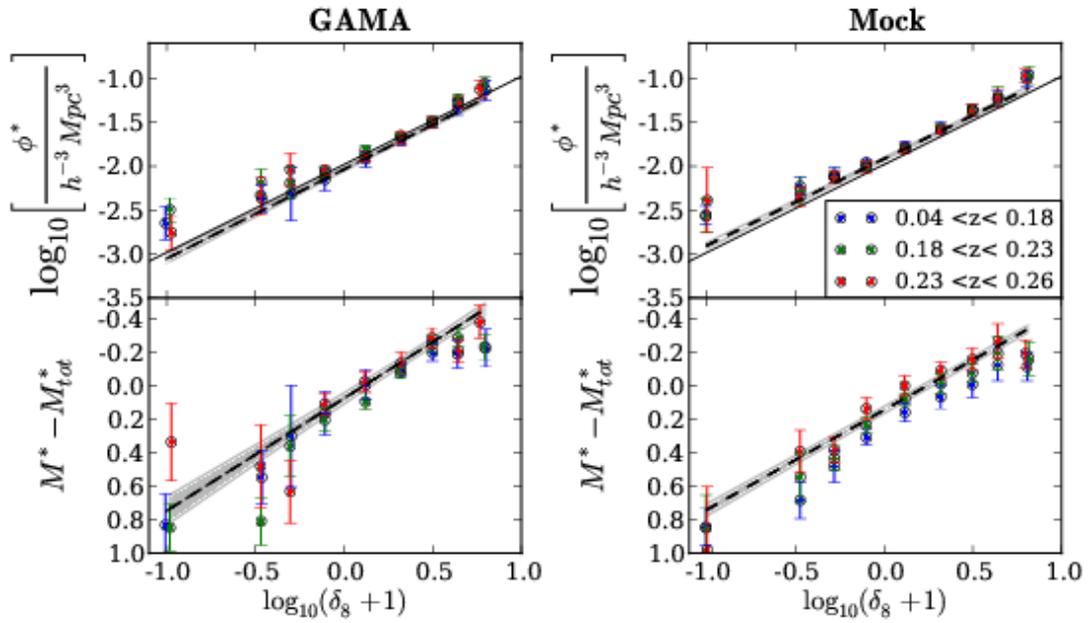
Figure 4.13: Best fitting Schechter function parameters ϕ^* and M^* as a function of overdensity for GAMA (*left*) and the mock catalogues (*right*) coloured according to redshift (see key). Uncertainties are jackknife errors (for GAMA) or scatter in the mock catalogues (for combined mock catalogue). The scalings of ϕ^* and M^* with overdensity for the total sample not split by redshift are shown by dashed lines and shaded regions. The black solid lines in the upper panels indicate a gradient of unity.
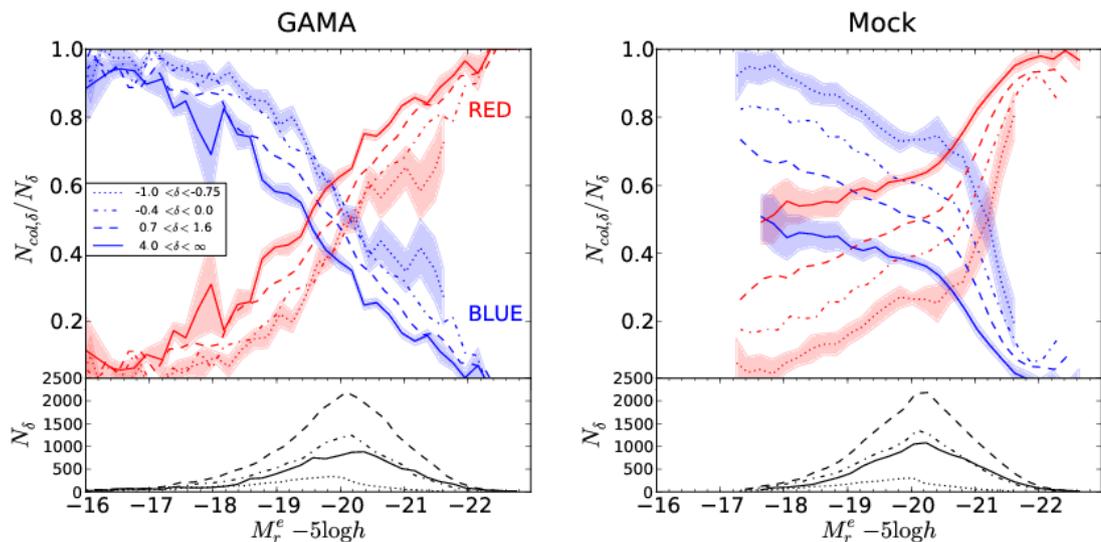
Figure 4.14: *Top panels*: Red and blue galaxy fractions for 4 environments (see key) as a function of absolute magnitude, for GAMA (*left*) and the mock catalogues (*right*). The shaded regions in the right panel show the scatter from individual mock catalogues and in the left panels show jackknife errors in GAMA for the most overdense and most underdense bins. Lines are coloured according to galaxy colour. The fraction of red galaxies increases with overdensity and brightness, whereas the fraction of blue galaxies decreases with increasing overdensity and brightness. *Bottom panels*: Distribution of absolute magnitudes for the overdensity bins shown in the top panel. While presenting similar overall trends, the mock catalogues have a significantly different distribution of colour fractions to GAMA. This is discussed in §4.4.2.

in conjunction with "too high" a value for ϕ^*. The evolution of the two parameters is not apparent in Fig. 4.13 over the luminosity evolution already accounted for.

4.3.3 Dependence of the Luminosity Function on Environment and Colour

To determine whether or not there is any environmental dependence of the LF over any colour-density relation, we look at how the LF varies for blue and red galaxies as a function of overdensity. The mock galaxy LFs can then be compared to the GAMA LFs to determine where the galaxy formation models do not agree with GAMA.
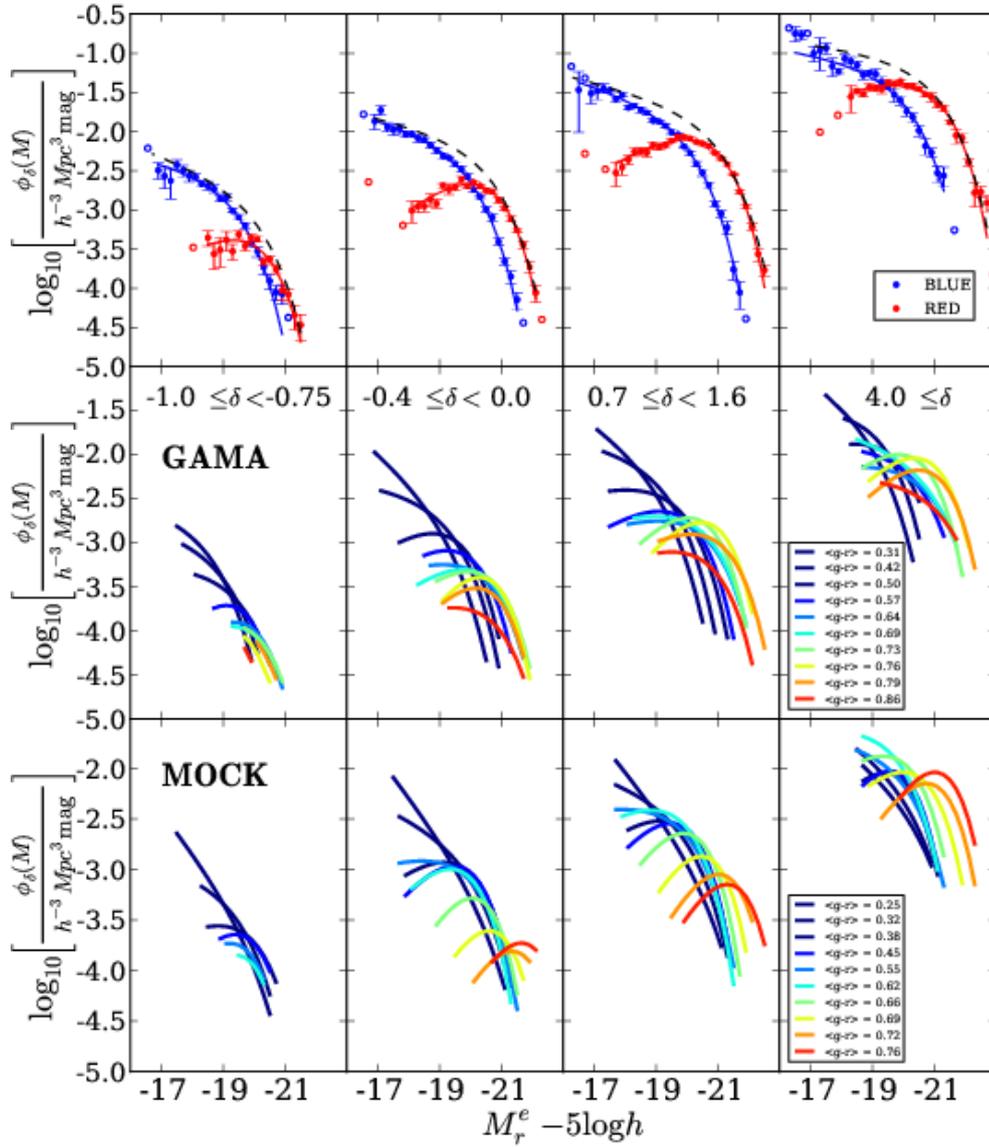
Figure 4.15: *Top*: GAMA LFs and best fitting Schechter functions for red and blue galaxies, split by environment as indicated in the central panels. The dashed lines show the total Schechter function in each overdensity bin (as in Fig. 4.8). Open circles are shown where LF errors cannot be reliably estimated. *Middle*: Schechter function fits as a function of colour, from the bluest to the reddest galaxies in 10 narrow colour bins (see Fig. 4.6). The shape of the LF depends strongly on colour, and the transition between the shapes of the blue and red LFs is clear. Schechter functions are not extrapolated beyond the range of the measured LF in each colour bin. *Bottom*: The same as the middle panels but for the mock catalogues. The mock catalogues show the same general trend from red to blue as GAMA, but in detail show some clear differences for the LFs measured for samples defined by narrow bins in colour.
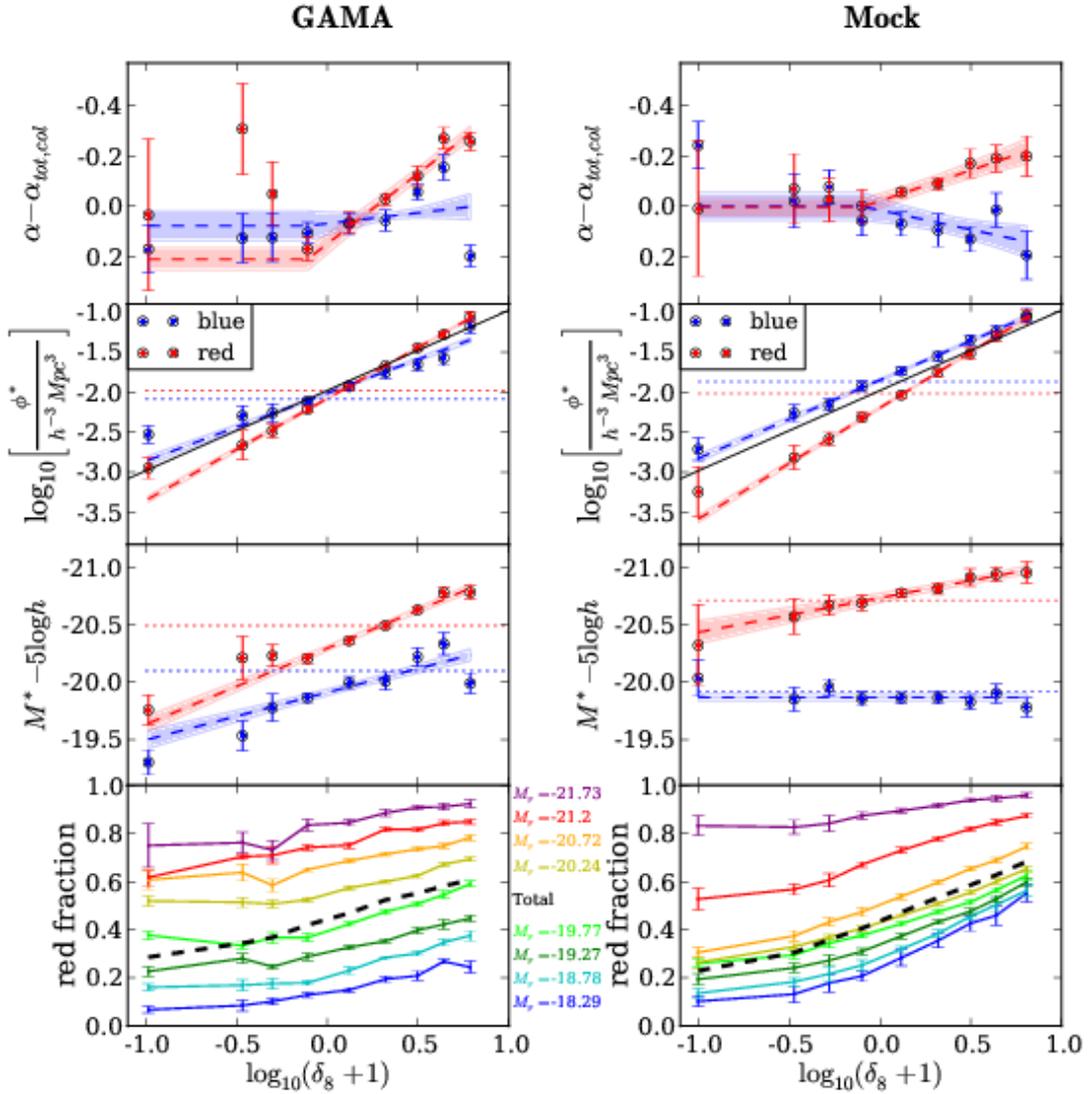
Figure 4.16: *Top 3 panels*: Schechter function parameters as a function of overdensity for blue and red galaxies in GAMA (*left*) and mock catalogues (*right*). α is plotted with respect to the reference Schechter function for each colour ($\alpha_{\mathrm{tot,col}}$, see §4.3.3 for values). The dotted lines show the Schechter function parameters for the samples not split by environment. As in Fig. 4.9, shaded regions show the uncertainty in the line fits, and the black solid lines shows a gradient of unity. *Bottom*: Fraction of galaxies classified as red as function of overdensity for 8 bins in absolute magnitude. Labels shown are the median absolute magnitudes in each bin. Uncertainties shown are jackknife errors (left) or scatter in the mock catalogues (right). The red fraction for the total sample is given by the black dashed line.

Colour	Schechter	GAMA		Mocks	
	parameter	a_0	a_1	a_0	a_1
all	α	-1.25 ± 0.01	-	-1.14 ± 0.01	-
	$\log_{10} \phi^*$	-2.03 ± 0.03	1.01 ± 0.06	-1.92 ± 0.02	0.98 ± 0.05
	$M^* - 5\log_{10} h$	-20.70 ± 0.03	-0.67 ± 0.07	-20.69 ± 0.02	-0.60 ± 0.06
blue	α	-1.30 ± 0.01	-0.08 ± 0.01	-0.95 ± 0.01	0.15 ± 0.01
	$\log_{10} \phi^*$	-2.01 ± 0.02	0.85 ± 0.07	-1.85 ± 0.03	0.97 ± 0.07
	$M^* - 5\log_{10} h$	-19.91 ± 0.03	-0.42 ± 0.08	-19.87 ± 0.02	-0.00 ± 0.03
red	α	-0.23 ± 0.12	-0.56 ± 0.25	-0.67 ± 0.04	-0.25 ± 0.12
	$\log_{10} \phi^*$	-2.08 ± 0.02	1.27 ± 0.05	-2.19 ± 0.03	1.38 ± 0.07
	$M^* - 5\log_{10} h$	-20.30 ± 0.02	-0.67 ± 0.06	-20.74 ± 0.03	-0.30 ± 0.07

Table 4.4: Table of coefficients for best fitting relations describing how the Schechter function parameters vary with overdensity for all, red and blue galaxies, as shown in Fig. 4.9 and Fig. 4.16 for GAMA and the mock catalogues. Scaling coefficients are given for $Y = a_0 + a_1 \log_{10}(1 + \delta_8)$ where $Y = \log_{10} \phi^*/h^3 \mathrm{Mpc}^{-3}$ or $Y = M^* - 5\log_{10} h$. α (all) is fit by a_0, while α (colours) is fit by the relation given in Eqn. 4.12. Statistical errors from the jackknife resamplings (data) or variations in the mock catalogues (mocks) are given.

It can clearly be seen from Fig. 4.11 that although remarkably similar, the shapes of the LFs for the mock galaxies do not entirely agree with the shapes of the GAMA LFs when split by colour. The total r-band LF for the mock galaxies matches the GAMA r-band LF by construction, thus the bottom right panel shows very good agreement between GAMA and the mock galaxies. However, when splitting the LFs by density and colour, it is clear that the mock catalogues predict too many bright blue galaxies in underdense environments. Similarly too few faint red galaxies are predicted by the mock catalogues in underdense regions, but too many faint red galaxies are predicted in overdense regions. The faint end of the blue LF in underdense environments and the bright end of the red LF in overdense environments agree very well with the GAMA LF. Fig. 4.14 shows that blue galaxies tend to dominate underdense and red dominate overdense environments, these are therefore most influential in determining the LF over all environments, as seen in the right hand panels of Fig. 4.11.

The LFs split by red and blue galaxies for 4 different environments in GAMA are shown in the top panels of Fig. 4.15. The shape of the LF clearly differs between red and blue galaxies (Loveday et al., 2012; De Propris et al., 2013), but it is not obvious that the shape of LFs for blue and red populations vary with environment. This can be investigated further by looking at the shape of the LF for 10 narrow splits in colour, representing 10 percentile intervals in the colour distribution (see Fig. 4.6). The LFs for these splits are shown in the middle (bottom) panels of Fig. 4.15 for GAMA (mock catalogues).

The shape of the LF for any given narrow range of colour can be seen to vary with increasing density. In particular, the LF of the extreme blue sample does not seem to vary significantly with density, while the faint-end slope of the LF for redder samples tends to become steeper with overdensity.

In Fig. 4.15, the mock galaxy LFs brighten as the sample gets redder, and the number of faint galaxies at a fixed luminosity decreases. Similar trends are seen in GAMA, where generally redder samples tend to contain brighter galaxies, but the variation between the LFs of the reddest samples is much smaller than is predicted by the mock catalogues. Although red galaxies clearly dominate the most overdense

regions at bright luminosities, Fig. 4.15 suggests that this increase in the number of red galaxies with overdensity is mainly caused by the intermediate red population rather than the very reddest.

The Schechter function parameters α, M^* and ϕ^* for the GAMA LFs are shown in the left panel of Fig. 4.16: α is shown with respect to $\alpha_{\text{tot,col}}$, the faint-end slope of the total LF for each colour sample. This allows the variation of α with overdensity to be compared between different colour samples, especially as the values of $\alpha_{\text{tot,col}}$ for GAMA and the mock catalogues are different between red samples (GAMA: $\alpha_{\text{tot,red}} = -0.38$, mock catalogues: $\alpha_{\text{tot,red}} = -0.65$) and blue samples (GAMA: $\alpha_{\text{tot,blue}} = -1.37$, mock catalogues: $\alpha_{\text{tot,blue}} = -0.96$).

Both red and blue galaxy samples display linear dependencies of ϕ^* and M^* with $\log_{10}(1 + \delta_8)$. The best fitting parameters describing these dependencies are given in Table 4.4. α appears to follow a relation of the form:

$$
\alpha = \begin{cases} a_0 & \delta_8 \leq -0.2 \\ a_0 + a_1 \log_{10}(1 + \delta_8) & \delta_8 > -0.2, \end{cases} \tag{4.12}
$$

This implies that the faint end of the LF steepens with overdensity only in overdense regions for a given galaxy population. ϕ^* increases at a significantly faster rate with overdensity for red galaxies than for blue galaxies, which is consistent with blue galaxies dominating underdense regions and red galaxies dominating overdense regions. The value of ϕ^* for red and blue samples with overdensities around $\delta_8 = 0$ is similar, suggesting a similar fraction of red and blue galaxies populate average density environments.

The 3$^{\text{rd}}$ panel down on the left in Fig. 4.16 shows that M^* brightens at a faster rate with overdensity for blue galaxies than for red galaxies in GAMA. In underdense regions, the offset between M^* for the two colour sub-samples is as small as ~ 0.1 mag, whereas in the most overdense regions their difference becomes as large as ~ 0.5 mag. The significant offset (~ 0.45 mag) between M^*_{tot} for blue and red galaxies (shown by the dotted horizontal lines), can be understood from the change in ϕ^* with environment: M^* in overdense regions is determined by red galaxies, whereas in underdense regions it is determined by blue galaxies.

The changes in best fitting Schechter function parameters with environment for the mock catalogues are qualitatively similar to the observational data (see right panels of Fig. 4.16). α shows a slightly different trend to that observed in GAMA. While the faint-end slope appears to steepen with environment in GAMA (more so for red galaxies than for blue), the faint-end slope for blue galaxies in the mock catalogues tends to become shallower for more overdense environments.

The variation in the amount of blue and red galaxies with overdensity predicted by the mock catalogues is as significant as that observed in GAMA (2nd panels down in Fig. 4.16), although the predicted number of blue galaxies at higher overdensities is slightly higher than is observed. The variation in M^* with environment for colour sub-samples predicted by the mock catalogues is inconsistent with GAMA. Although the mock catalogues correctly predict red galaxies brightening with overdensity, there is no dependence of M^* on environment predicted for blue galaxies, while M^* for red galaxies shows a weaker brightening with overdensity than is observed, causing M^* to be predicted too bright in the most underdense environments.

The fraction of red galaxies as a function of overdensity for bins in absolute magnitude is shown in the lower panel of Fig. 4.16, where as expected we find that brighter samples have a consistently higher red fraction than fainter samples, and that the fraction of red galaxies increases with overdensity for all luminosities. The mocks (right panel) show that although qualitatively similar, there are some differences in the red fraction of the bright magnitude bins (except the very brightest bins) for the most underdense environments, and in the faintest magnitude bins for the most overdense environments.

4.4 Discussion

We have used GAMA to measure luminosity functions for different environments, redshifts and galaxy colours. Here we summarise our findings and discuss the implications for galaxy formation.

4.4.1 Quantitative Description

A density defining population (DDP) of galaxies is used as a tracer of the underlying matter distribution. It provides a means by which to measure how the properties of the galaxy population, such as luminosity and colour, vary with environment. There is generally a good agreement between different DDP tracers used to measure overdensity, as discussed in §4.2.3. Mapping the most extreme environments is sensitive to the choice of DDP tracer, and so mock galaxy catalogues constructed from simulated galaxy data are required for quantitative comparisons to models of galaxy formation.

GAMA is a deeper (up to 2 mags) and more spectroscopically complete survey than those that have previously been used to investigate the variation in the galaxy LF with environment (2dFGRS, SDSS). Hence it provides more reliable environment measures over a large range of environments.

The galaxy LF is measured in 9 overdensity bins from GAMA, over the redshift range of $0.04 < z < 0.26$. The LFs for 4 of these density bins are shown in Fig. 4.8. The shape of the LF is found to vary smoothly with overdensity, with little change in the faint-end slope α, but where the characteristic magnitude M^* and characteristic number density $\log_{10} \phi^*$ vary linearly with $\log_{10} (1 + \delta_8)$, as can be seen in Fig. 4.9. Although a Schechter function is a poor fit to the total galaxy sample, it is a reasonable description in underdense regions.

Assuming galaxy overdensity relates to mass overdensity as $\delta_g = b_g \delta_{mass}$, like in a linear bias model, and that ϕ^* varies with mass overdensity as $\phi^* = (1 + \delta_{mass})$, we expect a linear relation between $\log_{10} \phi^*$ and $\log_{10} (1 + \delta_8)$ through our chosen method of measuring overdensity, the slope of which is $1/b_g$. We find a slope of $\log_{10} \phi^*$ with $\log_{10} (1 + \delta_8)$ of 1.01 ± 0.06, consistent with a galaxy bias of $b_g = 0.99$. This is slightly lower than $b_g = 1.20$ measured by Zehavi et al. (2011) for the absolute magnitude range of our DDP sample. This approximation for the scaling of ϕ^* is only valid for $\delta_8 \ll 1$, and so we do not expect this scaling to work for our most overdense bins. If only considering the 5 lowest density bins (lower than e.g. $\log_{10} (1 + \delta_8) = 0.3$, corresponding to the density beyond which our approximation is invalid), we find a slope of 0.87 ± 0.09, consistent with the bias measured by Zehavi

et al. (2011). Measuring the variation of the normalisation of the luminosity function in underdense regions with different DDP galaxies could be a way to measure the bias of galaxies. However due to the small range of overdensities for which the approximation works, a much larger galaxy sample is needed to actually measure the linear galaxy bias, for example using data from the future Dark Energy Spectroscopic Instrument (DESI) (see e.g. Levi et al., 2013) and its Bright Galaxy Survey (BGS), providing a much larger (~ 50 times) galaxy redshift survey but with a similar depth to GAMA.

The degeneracies between α, M^* and ϕ^* affect our ability to constrain the shape of the LF. These degeneracies have an impact on the best fitting Schechter functions for each jackknife sample or for individual mock catalogues (see Fig. 4.10), resulting in large uncertainties on these parameters. When using a larger sample over a large volume in the survey (e.g. the 5$^{\text{th}}$ density bin), degeneracies are more easily overcome by the ability to better constrain one parameter (ϕ^*). Fig. 4.10 shows that the variation of each parameter with overdensity is more significant than these degeneracies.

Comparing our results for the galaxy population as a whole to those of Croton et al. (2005), we find agreement that the galaxy LF varies smoothly with environment. The faint-end slope α does not show any significant variation with environment, suggesting the abundance of faint galaxies varies linearly with overdensity as ϕ^* only. This suggests that the physical process involved in suppressing the formation of faint galaxies is likely to be an internal process, such as supernovae or photo-ionisation, rather than an environmental one. From Fig. 4.9 it is clear that the values of α presented by Croton et al. (2005) are much shallower (by up to $\Delta \alpha \sim 0.3$) than those found for GAMA. The extra depth gained when using GAMA data allows the LF to be measured over a larger magnitude range $4.65 > M_\text{r} - M^* > -2.35$, which is 2 mags fainter than Croton et al. (2005) ($2.65 > M_\text{b_J} - Ms > -2.35$), providing the ability to better constrain the faint end of the LF using GAMA.

Our conclusion that M^* varies linearly with $\log_{10}(1 + \delta_8)$ is similar to the 2dF-GRS results of Croton et al. (2005). However, we find a slightly stronger dependence of M^* on overdensity. The 2dFGRS is selected in the b_J-band, and the sample con-

tains a predominantly blue population of galaxies compared with our r-band selected analysis. Fig. 4.16 shows clearly that blue galaxies have a much slower increase in ϕ^* with overdensity than red galaxies, and a fainter M^* in all environments. Thus when considering the whole sample, a smaller fraction of red galaxies in overdense environments will cause less brightening of M^* with overdensity. This highlights the importance of considering the galaxy population used when analysing the shape of the LF.

These results are also consistent with those presented in Figs. 11 and 12 of Verdes-Montenegro et al. (2005), who collate previous estimates of the LF for different environments and surveys and compare how M^* and α vary as a function of density, finding a brightening of M^* with environment density, and only a weak steepening of the faint end.

The brightening of M^* in denser environments suggests physical processes which either suppress the bright end of the LF in more underdense environments or induce a brightening of galaxies in overdense environments. Hamilton (1988) suggested that brighter galaxies reside in denser environments as a consequence of larger galaxy bias, such that more luminous galaxies form in more dense regions. Zehavi et al. (2011) and Norberg et al. (2002a) show how this bias depends on luminosity and colour.

Using data from GAMA also allows the LF to be constrained over a range of redshifts, providing a tool with which to measure the evolution of the LF dependence on environment. We find only a very small evolution in the GAMA LF over that already taken into account by the luminosity evolution parameter Q_0 (Fig. 4.12). This evolution is likely related to the known small amount of density evolution in GAMA (Loveday et al., 2012). However, the large degeneracies between M^* and ϕ^* make it difficult to determine the variation of ϕ^* with redshift, and hence we do not try to model any redshift dependent density evolution. We find the value of Q_0 to be different for red and blue galaxies. When comparing galaxy properties in different environments it is important to take this into account, since different galaxy populations dominate in different environments (see Fig. 4.14).

Splitting the sample into red and blue galaxies gives an indication of how dif-

ferent populations of galaxies behave in different environments. The left panel of
Fig. 4.14 shows how the fraction of red and blue galaxies varies with luminosity
for different density bins. In general blue galaxies tend to dominate in underdense
regions and tend to be fainter, and red galaxies dominate overdense regions and
tend to be brighter. This is also seen clearly in Fig. 4.16 when considering how
ϕ^* changes with overdensity for red and blue galaxies, and by comparing how the
fraction of red galaxies as a function of overdensity (bottom panel) changes with
absolute magnitude. Both red and blue samples show a faint-end slope that varies
with density for overdense environments only (as Equation 4.12), suggesting the
suppression of faint galaxies is not as effective in overdense environments when con-
sidering a specific galaxy population, but this is not as evident when considering the
sample as a whole. The shallower dependence on overdensity seen when considering
all galaxies can be attributed to the varying fractions of blue and red populations
residing in different environments. This result is in good agreement with the LF
found for cluster galaxies in the 2dFGRS (De Propris et al., 2003), for which the
LF for early type galaxies is found to be considerably steeper in clusters than the
LF for field galaxies. A galaxy's local environment has different effects on its colour
and morphology (see Figure 8 of Bamford et al. 2009). We expect the morphology-
density relation (Dressler, 1980) to be similar to but not implicitly described by
Fig. 4.14.

4.4.2 Physical Interpretation

While the mock catalogues seem to predict a similar overall trend to the data in
the shape of the luminosity function for populations of galaxies residing in each
environment, there are some significant differences. Fig. 4.14 (right panel) shows
that the mock catalogues predict that the fraction of red and blue galaxies does not
vary as a function of magnitude in the same way as is observed (left panel). Instead,
the fraction appears to vary with a much shallower slope for $M_{\rm r}^e - 5\log_{10} h > -20.2$,
but with a steeper slope for $M_{\rm r}^e - 5\log_{10} h < -20.2$. This is true for all environments.
The absolute magnitude at which the fraction of blue galaxies and red galaxies are
equal gets fainter in denser environments, determining the luminosity at which the

dominating population of galaxies changes for a given environment. In the mock catalogues this luminosity is too faint in overdense regions and too bright in the most underdense regions.

A similar discrepancy in the mock catalogues can be seen by comparing the gradient of the fraction of red galaxies as a function of overdensity to GAMA as seen in the bottom panels of Fig. 4.16 for different absolute magnitude ranges. For bright galaxies in the approximate range $-20.0 < M_{\rm r}^e - 5 \log_{10} h < -21.0$ the mocks show a red fraction with a shallower dependence on overdensity, such that in the most underdense environments the fraction of galaxies which are red is higher than seen in GAMA. However, for the brightest galaxies the red fraction is predicted to be similar to GAMA. For faint galaxies this is the opposite case, the fraction of red galaxies varies with environment more strongly than is seen in GAMA, predicting too many (by up to a factor of two) faint red galaxies in the most overdense environments.

The LF for red galaxies predicted by the mock catalogues is mostly consistent with that measured in GAMA. However, the faint-end slope for red galaxies is predicted to be too steep compared to GAMA by up to $\Delta\alpha = 0.43$. For blue galaxies the faint-end slope is up to $\Delta\alpha = 0.58$ shallower in the mock catalogues than in GAMA in overdense regions. The variation of ϕ^* with environment suggests too many blue galaxies are predicted in overdense environments, slightly too few red galaxies in underdense environments. This discrepancy is reflected in the variation of M^* with environment, that is predicted to be weaker than is seen.

The shape of the LF for the very bluest galaxies does not seem to show much variation with environment. However, the redder LFs steepen and brighten with overdensity, and this variation is more significant for the intermediate red population (shown by the orange and red curves in the middle panel of Fig. 4.15). In general the mock catalogues predict the same result, although it is the reddest population that is seen to vary the most significantly in this case.

The comparison of the LFs of the mock galaxies and GAMA in different environments for different colours is summarised in Fig. 4.11. The total LF of GAMA and the mock galaxies when not split by colour or by environment is, by construction, extremely similar. It is therefore not surprising that the LFs in the bottom

right panel match particularly well. However, the LFs seem to agree remarkably well when split by environment and colour, barring a few discrepancies. Too many bright galaxies (specifically blue) are predicted in underdense environments. The faint end of the blue LF (which dominates these environments) agrees well, resulting in only a small deviation from the GAMA LF at the faint end in underdense regions. In overdense environments, however, the predicted bright end of the LF is in good agreement with the GAMA LF, and deviations are only apparent in the faint end, where too many faint red galaxies are predicted by the models (as is also visible in Fig. 4.16).

A similar result is found by Baldry et al. (2006), who investigate how the red fraction depends on stellar mass and environment in semi analytical models (Bower et al., 2006; Croton et al., 2006) and in SDSS, finding that both models qualitatively agree well with SSDS, particularly the Bower et al. (2006) model, but that there is an overabundance of red galaxies in more dense regions in both models.

This excess of faint red galaxies in the model can be attributed to the known problem of over-quenching of (dwarf) satellites in most semi-analytical models (Weinmann et al., 2006; Kimm et al., 2009). In the Bower et al. (2006) model, we find the faint end of the red LF is dominated by satellite galaxies. This is more apparent for the most overdense regions, since the majority of galaxies in overdense regions (massive haloes) are most likely satellite galaxies. Underdense regions are more likely to be occupied by isolated central galaxies, which will evolve with very little environmental influence.

In the Bower et al. (2006) model, when a galaxy falls into a larger halo and becomes a satellite, its hot gas reservoir is instantaneously lost to the host halo. Once it has depleted its supply of cold gas, star formation will cease. The excess of quenched (red) satellites can be attributed to this too efficient loss of hot gas on infall. Galaxies in isolation (predominantly central galaxies) have their star formation quenched through processes internal to the galaxy and its host halo, for example AGN feedback. By observationally studying how star formation is quenched in different environments, the prescriptions in the models for internal and environmental processes causing quenching can be refined. Font et al. (2008) incorporated a treat-

ment of stripping of hot gas based on the results of hydrodynamical simulations within the semi-analytic model of Bower et al. (2006), to investigate the behaviour of the hot gas reservoir of satellite galaxies. They find that satellite galaxies can retain a significant fraction of their hot gas after infall, allowing them to continue star formation for a significant period of time. This decreases the fraction of red satellite galaxies produced by the model, producing a satellite colour distribution in good agreement with that observed in SDSS.

Wheeler et al. (2014) find less than 30% of observed low mass ($M_* \simeq 10^{8.5-9.5} M_\odot$) dwarf satellites are quenched, a fraction much lower than is predicted by models, and suggest a long quenching timescale (> 9.5Gyrs) for satellites of these masses. When comparing these results to those of Wetzel et al. (2013) and De Lucia et al. (2012), who measure a quenching timescale for observed dwarf satellites of higher mass, Wheeler et al. (2014) discover the quenching timescale is dependent on stellar mass for satellite galaxies, such that lower stellar mass systems exhibit a longer timescale for quenching star formation. However galaxies also undergo quenching through internal processes, which also correlates strongly with stellar mass. It is likely that these internal processes also contribute to quenching in satellites. When taking this into account, Wheeler et al. (2014) and Wetzel et al. (2013) find the fraction of satellites quenched only through environmental processes is independent of stellar mass.

Taking into account studies of how hot gas is stripped from satellite galaxies on in-fall would help to provide a better model describing the evolution of satellite galaxies.

Another obvious discrepancy we find between the model and observations is an excess of bright blue galaxies in underdense environments predicted in the model. The majority of galaxies in these environments are centrals, most likely unaffected by processes external to the galaxy (since the number density of galaxies is low). This excess of bright blue galaxies could be due to the halo mass threshold below which AGN feedback is not efficient enough to suppress star formation, allowing for excess blue galaxies to be predicted at the bright end of the LF. The lowest density bin in our sample contains predominantly blue galaxies in haloes with masses

$M < 10^{12.2} h^{-1} \mathrm{M}_\odot$.

4.5   Conclusion

The results presented and discussed above can be summarised as follows.

- The GAMA galaxy LF varies smoothly with overdensity, such that denser environments contain brighter galaxies, the LF is described by a linear relation between M^* and $\log_{10}(1 + \delta_8)$. The faint-end slope, α, does not show any detectable variation with environment, consistent with results from other galaxy surveys. As expected, $\log_{10} \phi^*$ varies linearly with $\log_{10}(1 + \delta_8)$, such that the slope is related to galaxy bias as $1/b_\mathrm{g}$.

- When split by colour, the measured LFs confirm that red galaxies dominate overdense environments, and blue galaxies dominate underdense environments. A variation in the faint-end slope with environment becomes apparent, such that α steepens linearly with $\log_{10}(1 + \delta_8)$ for $\delta_8 \geq -0.2$ for red galaxies, but no obvious trend is seen for blue galaxies. The faint-end slope for all galaxies when not split by colour can be understood by considering which colours dominate in which environments.

- The mock galaxy catalogues constructed from the Bower et al. (2006) galaxy formation model produce LFs that agree qualitatively with those found in GAMA, when split by environment and by colour. Discrepancies tend to appear in the overabundance of bright blue galaxies predicted by the mock catalogues in underdense environments, which could possibly be attributed to AGN feedback in the lowest mass haloes not considered in the model, and the faint end of the red LF in overdense environments, where too many faint red galaxies are predicted. This is likely to be due to hot gas being stripped too efficiently when a galaxy becomes a satellite of in larger halo.

This work will be extended further to investigate results found in this analysis. In particular the availability of various models of galaxy formation, based on those

used here, provides a means by which to measure how various aspects of galaxy formation and evolution affect the ability to constrain the galaxy LF in different environments. Comparing the work done here to the work of Eardley et al. (2015) (see also Chapter 5), helps to determine whether or not the variation of the LF with environment is due to the local environment in which a galaxy resides, or a more global environment, defined by eg. voids and filaments (see Chapter 5). The ability to measure galaxy bias through the method described above can also be investigated by measuring how the LF changes with galaxy overdensity for DDP samples covering various magnitude ranges, and for different galaxy populations (eg. colours). Future data from the DESI BGS survey will provide a large galaxy sample to investigate this. The availability of multi-wavelength data as well as stellar masses measured in GAMA, allows for this work to be extended to determine whether or not the trends in the LF seen here are consistent over a larger range of wavelengths or stellar masses.

Chapter 5

The Dependence of the Luminosity function on the Cosmic Web Environment

In Chapter 4, the dependence of the galaxy luminosity function on local overdensity was measured and parameterised by considering how the Schechter function parameters vary with overdensity. A larger scale geometric environment can be defined to classify the structure seen in the cosmic web. The work presented in this chapter investigates whether the cosmic web has any influence on the galaxy luminosity function, over the previously measured dependence on local environment. No significant deviation is found in the form of the luminosity function above that predicted using the local overdensity distribution which corresponds to each large-scale environment and the measured relationship between overdensity and Schechter function parameters. The work presented in this chapter, in particular the classification of the cosmic web, encompases and expands on the work presented in Eardley, Peacock, McNaught-Roberts, Heymans, Norberg, Alpaslan, Baldry, Bland-Hawthorn, Brough, Cluver, Driver, Farrow, Liske, Loveday, & Robotham (2015).

5.1 Introduction

The observable Universe is the result of the growth of initially small density perturbations in a nearly smooth density field through gravitational instability. Over time a network of structures is created, defining the so called "cosmic web". Virialised dark matter structures (called haloes) within this cosmic web contain potential wells in which galaxies may form and evolve, allowing a luminous, observable visualisation of structure. The cosmic web is visibly composed of distinct geometric structures, commonly labelled as voids, sheets, filaments and knots and is observed not only in the dark matter in simulations, but also in large scale galaxy redshift surveys such as SDSS, 2dFGRS and GAMA (e.g. see Fig. 1.2).

It is commonly found that galaxy properties are driven by the mass of their underlying dark matter haloes (Tinker et al., 2011; Robotham et al., 2010; Weinmann et al., 2006). In simulations, the cosmic web is found to be strongly dependent on the halo mass function (Metuki et al., 2015), therefore implying a dependence of galaxy properties on structure within the cosmic web.

Classifying the cosmic web in simulations is relatively straightforward through the availability of both spatial and dynamical galaxy information (Cautun et al., 2013), since the dynamics of galaxies provides a measure of the collapse of structures in the Universe through the velocity shear in a system. The lack of sufficient velocity information for galaxies restricts the ability to measure the cosmic web by dynamical means, and so an estimate must be based soley on the spatial distribution of galaxies. An explicit determination of the shape of structure in the Universe can be determined using a minimal spanning tree (Alpaslan et al., 2014). However, it is not obvious how the cosmic web defined in this way is connected to collapsed structures. An alternative to directly measuring the velocity shear is to instead indicate the geometric environment using a tidal tensor, which accounts for the gravitational potential of the system through the density field (Zhao et al., 2015; Alonso et al., 2015). Measuring the cosmic web using the density field is found to result in a clumpier distribution of structure than is found when using velocity shear measurements (Cautun et al., 2013).

Although the influence of the local density field on galaxy properties has been

well determined and parameterised (McNaught-Roberts et al. (2014), Chapter 4), it is less clear that a larger scale environment, as characterised by the cosmic web, has any direct impact on galaxy properties. The work presented in this chapter builds on the previous results from Chapter 4, measuring any additional influence the cosmic web might have on the galaxy luminosty function (LF), as measured by geometric environment, over the known dependence of the LF on local overdensity.

This chapter is laid out as follows. In §5.2 the method of classifying the cosmic web adopted for this study is described. §5.3 describes the GAMA galaxy sample used, gives brief recap of the measure of local overdensity, and the specific parameters used to classify the cosmic web. A direct comparison of the local and geometric environment is given in §5.4. In §5.5, the LF measured in each environment is presented, along with a parameterisation of the shape of the LF. Any residual dependence of the LF on the cosmic web over that previously determined is explored in §5.6. A discussion of the findings in this chapter is presented in §5.7.

5.2   Classification of the Cosmic Web

The method used to measure the large-scale geometric environment adopted here follows the approach of Hahn et al. (2007), which uses knowledge of the gravitational potential field Φ, to determine a tidal tensor, $T_{i,j}$, in order to assess the stability of structure at a given location in a cosmic volume. The tidal tensor is a measure of the tidal forces on a particle due to the gravitational field and therefore reflects the gravitational collapse within the cosmic web. A short summary of this method of measuring environment is given here, though a more complete description can be found in Eardley et al. (2015).

The tidal tensor is defined by the second derivatives of the potential at a given position in space with respect to the coordinates (r_i, r_j, r_k):

$$T_{i,j} = \frac{\partial^2 \Phi}{\partial r_i r_j}. \tag{5.1}$$

To measure this tidal tensor, the gravitational potential must be calculated using a density field. The 3D density field is constructed by assigning galaxies to a Cartesian grid of cell size $3\,h^{-1}\mathrm{Mpc}$. Galaxies are assigned to the grid using cloud-in-cell (CiC)

interpolation, such that the density of a cell receives contributions from galaxies in the 8 cells surrounding it, weighted by their distance from the cell centre. The overdensity in each cell is then found by comparing the weighted number of galaxies contributing to the cell, N_{obs}, to the number expected without clustering, N_{R}. This gives a measurement of overdensity, δ,

$$\delta = \frac{N_{\mathrm{obs}}}{N_{\mathrm{R}}} - 1. \tag{5.2}$$

To suppress shot noise within the density field, the field is smoothed in Fourier space with a Gaussian window function with a width of σ_{s} (given in the first column of Table. 5.1).

Since the density field depends to some extent on the density of surrounding cells, the density field is underestimated close to the survey boundaries (beyond which the density is zero). To account for this, galaxies are replicated such that the volume is reflected through the boundaries. A more detailed description of this procedure and its effects on the measurment of environment are given in Appendix A of Eardley et al. (2015).

Once the density field has been determined in Fourier space, the second derivative of the gravitational potential, $\nabla^2\Phi$, within each cell can be obtained from Poisson's equation:

$$\nabla^2\Phi = 4\pi G\bar{\rho}\delta, \tag{5.3}$$

where G is the gravitational constant, $\bar{\rho}$ is the average matter density of the Universe, and δ is the overdensity measured for a given cell in the density field. The potential is normalised by factoring out $4\pi G\bar{\rho}$ such that dimensionless eigenvalues, λ_1, λ_2 and λ_3, of the diagonalized Hessian of Φ can be obtained in fourier space. The dimensionless tidal tensor of a cell is then simply:

$$\tilde{T}_{\mathrm{i,j}} = \frac{k_i k_j \delta_k}{k^2}, \tag{5.4}$$

where δ_k is the Fourier transform of the density field in the cell, and $k = \sqrt{k_i^2 + k_j^2 + k_k^2}$.

The eigenvalues determine the direction of collapse in each dimension for each cell. The number of dimensions along which structure is collapsing within a cell

determines the geometric environment at that location. This is determined by the number of eigenvalues larger than a given threshold, λ_{th}. The environment of the cell is then classified as one of the following:

- Voids: all eigenvalues are below the threshold.

- Sheets: one eigenvalue is above the threshold.

- Filaments: two eigenvalues are above the threshold.

- Knots: all eigenvalues are above the threshold.

The value of λ_{th} is arbitrary but determines the fraction of cells which contribute to each geometric environment (see Table. 5.1). The classifications of environments can be considered to indicate the *dimensionality* of collapse, such that knots have the lowest dimensionality, as they correspond to regions that have collapsed in all dimensions.

5.3 Data and Method

The sample of galaxies used in this analysis, as well as a brief recap of the measure of local overdensity, and the specific parameters chosen to measure the cosmic web in GAMA are discussed in this section.

5.3.1 GAMA sample

The sample of galaxies used here is the same sample as described in Chapter 4 (see Figs. 4.2 and 4.5, Table 4.2), enabling a simple comparison between the two descriptions of environment. This sample covers the redshift range $0.040 < z < 0.263$, and only includes galaxies with a completeness greater than 80% (see Fig. 4.3). Absolute magnitudes are calculated allowing for luminosity evolution and a colour-dependent k-correction as in §4.2.1.

5.3.2 Measure of Local Environment

The local environment is measured as the overdensity assigned to a galaxy, i, in the GAMA sample as determined in Chapter 4. To summarize, the density around the galaxy is measured using equation 4.4, in a sphere of radius r_s centred on the galaxy. The density is corrected for spectroscopic completeness within the sphere and volume completeness to account for the survey boundaries. $r_s = 8\,h^{-1}\mathrm{Mpc}$ is adopted here, unless otherwise mentioned.

The overdensity, δ_8 is measured using equation 4.5, relative to the effective mean density of DDP galaxies in the volume.

5.3.3 Geometric environment in GAMA

To measure the density field (see equation 5.2), the expected number of unclustered galaxies within a cell, N_R, is required. This is determined by a random catalogue of cloned GAMA galaxies. The cloned galaxies are generated within the survey volume, V_{max}, over which they could be observed while retaining their intrinsic properties. V_{max} for a galaxy with an absolute magnitude M_r, is the maximum volume within which a galaxy can be observed, limited by z_{max} (m_{faint}) and z_{min} (m_{bright}).

A density weighted V_{max} is used to account for density fluctuations within the catalogue. This method is described in more detail in Farrow et al. (2015), and essentially gives larger weight to galaxies in underdense regions. Galaxies are cloned an arbitrarily large number of times (400 in this case) to reduce shot noise over the smoothing scales considered here.

The scale over which the density field is smoothed represents the scale of dynamic stability being measured, so to test whether or not the classification of geometric environment depends on smoothing scale, two scales $\sigma_s = 4$ and $10\,h^{-1}\mathrm{Mpc}$ are considered in this analysis. Two values of the threshold are also considered, $\lambda_{\mathrm{th}} = 0.40$ and 0.10, corresponding to the chosen smoothing scales $\sigma_s = 4$ and $10\,h^{-1}\mathrm{Mpc}$ respectively, such that both combinations of smoothing parameter and threshold values give comparable statistics within each environment, therefore giving the smallest dispersion in the numbers of galaxies contributing to each environment. See Ta-

$\sigma_{\rm s}$ (h^{-1}Mpc)	$\lambda_{\rm th}$	Environment	$N_{\rm env}$	$f_{\rm num,env}$	$f_{\rm vol,env}$
4.00	0.40	Voids	15723	0.19	0.36
		Sheets	30210	0.37	0.41
		Filaments	27875	0.34	0.20
		Knots	7114	0.09	0.03
10.0	0.10	Voids	11008	0.14	0.59
		Sheets	27584	0.34	0.30
		Filaments	32149	0.40	0.10
		Knots	10181	0.13	0.01

Table 5.1: Combinations of the smoothing scale (used to determine the local density field), $\sigma_{\rm s}$, and threshold parameters (used to classify the cosmic web), $\lambda_{\rm th}$, the environment classification, the number ($N_{\rm env}$) and fraction ($f_{\rm num,env}$) of galaxies in the sample considered falling in each environment, and the fraction of the total volume each environment covers($f_{\rm vol,env}$).

ble. 5.1 for a quantative comparison of these threshold parameters and smoothing scales.

A comparison of the smoothed CiC overdensities used when measuring the tidal tensor, to the spherical top-hat overdensities (§5.3.2) is shown in Fig. 5.1. The left panel shows how the top-hat overdensity compares with the CiC density field smoothed with a gaussian of width $\sigma_{\rm s} = 4.0 \, h^{-1}$Mpc, and the right panel shows the comparison to the density field smoothed with $\sigma_{\rm s} = 10 \, h^{-1}$Mpc. Overdensities measured with smaller sphere sizes cover a larger dynamic range, such that underdense regions can be more thoroughly probed. It is clear that the geometric density field measured using a smoothing scale of $4 \, h^{-1}$Mpc gives a very similar overdensity distribution to that of overdensities measured in a sphere with radius $8 \, h^{-1}$Mpc, while the density field measured using a smoothing scale of $10 \, h^{-1}$Mpc more closely agrees with overdensities measured using much larger sphere sizes. While adopting a local overdensity defined by a sphere of radius $8 \, h^{-1}$Mpc, it is possible to compare local and geometric environments probed by scales with comparable ($\sigma_{\rm s} = 4 \, h^{-1}$Mpc) as well as significantly different ($\sigma_{\rm s} = 10 \, h^{-1}$Mpc) overdensity distributions.
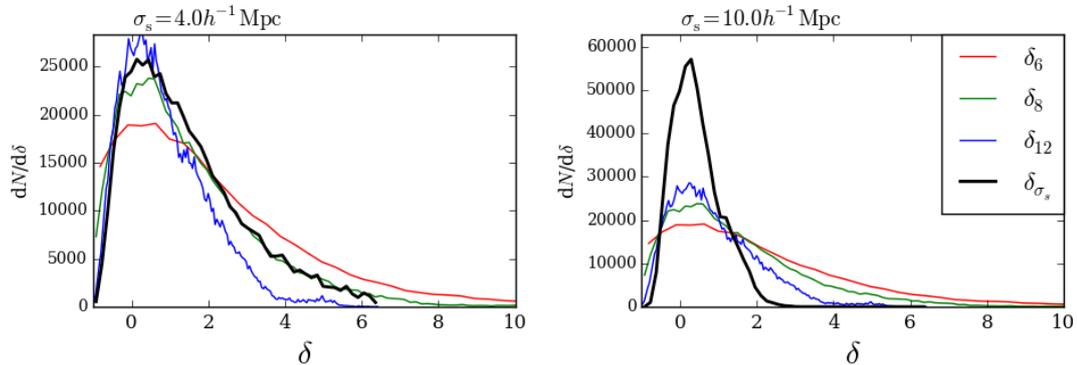
Figure 5.1: Distribution of overdensities in the magnitude limited galaxy sample as measured by a CiC algorithm, δ_{σ_s}, smoothed with a Gaussian filter of width σ_s (black), with $\sigma_s = 4\,h^{-1}$Mpc (*left*), and $\sigma_s = 10\,h^{-1}$Mpc (*right*), and the distribution of spherical overdensities within radii $6\,h^{-1}$Mpc (red), $8\,h^{-1}$Mpc (green) and $12\,h^{-1}$Mpc (blue). A CiC smoothed with $\sigma_s = 4\,h^{-1}$Mpc is most comparable to a spherical overdensity with a top-hat smoothing of radius $8\,h^{-1}$Mpc, whereas a CiC with $\sigma_s = 10\,h^{-1}$Mpc is more comparable to spherical overdensities with larger radii.

From here on, the local environment measured using a top-hat function as described in this section is referred to simply as the "overdensity", while the larger scale definition of environment characterising the cosmic web is referred to as the "geometric environment".

5.4 Direct comparisons of environment measures

The distribution of overdensities is measured for each geometric environment, as shown in Fig. 5.2. It is clear that regardless of the smoothing scale or threshold parameter chosen, voids are dominated by lower overdensities and knots are dominated by higher overdensities. However, over the scales considered, it is not accurate to assume that galaxies residing in a local environment with a low overdensity belong to voids, or that galaxies classified as knots must have a high local overdensity. When using a smoothing scale of $10\,h^{-1}$Mpc, the spread in overdensities is slightly larger than for a smoothing scale of $4\,h^{-1}$Mpc, suggesting that with a larger smoothing
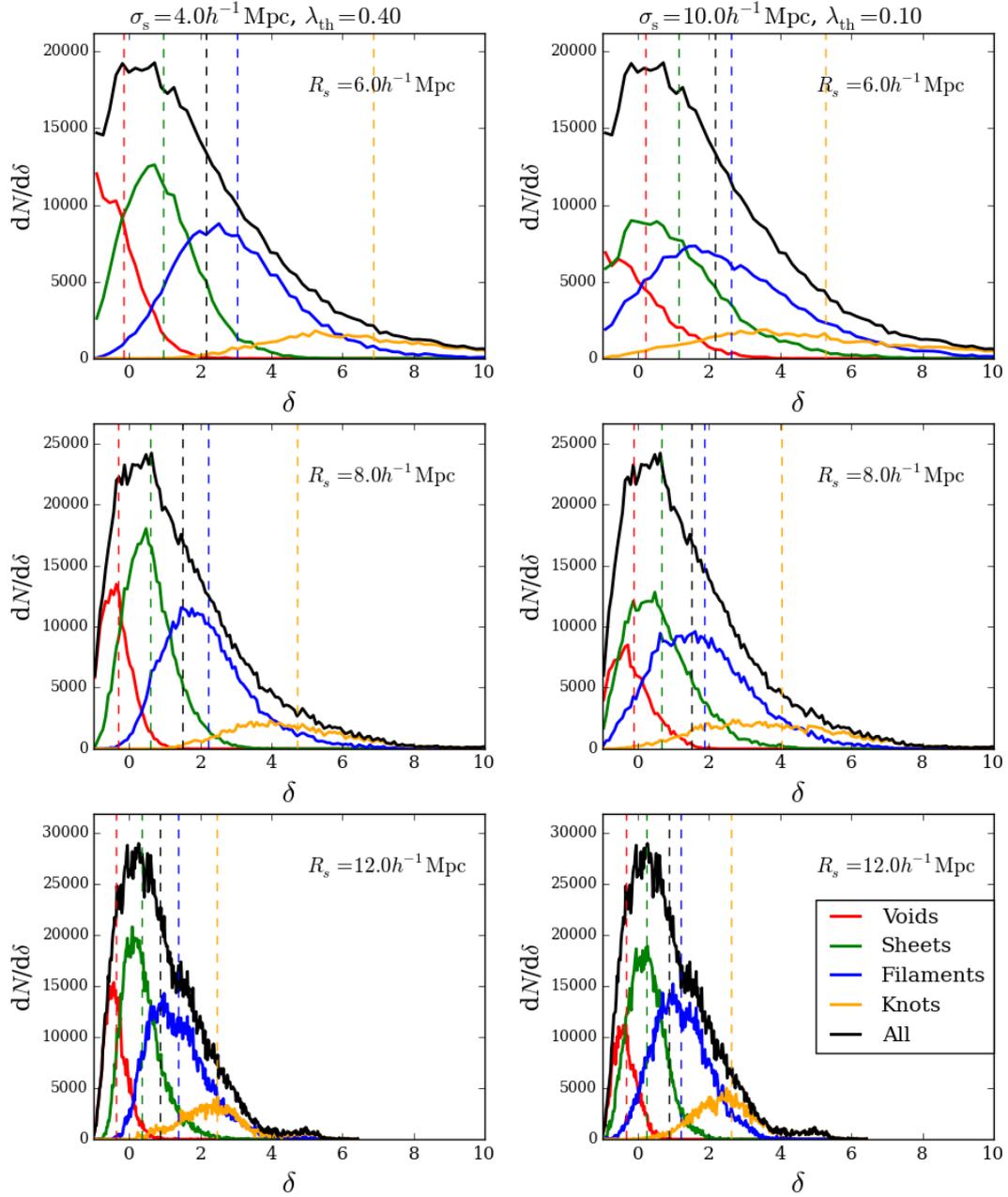
Figure 5.2: Distribution of local overdensity for each geometric environment in the magnitude limited galaxy sample. The dashed lines show the mean overdensity, coloured by environment. Spherical top-hat overdensities are calculated for sphere radii of $6\,h^{-1}$Mpc (*top*), $8\,h^{-1}$Mpc (*middle*), and $12\,h^{-1}$Mpc (*bottom*). Environments are calculated using a smoothing scale and threshold of $\sigma_\mathrm{s}{=}4\,h^{-1}$Mpc and $\lambda_\mathrm{th}{=}0.40$ (*left*) or $\sigma_\mathrm{s}{=}10\,h^{-1}$Mpc and $\lambda_\mathrm{th}{=}0.10$ (*right*). The total overdensity distribution (black) is the sum of the distributions in each environment.

scale, the geometric environment classification loses some of its dependence on local environment. Likewise when using a larger sphere size to determine local overdensity, the overall density distribution becomes much narrower, significantly reducing the overdensity range probed (as is also seen in Fig. 5.1).

The large range of overdensities within a given environment provides evidence that large-scale geometric environment is not directly implied by local overdensity. By comparing galaxy properties within the cosmic web, we can determine if the physical processes involved in the evolution of galaxies in the cosmic web is a direct impact of local overdensity or if some aspect is independently related to geometric environment.

5.5   The cosmic web dependence of the LF

The LF is measured for each geometric environment and shown in Fig. 5.3 for both combinations of smoothing scales and threshold parameters considered. The measurement of the LF is as described in §4.2.5, but normalised to take into account the effective volume occupied by an environment. By factoring out the reference Schechter function given in Eqn. 4.11 (which is in this case scaled to the mean overdensity within each environment, $\delta_{8,\mathrm{env}}$), the variation in shape of the LF between environments can be seen clearly. As expected the knee of the LF, characterised by M^*, becomes brighter towards environments with lower dimensionalities, and the number density, characterised by ϕ^*, increases. There is no obvious change in the slope of the faint end. The variation of these parameters between environments is seen more clearly in Fig. 5.4. The errors on the Schechter parameters here are jackknife errors, and the best fit parameters to the LF of the total sample are shown by the horizontal dashed lines. M^* and ϕ^* clearly brighten and increase with lower dimensionalities, with no clear trend between the faint end slope, α, and environment. For the larger smoothing scale and smaller threshold parameter the trends with M^* and ϕ^* appear to be less strong. This result can be considered as the effect of smoothing the density field over a larger volume, resulting in the environments becoming less distinct, as can be seen by the broad distribution of the right panel
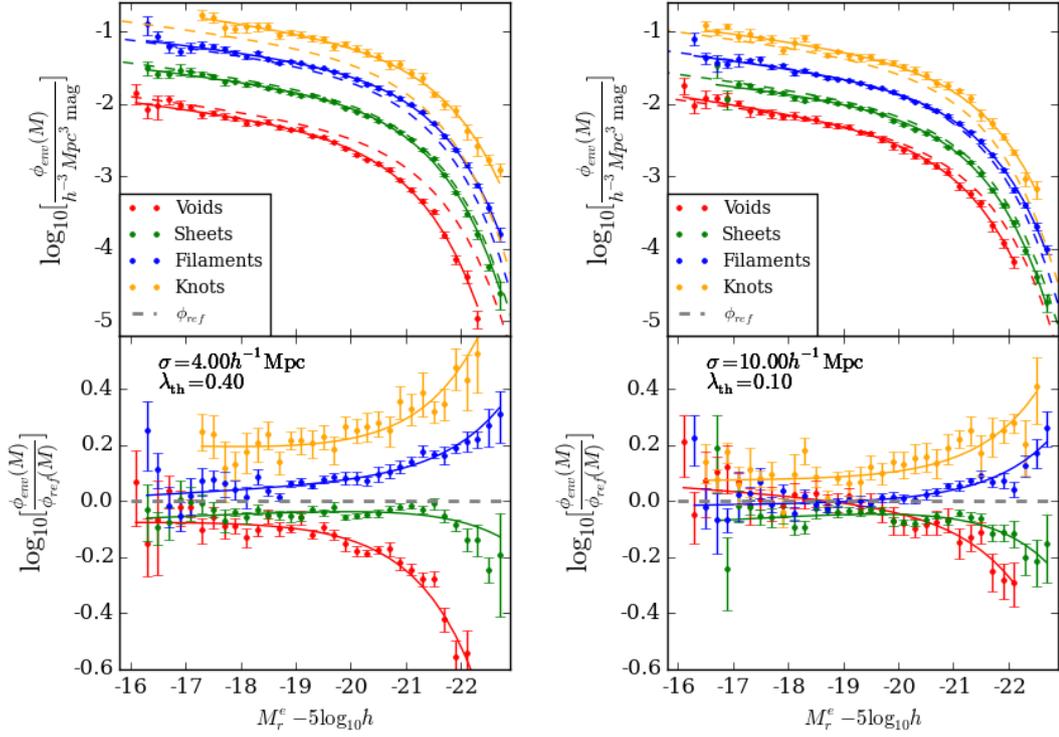
Figure 5.3: *Top*: LFs measured in each environment, with jackknife errors and best fitting Schechter functions. The reference Schechter function (as described by Eqn. 4.11) scaled to the mean overdensity in each environment is shown by the dashed coloured lines. *Bottom*: Ratio of LFs in each environment to the reference Schechter function. Environments are calculated using a smoothing scale and threshold of $\sigma_s=4\,h^{-1}$Mpc and $\lambda_{\rm th}=0.40$ (*left*) or $\sigma_s=10\,h^{-1}$Mpc and $\lambda_{\rm th}=0.10$ (*right*). LFs vary significantly between environments, particularly for a lower density field smoothing scale.
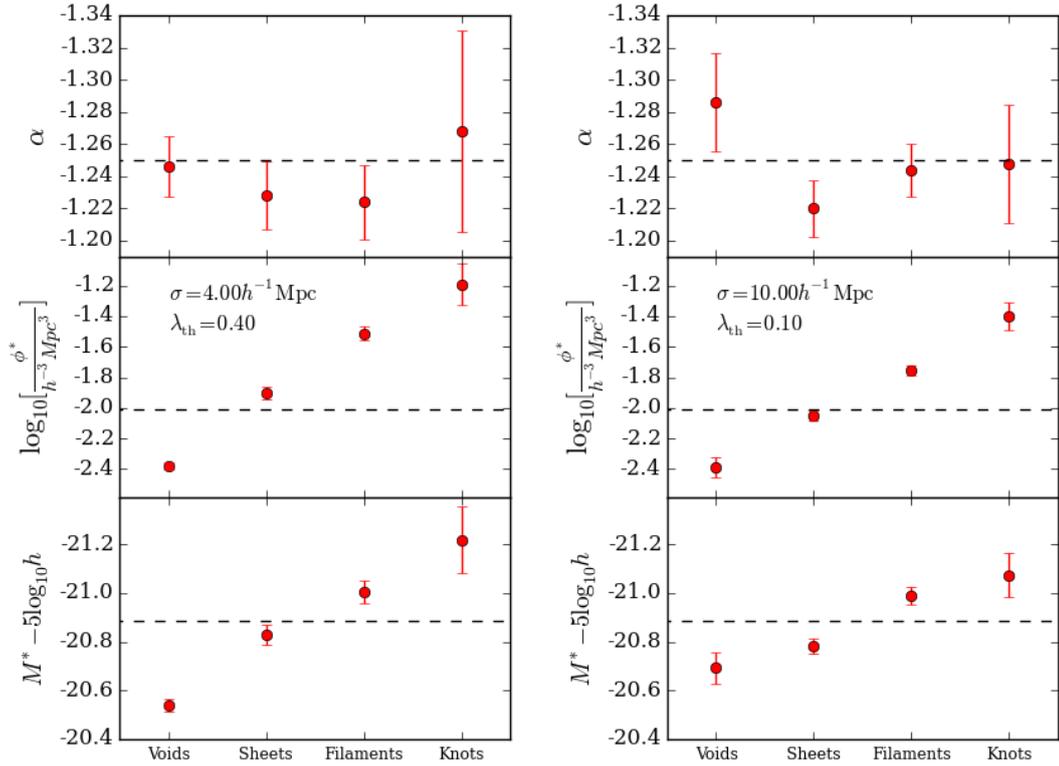
Figure 5.4: Best fitting Schechter function parameters α (*top*), ϕ^* (*middle*) and M^* (*bottom*) to the LFs shown in Fig. 5.3. Uncertainties on the parameters are jackknife errors. The dashed horizontal lines show the best fitting parameters to the total LF, used to define the reference Schechter function shown in Fig. 5.3. Environments are calculated using a smoothing scale and threshold of $\sigma_s=4\,h^{-1}$Mpc and $\lambda_{th}=0.40$ (*left*) or $\sigma_s=10\,h^{-1}$Mpc and $\lambda_{th}=0.10$ (*right*).

of Fig. 5.2.

It is clear that environment does affect the shape of the LF and thus brighter galaxies reside in environments with lower dimensionalities, but it is not clear whether these trends are affected by the geometric environment in which a galaxy resides, or simply just by the local density. Fig. 5.2 shows clearly that there is a large range of overdensities contributing to a given environment classification. It is important therefore to compare these results taking into account the overdensity distribution of the sample. In §5.6 we test any dependence of the LF on large-scale geometric environment over the local environment.

5.6 Inferring the LF from local overdensity

By assuming galaxy properties such as the LF are driven by local overdensity alone, the shape of the galaxy LF for a given geometric environment can be predicted by the overdensity distribution of each environment within the cosmic web. This assumption can be tested to assess how much the cosmic web has an impact on galaxy properties over and above the effect of local environment.

5.6.1 Parameterised prediction of the LF in the cosmic web

The dependence of the Schechter function parameters on local overdensity was investigated in Chapter 4. These results, shown in Fig. 4.9, can be used to infer an LF from the overdensity distribution for a given geometric environment (as shown in Fig. 5.2), by parameterising the LF by a Schechter function. For a spatial position with a given overdensity, the expected Schechter function at that position can be found using the analytical fits to each Schechter function parameter (Table. 4.4). The expected LF is then calculated by averaging the expected Schechter functions over the volume contributing to a geometric environment. The analytical fits allow Schechter function parameters to be determined for any overdensity. However, due to the large uncertainty in these fits and the clear degeneracy between Schechter function parameters, it is not clear that they accurately describe the variation in the LF with overdensity. For this reason the predicted Schechter function parameters
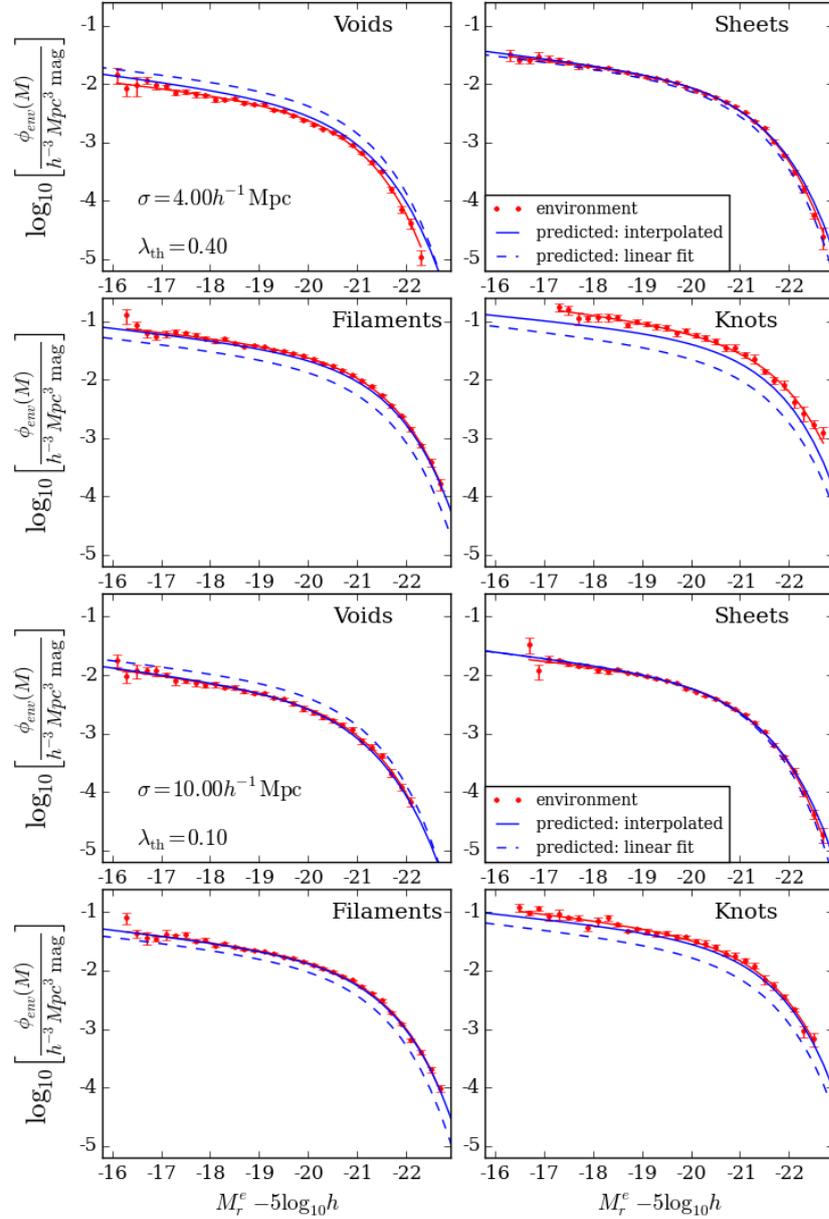
Figure 5.5: LFs measured in each environment, with jackknife errors and best fitting Schechter functions (red). Blue lines show the Schechter function predicted by the over-density distribution within each environment using $R_s = 8\,h^{-1}\mathrm{Mpc}$, with the linestyle indicating predictions from interpolation between density bins (solid) and the linear an-alytical fit to density bins (dashed). *Top 4 panels*: Environments are classified using a smoothing scale and threshold of $\sigma_s{=}4\,h^{-1}\mathrm{Mpc}$ and $\lambda_{\mathrm{th}}{=}0.40$. *bottom 4 panels*: Environ-ments are classified using a smoothing scale and threshold of $\sigma_s{=}10\,h^{-1}\mathrm{Mpc}$ and $\lambda_{\mathrm{th}}{=}0.10$.

are found by interpolating between measured overdensity bins. This method does not rely on a simple linear relation between Schechter parameters and overdensity, but instead takes into account variations over a small overdensity range. For the most extreme overdensities, Schechter function parameters are assumed to be fixed to the best fit ones for the closest density bin. We find very little difference in the resulting Schechter function between this approach and assuming the analytical fit for the most extreme densities.

The expected Schechter function, $\phi_{\mathrm{pred,env}}$ is described by the sum of the Schechter functions predicted by the local overdensity, $\phi(\delta_{\mathrm{i}})$ at randomly distributed points within a geometric environment:

$$\phi_{\mathrm{pred,env}}(M) = \frac{1}{N_{\mathrm{env}}} \sum_{\mathrm{i}=1}^{N_{\mathrm{env}}} \phi(\delta_{\mathrm{i}}, M), \tag{5.5}$$

where N_{env} is the fraction of randomly distributed points within the volume classified as a given geometric environment, and for a given magnitude bin, M, the LF $\phi(\delta_{\mathrm{i}}, M)$ is measured by a Schechter function (Equation 4.10), with best fit parameters at a given overdensity, $\alpha(\delta_i)$, $M^*(\delta_i)$ and $\phi^*(\delta_i)$.

These expected Schechter functions are shown in Fig. 5.5 for each combination of smoothing scale and threshold parameters. The predicted Schechter functions determined by Schechter function parameters found by interpolating between overdensity bins and by using the analytical fits are shown by the blue solid and dashed lines respectively. It is clear that these two methods of predicting the Schechter function do not agree particularly well for the environment classifications with the most extreme dimensionalities, where the overdensity distribution is heavily weighted towards particularly underdense or overdense environments. Since there are large uncertainties in the linear analytical fits for the most extreme overdensities, from here on only the Schechter function predicted by interpolation is used when comparing the Schechter function to that measured for each environment.

At a first glance the LF for a given environment appears to agree particularly well with the predicted Schechter function. The only significant differences appear to be between the measured LF and the predicted Schechter function for galaxies in knots when using a density field with $\sigma_{\mathrm{s}} = 4\,h^{-1}\mathrm{Mpc}$, for all luminosities, and
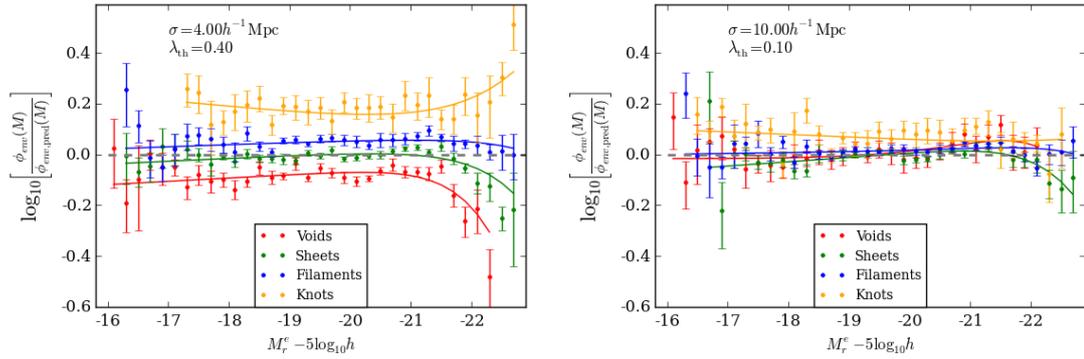
Figure 5.6: The ratio of the LF measured in each environment to the interpolated predicted Schechter function as shown in Fig. 5.5. Environments are classified using a smoothing scale and threshold of $\sigma_s=4\,h^{-1}$Mpc and $\lambda_{th}=0.40$ (*left*) or $\sigma_s=10\,h^{-1}$Mpc and $\lambda_{th}=0.10$ (*right*). Overdensities to create the predicted Schechter function are calculated using spheres radius $8\,h^{-1}$Mpc. An agreement between the measured LF and the predicted Schechter function in each environment suggests that all environmental dependence is described by the dependence on local overdensity.
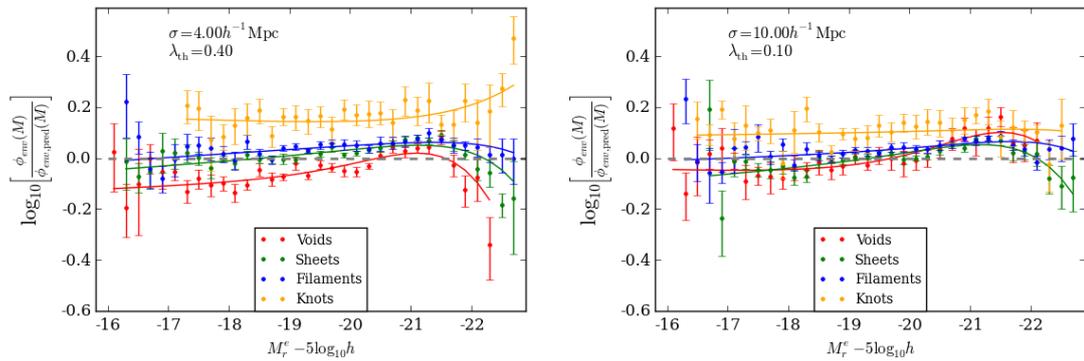
Figure 5.7: The same as Fig. 5.6 but for predicted Schechter functions using a local overdensity distribution defined using spheres of radius $6\,h^{-1}$Mpc.

the very bright end of the void LF for the same smoothing scale, where the LF is predicted to be too high.

The ratio between the measured LF and the predicted Schechter function shows differences in the shape of the LF, as shown in Fig. 5.6. There is a strong agreement between the measured LF and the LF predicted in different geometric environments when considering a smoothing scale of $10\,h^{-1}$Mpc. However, the measured and predicted LFs do not agree as well when using a smoothing scale of $4\,h^{-1}$Mpc, for which the density field gives a galaxy overdensity distribution more indicative of the spherical overdensity distribution for spheres of radius $8\,h^{-1}$Mpc (see Fig. 5.1). For a smoothing scale of $4\,h^{-1}$Mpc, the LF of galaxies in the most extreme environments diverges significantly from the predicted Schechter function, particularly at the bright end of the LF. More galaxies, particularly bright galaxies, are found in knots than is predicted by galaxies following the same local overdensity distribution as knot galaxies. Likewise, fewer bright galaxies appear in voids than are predicted. The disagreement between the measured LF and the predicted LF appears to be mostly due to the normalisation (ϕ^*) of the LF for $M_\mathrm{r}^e - 5\log_{10}h < -21$.

To check whether this is just an effect of the scale over which overdensity is measured, the same test is done for the LF predicted by an overdensity distribution calculated within spheres of radii $6\,h^{-1}$Mpc. The result of this is shown in Fig. 5.7, where around the knee, the LF for voids is more accurately predicted, but the bright and faint ends of the LF are still predicted to be too high. There is still a disagreement between the predicted and measured LFs for knots, suggesting that on these small scales that there is a greater number density of galaxies in knots than can be probed by the local overdensity. When comparing the predicted and measured LFs for an overdensity distribution measured with larger spheres of radius $12\,h^{-1}$Mpc, the disagreement increases. While agreement is found between the predicted and measured LFs when considering large smoothing scales, environment classified using a density field with smaller smoothing scales is much more sensitive to the sphere size used to measuring local overdensity.

The difference in shape exhibited by the predicted void LF when considering overdensities with radius $6\,h^{-1}$Mpc could be caused by the faint end slope, α, being

predicted to be too steep while M^* is too faint and is consistent with previous results showing that fainter galaxies reside in voids. Therefore when considering an overdensity within a smaller sphere size, a smaller volume within the void is probed, which is likely to contain fainter galaxies with less contamination from non-void (and possibly brighter) galaxies.

When predicting the Schechter function in each environment, galaxies with the highest overdensities are assigned the Schechter function parameters which correspond to the mean overdensity of the highest overdensity bin ($\bar{\delta_8} = 5.13$ for a sphere of radius $8\,h^{-1}\mathrm{Mpc}$, $\bar{\delta_8} = 5.63$ for $6\,h^{-1}\mathrm{Mpc}$). It is very likely that this assumption is incorrect, affecting the ability to predict the LF particularly in knots (since almost half the galaxies in knots have a local overdensity $\delta_8 > 5.13$ for $\sigma_\mathrm{s} = 4\,h^{-1}\mathrm{Mpc}$). If the highest overdensity bin is split in order to obtain a prediction for the LF for galaxies with higher overdensities, the uncertainties on the measured Schechter parameters become very large due to the smaller numbers of galaxies contributing to these overdensity bins, and so this does not improve the predicted LF. It is likely that this effect is reduced when using a larger smoothing scale ($\sigma_\mathrm{s} = 10\,h^{-1}\mathrm{Mpc}$) due to the broader overdensity distributions within a given environment, such that knots are not as significantly dominated by the most extreme local overdensities.

5.6.2 Direct prediction of the LF given an overdensity distribution

Another method with which to test the influence of geometric environment on the galaxy LF over that of local overdensity involves resampling the galaxy catalogue in order to remove any geometric information, but while retaining the same local overdensity distribution.

Four "shuffled" galaxy catalogues are created such that each reproduces the same local overdensity distribution as one of the geometric environments (voids, sheets, filaments or knots). Essentially this process involves replacing a galaxy with a given geometric environment and local overdensity, with another galaxy with the same local overdensity but not necessarily with the same geometric environment classification. To choose a galaxy of the same local overdensity, the requirement is imposed

that the replacement galaxy must have a local overdensity within $\Delta\delta_8 = 0.05$ of the original galaxy's overdensity. The galaxy sample used is volume limited, such that any galaxy in the sample can be moved to any position within the defined redshift limits and still be seen, while avoiding selection biases. A volume limited sample is defined by the absolute magnitude range $-18.5 < M_r < -22.0$, corresponding to a volume covered between $0.021 < z < 0.137$. Such a chosen sample allows the absolute magnitude range probed to cover a large range of the galaxy LF, in particular including the knee of the LF (since Fig. 5.4 shows no obvious variation in the slope of the faint end between environments), while allowing the sample statistics to be large enough to minimise the uncertainty on the calculated LF.

The LFs are shown in Fig. 5.8, where errors on the shuffled LF are calculated as the scatter from 9 different realisations of the shuffled catalogue.

Fig. 5.9 gives the probability of a galaxy within a geometric environment being replaced with another geometric environment. While void, sheet and filament galaxies are likely to be replaced with other galaxies with the same geometric environment, knot galaxies are more likely to be replaced with filament galaxies. There is a larger overlap in the overdensity distributions of geometric environments defined with a density field smoothed over $10\,h^{-1}\mathrm{Mpc}$, and so it is likely that the fraction of galaxies replaced by a galaxy with the same geometric environment classification is smaller.

A direct comparison of the measured LF for geometric environments in the volume limited sample, and the sample shuffled between environments, is given in Fig. 5.8, for both smoothing scales and threshold parameters. There is no clear variation in the LFs more than the scatter from realisations. This is not unexpected, since the overdensity distributions of the true environments are themselves realisations of the shuffling process.

This can be seen more clearly when dividing the LF for each environment by the shuffled LF, as shown in Fig. 5.10. When using a local overdensity distribution measured using spheres of radius $8\,h^{-1}\mathrm{Mpc}$, no significant differences can be seen between the LF for the true environments and the shuffled environments. Most importantly this result is seen for knots (particularly for a density field smoothed
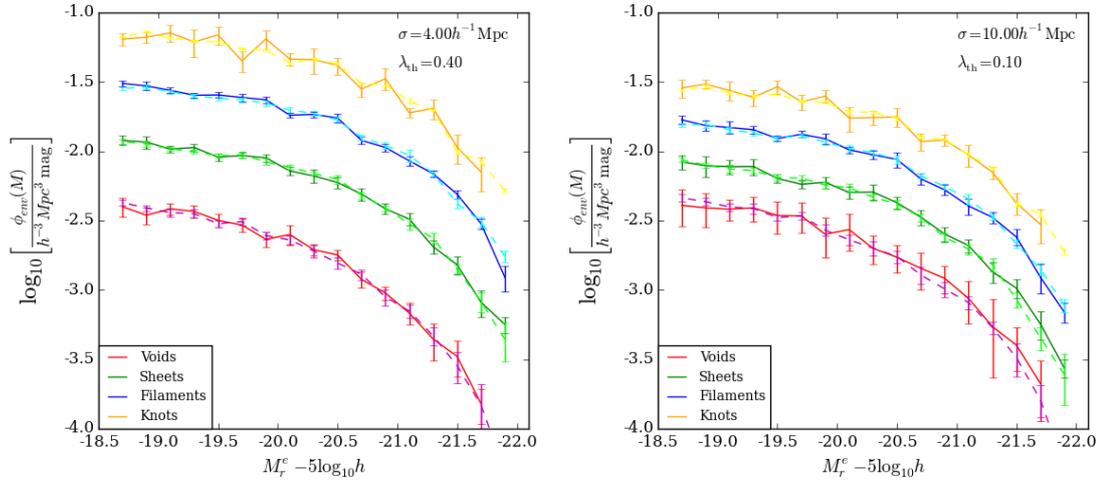
Figure 5.8: Comparison of the LFs measured in each environment (solid lines) and the LF for the sample shuffled within density bins (dashed lines). Environments are classified using a smoothing scale and threshold of $\sigma_s = 4\,h^{-1}$Mpc and $\lambda_{th} = 0.40$ (*left*) or $\sigma_s = 10\,h^{-1}$Mpc and $\lambda_{th} = 0.10$ (*right*). There is no disagreement between the measured and shuffled LFs.
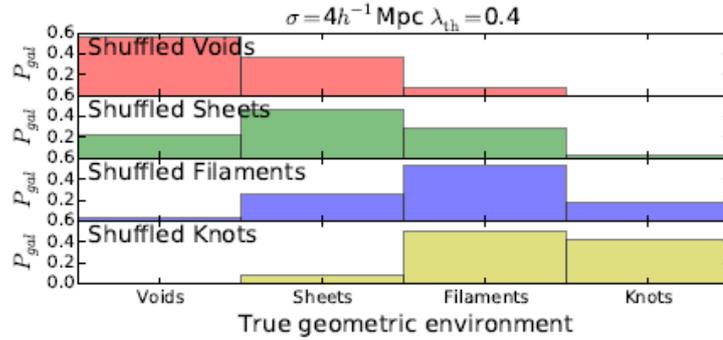
Figure 5.9: The probability of a galaxy (P_{gal}) being replaced with a galaxy from a given geometric environment, while keeping the same local density information. As expected a large fraction of shuffled galaxies populate the environment of the original galaxy, but for the most extreme environments this fraction dominates the whole distribution. These results are shown for a smoothing scale and threshold of $\sigma_s = 4\,h^{-1}$Mpc and $\lambda_{th} = 0.40$ (Fig. 7 from Eardley et al. 2015).
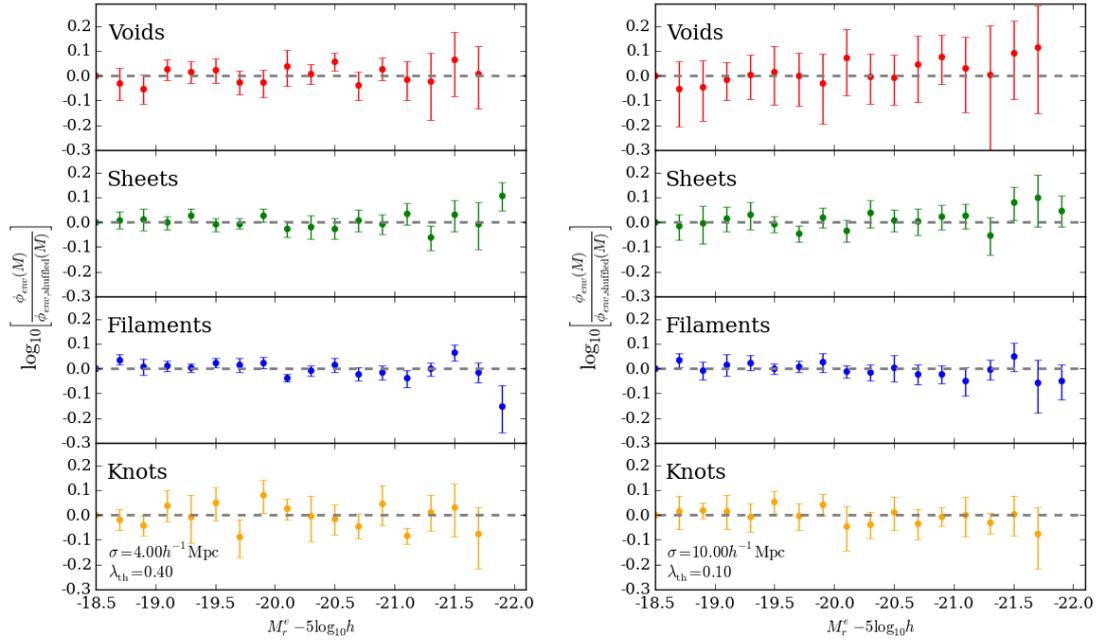
Figure 5.10: The ratio of the LF measured for the volume limited sample in each environment to the LF of the sample shuffled within density bins. Environments are classified using a smoothing scale and threshold of $\sigma_\mathrm{s}{=}4\,h^{-1}\mathrm{Mpc}$ and $\lambda_\mathrm{th}{=}0.40$ (*left*) or $\sigma_\mathrm{s}{=}10\,h^{-1}\mathrm{Mpc}$ and $\lambda_\mathrm{th}{=}0.10$ (*right*). The LFs do not diverge from each other, regardless of smoothing scale and threshold used.

over $10\,h^{-1}$Mpc) where the distribution of local overdensities is broad enough that more than half of galaxies are expected to be replaced with a galaxy with a different environment classification.

The LF measured for samples shuffled in the local overdensity distributions measured using spheres with radii $6\,h^{-1}$Mpc and $12\,h^{-1}$Mpc gives the same results, such that there is no clear difference between the predicted LF and the measured LF in each environment.

It seems evidential that there is no further information to be gained from considering geometric environment over that from the local density distribution when considering a volume limited sample.

5.6.3 Direct prediction of the LF given a density field

We have shown that for a volume limited sample, the geometric environment does not add information to the galaxy LF over that already determined by the local overdensity distribution when considering only the magnitude range of $-18.5 > M_r^e > -22.0$. To test this over the the full magnitude range, fixed cell volumes within the survey can be shuffled between environments instead of galaxies. All cells contain the same geometric volume, so when replacing a cell with another of the same overdensity, all information contained within that cell is retained, such that the galaxy information does not change. The LF is normalised by the fraction of cells within the shuffled sample, as the effective volume of the LF. For simplicity, the cells are chosen to be those with which the density field (§5.2) was constructed. The density field provides overdensity information for each cell, and a cell can be replaced with another cell with the same overdensity from the density field. This method therefore does not require a volume limited sample and can probe the whole magnitude range of the LF.

The LF for each environment divided through by the cell shuffled LF is shown in Fig. 5.11. The vertical offset is due to the selection function of the survey which is not taken into account when shuffling cells over the whole redshift range. Other than the offset, there is no significant difference in the shape of the LF in each geometric environment over that expected by the overdensity distribution of cells.
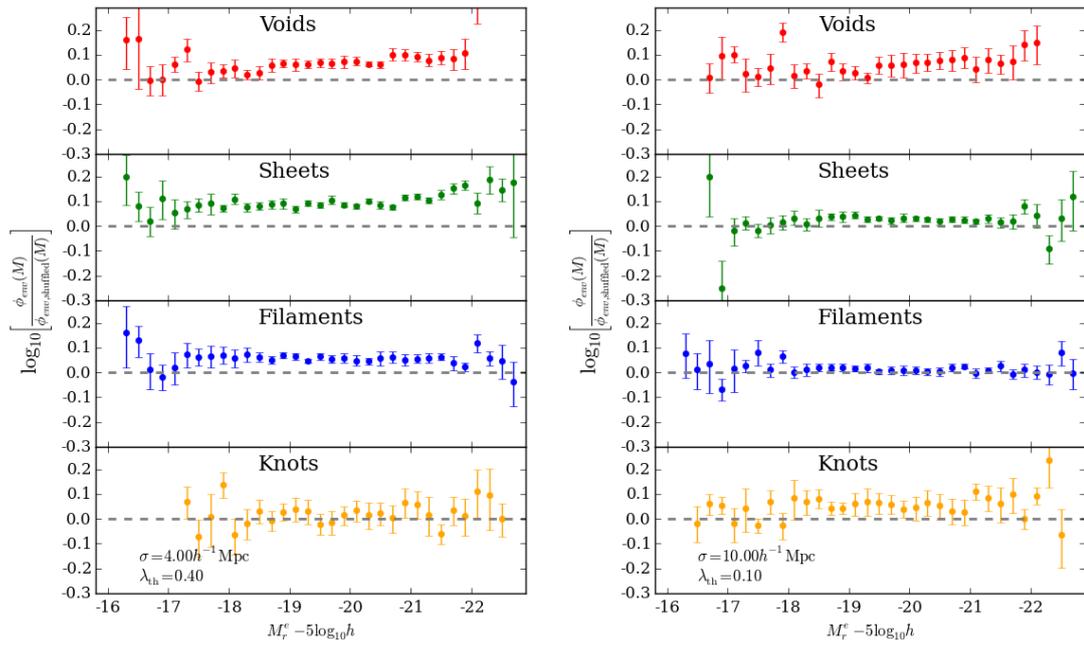
Figure 5.11: The ratio of the LF measured in each environment to the LF of the sample constructed by shuffling within density bins. Environments are classified using a smoothing scale and threshold of $\sigma_{\rm s}{=}4\,h^{-1}$Mpc and $\lambda_{\rm th}{=}0.40$ (*left*) or $\sigma_{\rm s}{=}10\,h^{-1}$Mpc and $\lambda_{\rm th}{=}0.10$ (*right*).

5.7   Discussion and Conclusions

Methods have been presented for testing the influence of the cosmic web on the galaxy LF, over and above the known dependence of the LF on local overdensity. The correlation between local overdensity and Schechter function parameters presented in Chapter 4 is used to predict an LF given the overdensity distribution in each geometric environment. The LF is also measured for shuffled galaxy samples which imitate the each local overdensity distribution for a volume limited sample. This is also done for shuffled cells within the smoothed density field used to classify the cosmic web, to probe a larger magnitude range. These tests show that the LF does not significantly deviate from that expected by the underlying distribution of overdensities within a given geometric environment.

When considering the LFs predicted by the relationship between overdensity and the Schechter function parameters, the only significant differences are seen in the geometric environments with the most extreme dimensionalities. For smoothing of $4\,h^{-1}$Mpc, more galaxies are found in knots than predicted given the overdensity distribution of knot galaxies, and fewer in voids, particularly at the bright end of the LF. However for a larger smoothing scale of $10\,h^{-1}$Mpc there is no difference. When probing overdensity with a smaller sphere size ($6\,h^{-1}$Mpc radius), the void LF is much better predicted. Void regions contain faint galaxies (Croton et al., 2005), and it is likely that when using a smaller sphere size, the measure of overdensity in void regions is less contaminated by nearby brighter galaxies.

Previous investigations have studied the relationship between galaxy properties and the various parameterisations of the cosmic web (Metuki et al., 2015; Alpaslan et al., 2015). It has been well determined that the properties of galaxies are strongly correlated with where they reside within the cosmic web. The results presented here show that any change in the galaxy LF with environment can be characterised by the changes with local environment defined by spherical top-hat overdensity, and that tidal forces (parameterised by the tidal tensor $T_{i,j}$) do not appear to have any further influence on galaxy formation and evolution over the scales probed in this work. This result is consistent with Yan et al. (2013), who used SDSS data to study the tidal dependence of galaxy properties by characterising a morphological environment

based on the ellipticity of the potential field. They determine that galaxy properties (in particular colour, age, concentration and size) are affected mostly by the local environments in which they reside and that any further dependence on the ellipticity of the potential field is very weak. Likewise Alonso et al. (2015) find the abundance of haloes in different environments within the cosmic web to be dependent only on the local density, such that the halo mass function is the same for a given overdensity regardless of geometric environment.

However, it is not obvious that the apparent lack of influence of the cosmic web on galaxy properties is not due to the definition of geometric environment. The cosmic web is classified by positional galaxy information alone, and the tidal tensor is directly related to the smoothed density field. Assessing the cosmic web using the dynamics of galaxies might help to determine whether the apparent independence of the LF on the cosmic web is an effect of the dependence of the tidal tensor on density.

The choice of parameters chosen to classify the cosmic web influence the resulting geometric environments. There is a clear degeneracy between the gaussian smoothing width, σ_s, and the tidal tensor eigenvalue threshold parameter, λ_th, when considering the variance of the number of galaxies residing within each geometric environment (see Fig. 1 of Eardley et al. 2015). The choice of smoothing width and eigenvalue threshold chosen for this work is motivated to give a roughly equal number of galaxies in each geometric environment. It is possible that this choice has an effect on the sampling of the most extreme environments within the cosmic web. The resulting dependence of galaxy properties could be assessed by chosing parameters which do not follow this degeneracy.

In addition to the dependence of the galaxy LF presented here, further studies on the dependence of other galaxy properties, such as stellar mass, colour and morphology would provide an insight into whether or not the more intrinisic properties of galaxies show any evidence for the influence of the cosmic web on their evolution. This work can also be implemented on the GAMA lightcone mocks to provide a comparison to galaxy formation models. The availability of information on the dynamics of galaxies in the mock catalogues also provides the ability to classify the

cosmic web by using dynamical information of galaxies, to test whether a dynamical classification provides further information on the cosmic web dependence of galaxy properties.

Chapter 6

Properties of Dark Matter haloes in the GAMA Lightcone Mocks

To understand how the galaxies form and evolve within the dark matter environment, the properties of dark matter haloes must first be understood. The property of a dark matter halo which has the most influence on galaxy properties is its mass, which can have different definitions. The aim of this chapter is to introduce a pipeline which measures the properties of haloes from dark matter simulations, specifically the halo radius and mass, $R_{200,c}$ and $M_{200,c}$, the density profile and concentration, c, the circular velocity profile, providing a maximum circular velocity, $V_{\max}$, and its position in the halo, $R_{\max}$, and the velocity dispersion of dark matter particles in the halo, σ. These properties are analysed for haloes in the GAMA lightcone mock catalogues described in Chapter 3, so that the galaxy density profile of groups in the GAMA survey may be investigated in Chapter 7.

6.1 Introduction

The most fundamental measure of environment is the underlying density field in which galaxies reside, dominated by dark matter. The influence of the dark matter environment on the formation of galaxies and their evolution is an important aspect to understand in models of galaxy formation. Before links can be made between the distributions and properties of galaxies and their host haloes, the intrinsic properties

of the dark matter haloes, such as mass, must first be characterised.

The internal structure to a dark matter halo is described by the shape of the dark matter density profile. Commonly an NFW profile (Navarro et al., 1997) is adopted to parameterise the dark matter density profile. The shape, characterised by a concentration parameter, c, and its dependence on halo mass has been explored in various simulations in the past (Neto et al., 2007; Klypin et al., 2014), where the change in the concentration parameter with halo mass and redshift is now reasonably well determined.

Halo mass can be defined in many ways. If a halo is defined using a friends-of-friends (FoF) algorithm (Davis et al., 1985), the mass is defined as the sum of dark matter particles in the FoF halo. Alternatively the halo may be defined by locating an overdensity maximum, in which case the mass is determined by the dark matter particles enclosed within a radius defined by a minimum density (Press & Schechter, 1974). Lukić et al. (2009) explore the ability to directly convert between these two masses by comparing mass estimates of haloes constructed using realisations of idealised haloes with the shape of their dark matter density profiles described by NFW profiles (Navarro et al., 1997). They find that any conversion depends on the halo concentration, but that FoF haloes tend to link locally overdense regions together through tenuous bridges of matter, causing errors in the mass estimate. Another halo definition, a Dhalo, is given in §3.1, for which a mass, M_{Dhalo}, is calculated again as the sum of the constituting dark matter particles. Jiang et al. (2014) compare FoF halo masses to M_{Dhalo} and $M_{\mathrm{200,c}}$ (the mass enclosed within the radius for which the mean density is 200 times ρ_{crit}, the critical density of the Universe) for haloes at $z = 0$ in the Millennium-II dark matter simulation (see table 3.1). M_{Dhalo} splits up the tenuous matter bridges found by Lukić et al. (2009), and consequently is found to be more tightly related to $M_{\mathrm{200,c}}$ than the masses of FoF haloes.

While previous comparisons of halo properties have been made for haloes in the Millennium dark matter simulations (Jiang et al., 2014), these are generally only for $z = 0$, and not restricted to only haloes which could be observed in the Universe (i.e. inside which a galaxy would form). The construction of this pipeline is for the

purpose of providing dark matter halo properties for comparison to galaxy groups in galaxy redshift surveys.

In this chapter the pipeline is used to characterise the properties of dark matter haloes in the GAMA lightcone mocks, which are later used in Chapter 7 to investigate how galaxies are distributed in groups in the GAMA survey. The description of this pipeline begins by outlining the halo sample used in §6.2, and the method used to estimate the spherical halo mass and radius from dark matter particles in the simulation in §6.3. The density profiles of the lightcone haloes are measured in §6.4, and the method for fitting an NFW profile and its uncertainties are described (§6.4.1), along with the power of the NFW profile to predict further spherical mass estimates (§6.4.4). A discussion of the resulting concentration-mass relation is given in §6.5. In §6.6 the velocity profiles of haloes are measured, and the ability of the NFW profile to predict the peak of the velocity profile is discussed. The velocity dispersion is measured for dark matter particles in the haloes in §6.7, and its usefulness in constraining halo mass is assessed. Finally §6.8 summarises the work presented in this chapter.

6.2   Selection of haloes

The MS-W7 dark matter simulation and the process for defining dark matter haloes, Dhaloes, along with an overview of the GALFORM model (Gonzalez-Perez et al., 2014) and the method for constructing the GAMA lightcone mocks, is described in Chapter 3.

Halo lightcone mock catalogues utilised here contain all dark matter haloes which are massive enough to form galaxies and therefore relevent to the observable Universe, the properties of which can then be measured using the spatial and dynamical information of their constituting dark matter particles. The haloes studied in this chapter therefore do not necessarily satisfy the full selection effects of the GAMA survey, but are constrained to $z < 0.6$, with halo masses of $M_{\mathrm{Dhalo}} > 10^{11} h^{-1} \mathrm{M}_\odot$. Haloes with masses lower than this are unlikely to be detected in the GAMA survey and estimates of halo properties will have high uncertainties due to the resolution

limit of the simulation (a halo of mass $M_{\rm Dhalo} = 10^{11} h^{-1} {\rm M}_\odot$ corresponds to 107 particles in MS-W7).

The redshift distribution and mass functions of the resulting halo sample are shown in Fig. 6.1. The upper left panel gives the redshift distribution, showing the effects of the survey volume on the number of haloes, and a comparison of the Dhalo mass and various spherically averaged mass estimates are given in the upper right panel.

The definition of halo mass is an important aspect to consider when characterising haloes and their properties. The decline in the mass function at low masses is due to the cut of $M_{\rm Dhalo} > 10^{11} h^{-1} {\rm M}_\odot$ imposed on the sample. Depending on the mass definition used, this $M_{\rm Dhalo}$ cut has different effects on the resulting mass function. The lower panels show how the mass function evolves with redshift. The evolution is most significant for the highest masses, with the most massive haloes forming more recently than low mas haloes. This is consistent with hierarchical structure formation, and is built into the Dhalo algorithm such that a Dhalo can only gain mass. The lower right panel shows that this evolution is also seen for halo masses defined by $M_{\rm 200,c}$. The effect of the $M_{\rm Dhalo}$ cut is such that the sample of haloes is only 95% complete for $M_{\rm 200,c} = 10^{11} h^{-1} {\rm M}_\odot$.

6.3 Haloes defined by spherical overdensity

In the models, Dhaloes are constructed using a Dhalo merger tree, and are defined by the dark matter particles associated with them, as is discussed in §3.1. Intrinsic and geometric halo properties such as mass, halo size and the dynamics of the halo can be readily calculated from the halo's dark matter particle membership. In GALFORM, the halo mass is defined as $M_{\rm Dhalo}$. The definition of halo mass can be made more applicable to the mass of dark matter haloes in the real Universe, as traced by galaxies, by considering particles which fall within a sphere around the Dhalo centre. These particles can then be used to calculate the halo properties, with the halo centre taken to be at the position of the central galaxy in the Dhalo (defined in Chapter 3).
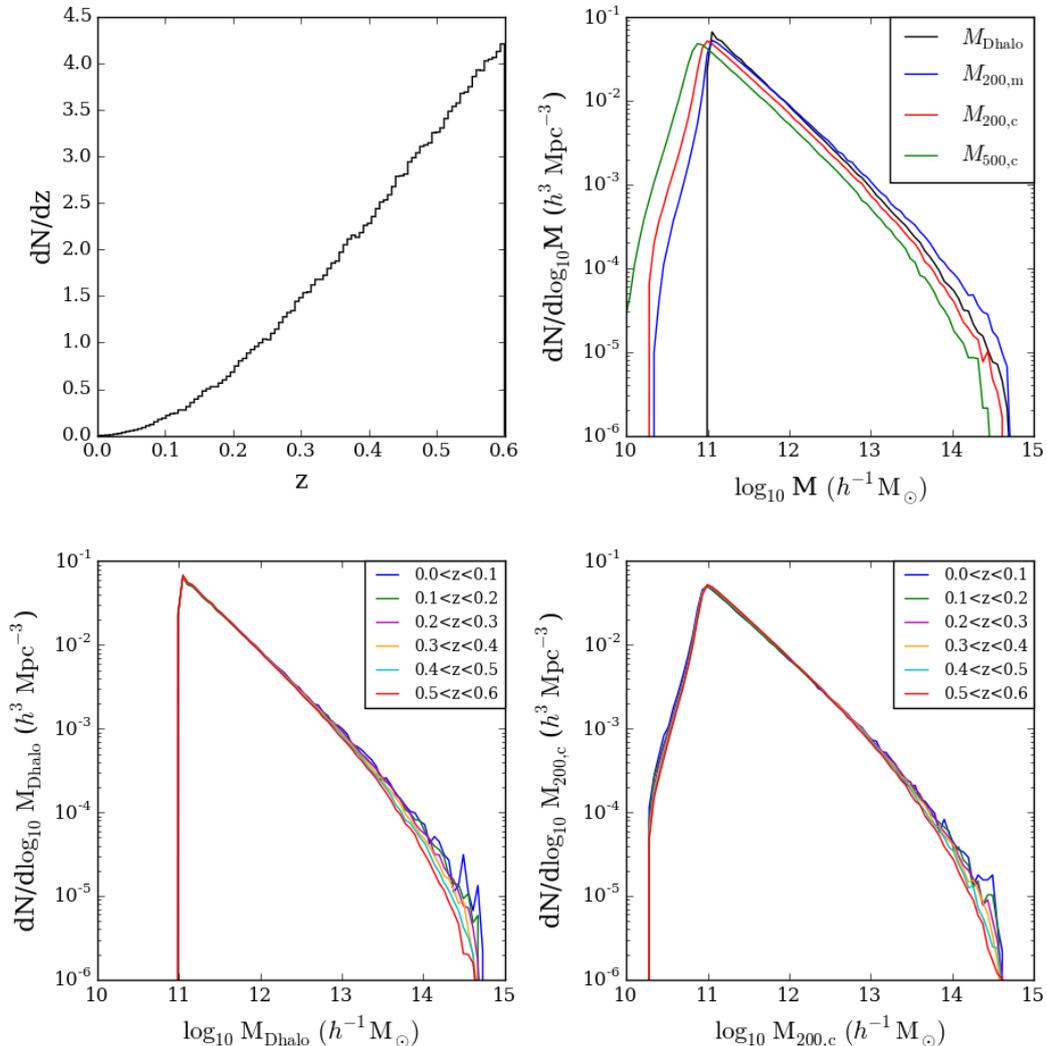
Figure 6.1: *Top left*: Distribution of halo redshifts in the GAMA halo lightcone, averaged over 10 mocks. *Top right*: Mass function for different mass estimates: M_{Dhalo} (black), the Dhalo mass as defined by GALFORM; $M_{200,\mathrm{m}}$ (blue), defined by a density of $200\rho_{\mathrm{mean}}$; $M_{200,\mathrm{c}}$ (red), defined by $200\rho_{\mathrm{crit}}$; $M_{500,\mathrm{c}}$ (green), defined by $500\rho_{\mathrm{crit}}$. The mass function is measured for haloes in the redshift range $0.25 < z < 0.30$ and averaged over 10 mocks. *Bottom*: The M_{Dhalo} (*left*) and $M_{200,\mathrm{c}}$ (*right*) halo mass functions for different redshifts (see key), showing the evolution of the high mass end, again averaged over 10 mocks.

A radius, R_Δ, is defined as the radius within which the density is a factor of Δ times the density of the Universe, ρ_{univ}, and the halo mass, M_Δ, enclosed within this radius is measured as:

$$M_\Delta = \frac{4}{3}\pi R_\Delta^3 \Delta \rho_{\mathrm{univ}}. \tag{6.1}$$

Conventionally, the value of Δ is chosen to be 200, and ρ_{univ} which may be defined as the critical density, ρ_{crit}, or the mean density, ρ_{mean} of the Universe. This roughly corresponds to a spherical overdensity of 178 times the mean overdensity for spherical collapse in a Universe described by $\Omega_{\mathrm{M}} = 1$.

For studies of the hot x-ray emitting gas which typically resides only in the inner regions of the halo (e.g. Ettori et al., 2013; Pearson et al., 2015), it is more common to use a smaller mass definition with Δ=500. In some cases, (e.g. Bryan & Norman, 1998), Δ may vary with redshift to take into account the dependence of the spherical collapse threshold on cosmology through $\Omega_{\mathrm{M}}(z)$.

For this analysis a redshift independent value of Δ=200 is adopted and the density of the Universe is taken to be ρ_{crit}, unless otherwise stated. Equation 1.10 is used to determine the value of ρ_{crit} at a redshift corresponding to the simulation snapshot from which the halo information is taken. The dependence of ρ_{crit} on redshift creates a variation in the estimated halo mass, $M_{200,\mathrm{c}}$, for a fixed halo radius, such that from $z = 0.0$ to $z = 0.6$ halo mass for a given radius decreases by a factor of 2.

Since it is unlikely that a particle will lie exactly at the radius enclosing $\Delta\,\rho_{\mathrm{crit}}$, $R_{200,\mathrm{c}}$ is found by linear interpolation around $\rho(<R) = \Delta\,\rho_{\mathrm{crit}}$. This can be a problem for haloes containing significant substructure which create distortions in the density profile near $R_{200,\mathrm{c}}$, or low mass haloes containing only a small number of particles. However, the haloes considered here contain a sufficient number of particles (>100) and substructure does not have a significant effect on the measured position of $R_{200,\mathrm{c}}$.

Having measured spherical mass estimates as determined by $M_{200,\mathrm{c}}$ for all haloes in the lightcone, $M_{200,\mathrm{c}}$ and M_{Dhalo} can be compared to assess whether a direct conversion between them is appropriate. Fig. 6.2 shows how the ratio of the masses, $M_{\mathrm{Dhalo}}/M_{200,\mathrm{c}}$, varies as a function of M_{Dhalo} and redshift. There is clearly a sys-
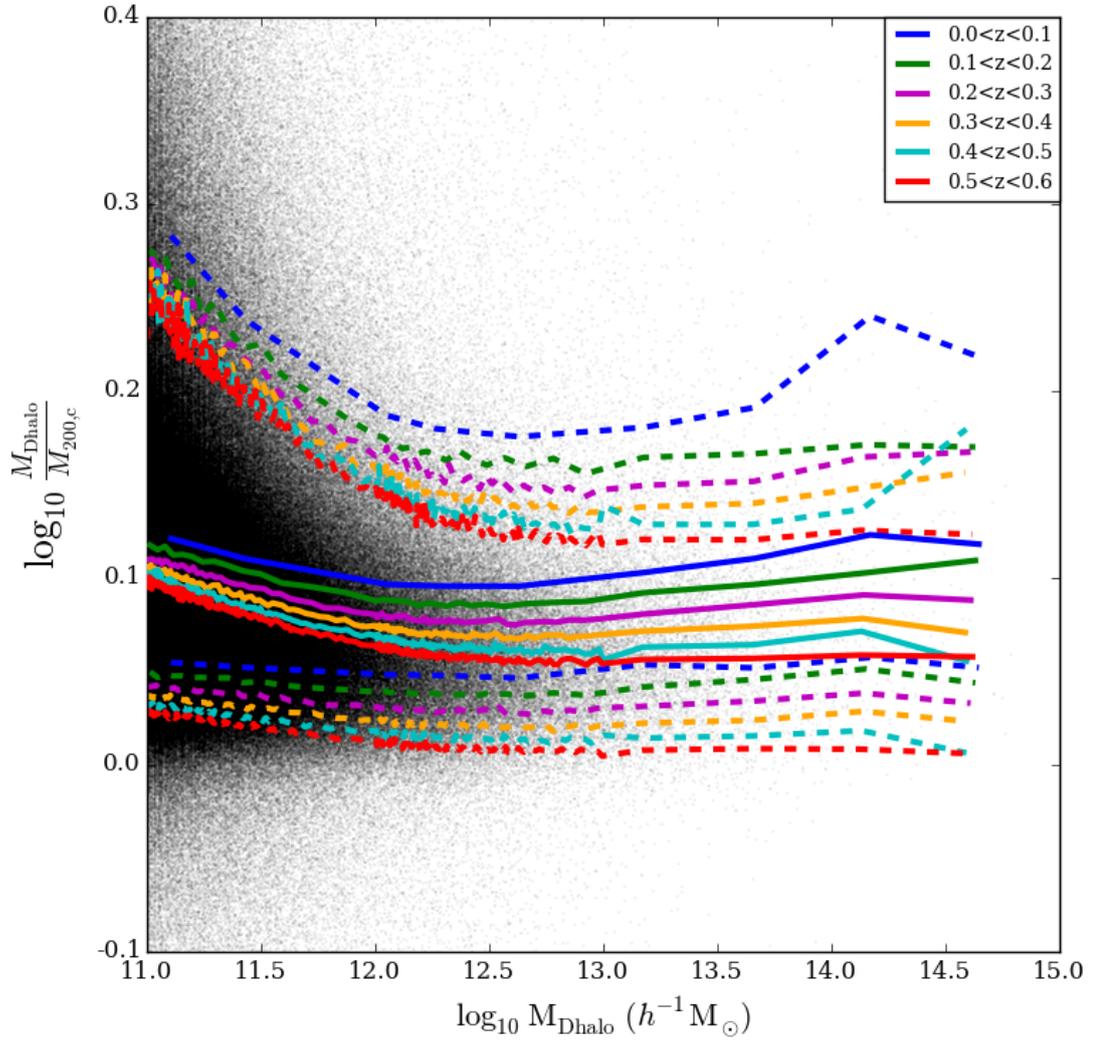
Figure 6.2: Ratio of Dhalo mass M_{Dhalo} to $M_{200,\mathrm{c}}$ as function of M_{Dhalo}. For halo masses $> 10^{12}h^{-1}\mathrm{M}_\odot$, the ratio converges to $M_{\mathrm{Dhalo}}/M_{200,\mathrm{c}} \sim 1.2$ for high redshifts. The solid (dashed) coloured lines show the median (10th and 90th percentiles) as a function of $M_{200,\mathrm{c}}$, for different redshift bins (see key).

tematic offset between the masses of $M_{\mathrm{Dhalo}} = 1.25 M_{200,\mathrm{c}}$ for haloes with $M_{\mathrm{Dhalo}} >$ $10^{12} h^{-1} \mathrm{M}_\odot$ in the range $0.0 < z < 0.1$, and a scatter implying 80% of haloes have $1.12 < M_{\mathrm{Dhalo}}/M_{200,\mathrm{c}} < 1.58$. The offset varies with redshift such that in the range $0.5 < z < 0.6$, the median is described by $M_{\mathrm{Dhalo}} = 1.17 M_{200,\mathrm{c}}$, but the scatter remains approximately constant with redshift. The bias and scatter appear to become larger for haloes close to $M_{\mathrm{Dhalo}} = 10^{11} h^{-1} \mathrm{M}_\odot$, but haloes with such a low mass are likely to be affected by the resolution limit of the simulation. In general, Dhaloes are unlikely to be spherical and so the Dhalo mass is unlikely to be well traced by $M_{200,\mathrm{c}}$. A small number of haloes (4% of haloes in the sample) have $M_{200,\mathrm{c}} > M_{\mathrm{Dhalo}}$, such that $R_{200,\mathrm{c}}$ encloses a larger mass than is encompassed within the Dhalo.

The bias and scatter seen here is in agreement with the ratio of masses measured by Jiang et al. (2014) for Millennium II haloes at $z = 0$. Jiang et al. (2014) also saw a small upturn in the ratio (~ 0.04 between $10^{12} < M_{\mathrm{Dhalo}}/h^{-1}\mathrm{M}_\odot < 10^{13}$) towards higher masses. In the sample of haloes analysed here (spanning the redshift range $0.0 < z < 0.6$) only a slight upturn is visible for the intermediate redshifts in Fig. 6.2, but not for highest redshifts considered.

6.4 Density profiles and concentration

High density dark matter regions provide a potential well into which gas falls and cools, thus enabling star formation. Therefore it is important to understand the dark matter density profiles within haloes in the lightcone mocks in order to understand how structure formation is affected on different mass scales and at different points in the age of the Universe.

The halo density profiles can be characterised by an NFW profile (Navarro et al., 1997), where the density ρ_{NFW} at a radius r is given by:

$$\frac{\rho_{\mathrm{NFW}}(r)}{\rho_{\mathrm{crit}}} = \frac{\delta_c}{\left(\frac{r}{r_s}\right)\left(1 + \frac{r}{r_s}\right)^2}, \tag{6.2}$$

such that density is defined in units of critical density, ρ_{crit}, and the scale radius, r_s, indicates the radius at which the profile changes slope from $\rho(r) \propto r^{-1}$ to $\rho(r) \propto r^{-3}$. The scale radius and size of the halo, $R_{200,\mathrm{c}}$, define a concentration parameter c,

given by $c = R_{200,\mathrm{c}}/r_s$, which characterises the shape of the NFW profile. δ_c is by definition:

$$\delta_c = \frac{200}{3} \frac{c^3}{\ln(1+c) - c/(c+1)}, \tag{6.3}$$

such that the mass enclosed within $R_{200,\mathrm{c}}$ is always $M_{200,\mathrm{c}} = \frac{4}{3}\pi R_{200,\mathrm{c}}^3 200\rho_{\mathrm{crit}}$, independent of the concentration of the halo. The mass in a shell between radii r_1 and r_2 can be found by integrating the NFW profile over the volume enclosed by the radius limits, and is given by:

$$M_{\mathrm{NFW}}(r_1 < r < r_2, c) = 4\pi r_s^3 \delta_c \rho_{\mathrm{crit}} \left(\frac{r_s}{r_s + r_2} - \frac{r_s}{r_s + r_1} + \ln\left(\frac{r_s + r_2}{r_s + r_1}\right) \right). \tag{6.4}$$

Since the NFW profile is only dependent on $R_{200,\mathrm{c}}$ and c for a fixed $M_{200,\mathrm{c}}$ the only free parameter is halo concentration. By fitting an NFW profile to the dark matter density profile of a halo, the concentration of the halo can be determined. The concentration of a halo is strongly influenced by the halo's formation history.

To determine if the recovered halo concentration depends on the fitting procedure used, two methods for fitting an NFW profile to the dark matter density profile are described and compared below.

6.4.1 Binned density profile

Following the method used by Jiang et al. (2014) and Neto et al. (2007), the density profile of particles within $R_{200,\mathrm{c}}$ is measured in 32 equally spaced bins in $\log_{10} r/R_{200,\mathrm{c}}$, in the range $-2.5 < \log_{10}(r/R_{200,\mathrm{c}}) < 1.0$. For each shell, containing all particles falling between r_{min} and r_{max}, the density is measured as:

$$\rho(r) = \frac{M(r_{\mathrm{min}} < r < r_{\mathrm{max}})}{\frac{4}{3}\pi(r_{\mathrm{max}}^3 - r_{\mathrm{min}}^3)}, \tag{6.5}$$

where $M(r)$ is the mass contained within the shell, calculated by summing the masses of particles falling in the shell with $r_{\mathrm{min}} < r \leq r_{\mathrm{max}}$. Only radii in the range $0.1 < r/R_{200,\mathrm{c}} < 1$ are used in the fitting procedure. The lower limit is to account for the resolution limit of the Millennium simulation for smallest mass haloes considered here. An NFW profile is then fitted to the binned density profile by minimising χ^2:

$$\chi^2 = \sum_{r=0.1R_{200,c}}^{R_{200,c}} \left(\frac{(\log_{10} \rho(r) - \log_{10} \rho_{\text{NFW}}(r, c))^2}{\sigma(r)^2} \right), \qquad (6.6)$$

where the error, $\sigma(r)$, on the log of the density profile, $\log_{10} \rho(r)$, is determined assuming Poisson statistics in each density bin.

The fit is performed in $\log_{10} c$ in the range $0 < \log_{10} c < 1.3$ in increments of $\Delta_{\log_{10}} c = 0.001$, such that the error on c, σ_c, is found using the condition that $\Delta \chi^2 \leq 1$, corresponding to a confidence interval of 68%.

Eight example haloes are introduced in Fig. 6.3. These haloes are chosen to be "typical" haloes from the lightcone mocks at redshift $z = 0.5$, such that they have concentrations lying on the expected mass-concentration relation at $z = 0.5$ given by Klypin et al. (2014) for the WMAP7 cosmology, and cover a range of halo masses. The spatial distribution of particles, projected onto the x-y plane, is shown for each halo, giving an indication of how substructure affects the distribution of particles within $R_{200,c}$, as is particularly clear for halo F.

The binned density profiles and best fitting NFW profiles (using the binned fit described in §6.4.1) for the eight example haloes are given in Fig. 6.4. The open circles and dashed lines show the limiting inner radius to which a halo's density profile is measured for a given mass. The smallest haloes have ~ 100 particles only as far in as $\log_{10}(r/R_{200,c}) = -1.0$, which we have adopted as the limit above which an NFW profile is fit for all haloes. It is important to use the same range of $r/R_{200,c}$ when fitting an NFW profile, regardless of halo mass, to ensure the same fraction of the halo volume is considered in the fit. It is clear, however, that due to the resolution limit of the Millennium simulation, haloes containing fewer than ~ 100 particles will not have sufficient particles to reliably constrain an NFW profile. The density profile in haloes above $10^{11} h^{-1} \text{M}_\odot$ is sampled well enough to constrain the turnover radius, r_s, given that $r_s > 0.1R_{200,c}$ (and therefore $c < 10$). A higher resolution simulation such as Millennium-II (Boylan-Kolchin et al., 2009), with 5 times better spatial resolution (a Plummer equivalent softening 1.0kpc) and 125 times better mass resolution, allows halo concentration to be constrained down to a significantly smaller radius. Since haloes observed in the GAMA survey are unlikely to be less massive than $10^{12} h^{-1} \text{M}_\odot$, there is no need for a higher resolution simulation to be
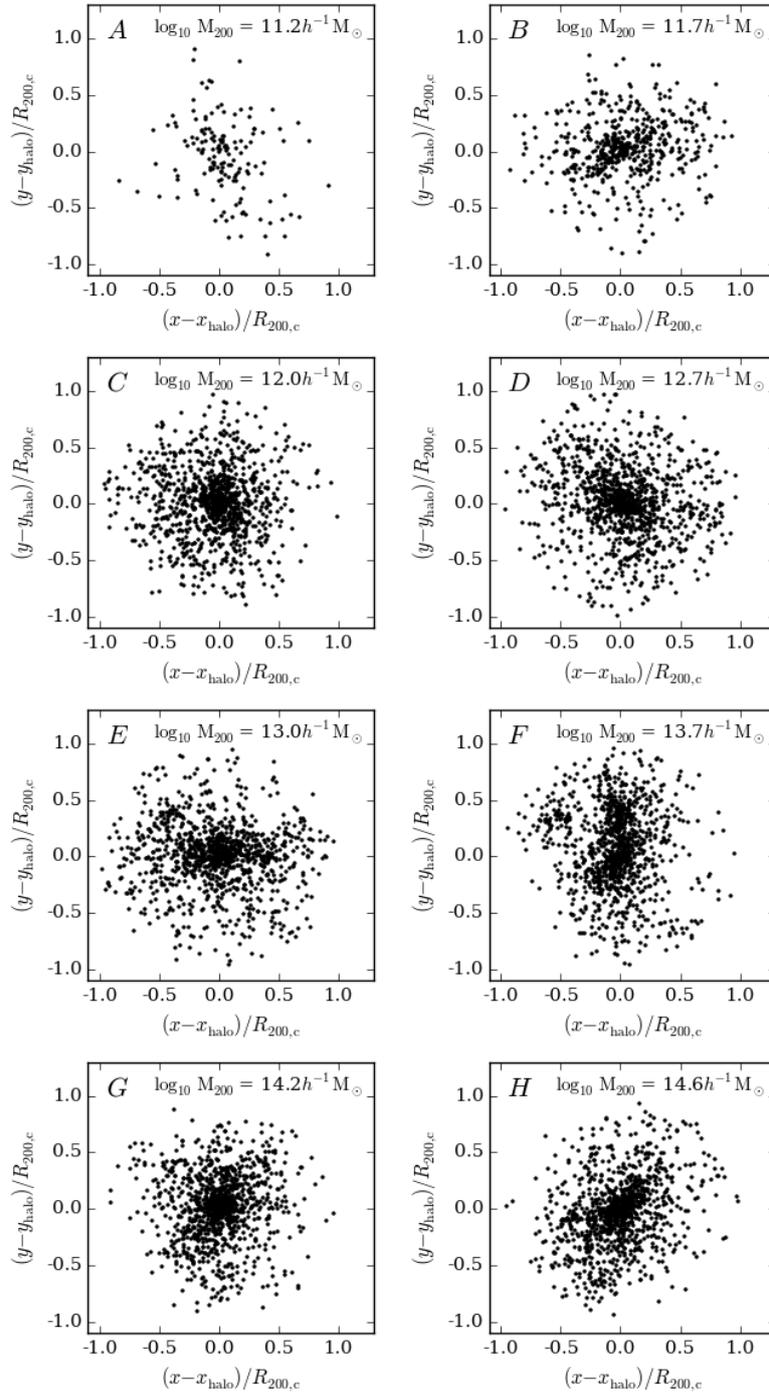
Figure 6.3: Spatial distribution of particles projected onto the x-y plane for 8 example lightcone haloes, with masses varying from $10^{11}h^{-1}\mathrm{M}_\odot$ (A) to $10^{14.6}h^{-1}\mathrm{M}_\odot$ (F). Particle positions (x, y), are shown relative to the halo centre $(x_{\mathrm{halo}}, y_{\mathrm{halo}})$, and as a fraction of the halo radius, $R_{200,\mathrm{c}}$. While all particles are indicated by black points for haloes A, B and C, for the higher mass haloes only a random sample of particles is shown, chosen to match the number of particles in halo C.
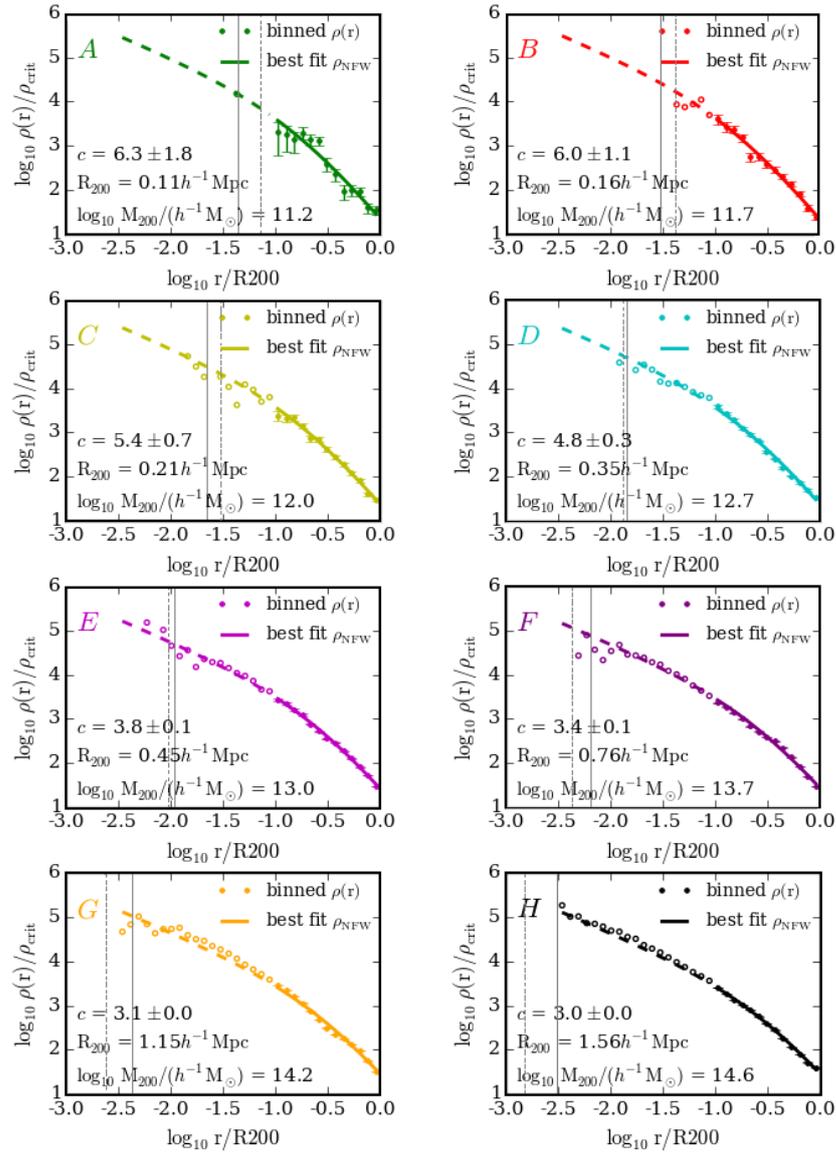
Figure 6.4: Density profiles for 8 example haloes of a range of masses, selected at $z \sim 0.5$ to have a concentration following the concentration-mass relation of Klypin et al. (2014). Points show the density $\rho(r)$ within shells of $\log_{10}(r/R_{200,c})$ with Poisson errors as used to fit an NFW profile. The solid lines show the best fit NFW profile for each halo fit using the binned density profile. Radii which are not used in the fitting procedure $(r/R_{200,c} < 0.1)$ are indicated by open points and dashed lines. In each panel the the solid grey line indicates the Plummer equivalent softening of 5kpc in the simulation and the dashed grey line indicates the lower limit to the softening required to limit discreteness effects (Power et al., 2003). Hereafter these example haloes are indicated by the same colours as shown here.

used in this work. It is important to use a simulation of the volume of the Millennium simulation so that examples of rare haloes can be found, corresponding to rich groups and clusters. The lower mass limit adopted for this work is a disadvantage for the largest halo masses where radii smaller than $0.1R_{200,\mathrm{c}}$ can be resolved. The log scale shown in the lower panels of Fig. 6.4 causes the fraction of volume unused in the fit to appear particularly large.

6.4.2 Maximum likelihood fit

Alternatively we have also tried a maximum likelihood approach to find the best fitting concentration parameter to the density profile of haloes. This method is based on the probability of finding a dark matter particle, i, at a given radius, r_i, within the halo within the halo, assuming an NFW profile with concentration c, given by:

$$p(r_i|c)\, dr = \frac{4\pi r_i^2 \rho_{\mathrm{NFW}}(r_i, c)\, dr}{M_{\mathrm{NFW}}(c)}, \tag{6.7}$$

where the mass of the NFW profile, $M_{\mathrm{NFW}}(c)$ is calculated using equation 6.4 over the radial range used in the fit, $0.1 < r/R_{200,\mathrm{c}} < 1$. Since the total mass within $R_{200,\mathrm{c}}$ does not depend on the concentration of the halo, the choice of c only has a small effect on $M_{\mathrm{NFW}}(c)$, caused by mass enclosed within $r/R_{200,\mathrm{c}} < 0.1$.

The likelihood function, $\mathcal{L}$, is calculated as the product of the probabilities for all N_{halo} particles in the halo at radii r_i, where r_i falls within the radial range used in the fit,

$$\mathcal{L}(c) = \prod_{i=1}^{N_{\mathrm{halo}}} p(r_i|c), \tag{6.8}$$

such that the log-likelihood is calculated as:

$$\ln \mathcal{L}(c) = \sum_{i=1}^{N_{\mathrm{halo}}} \ln \frac{4\pi r^2 \rho_{\mathrm{NFW}}(r_i, c)\, dr}{M_{\mathrm{NFW}}(c)}. \tag{6.9}$$

The 1σ error on the fit can then be determined given that the log of the likelihood, $\ln \mathcal{L}$, is the sum of the log of the probabilities $\ln p$, $\ln \mathcal{L} = \sum \ln p$, and that for a gaussian distribution the probability depends on χ^2 as $p \propto e^{-\chi^2/2}$, giving:

$$\Delta\chi^2 = 2\ln\mathcal{L}_{\text{max}} - 2\ln\mathcal{L}. \tag{6.10}$$

The error on the fit, σ_c, is again determined using $\Delta\chi^2 \leq 1$.

6.4.3 Uncertainty on halo concentration

Two estimates of the halo concentration parameter, c_{binned} and $c_{\text{likelihood}}$ are found for all haloes in the GAMA halo lightcone, using the binned and maximum likelihood methods respectively. Since the true concentration of the haloes is unknown it is not possible to test which method most accurately recovers the true concentration for haloes in the lightcone mocks. Instead, the amount by which the recovered concentration differs between the two methods can be assessed, and compared to the 1σ error on the concentration determined by one of the methods.

The ratio of the recovered concentrations for each fitting method as a function of halo mass is shown for each of the lightcone haloes in the top panel of Fig. 6.5. For halo masses above $10^{12}h^{-1}\text{M}_\odot$, there is essentially no difference between the concentrations found using the two approaches, and 80% of haloes have a difference in recovered concentration smaller than 5%. Most significantly, there is no bias in either fitting method, and the scatter is symmetrical for all but the lowest $(10^{11}h^{-1}\text{M}_\odot)$ masses. Clearly for halo masses less than $(< 10^{12}h^{-1}\text{M}_\odot)$ the difference between the two methods can be large, such that 20% of haloes at these small masses have more than a 25% difference in the recovered concentration (as indicated by the 10th and 90th percentiles), and there is a slight bias towards the binned density fitting recovering a lower concentration than the maximum likelihood method by $< 5\%$.

The coloured points show the example haloes with density profiles given in Fig. 6.4 for comparison. The majority of example haloes lie within the 90th and 10th percentiles. For the lowest mass haloes (e.g. A and C), it is clear from the density profiles that the concentration measured is likely to be heavily influenced by the small number of particles in the halo, and therefore the two methods can recover different concentrations in such cases.
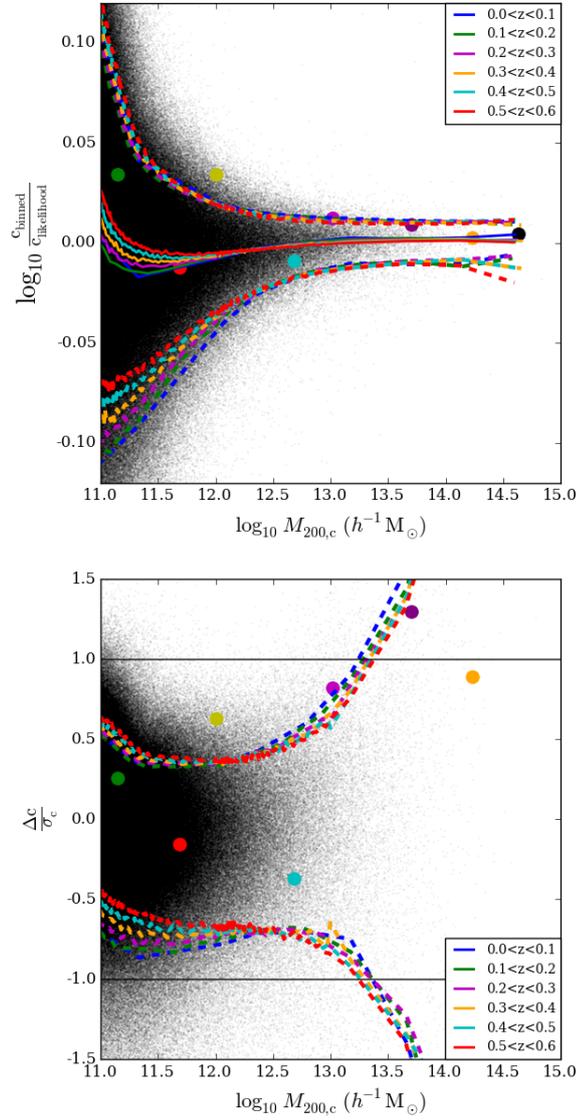
Figure 6.5: *Top*: Ratio of concentration parameters recovered for GAMA lightcone haloes when fitting an NFW profile to the binned density profile of the halo (c_{binned}) and using the maximum likelihood technique ($c_{\mathrm{likelihood}}$), as a function of $M_{200,c}$. *Bottom*: Ratio of Δc, the difference between concentration found between the two fitting methods, to σ_c, the error on the concentration fitted using a binned density profile, against $M_{200,c}$. The solid (dashed) coloured lines show the median (10th and 90th percentiles) as a function of $M_{200,c}$, for different redshift bins (see key). The coloured dots show where the example haloes (see Fig. 6.4) lie. The solid black lines in the lower panel indicate the region within which $\sigma_c > \Delta c$.

For the halo masses of interest in this work ($> 10^{12}h^{-1}\mathrm{M}_\odot$), the method used to fit an NFW profile does not bias the recovered concentration parameter of the halo (see top panel of Fig. 6.5). Hereafter concentration, c, and the error on the concentration σ_c, will be defined as the concentration recovered by fitting an NFW profile to the binned density profile, which is the technique used to obtain previous results (e.g. Jiang et al., 2014; Neto et al., 2007).

The lower panel of Fig. 6.5 compares the systematic difference in the recovered concentrations using the two fitting methods, $\Delta c = \mathrm{c_{binned}} - \mathrm{c_{likelihood}}$, to the uncertainty in the concentration parameter, σ_c. If the ratio $|\Delta c|/\sigma_c$ is less than 1, the most significant uncertainty in concentration can be attributed to the uncertainty on the fit. If the ratio is greater than 1, then systematics in the fitting procedure dominate the uncertainty. The lower panel of Fig. 6.5 shows that below $M_{200,\mathrm{c}} < 10^{13.5}h^{-1}\mathrm{M}_\odot$, more than 80% of haloes have $|\Delta c|/\sigma_c < 1$. For the majority of haloes in the light-cone, any systematics introduced by the fitting method introduce an uncertainty on the concentration parameter that is smaller than the uncertainty on the fit. For higher masses, the fraction of haloes for which $|\Delta c| > \sigma_c$ increases, and the method used for the fit becomes important. However, it is important to note that both Δc and σ_c decrease with halo mass, and the uncertainty in concentration for higher mass haloes is small. The larger decrease in σ_c than Δc with halo mass is the cause of the increase in $|\Delta c|/\sigma_c$.

6.4.4 NFW predictions for spherical mass estimates

It is conventional to consider the mass within the radius enclosing a density of $200\rho_{\mathrm{crit}}$ when defining a spherical halo mass. However, an estimate of the halo mass considering an enclosed density of $500\rho_{\mathrm{crit}}$ or $200\rho_{\mathrm{mean}}$ may be better motivated physically or observationally depending on the application. It is therefore instructive to understand the difference between these definitions of mass to investigate whether or not it is meaningful to directly translate from one mass definition to another assuming a functional form.

To compare different estimates of spherical halo mass, defined generically as $\Delta \rho_{\mathrm{univ}}$, it is possible to predict a mass based on the NFW profile of a halo. Two
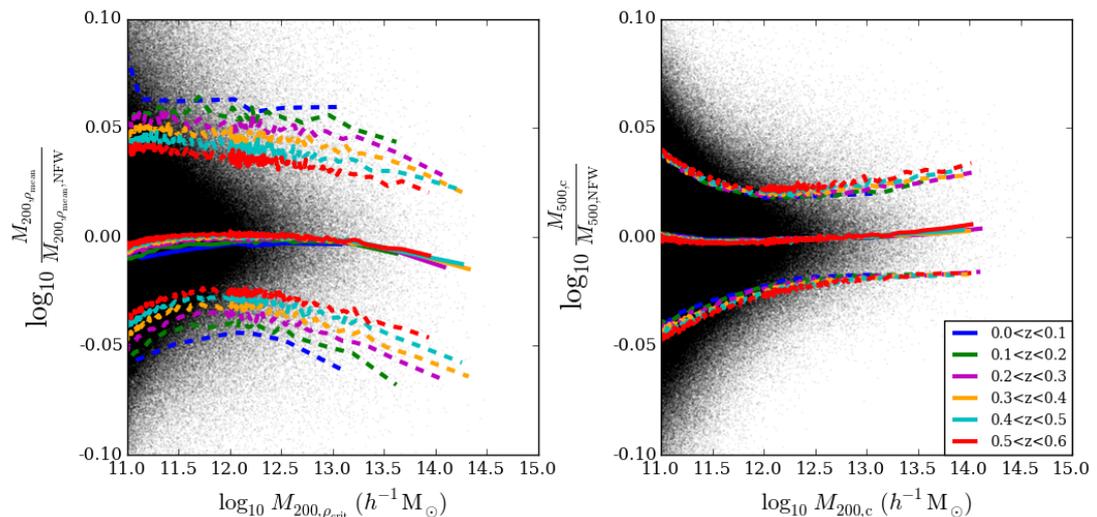
Figure 6.6: *Left*: Ratio of the measured M_{200} defined by $200\rho_{mean}$ to that expected assuming an NFW halo as function of $M_{200,\rho_{\rm crit}}$. The solid (dashed) coloured lines show the median ($10^{\rm th}$ and $90^{\rm th}$ percentiles) as a function of $M_{200,c}$, coloured by redshift (see key in right panel). *Right*: Ratio of the measured $M_{500,c}$ to that expected from the best fit NFW profile to each halo, as a function of $M_{200,c}$.

mass definitions are compared here, both commonly used in the literature, defined by $200\rho_{\rm mean}$ ($M_{200,m}$), and $500\rho_{\rm crit}$ ($M_{500,c}$). For each halo with a measured mass $M_{200,c}$ (and subsequently a value for $R_{200,c}$), an NFW profile can be determined assuming only a concentration parameter (see §6.4.1 for details on the fitting procedure). The halo radius, $R_{\rm vir}$, within which the density is $\Delta\,\rho_{\rm univ}$ is found by solving:

$$\rho(<R_{\Delta\,\rho_{\rm univ}}) = \frac{M(<R_{\Delta\,\rho_{\rm univ}})}{^4/_3\pi R^3_{\Delta\,\rho_{\rm univ}}} \equiv \Delta\,\rho_{\rm univ}, \tag{6.11}$$

and the corresponding enclosed mass is determined as in equation 6.1. This provides an expected NFW mass, $M_{\Delta,\rho_{\rm univ},NFW}$, which can be compared to the measured mass, $M_{\Delta,\rho_{\rm univ}}$ to determine how effective a direct scaling from $M_{200,c}$ would be by assuming an NFW profile with concentration c.

The left panel of Fig. 6.6 shows how the ratio of the measured $M_{200,m}$ to that expected from an NFW profile varies as a function of $M_{200,c}$. The measured $M_{200,m}$ is well predicted by an NFW profile for any redshift. The median does not deviate from unity by more than 1%. The scatter indicates that only 10% of haloes at low

redshifts have a measured $M_{200,\mathrm{m}}$ that is 15% or more greater than that expected by an NFW profile, and only 10% have $M_{200,\mathrm{m}}$ more than 11% smaller than expected. This scatter decreases with redshift such that by $0.5 < z < 0.6$, 80% of haloes are within 9% of the mass predicted using the NFW profile.

The estimated $M_{200\,\rho_{\mathrm{univ}}}$ depends on concentration but also on the value of ρ_{univ} used when defining $R_{200\,\rho_{\mathrm{univ}}}$. The redshift dependence exhibited by the scatter is caused by the redshift dependence of ρ_{crit}, indicating how much $R_{200,\mathrm{c}}$ and $R_{200,\mathrm{m}}$ differ by at different redshifts, which also causes a difference in the measurement of the concentration.

$R_{200,\mathrm{m}}$ is always larger than $R_{200,\mathrm{c}}$. Therefore the mass predicted by an NFW profile beyond $R_{200,\mathrm{c}}$ is essentially an extrapolation from the particles within $R_{200,\mathrm{c}}$. Therefore as redshift increases, ρ_{crit} becomes closer to ρ_{mean}, and the prediction is less of an extrapolation, since $R_{200,\mathrm{m}}$ becomes more similar to $R_{200,\mathrm{c}}$, and so the difference between $M_{200,\mathrm{m}}$ and $M_{200,\mathrm{c}}$ decreases, resulting in a decrease in scatter. Perfect NFW haloes would exhibit no scatter, since the change in mass would be predicted exactly by the NFW profile. Therefore the scatter at a given redshift is an indication of how much the haloes vary from an NFW profile. The small turnover for higher masses reflects the change in concentration as a function of mass which is discussed in §6.5.

The right panel of fig. 6.6 compares the measured value of $M_{500,\mathrm{c}}$ to that expected using an NFW profile, in the same way as was done for $M_{200,\mathrm{m}}$, but when the density enclosed within the radius is $500\rho_{\mathrm{crit}}$. There is no bias, and the scatter is small such that 80% of haloes have a measured $M_{500,\mathrm{c}}$ within 7% of that expected by an NFW profile. For 80% of haloes a mass $M_{500,\mathrm{c}}$ can be determined knowing the concentration and $M_{200,\mathrm{c}}$ of the halo, to within 7%, at any redshift.

In conclusion, a mass defined by $\Delta\,\rho_{\mathrm{univ}}$ can be estimated by simply assuming an NFW profile given a halo mass $M_{200,\mathrm{c}}$ and concentration c. This prediction has been shown for two typical cases, $\Delta\,\rho_{\mathrm{univ}} = 200\rho_{\mathrm{mean}}$ and $\Delta\,\rho_{\mathrm{univ}} = 500\rho_{\mathrm{crit}}$. The approximation is more accurate when considering a density higher than $200\rho_{\mathrm{crit}}$, such that the particles contributing to the mass are those used to recover the halo concentration. Likewise if $\Delta\,\rho_{\mathrm{univ}}$ does not exhibit the same dependence on redshift

as ρ_{crit} and the haloes do not exhibit perfect NFW profiles, there will be a change in the scatter with redshift.

6.5 Concentration Mass Relation

Having measured the concentration parameter for haloes in the GAMA lightcone, and knowing the limiting factors when considering the halo concentrations, we can assess how the recovered mass-concentration relation compares to those previously found for similar simulations.

Fig. 6.7 shows how concentration varies as a function of $M_{200,\mathrm{c}}$ for haloes in the GAMA lightcones. Concentration clearly decreases with halo mass, and the trend agrees closely with that found by Klypin et al. (2014) for a simulation run with the WMAP 7 cosmology (as used here), given as:

$$c(M) = 5.25 \left(\frac{M_{200,\mathrm{c}}}{10^{12} h^{-1} \mathrm{M}_\odot} \right)^{-0.105} \left[1 + \left(\frac{M_{200,\mathrm{c}}}{6 \times 10^{16} h^{-1} \mathrm{M}_\odot} \right)^{0.4} \right], \qquad (6.12)$$

for $z = 0.5$. The coloured dots show the example haloes introduced in Fig. 6.4, which were selected close to the concentration-mass relation expected at $z = 0.5$. Concentration is clearly dependent on redshift, as can be seen in Fig. 6.7, although the slope of the concentration-mass relation does not change over the redshift range probed here. This is consistent with the change in redshift reported by Klypin et al. (2014) between $z = 0.0$ and $z = 0.5$, such that the concentration is higher at lower redshifts for a fixed halo mass. This agreement is more obvious for higher redshifts, where the volume covered by the lightcone is largest and we can readily probe halo masses up to $M_{200,\mathrm{c}} = 10^{14.0} h^{-1} \mathrm{M}_\odot$. The scatter on the relation is large for all halo masses, such that 80% of haloes have concentrations within 50% of that expected using the relation for a given $M_{200,\mathrm{c}}$, and although the concentration-mass relation evolves with redshift, there is no change in the scatter with redshift for a given mass.

It is also noticeable that the relation flattens at low halo masses. For the lowest mass haloes the lowest radii used to fit a concentration parameter are affected by the resolution limit of the simulation, and so it is likely these inner radii cause the
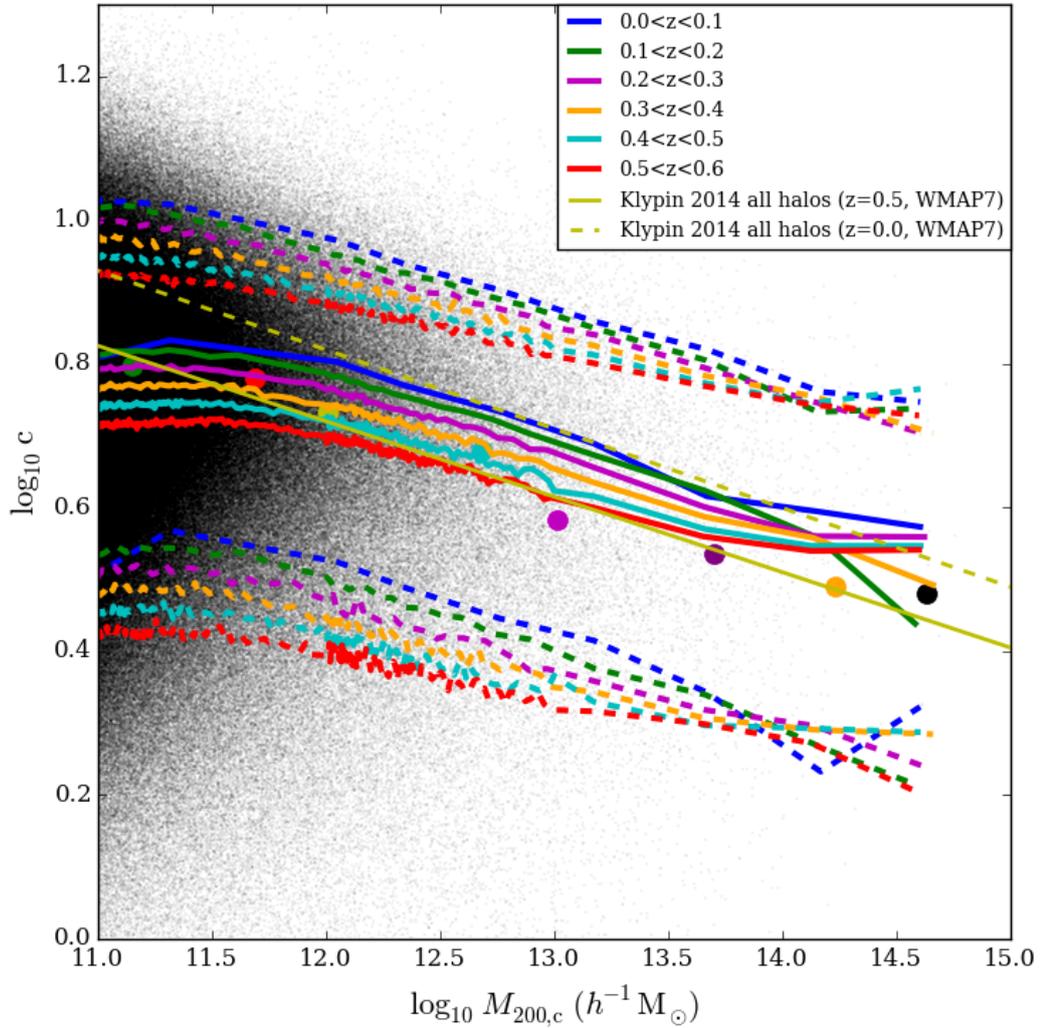
Figure 6.7: The concentration-mass relation for GAMA lightcone haloes for different redshifts (see key). The solid (dashed) coloured lines show the median (10th and 90th percentiles) as a function of $M_{200,c}$, for different redshift bins (see key). The concentration-mass relation given in Klypin et al. (2014) for the WMAP7 cosmology (as is used in this work), for redshifts $z = 0.5$ ($z = 0.0$) is shown by the yellow solid (dashed) line. The coloured dots give the concentration and mass of the example haloes, following the colour scheme of Fig. 6.4.

measurement of the halo concentration to be too low. If the relation and the scatter on the relation were to be extrapolated to smaller masses, the fraction of haloes with concentrations greater than $c = 10$ would become increasingly large such that for $M_{200,c} = 10^{11.7} h^{-1} M_\odot$, 10% of the haloes have $c > 10$. For such haloes the scale radius will not be included in the radial range over which the NFW profile is fitted, and the concentration is likely to be a poor fit. This apparent flattening of the relation at low masses is therefore unlikely to be real.

While other studies of the concentration-mass relation split haloes into relaxed (those which have virialised) and un-relaxed, we do not consider this in our analysis. There are many criteria with which to test if a halo is relaxed, such as finding the fraction of the halo mass within subhaloes, the fraction of subhaloes with their centre inside the virial radius of the halo, or the displacement of the centre of mass, or the virial ratio $2T/U$, of the halo. However, the purpose here is to understand the halo properties applicable to galaxy groups, where the sample is not expected to be relaxed.

The physical meaning of the concentration-mass relation has been explored in depth by several authors (Prada et al., 2012; Klypin et al., 2014; Neto et al., 2007; Duffy et al., 2008; Bullock et al., 2001). A popular explaination is the formation time of haloes of different masses. At higher redshifts, halo masses were smaller than haloes on average (see Fig. 10 of Neto et al. (2007)), these formed when the mean density of the Universe was higher, therefore causing them to have higher concentrations. More massive haloes tend to form at later times, and are hence less concentrated, explaining the decrease in concentration with halo mass.

Since more massive haloes formed later on, the typical halo mass increases towards present times (lower redshifts). It is therefore expected that the concentration of a halo of typical mass at redshift $z = 0$ should be smaller than the concentration of a halo of typical mass at $z = 0.5$, since larger haloes form at later times.

The scatter in concentration seen in Fig. 6.7 is the same for all masses and redshifts. Commonly the formation time of a halo is defined as the time at which the most massive progenitor of the halo exceeds half the halo mass at $z = 0$ (Neto et al., 2007). The formation times of larger mass haloes can then be considered to

be much earlier, thus creating a larger range of formation times for haloes of a given halo mass. The large range of halo formation times implies variation in the critical density of the Universe when haloes were formed, and hence a larger range in halo concentrations.

Another useful point to consider is how the concentration-mass relation changes when using the mean density of the Universe ρ_{mean}, rather than the critical density, ρ_{crit}, to define the halo. Assuming a perfect NFW profile, the scale radius of a halo is the same regardless of the density used. However, the size of the halo, $R_{200,\mathrm{m}}$, will always be larger than $R_{200,\mathrm{c}}$, since $\rho_{\mathrm{mean}}(z) \leq \rho_{\mathrm{crit}}(z)$ (see Fig. 1.1). Therefore the concentration (defined as $c = R_{200}/r_s$) will be larger when using ρ_{mean} (c_m) than with ρ_{crit} (c_c). The amount by which R_{200} (and therefore concentration) increases depends on the redshift of the halo. At $z = 0$, the difference in concentrations is such that $c_m = 1.7c_c$. However, halo mass also depends on the density used, but since M_{200} depends on both density and radius, the difference in masses is $M_{200,\mathrm{m}} = 1.34M_{200,\mathrm{c}}$ at $z = 0$. Due to the larger dynamic range of M_{200} probed compared to that of c, the effect of defining the halo using ρ_{mean} is that the concentration-mass relation appears to shift up such that for the $M_{200,\mathrm{m}} \sim 10^{11}h^{-1}\mathrm{M}_{\odot}$, the median concentration is $c \sim 10$ at $z = 0$. It is important to note that using a minimum radius of $r = 0.1R_{200}$ to fit an NFW profile when defining haloes by ρ_{mean} implies that for the lowest redshifts the scale radius of a halo is unlikely to be probed and thus the concentration recovered has a high uncertainty.

Hereafter concentration is defined using ρ_{crit} as the density of the Universe, and the concentration mass relation is as given in Fig. 6.7.

6.6 Circular velocities in haloes

Another useful way to quantify the structure of dark matter haloes is to consider the circular velocity profile. The shape of the velocity profile is another good indication of how accurately the distribution of particles is described by an NFW profile, and is related to the mass enclosed within some radius. The position in the halo at which the circular velocity profile peaks can be constrained using the concentration of the

halo. For galaxy sized haloes the position of the maximum circular velocity is more indicative of the extent of luminosity in the galaxy than the virial radius.

The circular velocity of a particle at a radius r, which encloses a mass $M(<r)$, is simply measured as

$$V_{\mathrm{circ}} = \sqrt{\frac{GM(<\mathrm{r})}{\mathrm{r}}}, \tag{6.13}$$

where G is the gravitational constant.

The circular velocity profiles for the 8 example haloes introduced in §6.4.1 are shown in Fig. 6.8. While the points indicate the measured circular velocity for each particle, the solid curves show the circular velocity profile expected from the best fitting NFW density profile (as described in §6.4.1). The concentration, c, recovered from the density profile gives an expected NFW circular velocity profile, $V_{\mathrm{circ,NFW}}(r)$, at radius r, for a given $R_{200,\mathrm{c}}$, by:

$$\left(\frac{V_{\mathrm{circ}}(r)}{V_{200,\mathrm{c}}}\right)^2 = \frac{1}{x}\frac{\ln\left(1+cx\right)-(cx)/(1+cx)}{\ln\left(1+c\right)-c/(1+c)}, \tag{6.14}$$

with $x = r/R_{200,\mathrm{c}}$, and where $V_{200,\mathrm{c}}$ is the circular velocity at $R_{200,\mathrm{c}}$.

The dashed lines and open circles in Fig. 6.8 indicate $r/R_{200,\mathrm{c}} < 0.1$, the minimum radius included in fitting the NFW profile. Clearly the concentration recovered by the density profiles also gives a velocity profile which is in very good agreement with the measured circular velocity profiles of the haloes. It is also interesting to note that for the higher mass haloes, where particles probe much further in than the minimum radius used in the fit, the NFW profile is still a good fit to the circular velocity profile. The velocity profile at the innermost radii no longer follows an NFW profile, but only for scales close to the Plummer equivalent softening in the simulation (5kpc).

6.6.1   Constraining the maximum circular velocity

The maximum circular velocity, V_{max}, is determined as the peak of the velocity profile. While it is feasible for the position of V_{max} to be outside the halo radius (for low concentrations), setting a maximum radius ensures that the radius at which
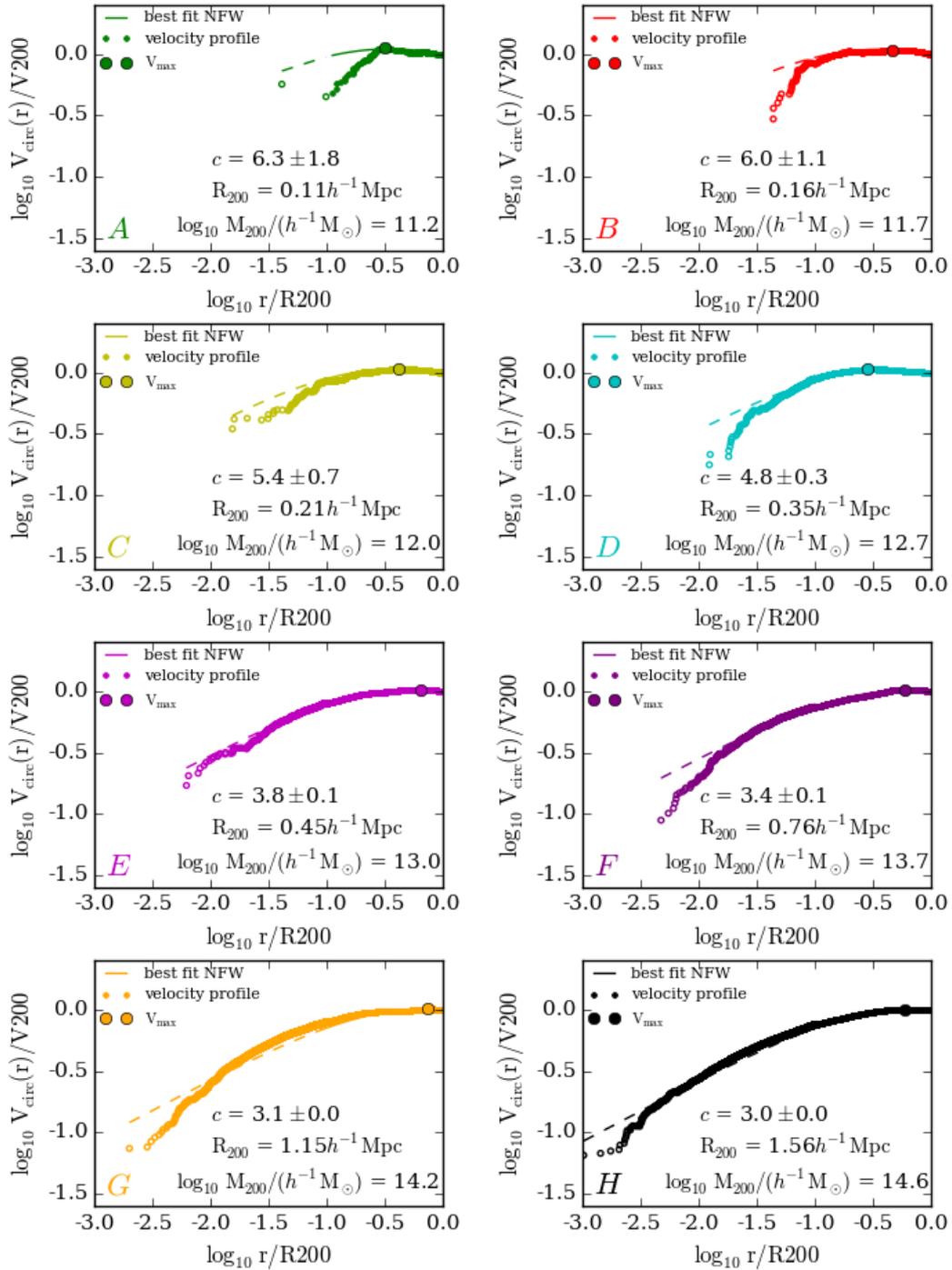
Figure 6.8: Circular velocity profiles for the example haloes given in Fig. 6.4. The large circle in each panel shows the maximum circular velocity in the halo (V_{max}). The solid curves show the expected circular velocity profile from the halo concentration as found in §6.4.
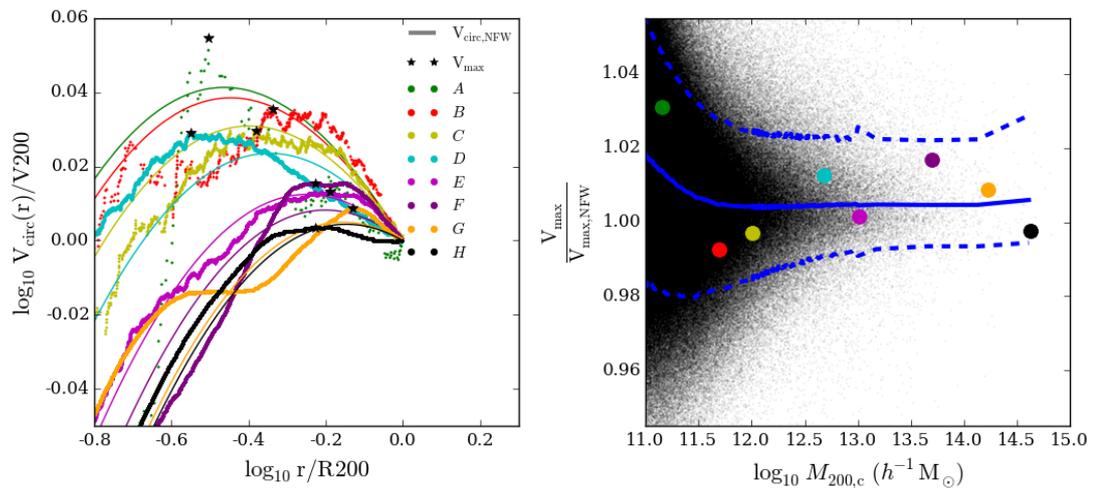
Figure 6.9: *Left*: Circular velocity profiles as in Fig. 6.8, for haloes normalised to $R_{200,c}$ and V_{200}, zoomed in around $R_{200,c}$. Stars show V_{max} for each halo. The mass of each halo can be found in Fig. 6.8; the legend lists the haloes in ascending mass. The shape of the velocity profile varies with mass, and V_{max} is well determined for the most massive haloes. The NFW profiles, $V_{circ,NFW}$ for each halo do not appear to agree well with the measured profile, V_{circ}, but the scale of the figure is small and apparent large discrepencies are only of order 1%. *Right*: The ratio of V_{max} determined from the measured circular velocity profile, to that expected from the concentration fit for the binned density profile, assuming an NFW profile, as a function of $M_{200,c}$. The solid (dashed) coloured lines show the median (10th and 90th percentiles) as a function of $M_{200,c}$, and the coloured dots show each of V_{max} for the example haloes given in the left panel.

V_{max} is found (R_{max}) is not significantly larger than $R_{200,c}$. The limit adopted for this work is arbitrarily chosen to be $1.25R_{200,c}$. The recovered maximum circular velocity is shown by the large coloured dots in Fig. 6.8. It is clear that the position within the halo, $R_{max}/R_{200,c}$ at which V_{max} is found increases as halo mass increases. Since the overall shape of the velocity profiles appear to be well defined for these haloes, substructure within the halo does not affect the radius at which V_{max} is found.

The left panel of Fig. 6.9 allows the location of the maximum circular velocity to be inspected more closely. While at first sight the velocity profile does not appear to agree with that predicted by an NFW profile, it is important to note that the scale of $V_{circ}/V_{200,c}$ in this figure is very small, and apparently large discrepencies

are in fact only of the order of 1%. However, since the variation in the measured $V_{\text{max}}/V_{200,\text{c}}$ (indicated by black stars) with halo mass is also very small ($< 6\%$ for the mass range shown), such small discrepencies become significant when assessing the usefulness of V_{max} as a proxy for halo mass.

For the smallest halo masses V_{max} (indicated by black stars) is not so easily constrained, due to the small number of particles in the halo. In such cases it seems that the peak of the NFW profile may give a clearer indication of the position V_{max}, since the process of fitting the NFW profile includes the majority of particles within the halo, although the uncertainty on the concentration is large for these haloes. For higher mass haloes the position of V_{max} may still be affected by substructure in the halo.

Prada et al. (2012) look at the $V_{\text{max}}/V_{200,\text{c}}$-mass relation for Millennium-I and Millennium-II simulations over a much larger range in redshift than is considered here. Given that Millennium-II has a much higher (125 times) mass resolution than Millennium-I, halo velocity profiles will be better measured for haloes of a comparable mass in Millennium-II. However, Prada et al. (2012) only find a difference between the simulations at high redshift, suggesting that significantly increasing the mass resolution of the simulation does not noticeably improve the ability to measure $V_{\text{max}}/V_{200,\text{c}}$.

The right panel of Fig. 6.9 shows how the measured V_{max} deviates from that expected using the best fitting NFW profile. The expected V_{max} ($V_{\text{max,NFW}}$) and R_{max} ($R_{\text{max,NFW}}$) for a given concentration, c, are found at the turning point of NFW velocity profile described by equation 6.14. 80% of haloes have a measured V_{max} which agrees with the expected $V_{\text{max,NFW}}$ to within 3% for halo masses larger than $10^{11.5}h^{-1}\text{M}_\odot$. There is a very small offset in the ratio $V_{\text{max}}/V_{\text{max,NFW}}$, such that the median V_{max} is consistently 0.5% higher than $V_{\text{max,NFW}}$ for all but the smallest halo masses. The scatter indicates that 10% of haloes have a measured V_{max} at least 2.2% larger than expected by an NFW profile. Although the offset and the scatter appear negligibly small, they are comparable to the variation in $V_{\text{max}}/V_{200,\text{c}}$ with halo mass (as is seen in the left panel of Fig. 6.9) and should not be neglected.

As expected from the left panel of Fig. 6.9, there is an upturn of up to 2% at

low masses. The smallest halo, A (indicated by the green points), gives an example where the velocity profile is not smooth, and therefore V_{max} is driven by noise in the profile and deviates from the peak of the NFW profile (halo A, green), although the peak occurs at the same radius. Halo B (red), however, gives an example of where structure within the halo significantly affects R_{max}. Substructure in the halo affects all halo masses and is likely to be the cause of the small bias in the median, with V_{max} being higher than predicted.

The maximum circular velocity can be predicted using the best fitting NFW profile to within a few percent, even for the smallest halo masses, given that the halo concentration is already known. Given the concentration-mass relation in Fig. 6.7, a velocity profile can be predicted by an NFW profile for a given halo mass, without requiring a direct measurement of concentration. By assessing how V_{max} and R_{max} vary with $M_{200,\mathrm{c}}$, and how this compares to that expected using an NFW profile with a concentration drawn from the concentration-mass relation (§6.5), we can determine whether R_{max} or V_{max} exhibit a stronger dependence on $M_{200,\mathrm{c}}$ than would be expected from the concentration-mass relation.

For NFW haloes, $V_{\mathrm{max}}/V_{200,\mathrm{c}}$ depends only on the concentration of the halo (equation 6.14). Fig. 6.7 shows a clear decline in concentration with halo mass and redshift, but with significant scatter. It is expected that NFW haloes will exhibit a similar decrease in $V_{\mathrm{max}}/V_{200,\mathrm{c}}$ with $M_{200,\mathrm{c}}$ and redshift. We find a decrease in $V_{\mathrm{max}}/V_{200,\mathrm{c}}$ with halo mass which is in very good agreement with that expected by the concentration-mass relation, suggesting that for a given halo mass, the maximum circular velocity is well determined by assuming an NFW profile. There is an offset of 1% between the measured and expected V_{max} for halo masses greater than $10^{11.5}h^{-1}\mathrm{M}_{\odot}$, consistent with the offset seen in Fig. 6.9. However the decrease with halo mass is small, at most $0.1V_{200,\mathrm{c}}$ from $10^{11}h^{-1}\mathrm{M}_{\odot}$ and $10^{14}h^{-1}\mathrm{M}_{\odot}$, and only $0.04V_{200,\mathrm{c}}$ over the redshift range considered here.

We also find $R_{\mathrm{max}}/R_{200,\mathrm{c}}$ becomes closer to unity as halo mass increases. This can be understood by considering higher mass haloes are less concentrated, and so the peak of the velocity profile is further from the centre of the halo (see Fig. 6 of Muldrew et al. (2011) for a comparison of R_{max} and concentration). The measured

$R_{\text{max}}/R_{200,\text{c}}$ again agrees particularly well with that expected by the concentration-mass relation. However, the range of $R_{200,\text{c}}$ is very large for a given mass. This is most likely an effect of substructure within $R_{200,\text{c}}$ causing the position of V_{max} to be unclear (e.g. Halo B in the left panel of Fig. 6.9).

For low mass haloes it is unlikely that $R_{\text{max}} > R_{200,\text{c}}$. We find 10% of haloes with $M_{200,\text{c}} = 10^{12}h^{-1}\text{M}_\odot$ have a maximum circular velocity outside $R_{200,\text{c}}$ and this fraction increasess within increasing mass.

In summary, the NFW profile gives a particularly accurate prediction of the value and position of V_{max} in haloes over the redshift and mass range considered here. The variation in both V_{max} and R_{max} with halo mass closely follows that expected from the concentration-mass relation. For a given halo mass, the uncertainty in determining R_{max} is large with respect to the size of the halo and the variation in R_{max} with mass. There is a clear trend in $V_{\text{max}}/V_{200,\text{c}}$ with $M_{200,\text{c}}$, although over a smaller dynamical range and with a slight but constant offset from the expected V_{max}, most likely caused by substructure in haloes.

6.7 Distribution of velocities within haloes

The dynamics of particles in a halo can be used to infer halo mass. Assuming a virialised system, the mass of the halo should only depend on the radius of the halo and the velocity dispersion of the particles within the halo. By measuring the velocity dispersion, σ_{vel}, of particles within a halo, we expect to be able to recover $M_{200,\text{c}}$ using the virial theorem:

$$\sigma_{vel}^2 \propto \frac{G\,M_{200,\text{c}}}{R_{200,\text{c}}}. \tag{6.15}$$

Since the mass of the halo scales with $R_{200,\text{c}}^3$, the velocity dispersion in a virialised system relates directly to mass as:

$$\sigma \propto M_{200,\text{c}}^{1/3}. \tag{6.16}$$

To infer mass from the velocity dispersion of a system, it is important to understand the distribution of particle velocities and how they affect the velocity dispersion estimate. Small errors in the estimate of velocity dispersion result in larger

errors in the mass. The standard deviation on the mean is a good estimate of the dispersion of a smooth Gaussian-like distribution of particles. A non-virialised system will likely not exhibit a smooth distribution, and therefore the measure of velocity is unlikely to be a good indication of halo mass in such cases.

Fig. 6.10 gives the velocity distribution relative to the mean velocity of the halo, v_{halo} in each dimension for the example haloes introduced in §6.4.1. The selection of these haloes is independent of their internal dynamics. While the distributions of velocities in the low mass haloes appear Gaussian (bearing in mind that a $10^{11}h^{-1}\mathrm{M}_{\odot}$ halo contains ~ 100 particles), two of the higher mass haloes (F, with $M_{200,\mathrm{c}} = 10^{3.7}h^{-1}\mathrm{M}_{\odot}$ and G, with $M_{200,\mathrm{c}} = 10^{14.2}h^{-1}\mathrm{M}_{\odot}$), have visibly non-Gaussian velocity distributions. A measure of dispersion on the mean of these distributions is large.

To investigate this further, Fig. 6.11 shows the distribution of particles in halo F in two projected planes. The particles are coloured by velocity with respect to the halo, in the y dimension, to assess why the distribution of particle velocities in this dimension significantly deviates from a Gaussian. Clearly the bump in the distribution around $v_y - v_{\mathrm{halo}} = -800\mathrm{km/s}$ is due to two substructures near the edge of the halo which are falling through the halo. These substructures have very small velocities in the x and z dimensions in the direction of the centre of the halo, suggesting that they are passing through the halo at high velocities, and happen to reside within $R_{200,\mathrm{c}}$ at that snapshot, but are not likely to be bound to the halo. This could be further tested by finding which Dhalo the particles in these substructures belong to. Such substructures can affect the distribution of velocities in the halo such that the velocity dispersion is over-estimated. In these cases using the velocity dispersion as a mass proxy causes an over-estimate of the halo mass. In the lightcone mocks the effect of the mass estimate of such unrelaxed systems can be assessed.

A popular estimation of the velocity dispersion is the gapper method, introduced by Beers et al. (1990). This method is adopted when estimating the velocity dispersion in galaxy groups, since it is less sensitive to interlopers than simply using the dispersion on the mean, particularly in haloes with a small number of galaxies. When using the dark matter particles belonging to a halo rather than galaxies, small number statistics are not as big an issue, since the smallest haloes considered
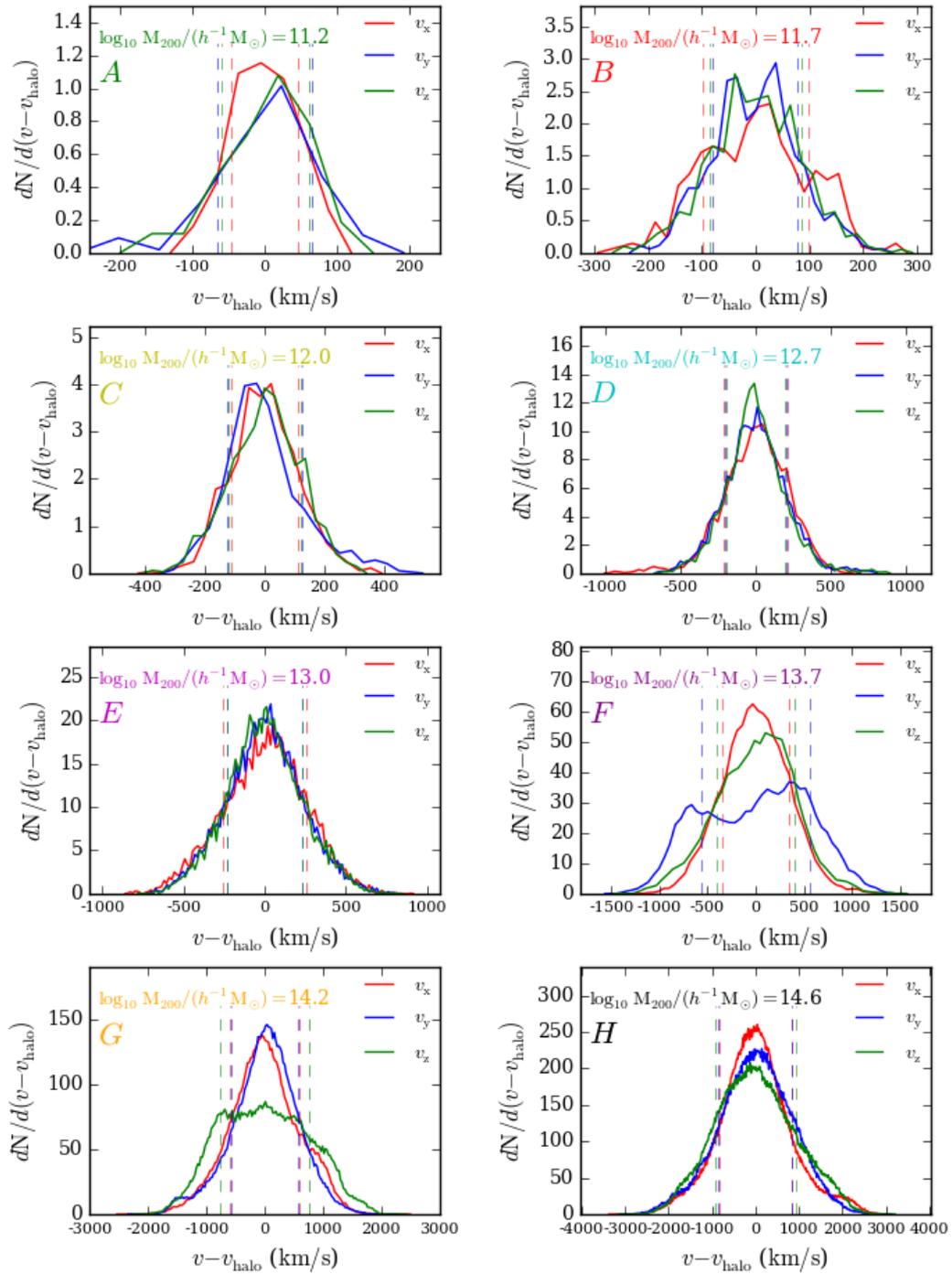
Figure 6.10: Distribution of particle velocities, v, in 3 dimensions (x, y, z) relative to the mean velocity of particles in the halo (v_{halo}) in each dimension, for the example haloes introduced in Fig. 6.3, with gapper velocity dispersion (equation 6.18) indicated by dashed lines.
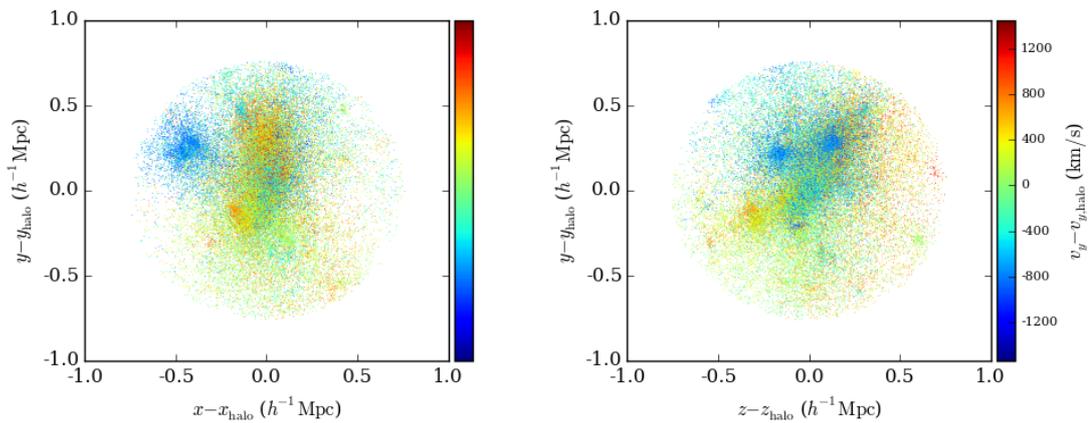
Figure 6.11: Position of particles in 2 projections for halo F (see Fig. 6.10), where distribution of velocities does not appear Gaussian, coloured by velocity in the y direction. 2 structures (coloured in blue due to high velocities) are causing the unusual distribution of velocities.

contain more than 100 particles. The gapper velocity dispersion is adopted here to keep the analysis of halo properties as consistent as possible with the methods for determining the velocity dispersion in galaxy groups. The gapper velocity dispersion in one dimension is estimated by first ordering particles in increasing velocity, then summing the difference between velocities v_i for each particle pair:

$$g_i = v_{i+1} - v_i, \tag{6.17}$$

weighted by $w_i = i(N - i)$, where N is the number of particles in the halo. The velocity dispersion in each dimension is then estimated as

$$\sigma_{gap} = \frac{\sqrt{\pi}}{N(N-1)} \sum_{i=1}^{N-1} w_i g_i. \tag{6.18}$$

A 3d velocity dispersion can be calculated as $\sigma_{gapper} = \sqrt{\sigma_{gap,x}^2 + \sigma_{gap,y}^2 + \sigma_{gap,z}^2}$. Although velocity information is available for particles in all 3 dimensions when considering simulations, it is important to remember that galaxy surveys only provide information about the line of sight velocities of galaxies.

The gapper velocity dispersion for each example halo is indicated by the dashed vertical lines in each panel of Fig. 6.10. Clearly for halo F the velocity dispersion

in the y dimension is still affected by the non-gaussian velocity distribution, since a significant fraction of the mass of this halo resides in the high velocity substructures.

The mean velocity dispersion is simply the standard deviation of particle velocities in a particular dimension, v_x, from the mean velocity of the halo, $\langle v_x \rangle$, and is calculated as:

$$\sigma_{mean,x} = \frac{1}{N-1} \sum_{i=1}^{N} (v_{x,i} - \langle v_x \rangle)^2, \tag{6.19}$$

and again the 3d velocity dispersion for each halo is given as:

$$\sigma_{mean} = \sqrt{\sigma_{mean,x}^2 + \sigma_{mean,y}^2 + \sigma_{mean,z}^2}. \tag{6.20}$$

A comparison of the velocity dispersion estimated using the gapper method to the velocity dispersion on the mean velocity of the halo is shown in Fig. 6.12, where the velocity dispersions shown are 3D velocity dispersions.

There is no significant bias between the velocity dispersions calculated using the gapper method and the dispersion on the mean, with less than 1% disagreement for haloes with $M_{200,c} > 10^{12} h^{-1} M_\odot$. For lower mass systems the scatter is slightly larger, such that 10% of haloes of masses around $10^{11} h^{-1} M_\odot$ have velocity dispersion estimates which disagree by more than 4%. It is likely that these low mass systems are not fully virialised and the tendency for $\sigma_{gapper} < \sigma_{mean}$ suggests that interlopers (i.e. particles within $R_{200,c}$ but not within the virialised halo) are present. The gapper method then accounts for these when estimating velocity dispersion, thus giving a lower velocity dispersion for the system. The difference between velocity dispersion estimates is less likely to be so consistent for galaxy groups, where the number of tracers in the system is smaller, and so it is important that there is no significant disagreement introduced when using a different estimator for larger particle number systems.

Having adopted the gapper method for estimating velocity dispersion, the relationship between velocity dispersion and halo mass can be investigated. This is shown in Fig. 6.13, where the median (shown by the blue solid line) indicates a clear relationship between velocity dispersion (estimated using the gapper method) and $M_{200,c}$. The yellow line shows the slope of $1/3$ expected assuming all haloes are
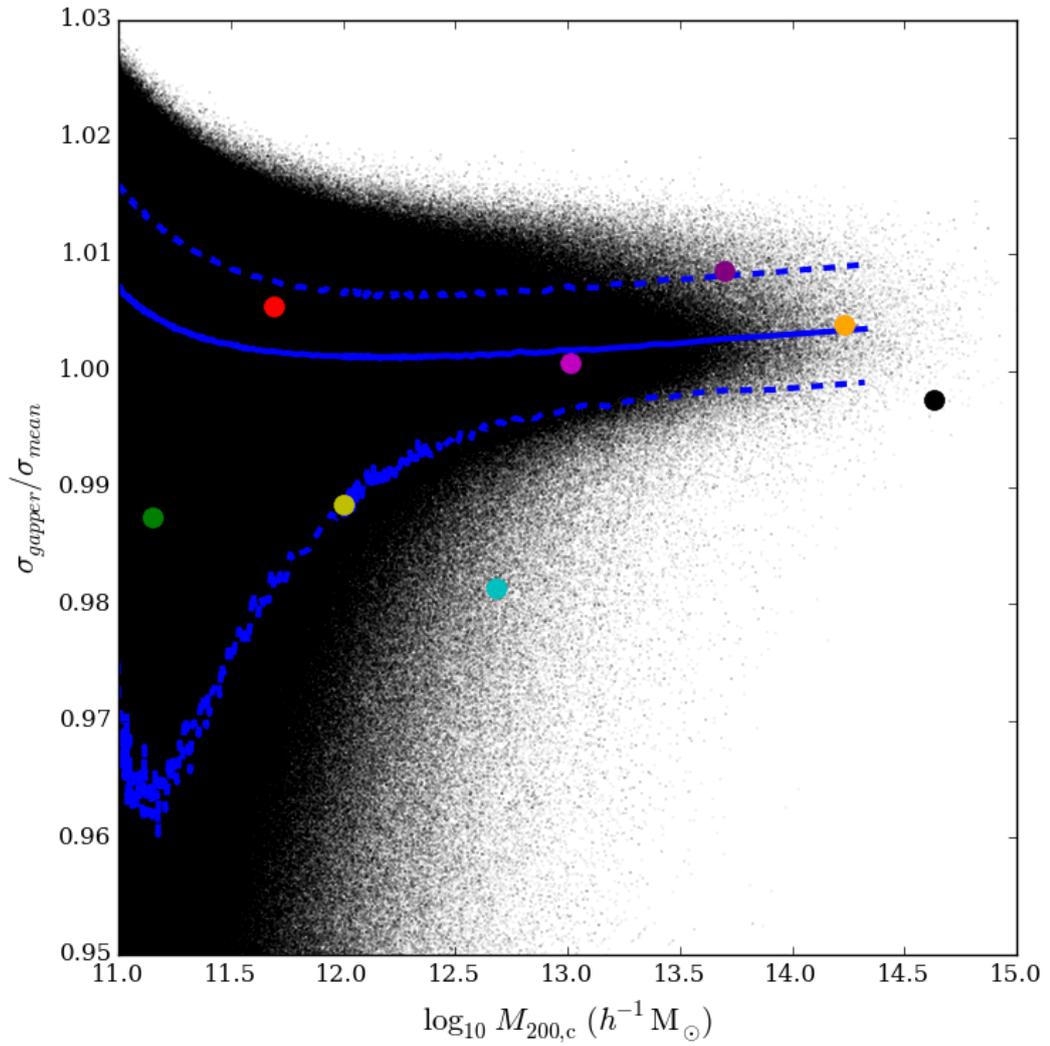
Figure 6.12: Ratio of (3d) velocity dispersion using the gapper method (σ_{gapper}) to the velocity dispersion on the mean velocity of the halo (σ_{mean}), as a function of $M_{200,c}$. The solid (dashed) coloured lines show the median (10th and 90th percentiles) at fixed $M_{200,c}$. The example haloes shown in Fig. 6.10 are shown by the coloured dots.
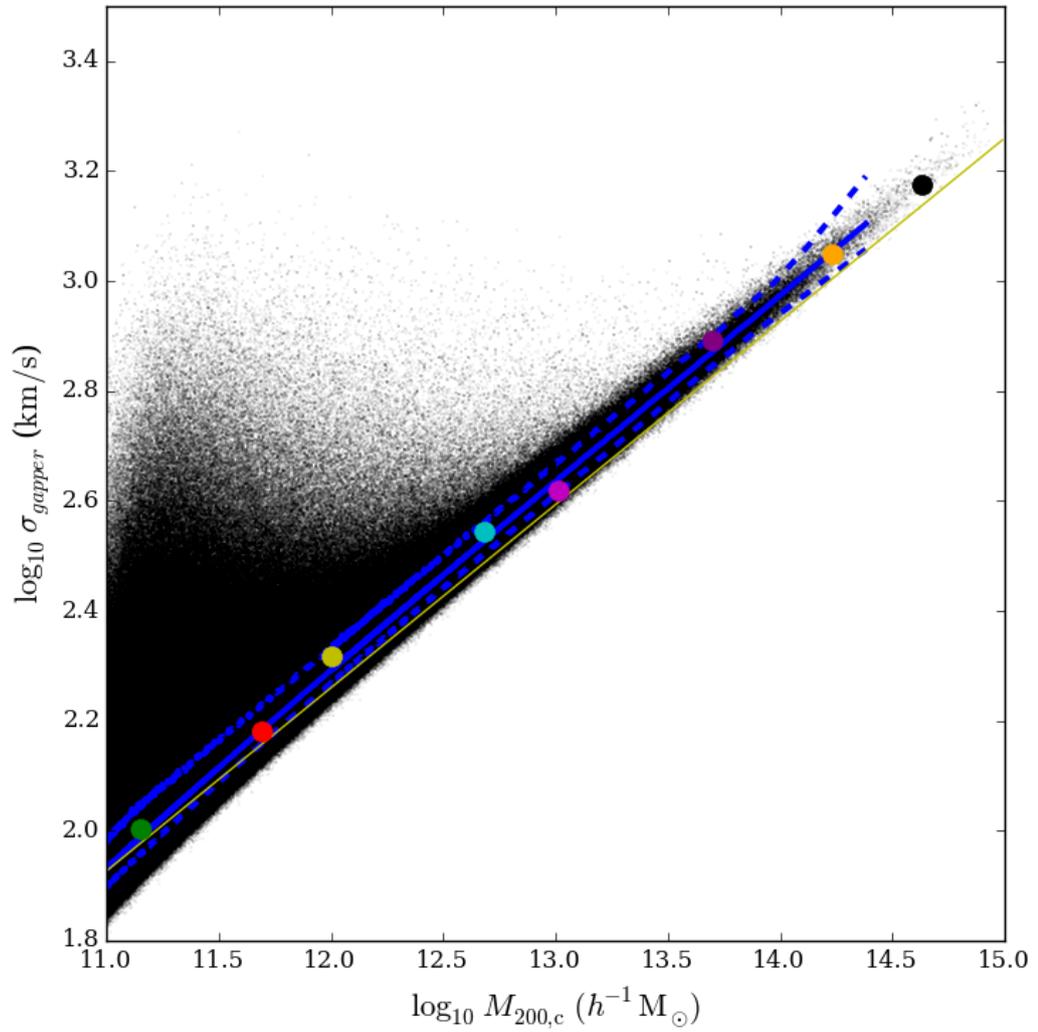
Figure 6.13: Gapper velocity dispersion as calculated using equation 6.18, as a function of $M_{200,c}$. The solid (dashed) coloured lines show the median (10th and 90th percentiles) as a function of $M_{200,c}$. Example haloes are shown by coloured dots. The velocity dispersion expected if the system is virialised is shown by the yellow solid line.

virialised, as given in equation 6.16. The median gives a slope of $^1/_{2.8}$, suggesting only a slightly steeper dependence of mass on velocity dispersion. The scatter on this relation is very small, only 2% as indicated by the 90th and 10th percentiles. For the smallest haloes there is a large range of velocity dispersions. The high velocity dispersion systems contribute to less than 5% of the sample at a given halo mass, and are mostly likely non-virial systems containing only a small number of particles. The halo mass defined by $M_{200,\text{c}}$ can be very well recovered for the majority of haloes in the lightcones by measuring the velocity dispersion in the halo with the relation $M_{200,\text{c}} \propto \sigma^{2.8}$.

6.8 Summary

In this chapter, halo properties are presented for all haloes in the GAMA lightcones. The haloes analysed here have an M_{Dhalo} mass (as determined by GALFORM) greater than $10^{11}h^{-1}\text{M}_\odot$, and redshifts $z < 0.6$.

For each halo a size is determined using $R_{200,\text{c}}$, and a mass using $M_{200,\text{c}}$, taking the critical density of the Universe to determine the extent of the halo.

Density profiles are measured using particles within $R_{200,\text{c}}$, and the concentration parameter is found by fitting an NFW profile to the binned density profile of each halo. Systematics in the choice of fitting method start to dominate the uncertainty in the concentration for the highest mass haloes ($M_{200,\text{c}} > 10^{13.5}h^{-1}\text{M}_\odot$). Other spherical mass estimates such as $M_{500,\text{c}}$ or $M_{200,\text{m}}$ can be determined by simply assuming an NFW profile with concentration and $M_{200,\text{c}}$. This NFW mass prediction works particularly well for mass estimates with a halo defined by a radius smaller than $R_{200,\text{c}}$, such as $M_{500,\text{c}}$ for which an NFW predicts the measured mass to within 7%.

Both the concentration-mass relation and the increase in concentration with redshift are in good agreement with Klypin et al. (2014). The scatter in the concentration-mass relation is large, which is likely an effect of the different formation times of haloes as they appear in the lightcones.

The circular velocity profile provides another indication of how closely the light-

cone haloes follow an NFW profile. The maximum circular velocity, V_{max}, is measured and compared to that expected with an NFW profile. Assuming the concentration obtained from the best fit to the density profile, an NFW profile predicts the measured value of V_{max} very well, with a slight offset which is mostly likely due to substructure affecting how accurately V_{max} is defined within the halo. There is a strong trend in $V_{\mathrm{max}}/V_{200,\mathrm{c}}$ with halo mass, which follows that of the concentration-mass relation. R_{max}, describing the position of V_{max} within the halo, also exhibits a trend with halo mass but is more sensitive to substructure in the halo.

For virialised haloes, the velocity dispersion of particles in a halo indicates the halo mass as $\sigma \propto M_{200,\mathrm{c}}^{1/2.8}$. There is little difference between the dispersion on the mean and the velocity dispersion defined using a gapper method when considering such a large quantity of particles. Unbound structures residing inside $R_{200,\mathrm{c}}$ are likely to have an impact on the velocity dispersion measurement and therefore overestimate the mass of the halo. Velocity dispersion is found to be tightly related to halo mass as $\sigma \propto M_{200,\mathrm{c}}^{1/2.8}$, suggesting that the haloes are not virialised systems.

The method of measuring halo properties presented in this chapter simply requires the positions and velocities of particles and the position of the halo centre, as determined in Chapter 3. Having measured a spherical halo mass ($M_{200,\mathrm{c}}$), and assuming a halo concentration (for example following the concentration-mass relation), other spherical mass estimates and the maximum circular velocity, V_{max}, and position its R_{max} in a halo, can be directly extrapolated by assuming an NFW profile.

The application of the pipeline presented here is specifically for the purpose of introducing and characterising the properties of haloes in the GAMA lightcone mocks, an important step to interpreting the density profiles of galaxy groups (Chapter 7). However, the pipeline for extracting halo properties from simulations is generally applicable to any simulation or cosmology.

Chapter 7

The Galaxy Density Profile of Groups in ΛCDM Lightcone Mock Catalogues and the GAMA Survey

The way in which galaxies are distributed in groups provides insight into how galaxies populate dark matter haloes, thereby leading to better models of galaxy formation. The aim of this chapter is to measure the galaxy density profile in groups in the GAMA survey, and provide comparisons to theoretical models using the GAMA lightcone mocks. Measurements of the galaxy density profile require the application of a group finder to recover galaxy groups that are indicative of the dark matter environment. Halo properties are then inferred using the galaxies in groups and their density number profile within groups is measured. The galaxy density profiles in groups in the GAMA lightcone mocks and in the GAMA survey are measured and presented here, paving the way for future investigations exploring the physical processes which shape the galaxy density profile.

7.1 Introduction

In the ΛCDM paradigm, galaxies are situated in the gravitational potential wells of dark matter haloes, providing visible, dynamical tracers of the distribution of dark matter. Therefore, by identifying galaxy groups and studying how galaxies

are distributed within groups, the distribution of dark matter in these groups can be constrained. In addition, the relationship between the properties of galaxies and the mass of their host haloes provides information about how the formation and evolution of galaxies is affected by the dark matter environment in which they reside.

Historically, studies of groups and clusters of galaxies used the work of Abell (1958), who visually identified 2712 rich galaxy clusters on the sky in the National Geographic Society Palomar Observatory Sky Survey by considering the compactness of groups of galaxies with more than 50 members. However, chance projections of unrelated structures along the line of sight can give rise to spurious clusters (Dalton et al., 1992). With the subsequent availability of galaxy redshift surveys, the construction of group catalogues became more robust and the contamination from projection interlopers was reduced with the availability of line-of-sight velocity information (e.g. Huchra & Geller, 1982). Modern galaxy group finders (e.g. Eke et al., 2004; Robotham et al., 2011; Gerke et al., 2012) are theoretically calibrated to optimise the recovery of dark matter haloes using mock galaxy catalogues derived from galaxy formation models implemented in N-body simulations (see Chapter 3). The properties and dynamics of galaxies in a group, such as the total group luminosity and the velocity dispersion of galaxies, are found to be closely related to the mass of the underlying dark matter halo (Han et al., 2015; Beers et al., 1990; Robotham et al., 2010), implying that the formation and evolution of galaxies is strongly influenced by their dark matter environment.

Group finders have been applied to wide-field galaxy redshift surveys such as SDSS (Yang et al., 2007), 2dFGRS (Eke et al., 2004) and the 2MASS redshift survey (Tully, 2015), as well as for deeper, smaller solid angle surveys such as zCOSMOS (Knobel et al., 2012) and DEEP2 (Gerke et al., 2012), identifying groups to $z = 1$ and $z = 1.5$ respectively. This has enabled robust tests of the evolution of group properties and provides a valuable tool with which to measure the growth of structure in the dark matter.

The density profile of dark matter in haloes can be inferred by measuring the rotation curves of spiral galaxies through HI observations, thereby probing the dis-

tribution of matter on galactic scales. The rotation curves at large galactic radii are found to be flat suggesting a high mass to light ratio in the outer parts of galaxies (Roberts & Rots, 1973; Bosma, 1981), regardless of morphological type of the galaxy.

For larger radii than can be observed with galaxy rotation curves, the distribution and dynamics of satellite galaxies within dark matter haloes offer a useful probe of the density profile and extent of dark matter haloes. With the use of mock galaxy catalogues, the galaxy density profile can be compared to the dark matter density profile in dark matter haloes, to determine how closely the radial distribution of galaxies follows the radial distribution of dark matter within the halo.

While previous studies of the dynamics of satellite galaxies in haloes have suggested that the dark matter component extends well beyond the visible component of the central galaxy (Zaritsky & White, 1994; McKay et al., 2002), the shape of the galaxy density profile in haloes remains somewhat uncertain. The satellite galaxy density profile is often measured around isolated primaries (Sales & Lambas, 2004; Guo et al., 2012). Prada et al. (2003) find that the galaxy density profile in the outer parts of the halo falls off as r^{-3}, in agreement with the dark matter density profile proposed by Navarro et al. (1997), and suggest that previous studies were affected by insufficient number statistics and interlopers. A dependence of the density profile on the luminosity of the central galaxy is also seen by Prada et al. (2003). However, due to the magnitude limits of these surveys, the number of satellites around each primary is small (typically one or two), and photometric samples (without spectroscopic redshifts) are sometimes employed (e.g. Guo et al., 2012) to increase satellite statistics. With the availablility of large galaxy surveys, the construction of galaxy group catalogues provides a representation of individual dark matter haloes in the Universe. Group catalogues such as those described in Robotham et al. (2011), Eke et al. (2004) and Yang et al. (2009) can be utilised to provide a sample of satellite galaxies associated with each central galaxy, where limitations due to low satellite numbers in groups can be overcome by stacking groups according to a property related to halo mass.

Alternatively, the distribution of dark matter in groups of galaxies can be de-

duced through weak lensing measurements of background source galaxies (Han et al., 2015; Viola et al., 2015). This approach does not need a precise measurement of the dynamics of galaxies, but requires a model describing the distribution of dark matter, for example an NFW profile, with a concentration-mass relation as measured in simulations (e.g. §6.5, Neto et al. 2007; Duffy et al. 2008; Klypin et al. 2014). Weak lensing measurements also provide tight constraints on the halo mass, providing a means to calibrate group masses against directly observable group properties such as luminosity.

In this chapter we measure the galaxy density profiles in groups in the GAMA survey by stacking groups of similar mass to increase number statistics. The pipeline for measuring the properties of haloes in the lightcone mock catalogues was described in Chapter 6, and is utilised here to investigate the impact of inferring the underlying halo properties using galaxies as tracers, leading to a better understanding of the ability to constrain the dark matter density profile by this method.

In §7.2, the application of the GAMA group finder to the lightcone mock galaxies and to galaxies in GAMA is described, and a comparison of the global properties of haloes and groups is given. The definition of group properties, such as centre, size, and mass, as inferred from the galaxies in groups is laid out in §7.3. The inferred properties of groups and haloes are then compared in §7.4, with the aim of finding those which best describe the underlying dark matter properties. The application of these properties to characterise a stacked galaxy density profile for groups in the lightcones and GAMA is given in §7.5, and §7.6 provides a summary of these results and outlines the future work required in order to provide theoretical interpretations of the galaxy density profile in GAMA groups.

7.2   Haloes and Groups in the GAMA Lightcone and Survey

The lightcone mock catalogues (described in Chapter 3) provide a means to assess how galaxies populate dark matter haloes while considering the selection effects of a galaxy survey. Galaxies in the lightcone reside in subhaloes and are assigned to

dark matter haloes, the Dhaloes. With the survey selection criteria applied to the mock galaxies, the ability of a group finding algorithm to recover the known galaxy membership of Dhaloes in the galaxy formation model can be investigated.

7.2.1 Galaxies in Haloes in the GAMA Lightcone

The Gonzalez-Perez et al. (2014) GALFORM model used to populate dark matter haloes with galaxies to construct lightcones was outlined in §3.2.1. An r-band apparent magnitude limit of 19.9 is imposed on the lightcone galaxies, which is somewhat deeper than the GAMA limit. This is done to account for the discrepancy seen between the abundance of GAMA and lightcone galaxies at the faintest apparent magnitudes (right panel of Fig. 3.5), leading to fewer galaxies observed in the lightcones than in GAMA. The mean galaxy density is an important aspect when recovering galaxy groups. The pipeline for calculating properties of the dark matter haloes in the lightcone, such as masses and density profiles, is discussed and implemented in Chapter 6. This allows direct investigations of how galaxies trace the underlying dark matter density field in lightcone haloes. The known halo membership also allows the fidelity of groups recovered by a group finder to be determined, as well as the ability to infer halo properties using galaxy properties as proxies.

7.2.2 Galaxies in Groups in the GAMA Lightcone

The group finder used in this work was introduced in Robotham et al. (2011). The parameters of the group finder adopted for this work are those given in Robotham et al. (2011), which are constrained to optimise the number of haloes recovered in the lightcone mocks constructed using the Bower et al. (2006) GALFORM model (in the WMAP 1 cosmology). It is assumed that the optimal parameters of the group finder are independent of the GALFORM model used, and in particular very little difference is found in the redshift distribution of the recovered groups when the group finder is implemented in the WMAP 7 cosmology. Changing the cosmological parameters does not have a significant impact on the formation of structure over the scales probed by groups in GAMA.

Briefly, groups are detected using a Friends-of-Friends (FoF) algorithm with a projected linking length related to the mean intergalaxy separation. The mean galaxy density is calculated from the integral of the luminosity function (LF) down to a faint absolute magnitude limit, $M_{\text{lim}}(z)$, corresponding to the faintest absolute magnitude visible in the survey at the redshift of the galaxy. An extra factor in the linking length is introduced to account for the luminosity of the galaxy. Brighter, more massive galaxies are expected to reside in larger haloes and therefore have a more far-reaching gravitational effect on surrounding galaxies, and so the linking length is slightly increased for intrinsically brighter galaxies by considering the ratio of the luminosity function between the faintest absolute magnitude considered at that redshift and the absolute magnitude of the galaxy. The LF is assumed to increase for fainter magnitudes, which is seen in Fig. 3.6. The mean galaxy separation including this correction factor, $D_{\text{lim},i}$ for a galaxy i, at redshift z_i with absolute magnitude $M_{\text{gal},i}$ is then given by:

$$D_{\text{lim},i} = \left(\frac{\phi(M_{\text{lim}}(z_i))}{\phi(M_{\text{gal},i})} \right)^{0.63/3} \left[\int_{-\infty}^{M_{\text{lim}}(z_i)} \phi(M)\, dM \right]^{-1/3}. \tag{7.1}$$

While the factor introduced to account for galaxy luminosity (the value of which is optimised by Robotham et al. 2011) is small for galaxies fainter than M^* ($M_r - 5\log h = -20.7$), for galaxies with an absolute magnitude of $M_r = 22.0$ the increase in D_{lim} is as much as a factor of ~ 3 for low redshifts.

When considering dark matter particles, the value of the linking parameter, b, is motivated by the definition of halo virial radius corresponding to a mean overdensity of 178 times the critical density, required for spherical collapse in a Universe with $\Omega_{\text{M}}=1$ (Cole & Lacey, 1996). For the purposes of linking galaxies, the value of $b = 0.06$ was found by optimising the groups to match the number of haloes in the lightcone mocks containing five or more galaxies (Robotham et al., 2011). The maximum projected separation for two galaxies at different redshifts, i and j, to be considered as linked is therefore $D_{\text{max,proj},ij} = b(D_{\text{lim},i} + D_{\text{lim},j})/2$.

The positions of galaxies in real-space are known in the lightcone mocks. When finding groups of galaxies using the real-space information, the line-of-sight linking length is the same as the projected linking length for each galaxy. However, galaxy
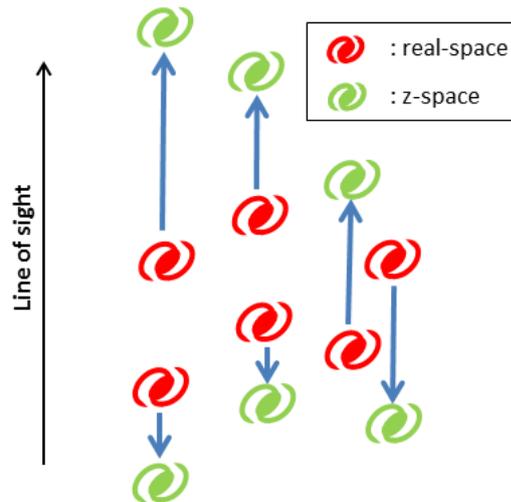
Figure 7.1: Diagram visualising the effect of redshift space distortions on a lightcone halo. The linking length must be adjusted in the line of sight direction when considering galaxies in redshift space. Blue arrows reflect the direction of the peculiar velocity when projected along the line of sight.

surveys provide galaxy information in redshift space, where the redshift of a galaxy is due to both the Hubble flow and the peculiar motion of the galaxy along the line of sight. Consequently, gravitationally bound structures appear elongated along the line of sight, and an extra parameter, R, must therefore be introduced to account for the redshift-space distortions in haloes. As shown in Fig. 7.1, the effect of peculiar velocities is to increase the apparent radial separation between galaxies. R must therefore be large to sufficiently increase the maximum line-of-sight galaxy separation, $D_{\mathrm{max,los},ij} = RD_{\mathrm{max,proj},ij}$. The adopted value of $R = 18$ was again optimised by Robotham et al. (2011) using the mocks.

7.2.3 Galaxies in Groups in the GAMA survey

The group finder is applied to galaxies in the GAMA survey in the same way as described above. Since GAMA is a highly complete survey, the effect of the incompleteness on the recovered groups is negligible. The measured GAMA LF (the red curve in Fig. 3.6) is used to determine the mean galaxy separation. The application of the group finder here differs from Robotham et al. (2011) in terms of the galaxy sample used. The sample used here is GAMA-II, with an apparent magnitude limit

over all 3 GAMA regions down to $m_r = 19.8$, while the parameters in the group finder were optimised by Robotham et al. to GAMA-I data with $m_r = 19.4$.

7.2.4 Global Group and Halo Comparisons

For the remainder of this chapter, the term *group* refers to a collection of GAMA or lightcone galaxies grouped together by a group finder, and the term *halo* is used to describe the collection of galaxies (or dark matter particles) belonging to a single Dhalo in the lightcones. The galaxy membership of haloes or groups is commonly called the *multiplicity*, which gives the number of galaxies belonging to a halo, N_{halo} or group, N_{FoF}. A group is defined (in this work) as having a multiplicity of $N_{\mathrm{FoF}} \geq 2$. Since a halo is defined by a membership of dark matter particles, haloes are not required to have a galaxy membership. For compatibility with the groups, in this work haloes are chosen to be those with a multiplicity of $N_{\mathrm{halo}} \geq 2$.

The redshift distributions for haloes and groups in the 26 lightcone mocks, and for groups in the GAMA survey are shown in the top left panel of Fig. 7.2. At first glance it is clear that the group finder recovers more groups (both in GAMA and the lightcones) than there are haloes in the lightcones. The group finder has been optimised to recover the abundance of haloes in the lightcones for groups with $N_{\mathrm{FoF}} \geq 5$ (Robotham et al., 2011), and it is likely that the discrepency is due to the splitting up of larger haloes into multiple groups with lower multiplicity, and to unassociated galaxies being artificially grouped together by the group finder. While this effect is larger for groups in the lightcones recovered in redshift-space than in real-space, the distribution of redshifts for GAMA groups is very similar to the distribution of lightcone groups found in redshift-space, for redshifts $z < 0.3$. We adopt this as an upper redshift limit for the work presented in this Chapter.

To further investigate the discrepancy between the number of recovered groups and haloes, the other 3 panels of Fig. 7.2 show the distribution of multiplicities within redshift bins of $\delta z = 0.05$. Due to the apparent magnitude limit imposed on the galaxy sample, the multiplicity of groups of similar mass changes with redshift, since intrinsically fainter galaxies are not visible at high redshifts. Small redshift ranges are required when assessing the distribution of group multiplicities such that
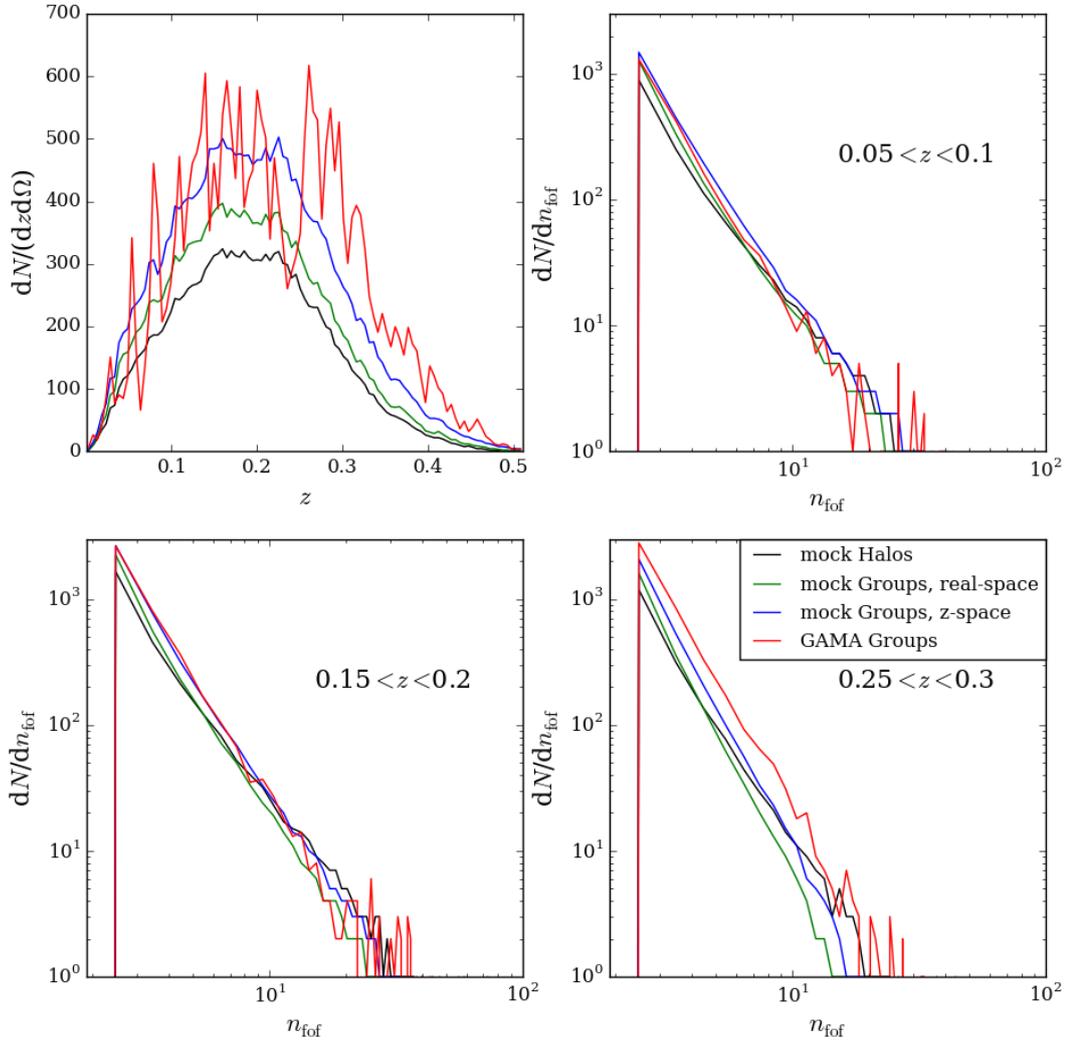
Figure 7.2: *Top left*: Redshift distribution (per deg^2) of haloes (black) and groups recovered in real-space (green) and redshift-space (blue) in the lightcones, averaged over 26 mocks, and groups found in GAMA (red), for 3 fields. *Top right and bottom*: Distribution of halo and group multiplicities in the lightcones and group multiplicities in the GAMA survey, for 3 redshift ranges as labelled on each panel.
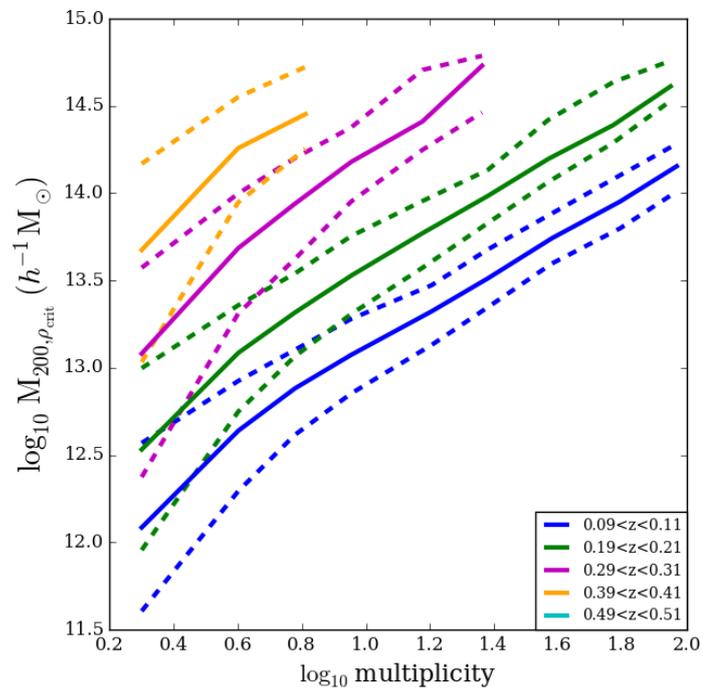
Figure 7.3: Halo mass ($M_{200,c}$) as a function of halo multiplicity. Solid lines show the median mass as a function of multiplicity for bins in redshift (see key), and the 10th and 90th percentiles are shown by dashed lines of the same colour.

haloes of similar masses are probed for a given multiplicity. Clearly both groups and haloes are dominated by low multiplicities at any redshift, but the number of high multiplicity groups and haloes decreases with redshift. The largest differences are visible at the lowest multiplicities, mimicking the offset seen in the redshift distribution, and the excess of low multiplicity groups is most likely to be due to the group finder artificially linking pairs of galaxies. However the number of high multiplicity haloes is slightly higher than the number of groups, and so it is also possible that some higher multiplicity haloes are being split up by the group finder.

Since a sufficiently massive halo will host a galaxy in the lightcone, halo mass is expected to correlate with multiplicity, as is shown in Fig. 7.3, such that, at a given redshift, halo mass ($M_{200,c}$ in the case of Fig. 7.3) can be approximately inferred from the multiplicity of the halo. The median $M_{200,c}$ as a function of multiplicity for the median GAMA redshift, $z = 0.2$, is in agreement with Fig. 16 of Viola et al. (2015), which shows the median halo mass as a function of N_{FoF}, for $N_{\mathrm{FoF}} \geq 5$ over all redshifts in GAMA. The survey selection function reduces the number of galaxies visible in a halo of a given mass with increasing redshift, and so only the most massive haloes ($M_{200,c} > 10^{13}h^{-1}\mathrm{M}_\odot$) host detectable galaxies at redshift $z = 0.4$.

7.3 Group and Halo Property Definitions

7.3.1 Halo Centre

In order to determine group or halo properties such as the size or the density profile, a centre must first be defined. In the models, the halo centre is defined as the position of the central galaxy in the halo (discussed in Chapter 3) with all other galaxies in the halo considered as satellites.

The centre of mass of a group of galaxies is sensitive to the presence of interlopers. The iterative algorithm adopted here to find the group centre is described in Robotham et al. (2011) and consists of finding the centre of light for a group of galaxies, removing the most distant galaxy and recalculating the centre of light. This process is repeated until there are two remaining galaxies, the brightest of which is chosen as the group centre. The centre of light and galaxy distances are calculated
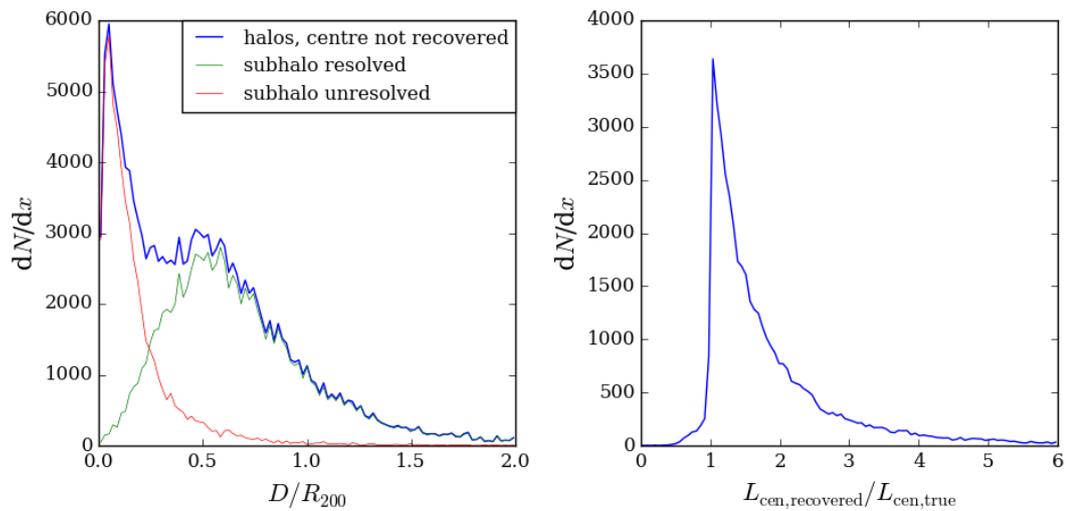
Figure 7.4: *Left*: Distribution of the displacement, D, indicated as a fraction of $R_{200,c}$, between the recovered and true centres of lightcone haloes, for cases when the true centre is not recovered (27% of the time). The two peaks at $D/R_{200,c} \simeq 0.5$ and $D/R_{200,c} \simeq 0$ are caused by galaxies for which the host subhalo is resolved in the simulation (green) and galaxies with an unresolved subhalo (red). *Right*: The ratio of the r-band luminosity of the recovered central to the luminosity of the true central galaxy in haloes, for the 27% of haloes for which the true centre is not recovered.

as projected on the sky and so peculiar velocities do not affect the position of the recovered centre.

The algorithm is tested using galaxies in haloes where the true centre is known, and recovers the true centre for 73% of haloes. For the 27% of haloes for which the centre is wrongly recovered, the distribution of the projected separation between the recovered and true centres is shown in Fig. 7.4. The two clear peaks seen in the left panel are caused by the treatment of satellite galaxies in GALFORM. The peak at $\sim 0.5 R_{200,c}$ is dominated by satellite galaxies with a resolved subhalo. When the galaxy gets close to the halo centre, the dark matter density is higher and the galaxy's subhalo becomes unresolved compared to the background density field before the galaxy merges with the central galaxy (see Jiang et al. 2014). Galaxies can then reside close to the centre of the halo without a resolved subhalo. This process is discussed in §3.2.1.

The right panel of Fig. 7.4 compares the ratio of luminosities between the re-

covered and true central galaxy in the 27% of cases where the true centre is not recovered. In 97.4% of these cases the recovered central is brighter than the true central. Since the algorithm gives preference to brighter galaxies when recovering the halo centre, if the true central is not the brightest it is unlikely to be recovered. In such cases the algorithm could be adapted to account for a more intrinisic galaxy property, such as stellar mass, instead requiring the assumption that the central galaxy is more massive than satellites in the halo.

7.3.2 Matching of groups and haloes in the lightcone

To be able to directly compare like for like haloes in the lightcone with groups found using the group finder in §7.2.2, a method must be defined to match groups and haloes. This process also allows for the quality of the group finder to be tested, determining how efficiently haloes in the lightcone are recovered.

Bijective matching

Bijective matching is commonly used when matching two sets of points. Two sets of particles are bijectively matched if both contain more than half of the particles also belonging to the other set, such that the majority of particles in each of the sets belong to both sets.

Central matching

Alternatively, two sets of particles can be considered to be matched if they both have the same particle as the centre. This matching process requires the centre of the set to be the position of a specific particle, and relies on a reliable algorithm for determining the centre (e.g. as described in §7.3.1). The group centre can be matched either to the true halo centre (as defined by GALFORM) or to the halo centre recovered using the same iterative algorithm as is done for the groups.

Comparison of matching methods

If a group is bijectively matched to a halo it is not automatically also centrally matched. Likewise for a group and halo to be centrally matched all other member-
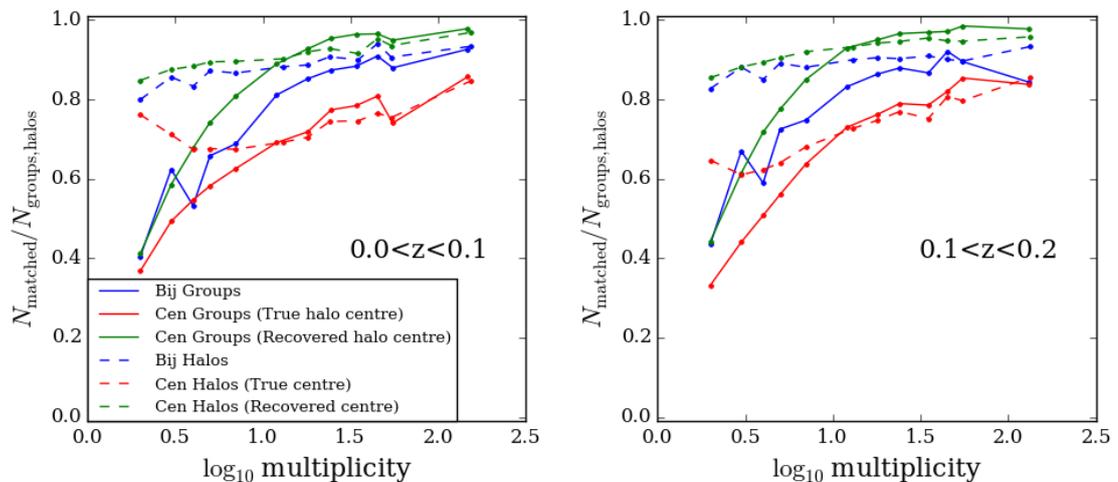
Figure 7.5: The fraction of groups (solid lines) or haloes (dashed lines) that are bijectively matched (blue), centrally matched using the recovered group centre and the true halo centre (red) or centrally matched using the recovered group and halo centres (green), as a function of group or halo multiplicity, for 2 redshift ranges, as labelled in each panel.

ship is irrelevant. A halo which has been fragmented into multiple groups may not have a bijective group counterpart, but will be likely to be centrally matched to one of the fragmented groups. However, the centrally matched group and halo may not be comparable in terms of group properties (as determined by galaxy membership).

Fig. 7.5 shows how well the group finder recovers the true haloes by comparing the fraction of groups or haloes which are matched, for 3 different methods of matching (bijective matching, matching by true halo centre, and matching by recovered halo centre). The results of the matching methods are shown by different colours in the figure.

The fraction of haloes and groups which are centrally matched is strongly affected by the failure of the algorithm to recover the true halo centre. However, when matching groups to the recovered halo centre, the fraction which are centrally matched increases significantly, particularly for the highest multiplicities (>30), where more than 96% of both haloes and groups are centrally matched.

$\sim$90% of haloes have a bijectively matched group for all redshifts and for multiplicities greater than 2. However, for the reverse case this fraction is much lower, such that only $\sim$60% of groups with 3 galaxies have a bijectively matched halo.

As mentioned previously this is most likely a combined effect of the group finder artificially linking pairs of galaxies, while also fragmenting haloes into much smaller multiplicity systems. For any of the three matching methods, less than 40% of $N_{\mathrm{FoF}} = 2$ groups have a halo counterpart. To discount the large fraction of low multiplicity false groups we only consider groups with $N_{\mathrm{FoF}} > 2$ in the rest of this chapter.

Since the purpose of matching groups and galaxies is to define a halo counterpart for each galaxy group found in the lightcones, it might seem most logical to match groups and haloes on their recovered centre. However, our reason for finding a halo counterpart is to be able to determine how well galaxies in groups trace the underlying dark matter halo properties, such as mass, and we therefore adopt bijective matching, such that group properties defined by galaxy membership are more comparable to the dark matter properties of the halo counterpart.

Galaxies in six examples of bijectively matched groups are shown in Fig. 7.6, along with the galaxies belonging to the halo counterparts for each group. Haloes B, D and E are not centrally matched. In these cases the recovered group centre is the brightest galaxy in the group. In the case of D, the central galaxy of the group does not belong to the bijectively matched halo, but is particularly bright in comparison to the other group members and is therefore defined as the centre.

7.3.3 Working definitions

Having defined the centre of a group, a group radius which traces that of the underlying dark matter halo can be defined. Potential radius estimates are described below, along with the chosen estimate for velocity dispersion, group luminosity and most importantly group mass. The methods adopted here to define group luminosity and velocity dispersion the same as those used to calculate properties in the GAMA group catalogue (Robotham et al., 2011). Since the underlying dark matter properties have been explored and characterised (Chapter 6), the ability to link galaxy properties to the underlying dark matter can be tested using haloes in the lightcone mocks.
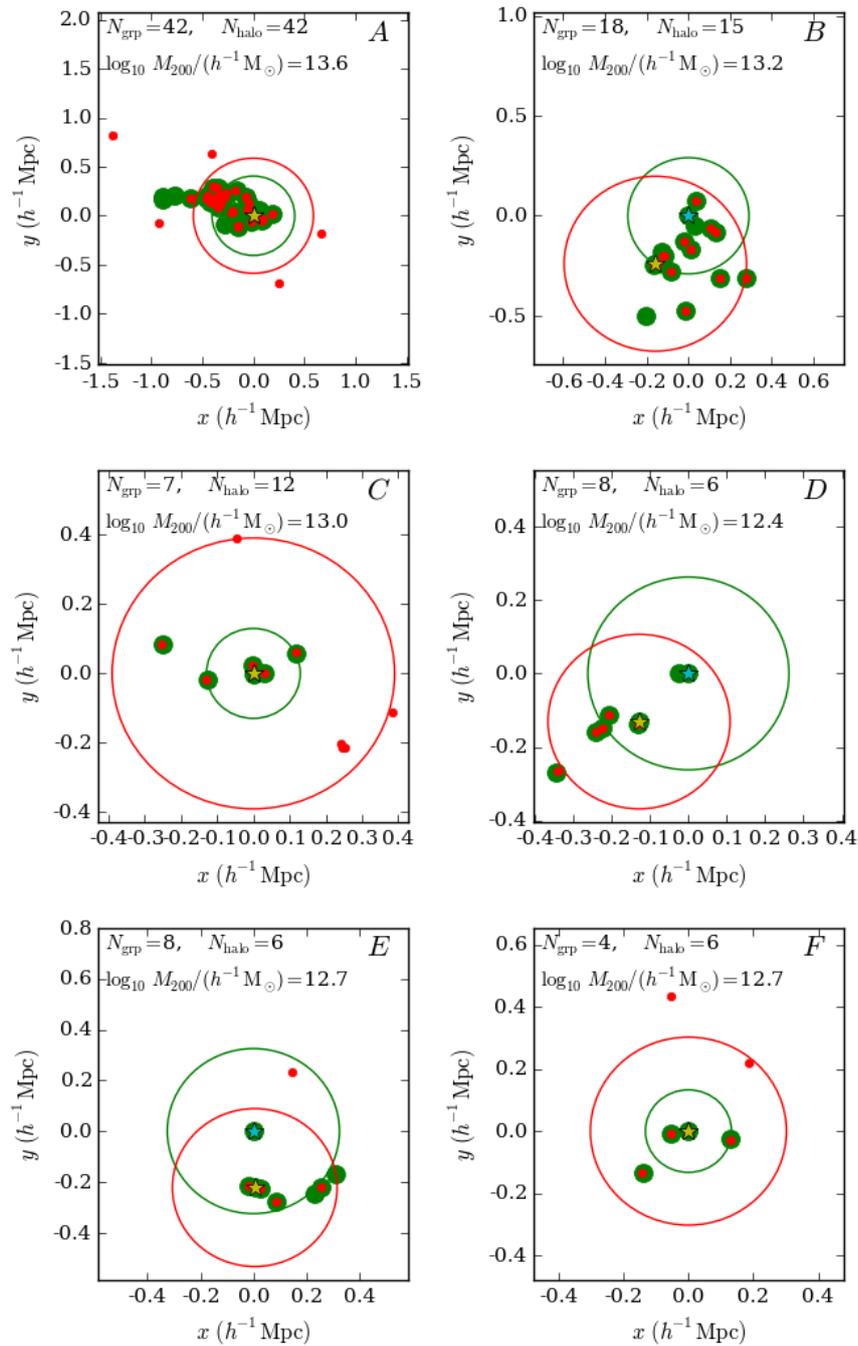
Figure 7.6: Examples of galaxies in groups (green dots) and their bijectively matched halo counterparts (red dots). The cyan stars indicate the recovered central galaxy in each group, while the yellow stars indicate the true central galaxy in the halo (as defined by GALFORM). For groups A, C and F the central galaxies of the group and halo are the same and the group and halo are both bijectively and centrally matched. The red circle indicates the extent of the dark matter halo, defined as $R_{200,c}$ (centred on the halo centre), and the green circle indicates r_{68}, defined by the 68th percentile radius of galaxies in the group.

Radius

An estimate of the radius can be derived from the 50th or 68th percentile radius from the group centre as traced by galaxies, r_{50} or r_{68} respectively, or simply the furthest galaxy from the centre, r_{100}. To avoid effects of peculiar velocities, the positions of galaxies are taken to be projected on the sky. r_{50} and r_{68}, as with the dark matter particles, are likely to reflect the concentration of the group, describing how galaxies are distributed, while r_{100} simply describes the extent of the galaxies in the group. However, these estimates are sensitive to recovery of the group centre and to interlopers.

An alternative measure of group size is to use a convex hull. The convex hull of a set of points describes the minimum area enclosing all points on a projected 2D plane, or the volume enclosing the points in three dimensions. By assuming a hull shape, most ideally a sphere or circle, group radius estimates $r_{\text{Hull,3D}}$ and $r_{\text{Hull,proj}}$ are calculated from the hull volume and projected area. Convex hull properties do not require the definition of group centre, but use the edgemost particles in a group. The convex hull properties are likely to be dominated by interlopers if a group contains a large number of interlopers near the edge. 3D hull properties such as volume require the use of the line of sight positions of galaxies, and so we only consider the radius determined by the projected on-sky area, $r_{\text{Hull,proj}}$.

Luminosity

The total luminosity of a group is found to be a very good indicator of halo mass (Eke et al., 2004; Yang et al., 2005; Robotham et al., 2011; Lu et al., 2015; Han et al., 2015).

The observed group luminosity can be determined simply by summing the luminosities, L_i, of all galaxies, i, in a group:

$$L_{\text{obs}} = \sum_{i=1}^{N_{gal}} L_i. \tag{7.2}$$

However, due to the apparent magnitude limit of the survey, the total luminosity, L_{obs} is not comparable for groups at different redshift without a correction. To

account for the varying limit in absolute magnitude, a faint luminosity cut can be imposed on groups such that the luminosity density of the sample is complete for all redshifts. At $z = 0.2$ the faintest absolute magnitude observed is $M_r - 5\log_{10} h = -20.0$, which is very close to the knee of the luminosity function. Imposing a faint luminosity limit therefore means sacrificing a large fraction of galaxies, particularly at lower redshifts. Alternatively, the galaxy luminosity function (Fig. 3.6) can be used to estimate the fraction of galaxies fainter than the observable luminosity of the group. This method involves correcting a group for the range of luminosities which are undetected, assuming the shape of the LF (most importantly the faint end) is consistent for all galaxy populations in any environment. This assumption is found to be valid for the faint end of the LF for all but void regions, which are not probed here (see Chapter 4).

The total group luminosity, L_{grp}, is corrected for the missing luminosity density as:

$$L_{\mathrm{grp}} = B\, L_{\mathrm{obs}} \frac{\int_{L_{min}}^{L_{max}} L\,\phi(L)\,dL}{\int_{L_f}^{L_{max}} L\,\phi(L)\,dL}. \tag{7.3}$$

Since there is large uncertainty on the luminosity function for magnitudes fainter than $M_r - 5\log_{10} h = -14.0$, this value is taken to be the lowest absolute magnitude considered, M_{min}, corresponding to Luminosity cut of L_{min}. The bright limit L_{max} corresponds to $M_r - 5\log_{10} h = -30.0$, chosen to be brighter than any observed galaxy, and L_f is the faintest luminosity that can be observed at the redshift of the galaxy. $\phi(L)$ gives the number density of galaxies of luminosity L, and $L\,\phi(L)$ gives the corresponding luminosity density. The scaling factor, $B = 1.04$, is tuned by Robotham et al. (2011) to account for variations in the luminosity function (e.g. with environment) and the effect of interlopers, and has little effect on the total group luminosity.

Velocity Dispersion

The dynamics of particles give a good indication of halo mass for a virialised halo. The line of sight peculiar velocities of galaxies relative to the mean line of sight velocity of the group are used to determine the velocity dispersion, σ_g, which is measured

simply as the dispersion on the mean, or using the gapper method, described in §6.7 of Chapter 6. Although there is little difference between these two methods when considering dark matter particles, the gapper method (equation 6.18) is generally adopted to measure the velocity dispersion in galaxy groups (e.g. Robotham et al., 2011; Eke et al., 2004), since it is less sensitive to interlopers and more robust for low number statistics.

Mass

Having determined the observable properties of galaxy groups, estimates of the halo mass can be inferred from these observable properties.

For a virialised group the mass is related to the velocity dispersion, σ_g, of particles in the system and a measure of the radius, R, in equation 6.15. The measure of radius is chosen to be indicative of the underlying $R_{200,c}$ of the halo, and the velocity dispersion is measured using the gapper method. The dynamical mass, M_{dyn} is then simply:

$$M_{\mathrm{dyn}} = A_D \, \frac{\sigma_g^2 R}{G}, \tag{7.4}$$

where A_D is a scaling factor to account for factors such as the scaling of R to $R_{200,c}$, and the velocity dispersion and density profiles, reproducing a median unbiased estimate of the halo mass. The preliminary value for this scaling factor is $A = 10$, as determined by Robotham et al. (2011) when adopting a radius proxy of r_{50}.

An alternative proxy for halo mass is to use the total luminosity, L_{grp}, of the system, since total galaxy luminosity of a group is tightly correlated with the halo mass (e.g. Fig. 3 of Han et al. 2015 and Fig. 13 of Viola et al. 2015). This approach does not require the system to be virialised and only requires an adequate estimate of the luminosity function to correct for the unobserved group luminosity.

The luminosity mass, M_{lum}, is given by Han et al. (2015) as:

$$M_{\mathrm{lum}} = M_0 \left(\frac{L_{\mathrm{grp}}}{L_0} \right)^{\alpha}. \tag{7.5}$$

The constants M_0 and α are calibrated using the halo mass in GAMA groups as measured by the weak lensing of galaxies in KiDS (Viola et al., 2015). The cal-

ibration gives $M_0/(10^{14}h^{-1}M_\odot) = 0.95 \pm 0.14$ and $\alpha = 1.16 \pm 0.13$, with a pivot luminosity scale defined as $L_0 = 10^{11.5}L_\odot\,h^{-2}$.

Having determined a halo mass, for example M_{lum}, indicative of the halo mass $M_{200,\mathrm{c}}$, an estimate of halo radius can be inferred. The radius of the dark matter halo, $R_{200,\mathrm{c}}$ is directly linked to $M_{200,\mathrm{c}}$ through equation. 6.1, given the critical density of the Universe at the redshift of the halo. Therefore assuming M_{lum} is a good indication of the dark matter halo mass, the size of the dark matter halo can be inferred using:

$$R_{\mathrm{lum}} = \left(\frac{M_{\mathrm{lum}}}{\frac{4}{3}\pi\, 200\, \rho_{\mathrm{crit}}(z)} \right)^{1/3}. \tag{7.6}$$

7.4   Halo and Group Property Comparisons

To estimate the projected galaxy density profile in groups, groups must be stacked by mass and the density profile measured with respect to a scale radius. Ideally the choice of group mass and radius should be indicative of the underlying dark matter halo, and so the choice of estimators must provide good approximations to the halo properties, $R_{200,\mathrm{c}}$ and $M_{200,\mathrm{c}}$ in the lightcones.

7.4.1   Radius

Ideally the chosen estimate of the group radius should give an approximation to the halo radius, $R_{200,\mathrm{c}}$, which is unbiased with mass, and with little scatter.

To assess how well each of the radius estimates recover the radius of the dark matter halo $R_{200,\mathrm{c}}$, Fig. 7.7 shows how the estimate of radius, r, plotted as a fraction of $R_{200,\mathrm{c}}$, varies with the underlying halo mass, $M_{200,\mathrm{c}}$ (left panel), and the inferred halo mass, chosen as M_{lum} (right panel). While $R_{200,\mathrm{c}}$ and $M_{200,\mathrm{c}}$ are known for haloes, for each group the values of $R_{200,\mathrm{c}}$ and $M_{200,\mathrm{c}}$ used for comparison are those of the bijectively matched halo. For this reason only groups which are bijectively matched are included.

The values of r_{50} and r_{68} are affected by how centrally concentrated galaxies are in the group, as is seen for groups B and C in Fig. 7.6, particularly affecting
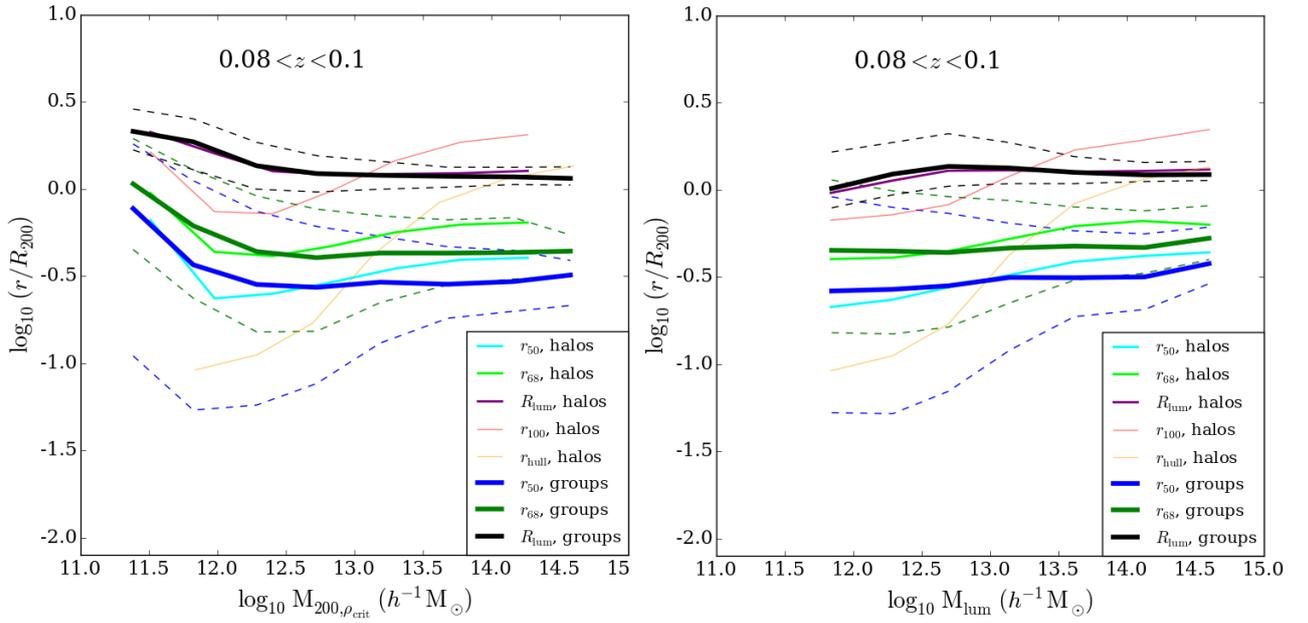
Figure 7.7: The ratio of radius estimates, r_{50}, r_{68}, r_{100}, r_{Hull}, and R_{lum} to halo radius, $R_{200,\mathrm{c}}$, as a function of halo mass, $M_{200,\mathrm{c}}$ (*left*) or inferred mass, M_{lum} (*right*), for a small redshift range as labelled. Estimates are shown for true haloes, and bijectively matched groups (see key), where $R_{200,\mathrm{c}}$ is that of the bijectively matched halo. r_{100} and r_{Hull} show a clear bias with halo mass and are only shown for haloes. The 10th and 90th percentiles are shown by dashed lines for r_{50}, r_{68} and R_{lum} for group estimates.

groups with low multiplicities. r_{100} is entirely driven by the position of the galaxy that is the furthest from the group centre, and is therefore highly undesirable when considering Dhaloes. If a galaxy is considered to belong to a Dhalo, but at a later time ends up at a large distance from the halo (see §3.2.1), the value of r_{100} will be a severe overestimate of the halo radius. $r_{\mathrm{Hull,proj}}$ is also affected by outliers, since the minimum area enclosing all galaxies in the group will include any galaxies well outside $R_{200,\mathrm{c}}$. The group finder is unlikely to group these escaped galaxies, but r_{100} and $r_{\mathrm{Hull,proj}}$ are still sensitive to interlopers in the outskirts of the group.

Clearly $r_{100}/R_{200,\mathrm{c}}$ and $r_{\mathrm{Hull,proj}}/R_{200,\mathrm{c}}$ vary significantly with halo mass. $r_{50}/R_{200,\mathrm{c}}$ and $r_{68}/R_{200,\mathrm{c}}$ are roughly constant with $M_{200,\mathrm{c}}$, with similar scatter, providing good approximations to the extent of the underlying dark matter halo. Comparing the estimates of radius in bijectively matched groups does not introduce any additional mass bias or scatter.

A luminosity inferred radius, R_{lum}, defined using equation 7.6, is also considered as a proxy for $R_{200,\mathrm{c}}$. $R_{\mathrm{lum}}/R_{200,\mathrm{c}}$ is included in Fig. 7.7 and is close to unity for all but the lowest mass haloes, with scatter indicating 80% of groups have an inferred radius in the range $1 < R_{\mathrm{lum}}/R_{200,\mathrm{c}} < 1.6$ at $M_{200,\mathrm{c}} = 10^{13}h^{-1}\mathrm{M}_{\odot}$. While the scatter on r_{68} is similar, $0.2 < r_{68}/R_{200,\mathrm{c}} < 0.8$, R_{lum} has the advantage that it does not depend on the specific spatial information of galaxies within groups.

7.4.2   Total group and halo luminosity

The calculation of group or halo luminosity, L_{grp}, is straightforward, given an estimate of the galaxy LF. Fig. 7.8 shows that for a given luminosity, 80% of groups and haloes vary from the median halo mass by less than half an order of magnitude for the most luminous haloes, without considering any redshift dependence. Fig. 7.3 shows that haloes with low luminosity are those with a low multiplicity, and for higher redshifts the correction for the undetected luminosity is larger. The effect of multiplicity on the luminosity of the system could be further tested by varying the apparent magnitude limit in the mocks. The luminosity inferred by galaxies in bijectively matched groups follows the same trend with halo mass as is seen for the luminosity inferred by galaxies in haloes, with only small differences seen for the
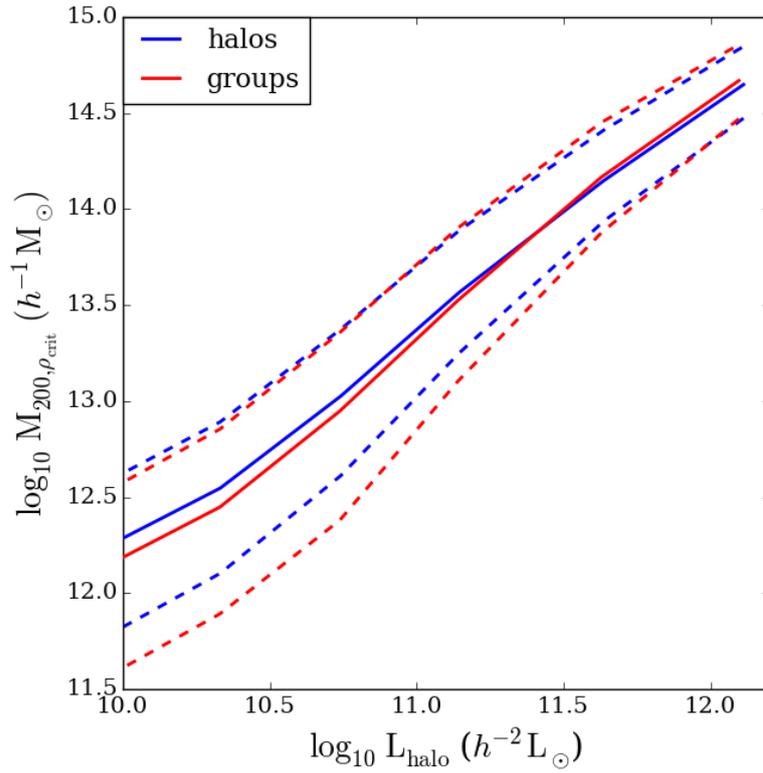
Figure 7.8: Median (solid lines) and 10th and 90th percentile (dashed lines) halo mass, $M_{200,\text{c}}$, as a function of group luminosity, L_{group} (red) or halo luminosity L_{halo} (blue), in the redshift range $0.0 < z < 0.3$. Only bijectively matched groups are included, where $M_{200,\text{c}}$ is that of the bijective halo counterpart. There is a clear correlation between group and halo luminosity and the underlying halo mass.

faintest luminosities.

7.4.3 Mass

The methods for calibrating the underlying dark matter mass in groups using galaxy dynamics, $M_{\rm dyn}$, and luminosities, $M_{\rm lum}$, are given in Robotham et al. (2011) and Viola et al. (2015) respectively. The upper panels in Fig. 7.9 show how well the true halo mass, $M_{200,\rm c}$, is recovered for haloes in the lightcones using the two mass estimates, while the lower panels show the equivalent for bijectively matched groups, where the group mass estimates are compared to $M_{200,\rm c}$ of the bijectively matched halo.

In agreement with the results of Han et al. (2015), who compared $M_{\rm dyn}$ to the Dhalo mass, $M_{\rm Dhalo}$, the mass recovered with $M_{\rm dyn}$ is found to be biased, significantly overestimating $M_{200,\rm c}$ for low masses, while underestimating for high masses. $M_{\rm lum}$ recovers $M_{200,\rm c}$ much more accurately, with no obvious bias. The scatter indicates the true $M_{200,\rm c}$ deviates from the inferred $M_{\rm lum}$ by a factor of <3, decreasing to <0.25 for haloes with $M_{\rm lum} > 10^{14} h^{-1} {\rm M}_\odot$.

The masses estimated using galaxies in groups do not display any additional bias or significant increase in the scatter on the recovered $M_{200,\rm c}$. $M_{\rm lum}$ therefore provides a reliable, unbiased estimate of the underlying dark matter halo mass, with 80% of groups inferring a halo mass which deviates from the true halo mass by a factor of <5 for $M_{\rm lum} = 10^{13} h^{-1} {\rm M}_\odot$.

There is an increase in the median and scatter in $\log_{10}(M_{200,\rm c}/M_{\rm lum})$ for the lowest mass groups and haloes, which have the lowest multiplicities. The total luminosity of these groups is not probed well by the detectable galaxies, causing the observed increase in scatter. Similarly at higher redshifts ($0.2 < z < 0.3$), groups less massive than $M_{\rm lum} = 10^{13} h^{-1} {\rm M}_\odot$ cannot be observed (see Fig. 7.3), and so due to the imposed selection function, using $M_{\rm lum}$ as a proxy for halo mass imposes a lower luminosity-inferred mass limit for a given redshift.
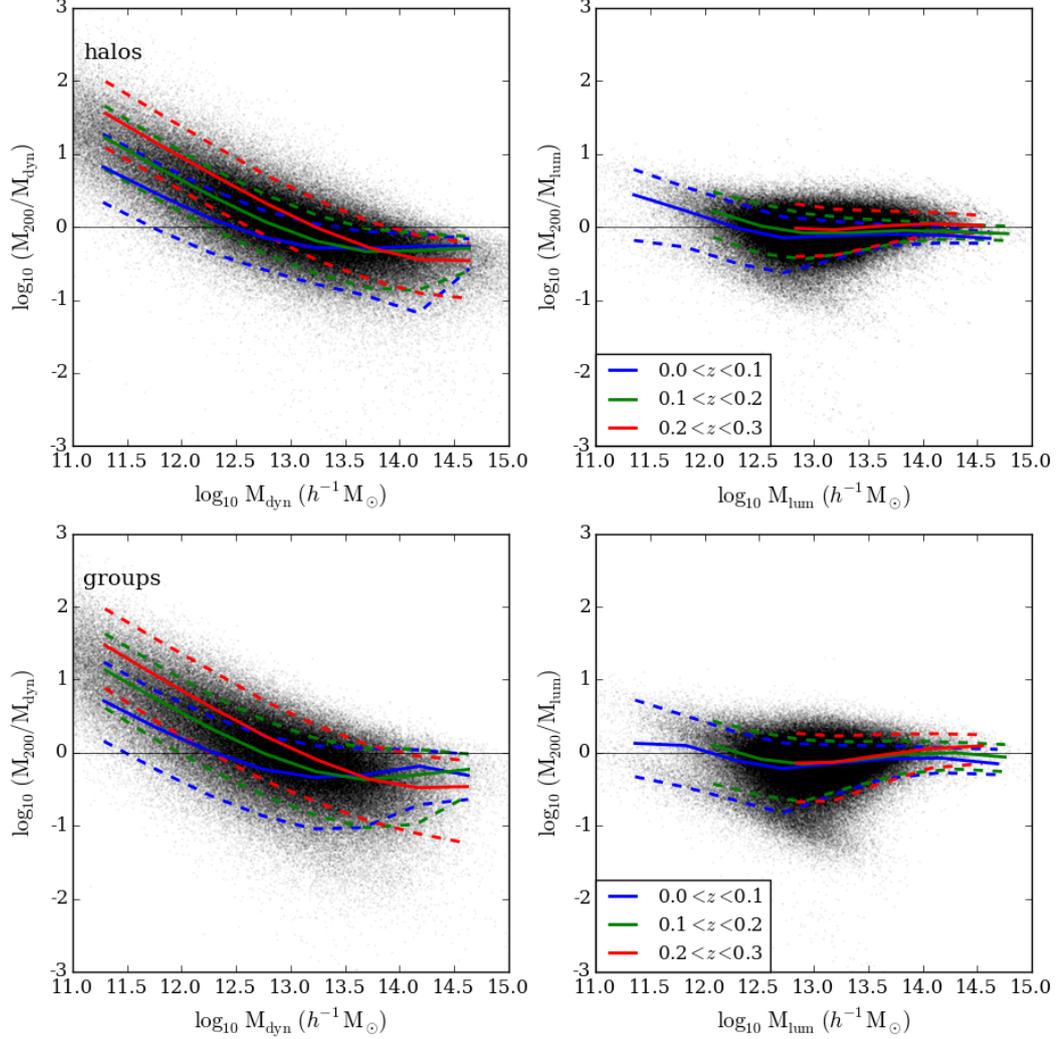
Figure 7.9: The ratio of true halo mass, $M_{200,c}$, to the mass inferred from galaxy dynamics, M_{dyn} (*left*, equation 7.4), and group luminosity, M_{lum} (*right*, equation 7.5), as a function of the inferred mass. *Upper panels*: Inferred mass determined using galaxies in haloes. *Bottom panels*: Inferred mass determined by galaxies in groups, where for each group, the $M_{200,c}$ used for comparison is that of the bijectively matched halo. Medians (solid lines) and 10th and 90th percentiles (dashed lines) are shown for different redshift ranges (see key).

7.4.4   Velocity Dispersion

The distribution of line-of-sight peculiar velocities of galaxies in groups with respect to the mean velocity of the group provides a measure of the velocity dispersion of the group, σ_{gal}. The velocity dispersion of dark matter particles, σ_{DM}, within haloes is discussed in §6.7, where dark matter particles are found to deviate from the velocity dispersion expected in a virialised system. By comparing the velocity dispersion of galaxies in haloes to that of the dark matter, a velocity bias can be determined for haloes in the lightcone.

Galaxy velocity bias in the lightcones can be found by directly comparing σ_{gal} to σ_{DM} in haloes, as is shown by the green line in Fig. 7.10. Since σ_{gal} is measured in one dimension (line-of-sight), for comparison σ_{DM} is taken to be one-dimensional. The median ratio of $\sigma_{\mathrm{gal}}/\sigma_{\mathrm{DM}}$ is between 0.8 and 0.9 for all halo masses, but the scatter is large. The velocity dispersion of galaxies in low mass groups (blue) increases with respect to the σ_{DM} of bijectively matched haloes. This could be an effect of high velocity interlopers in the group. The velocity dispersion of GAMA groups is included for comparison by the red line, where the corresponding comparative value for σ_{DM} is the median, 10th and 90th percentile dark matter velocity dispersion for each $M_{\mathrm{200,c}}$ bin (Fig. 6.13), inferred by M_{lum}. While the lightcone groups included in Fig. 7.10 are only those which are bijectively matched, all GAMA groups are included. There is very good agreement between the velocity bias found for groups in GAMA and groups in the lightcone mocks. In GALFORM, galaxies are placed at the centre of their subhalo, or attached to the previous most bound particle if the subhalo is unresolved (see Chapter 3). The galaxy bias observed is most likely due to the selection of dark matter particles (through the requirement that they must host a galaxy) which causes them to be biased tracers. In reality galaxies are likely to not have the dark matter velocity dispersion due to processes such as dynamical friction and ram-pressure stripping within the dark matter halo.
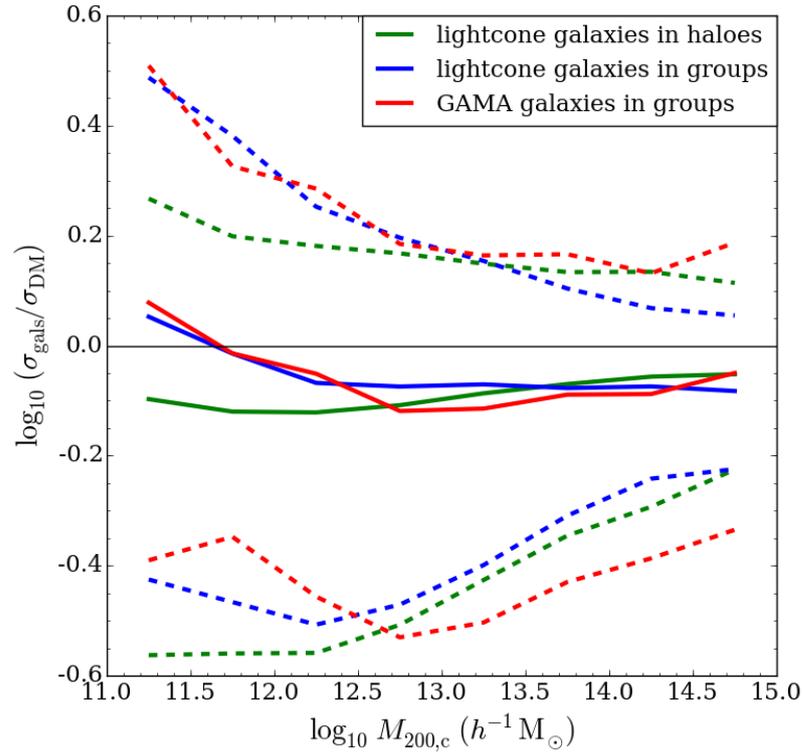
Figure 7.10: Velocity bias in haloes (green) and bijectively matched groups (blue) in the GAMA lightcones, and in groups in the GAMA survey (red). For haloes, $\sigma_{\mathrm{gal}}/\sigma_{\mathrm{DM}}$ is calculated directly on a halo by halo basis. For groups in the lightcones, $M_{\mathrm{200,c}}$ and σ_{DM} are from the bijective counterpart haloes. For groups in GAMA, $M_{\mathrm{200,c}}$ is approximated by M_{lum}, and method for estimating the ratio $\sigma_{\mathrm{gal}}/\sigma_{\mathrm{DM}}$ is described in the text.

7.5   Galaxy Density Profile in Groups

The measurement of dark matter density profiles for haloes in the mocks is relatively straightforward, due to the large number of particles in a halo, and a defined halo radius allows the typical shape of the profile to be well characterised by, for example, an NFW profile (see §6.4). However, there are significantly fewer galaxies in a halo than there are dark matter particles, and measuring the galaxy profile for individual haloes is not feasible. Haloes must therefore be stacked according to some property, and groups must be stacked according to a property inferring that of the halo. The stacking also requires haloes and groups to be scaled using a similar radius definition.

To correctly interpret the density profile of galaxies in GAMA, it is important to know how each of these factors affect the measured density profile using haloes and groups in the mocks.

7.5.1   The 3D Galaxy Density Profile of Lightcone Haloes

Halo mass is an intrinsic property of dark matter haloes and has been shown to be well traced by galaxy properties such as luminosity. Within a narrow redshift range (to minimise the effect of the survey selection criteria), haloes are stacked according to their halo mass, $M_{200,c}$. The shape of the dark matter density profile is seen to vary with both mass and redshift (§6.5), and haloes are stacked in mass bins that are sufficiently small that the dark matter density profile does not exhibit a large variation in shape within them. The variation in the multiplicity of haloes with redshift due to the selection criteria of the survey is likely to have an effect on the shape of the density profile and so haloes are stacked in mass within very narrow redshift bins ($\Delta z = 0.02$).

Within each mass bin of width $\Delta \log_{10} M_{200,c}/(h^{-1}\mathrm{M_\odot}) = 0.5$, the variation in halo radius is $\sim 50\%$. To measure the shape of the profile over a comparable scale for all stacked haloes, the density profile is measured in bins of $r/R_{200,c}$.

Given a mass range and redshift range, the method for measuring the stacked galaxy density profile is similar to the measurement of the dark matter density profile (§6.4.1). Radial shells are chosen such that there are 20 shells evenly spaced

in $\log_{10}(r/R_{200,c})$ in the range $-2.5 < \log_{10}(r/R_{200,c}) < 0$. Radial bins are measured out to r_{max}, the largest radius traced by galaxies in the stacked haloes. The number of radial bins therefore depends on the extent of galaxies beyond $R_{200,c}$ ($\sim 20\%$ of galaxies are found outside $R_{200,c}$). The radial profile of each halo is normalised to $R_{200,c}$ to enable the comparsion of different sized haloes within each mass bin. The effective density profile, $n(x)$ in each radial bin, $x = r/R_{200,c}$, is calculated by summing over the galaxies in each shell in the range $x_{min} < x < x_{max}$.

$$n(x) = \frac{1}{N_h} \frac{N_{gal}(x_{min} < x < x_{max})}{\frac{4}{3}\pi(x_{max}^3 - x_{min}^3)}, \qquad (7.7)$$

and describes the mean number of galaxies per halo within a shell of $r/R_{200,c}$, weighted by the volume of the shell. The number of stacked haloes contributing to the mass and redshift bin is given by N_h.

An NFW profile (equation 6.2) is fit to the density profile using a simple χ^2 fit, assuming independent Poisson errors for each bin in $n(x)$. The NFW profile is normalised using the number of galaxies within $R_{200,c}$. The only free parameter is the concentration, c_{gal}, which is fit over the range $0.1 < r/R_{200,c} < 1$, as in §6.4.1. The lower limit of $r/R_{200,c} > 0.1$ allows for the same fractional volume to be used in the fit, and was chosen to ensure that the dark matter density profiles are insensitive to the resolution limit of the simulation affecting the inner radius in the smaller haloes. Although the process of stacking haloes by mass allows the inner regions of the density profile to be measured down to $\sim 15\,h^{-1}$kpc (the softening length in the simulation is $5\,h^{-1}$kpc), the range $0.1 < r/R_{200,c} < 1$ is adopted such that the recovered concentration can be compared to that of the underlying dark matter halo.

The 3D stacked galaxy density profiles averaged over all haloes with $N_{halo} \geq 2$ in the 26 lightcone mocks are shown in Fig. 7.11, for 3 halo mass ranges and 3 narrow redshift bins.

The stacked galaxy density profiles tend to roughly follow the shape expected from an NFW profile, such that the density is higher towards the inner regions of the halo. There is a clear dip in the density profile at $\log_{10}(r/R_{200,c}) \sim -0.3$. This is due to the different radial distributions of galaxies for which the subhalo is resolved in the simulation (causing a bump at $r/R_{200,c} \sim 0.5$), and where the galaxy's subhalo is
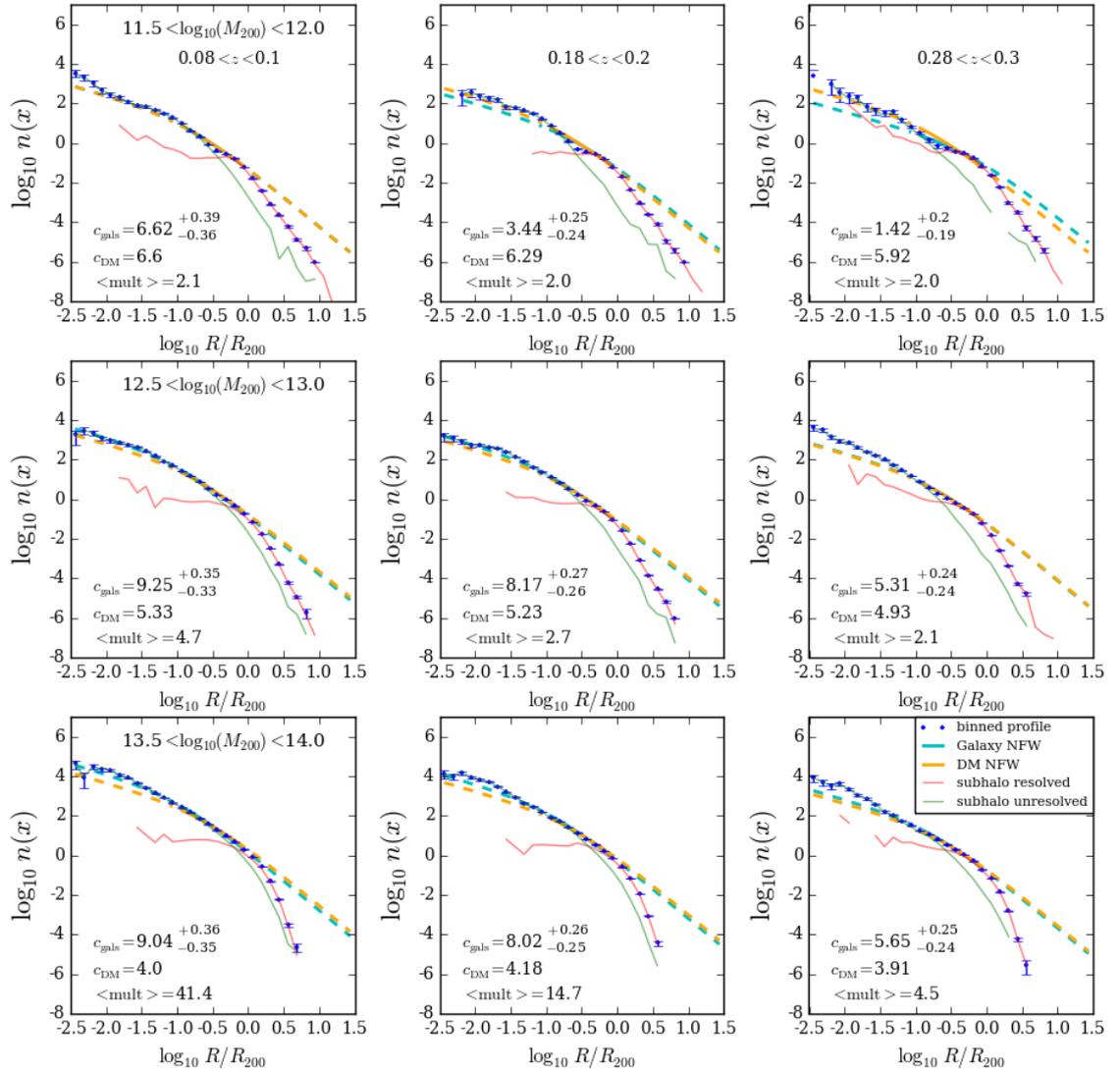
Figure 7.11: Stacked galaxy density profiles for haloes in the lightcone (see equation 7.7). The blue points and Poisson errorbars give the stacked galaxy density profile, $n(x)$. The best fitting NFW profile is shown by the cyan curve, for which concentration is indicated by c_{gals}. Dashed lines indicate the radial range which is not included when fitting an NFW profile. The NFW profile described by the median dark matter concentration, c_{DM}, in each mass and redshift bin is shown by the orange curve. Visually, the shape of the galaxy density profile is in remarkable agreement with the shape of the dark matter density profile. The red (green) curves show the contributions of galaxies with (without) resolved subhaloes in the simulation, creating the bump at $\log_{10}(r/R_{200,c}) \sim -0.3$. The mean number of galaxies per halo is indicated by $\langle \mathrm{mult} \rangle$ in each panel.

too close to the dense centre of the halo, and can no longer be resolved at very small $r/R_{200,c}$. This bimodality is also seen in Fig. 7.4. The contribution of galaxies with (red) and without (green) resolved subhaloes is shown in each panel of Fig. 7.11. The effect is greater for low multiplicity systems, such that for the lowest redshifts only the lowest mass bins ($11.5 < \log_{10} M_{200,c}/(h^{-1}\mathrm{M}_\odot) < 12.0$) are affected, while the effect remains prominent for higher masses at higher redshifts. This bimodality is purely an artifact of the treatment of galaxies in subhaloes in the simulations.

The normalisation of the density profile is affected by the selection function of GAMA. At higher redshifts, the number of galaxies in a halo of the same mass decreases (see Fig. 7.3). The effect is to lower the density profile at higher redshifts, but the shape of the profile does not change. This normalisation could be corrected to take into account the number of galaxies unobserved at a given redshift due to the selection effects of the survey.

The best fitting NFW profile is shown by the cyan line, and slightly underpredicts the density profile in the inner regions of haloes, which are not used in the fit (indicated by the dashed cyan line), and does not describe the outer regions well, $r/R_{200,c} > 1$, where the galaxy density profile drops off significantly. The range considered when fitting an NFW profile is affected by the previously discussed bump, which significantly alters the galaxy density profile around $\log_{10} r/R_{200,c} = -0.5$, where the shape is not described well by an NFW profile. Therefore the recovered galaxy concentration is not expected to be indicative of the underlying dark matter concentration. The NFW profile for median concentration of the dark matter haloes is shown by the orange curve for each mass bin and redshift. While the shape of the dark matter density profile visually appears to be consistent with the galaxy density profile over the scales shown, there is significant variation between the recovered concentrations, c_{gals} and c_{DM}.

7.5.2 The Projected Galaxy Density Profile of Lightcone Haloes

While real space spatial information for galaxies is readily available in the lightcones, the line-of-sight positions for galaxies in GAMA are significantly affected by redshift

space distortions. To avoid the effects of redshift space distortions, the projected surface density profile, $\Sigma(x)$ (which is unaffected by redshift space distortions), averaged over all stacked haloes, N_{h}, is measured as:

$$\Sigma(x) = \frac{1}{N_{\mathrm{h}}} \frac{N_{\mathrm{gal}}(x_{\mathrm{min}} < x < x_{\mathrm{max}})}{\pi(x_{\mathrm{max}}^2 - x_{\mathrm{min}}^2)}, \tag{7.8}$$

in annuli of $x = r_{\mathrm{p}}/R_{200,\mathrm{c}}$, where r_{p} is the projected radius.

Since there is a large uncertainty in the inferred properties of haloes with $N_{\mathrm{halo}} = 2$, the sample of haloes is restricted to those with $N_{\mathrm{halo}} \geq 3$. The projected density profiles of haloes in the 26 lightcones is shown in Fig. 7.12. The combined effects of projecting galaxies onto 2 dimensions and not including haloes with $N_{\mathrm{halo}} = 2$ lessens the amplitude of the bump seen in Fig. 7.11.

The projected density profile within an annulus of width $\mathrm{d}x$ depends on the number density of galaxies along the line of sight. For line of sight separation, z, and a projected radius, r_{p}, the 3D distance from the centre of the halo is equal to $r = \sqrt{r_{\mathrm{p}}^2 + z^2}$ and the density at r is given by an NFW profile, $\rho_{\mathrm{NFW}}(r)$. The projected NFW profile is found by integrating along the line of sight:

$$\Sigma(r_{\mathrm{p}}) = 2 \int_{z=0}^{z=\infty} \rho_{\mathrm{NFW}}(\sqrt{r_{\mathrm{p}}^2 + z^2}) \, \mathrm{d}z, \tag{7.9}$$

to give equation A3 of Guo et al. (2012):

$$\Sigma(r_{\mathrm{p}}) = 2\rho_0 r_s \int_{r_{\mathrm{p}}}^{\infty} \frac{1}{\sqrt{r^2 - r_{\mathrm{p}}^2}(r/r_s)(1 + r/r_s)^2} \, \mathrm{d}r, \tag{7.10}$$

where ρ_0 is the scale density defining the normalisation of the profile, fixed by the total density of galaxies within $r/R_{200,\mathrm{c}} = 1$. An analytical solution is given by equations 7 and 8 of Bartelmann (1996):

$$\Sigma(y) = \frac{2\rho_0 r_s}{y^2 - 1} g(y) \tag{7.11}$$

for $y = r_{\mathrm{p}}/r_s$, and where $g(y)$ given by:
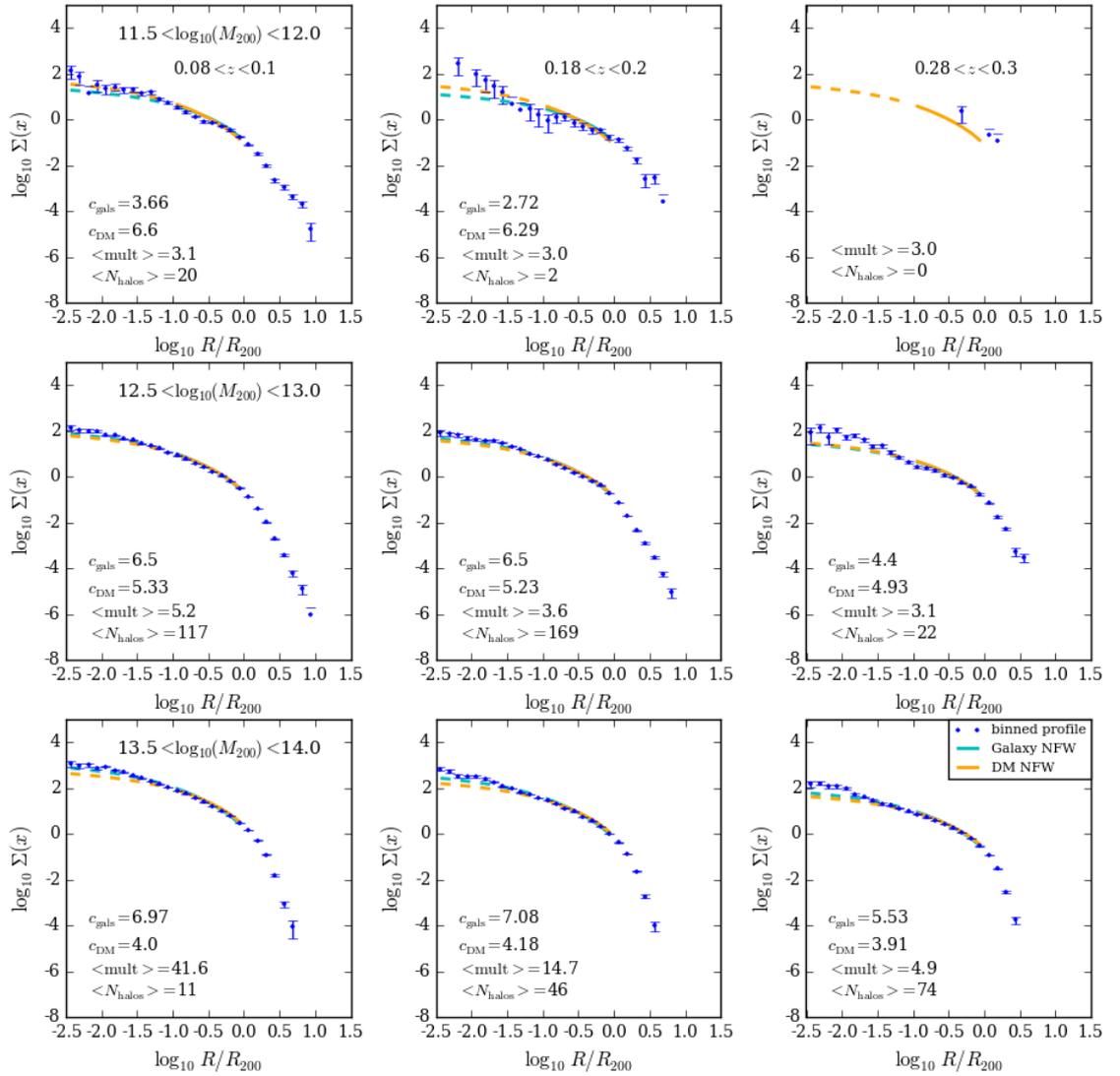
Figure 7.12: Same as Fig. 7.11 but the projected density profile of galaxies, $\Sigma(x)$ (equation 7.8), and only including haloes with more than 2 galaxy members. $<N_{\mathrm{halo}}>$ here indicates the mean number of haloes contributing to each mass and redshift bin.

$$g(y) = \begin{cases} 1 - \frac{2}{\sqrt{1-y^2}}\mathrm{arctanh}\sqrt{\frac{1-y}{1+y}}, & (y < 1) \\ 0, & (y = 1) \\ 1 - \frac{2}{\sqrt{y^2-1}}\arctan\sqrt{\frac{y-1}{y+1}}, & (y > 1). \end{cases} \tag{7.12}$$

Since the group galaxy density profile does not follow that expected for an NFW profile for radii larger than $R_{200,\mathrm{c}}$ (see Fig. 7.11), and instead the number of galaxies falls off sharply, the 3D projected NFW profile must be truncated to take this into account. The choice of truncation radius, $R_{\mathrm{trunc}} = f_{\mathrm{trunc}}R_{200,\mathrm{c}}$, must be within the region still following an NFW profile, but not too low that galaxies with $r > R_{200,\mathrm{c}}$, which significantly contribute to the inner regions of the projected density profile, are unaccounted for. We find $f_{\mathrm{trunc}} = 1.4$ gives a value for R_{trunc} indicative of the maximum 3D radius out to which galaxies still follow an NFW profile.

The projected NFW profile for $x = r_{\mathrm{p}}/R_{200,\mathrm{c}}$ is then given by:

$$\Sigma(x) = \frac{2\rho_0 r_s}{(cx)^2 - 1}g(cx) - \frac{2\rho_0 r_s}{(cf_{\mathrm{trunc}})^2 - 1}g(cf_{\mathrm{trunc}}). \tag{7.13}$$

The best fitting projected NFW profiles, stacked by $M_{200,\mathrm{c}}$ and scaled by $R_{200,\mathrm{c}}$, are again shown by cyan lines in Fig. 7.12. Due to the multiplicity cut of $N_{\mathrm{halo}} \geq 3$, the density profile for the lowest masses at $z = 0.3$ is not constrained. While the projected NFW profile fits the shape of the projected galaxy density profiles well, the innermost regions of haloes, with radii $r_{\mathrm{p}}/R_{200,\mathrm{c}} < 0.03$, and not considered in the fit, are underestimated by an NFW profile. Fitting a projected NFW profile appears to lower the recovered concentration for each stacked profile in comparison to the concentration recovered for the 3D profiles. This is likely to be an effect of smoothing the bump at $r/R_{200,\mathrm{c}} = 0.5$.

Fig. 7.13 compares the stacked galaxy density profiles in haloes over various mass ranges for a given redshift bin, and shows how the galaxy density profile in haloes differs from that expected from the measured concentration-mass relation of dark matter. For each mass and redshift bin, the NFW profile described by the median concentration c_{DM} of the dark matter provides a reference density profile, $\Sigma_{\mathrm{DM}}(x)$. The stacked galaxy density profiles are shown in the top panels, while
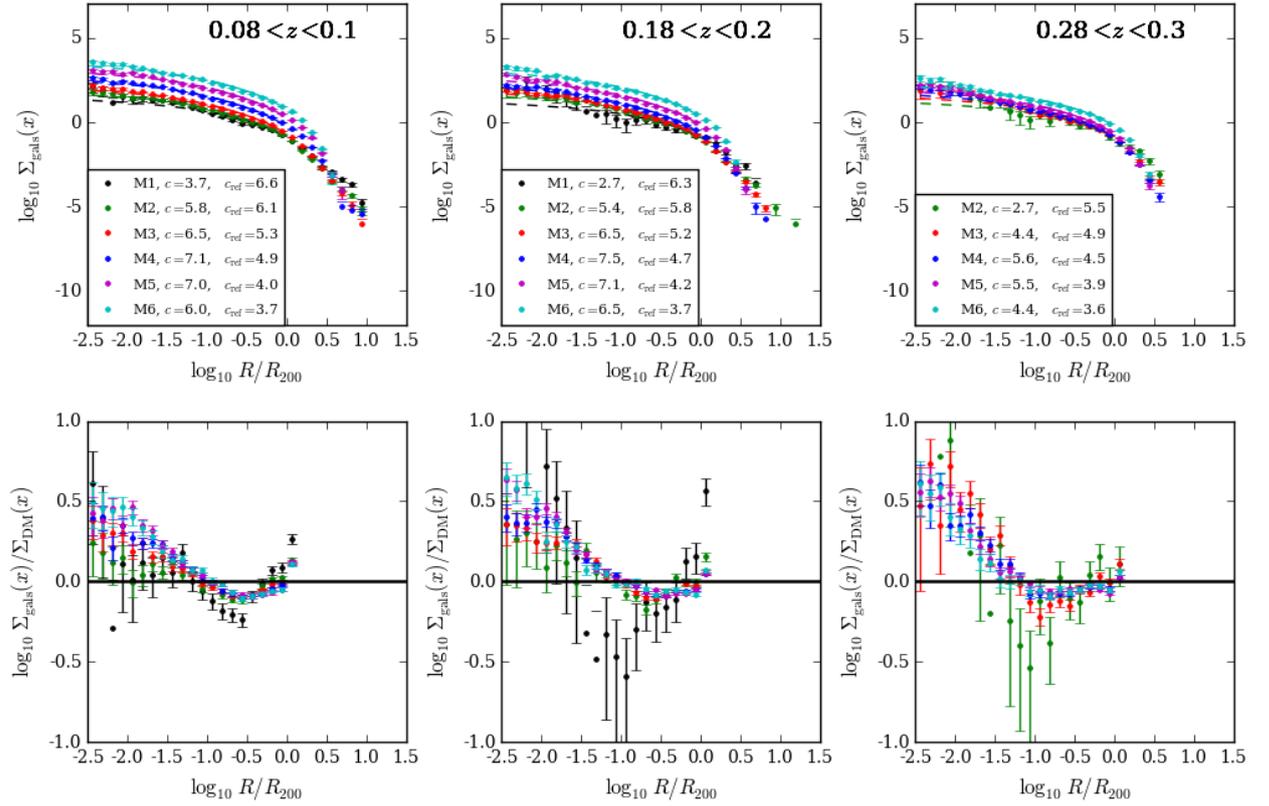
Figure 7.13: *Top*: Projected galaxy density profiles, $\Sigma_{\mathrm{gals}}(x)$, in haloes in the lightcones, for 3 different redshifts, coloured by group mass, $M_{200,\mathrm{c}}$ (M1 to M6, from $10^{11.5}h^{-1}\mathrm{M}_\odot$ to $10^{14}h^{-1}\mathrm{M}_\odot$). The radius is plotted relative to $R_{200,\mathrm{c}}$. *Bottom*: Ratio of the projected galaxy density profile in haloes, $\Sigma_{\mathrm{gals}}(x)$, to the projected NFW profile described by the median concentration of dark matter, $\Sigma_{\mathrm{DM}}(x)$, in the mass and redshift bin. The galaxy density profile in the haloes is steeper than the dark matter density profile for $r_{\mathrm{p}}/R_{200,\mathrm{c}}<0.3$.

the ratio of each profile to the reference dark matter density profile is shown in the bottom panels. For all but the lowest multiplicity systems (least massive bins in each panel), the galaxy density profile is always higher than the dark matter density profile for the inner regions of the halo ($r_{\rm p}/R_{200,\rm c}$<0.1). However, these radii are not considered in the fitting procedure. The normalisation of the profile increases with mass, simply because of the increase in multiplicity with mass. The normalisation at higher redshifts is lower due to the imposed selection effects (Fig. 7.3). The change in normalisation has no effect on the shape of the profile.

7.5.3 Inferring Group Properties

In the lightcones the underlying dark matter halo properties, $R_{200,\rm c}$ and $M_{200,\rm c}$, are well determined. However, in a galaxy survey these halo properties can only be inferred from the visible component of haloes, as traced by galaxy groups. The projected galaxy density profiles are stacked by halo mass and are characterised in terms of a halo radius. It is therefore important to assess the impact that inferring these halo properties has on the shape of stacked galaxy density profiles.

Stacking by Group Mass

Luminosity provides a well constrained proxy for halo mass, $M_{\rm lum}$. For each halo the luminosity, $L_{\rm grp}$, is estimated via equation 7.3 and an inferred halo mass, $M_{\rm lum}$, is found with equation 7.5. Haloes are then stacked by $M_{\rm lum}$ rather than $M_{200,\rm c}$.

Stacking haloes by $M_{\rm lum}$ rather than $M_{200,\rm c}$ has no significant effect on the projected galaxy density profile, since the scatter between the two masses is sufficiently small within a given mass bin.

Scaling by Group Radius

For the purposes of this analysis, the group radius inferred from $R_{\rm lum}$ gives a reasonable indication of the halo radius, $R_{200,\rm c}$, and is adopted to scale the projected density profiles. To account for any residual bias in $R_{\rm lum}/R_{200,\rm c}$ for a given mass (Fig. 7.7), group radii are scaled to account for the median $R_{\rm lum}/R_{200,\rm c}$ in the mass
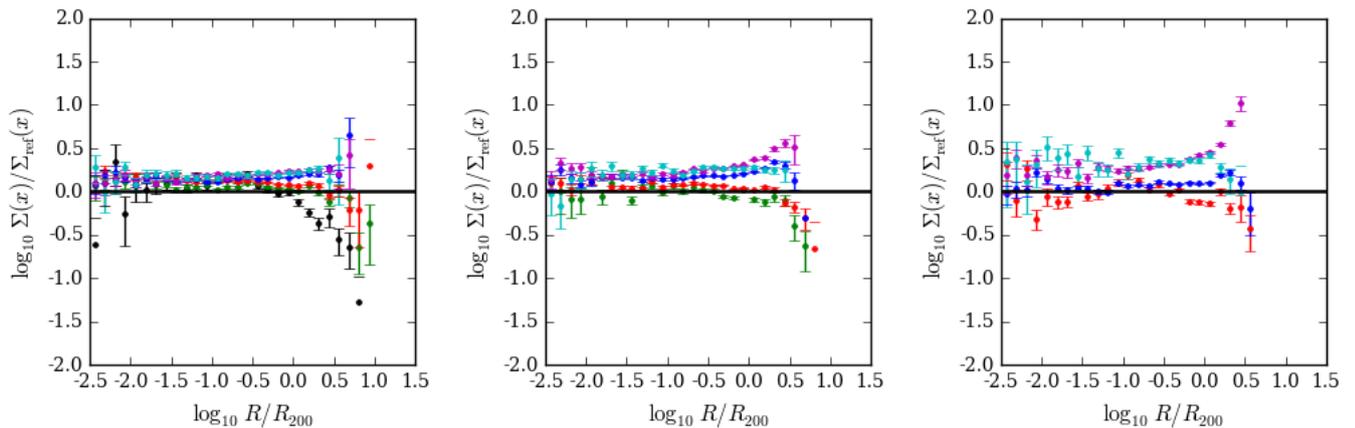
Figure 7.14: The ratio of the projected galaxy density profiles, $\Sigma(x)$, as stacked by M_{lum} and scaled to R_{lum}, to the projected galaxy density profiles, $\Sigma_{\mathrm{ref}}(x)$ (as previously shown as $\Sigma_{\mathrm{gal}}(x)$ in Fig. 7.13), stacked by $M_{200,\mathrm{c}}$ and scaled to $R_{200,\mathrm{c}}$, for galaxies in haloes in the lightcones, in 3 different redshift ranges (see Fig. 7.13) and coloured by mass, $M_{200,\mathrm{c}}$ (see caption of Fig. 7.13).

bin. Since any mass dependence is accounted for to provide a median unbiased relation between R_{lum} and $R_{200,\mathrm{c}}$, and the scatter on $R_{\mathrm{lum}}/R_{200,\mathrm{c}}$ is generally small for all mass bins, using R_{lum} as a proxy for $R_{200,\mathrm{c}}$ has very little impact on the shape of the stacked density profile for $R_{\mathrm{lum}}/R_{200,\mathrm{c}} < 1$.

The combined effects that stacking on M_{lum} and scaling to R_{lum} have on the shape of the projected galaxy density profile of haloes in the lightcone can be seen in Fig. 7.14. No clear variation in the shape of the density profile is seen within $R_{200,\mathrm{c}}$ between that stacked and scaled by inferred properties and by the true halo properties, other than a change in the offset (which increases with redshift). Outside of $R_{200,\mathrm{c}}$ the density profile appears slightly higher than is seen when stacking by $M_{200,\mathrm{c}}$ and scaling to $R_{200,\mathrm{c}}$, for the highest masses, but decreases at the lowest masses.

7.5.4   Projected Galaxy Density Profile of Groups in GAMA

Having measured the projected galaxy density profile for haloes in the mocks, and understood the effects of inferring a scaling radius and stacking mass, the projected

galaxy density profiles of groups in GAMA can be measured.

The projected galaxy density profiles for groups in GAMA, stacked by luminosity mass, M_{lum}, and split into three redshift bins, are shown in the top panels of Fig. 7.15. Only groups with a multiplicity $N_{\mathrm{FoF}} \geq 3$ are included. Groups with $N_{\mathrm{FoF}} = 2$ are generally least well matched to haloes in the lightcone, and so it is likely that excluding them significantly reduces the number of artificially linked groups. When restricting the sample to only haloes with $N_{\mathrm{FoF}} > 2$, a significant change in the shape of the galaxy density profile is seen. The projected galaxy radius, r_{p} is given with respect to the luminosity inferred radius, R_{lum}.

To enlarge the volume and increase the signal to noise in each stacked density profile, the width of each redshift range is increased to $\Delta z = 0.05$. Even with a larger volume, the least massive groups contain few members and few are observed at redshifts $z \sim 0.3$. While the small volume at low redshifts is not sufficiently large to constrain the density profile of the most massive groups, these are easily measured for $0.15 < z < 0.2$.

A slight increase is seen in the galaxy density profile towards smaller radii from $r_{\mathrm{p}}/R_{\mathrm{lum}} \sim 0.03$, which is most visible in the most massive haloes. The origin of this increase is unclear. However, other than the normalisation (which is due to variation in the typical number of galaxies per halo with mass) there is no obvious change in shape of the galaxy density profile with mass for a given redshift bin. The density profile falls off sharply at radii larger than $r_{\mathrm{p}}/R_{\mathrm{lum}}=1$, for all mass bins and redshifts considered.

To directly compare the galaxy density profile in groups found in GAMA to those found in the lightcone, the middle panels of Fig. 7.15 give the ratio of the projected galaxy density profile of groups in GAMA (given in the top panels), to that of groups in the lightcones. The shape of the density profile for GAMA groups is significantly shallower than the density profile in the lightcones at radii $r_{\mathrm{p}}/R_{\mathrm{lum}}<0.3$, and the decline in the number of galaxies at radii larger than this is significantly more drastic.

The ratios of the projected galaxy number density profile in GAMA groups to the expected dark matter density profile, given the median of the dark matter
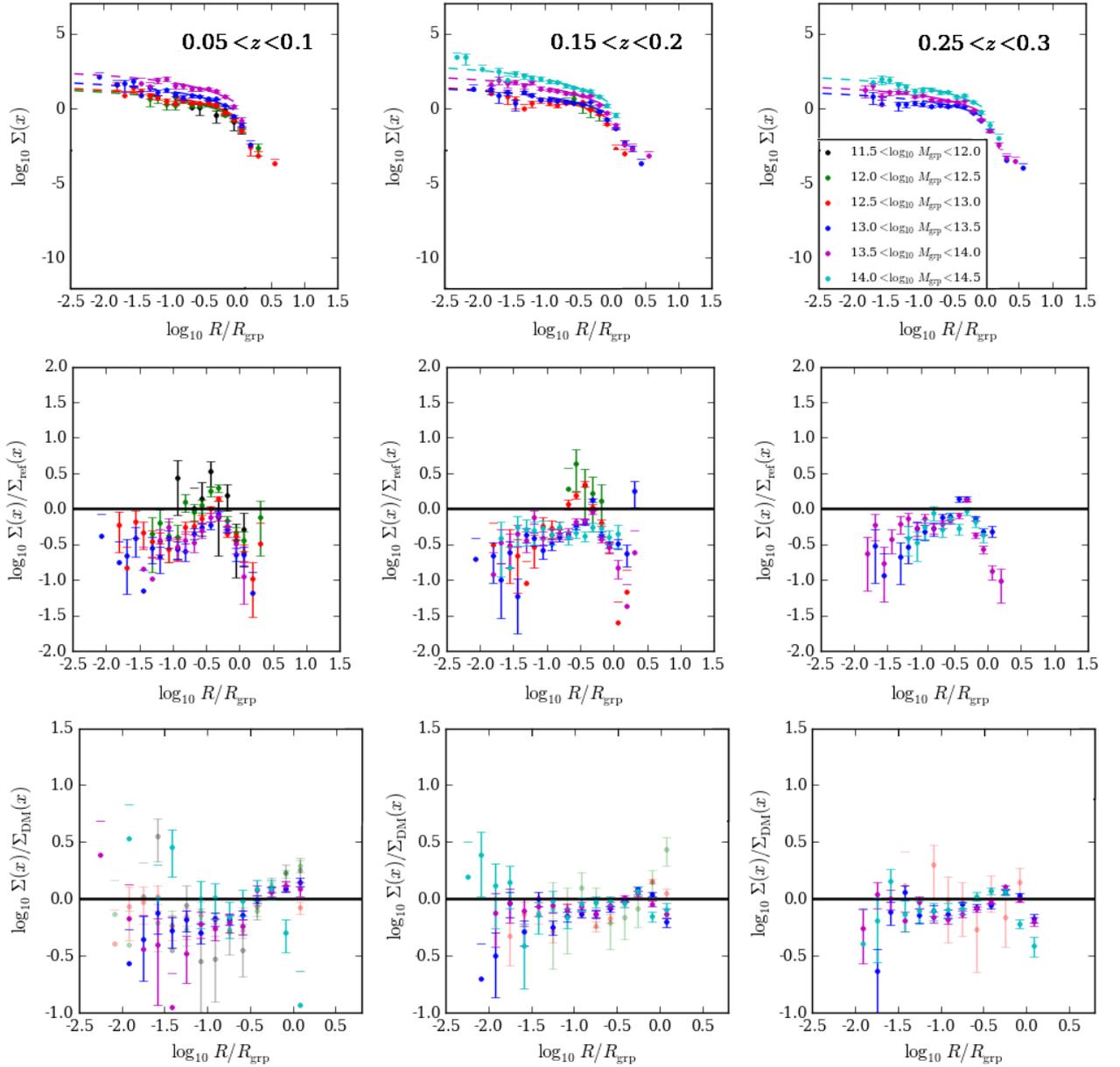
Figure 7.15: *Top*: Projected galaxy density profile for galaxies in GAMA groups, $\Sigma(x)$, for three different redshifts, coloured by mass, M_{lum} (see key). Poisson errors are shown, and the dashed lines show the best fitting NFW profile to each density profile. *Middle*: The ratio of the projected density profile for galaxies in GAMA groups, $\Sigma(x)$, to the density profile for galaxies in groups in the lightcone mocks, $\Sigma_{\mathrm{ref}}(x)$. *Bottom*: The ratio of the GAMA galaxy density profile to the expected dark matter density profile, $\Sigma_{\mathrm{DM}}(x)$, in each mass and redshift bin. The lower mass bins are given a high transparency, to allow the shape of higher mass density profiles to be more clearly visible.

halo concentrations in the halo lightcones, within a given mass and redshift bin, are shown in the bottom panels of Fig. 7.15. There is little detectable difference between the GAMA galaxy and lightcone dark matter density profiles, suggesting that the shape of the galaxy density profile in GAMA groups is broadly consistent with an NFW profile. The predicted dark matter concentrations are derived from all haloes in the halo lightcone mocks, and therefore do not exhibit any selection criteria other than the requirement they host a galaxy in GALFORM. A consistent galaxy and dark matter density profile suggests that if the distribution of dark matter in the simulation is indicative of that in the real Universe, galaxies within groups are generally unbiased tracers of their underlying dark matter environment.

7.6 Discussion and Conclusion

The shape of the galaxy density profile has been previously explored for satellite galaxies around isolated primaries and in galaxy groups in the 2dFGRS and SDSS (e.g. Diaz et al., 2005; Guo et al., 2012). The GAMA survey provides a highly complete galaxy sample down to fainter magnitudes than before, while covering a large enough volume to investigate the properties of galaxy groups. In addition, the GAMA lightcone mocks allow comparisons of the measured galaxy density profile to theoretical predictions from galaxy formation models implemented on dark matter simulations. The availability of such lightcone mock catalogues, and their properties as measured in Chapter 6, allow studies of the limitations involved when using galaxies to infer the properties of the underlying dark matter haloes.

A brief summary of the work presented in this chapter is given here.

- We use the GAMA group finding algorithm (Robotham et al., 2011) to extract galaxy groups from the GAMA lightcone mocks and the GAMA survey. Group properties are defined, such as group centre, radius, luminosity, mass and velocity dispersion of galaxies, and the ability and limitations of these properties to infer the underlying dark matter halo properties are explored. A luminosity inferred mass, M_{lum}, and a radius defined using this mass, R_{lum}, prove to be the most indicative of the underlying halo properties, $M_{\mathrm{200,c}}$ and

$R_{200,c}$ respectively.

- The galaxy density profile provides a measure of how galaxies trace their underlying haloes. To measure the galaxy density profile, haloes are stacked by mass to overcome the low number statistics due to the typically low number of detectable galaxies per halo. The galaxy density profile for galaxies in haloes in the lightcone mocks is measured by stacking haloes according to $M_{200,c}$, and scaling to $R_{200,c}$. While an NFW profile is a good fit to the galaxy density profiles in higher mass bins, there are two distinct peaks in the shape of the profiles when stacking haloes with low multiplicities. The origin of this bimodaility is found to be due to the different treatment of galaxies which have a resolved subhalo in the simulations, and galaxies for which the host subhalo has become unresolved when passing through a region of high density in a larger halo. However, it is unclear how the two different radial distributions come about, and further studies into the treatment of galaxy mergers in GALFORM are required to investigate this.

- Specific spatial information along the line of sight within groups is unavailable in galaxy surveys due to redshift space distortions, and instead the projected galaxy density profile is measured. The projected galaxy density profile of galaxies in haloes in GAMA lightcones is compared to the projected NFW profile of all dark matter haloes, determined by the mean dark matter concentration for a given mass and redshift bin (§6.5). The galaxy density profile in the lightcones is found to be steeper than the dark matter density profile for radii $r_{\mathrm{p}}/R_{200,c}{<}0.3$.

- To convert from halo properties to properties inferred by galaxies in groups, the effect of stacking on M_{lum} rather than $M_{200,c}$, and scaling by R_{lum} rather than $R_{200,c}$, on the resulting shape of the profile is investigated. Very little effect on the shape of the profile is found, indicating that the scatter on $M_{\mathrm{lum}}/M_{200,c}$ and $R_{\mathrm{lum}}/R_{200,c}$ has little influence on the galaxy density profile.

- Finally, the projected galaxy density profile for groups in the GAMA survey is measured and compared to the projected galaxy density profile of groups in

the lightcone mocks, and to the projected NFW profile corresponding to the median concentration of dark matter haloes in the simulations. The galaxy density profile in GAMA is much steeper than is measured for galaxies in groups in the lightcones, but consistent with the shape of the NFW profile determined by the dark matter density profile.

When investigating the galaxy density profiles of galaxy groups in SDSS and 2dFGRS, Diaz et al. (2005) suggest that a cored, King (King, 1962) profile provides a better description of the inner shape of the profile than an NFW profile. The galaxy group density profiles in GAMA presented here are not particularly well constrained in the innermost regions (and not included when fitting an NFW profile), but appear to be generally consistent with an NFW profile. A statistical analysis of how well an NFW profile fits the observed galaxy density profile for different radial ranges within GAMA groups is needed to determine whether or not an NFW profile is an adequate description of how galaxies are distributed within groups in the real Universe, or if a King profile would be more appropriate. This would provide insight into where galaxies preferentially form within dark matter haloes.

The discrepancy between the density profile of galaxies in groups in the GAMA survey and in groups in the GAMA lightcone mocks is also apparent in the clustering signal of galaxies in GAMA, as measured by Farrow et al. (2015). They find the clustering signal in the Gonzalez-Perez et al. (2014) GALFORM model is higher on smaller scales than is seen in GAMA, which is consistent with the result that GAMA galaxies are less centrally concentrated than mock galaxies within galaxy groups.

Further analysis must be carried out on the studies presented in this chapter, such as considering how the linking of spurious groups impacts the shape of the galaxy density profile; applying a correction to the normalisation of groups at various redshifts to account for the impact the imposed survey selection function has on the typical number of galaxies per halo; and statistical assessments describing how well the NFW profile fits the observed galaxy density profile in GAMA and in the lightcone mocks, thereby providing values for concentration parameters of galaxy density profiles in groups.

With the GAMA lightcone mocks at hand, physical interpretations of trends in

the shape of the galaxy density profile with halo properties such as mass and the properties of galaxies within haloes can then be addressed. For example, Guo et al. (2012) find that the best fitting concentration to the projected galaxy density profile in SDSS depends not only on the colours of satellites but that the dependence on the colour of the central is stronger. The concentration of groups with a red, early type central is lower than that for a blue, late type central. Diaz et al. (2005) also find the fraction of early type galaxies increases towards the centre, for SDSS and 2dFGRS galaxies. By studying the galaxy density profiles for different galaxy populations, further constraints can be placed on how galaxies form within their dark matter environment.

Chapter 8

Conclusions

This thesis attempts to address questions about the influence environment has on the formation and evolution of galaxies, such as how galaxies properties are influenced by the environment in which they reside, whether or not the scale of the environment matters, and how the spatial distribution and properties of galaxies depend on their dark matter environment.

Observations from the GAMA survey, a multi-wavelength galaxy redshift survey, are analysed to address these questions. The GAMA survey provides a highly complete sample of galaxies over a large volume, covering a redshift range within which galaxy properties and their evolution can be studied.

In order to provide a theoretical interpretation of the scientific results obtained using GAMA observations, lightcone mock catalogues are used which imitate the selection effects and geometry of the GAMA survey. The lightcone mocks were constructed using the semi-analytical model of galaxy formation, GALFORM, implemented in the Millennium N-body dark matter simulation.

The environment in which galaxies reside can be characterised locally, for example using the galaxy overdensity measured in spheres or by constructing galaxy group catalogues which are theoretically motivated to be indicative of the underlying dark matter halo environment. Alternatively, a larger scale environment can be characterised using a geometric measure of structure within the cosmic web. By studying the spatial distribution of galaxies and their properties such as the luminosity function on environment, and comparing to the predictions of galaxy formation

models, a deeper understanding of the impact that environment has on the formation and evolution of galaxies can be gained, allowing future investigations of the physical processes which influence the dependencies.

8.1   Environmental dependence of galaxy properties

The dependence of the galaxy luminosity function on local overdensity, δ, is investigated in Chapter 4. Consistent with the results of previous galaxy surveys, the shape of the luminosity function is found to vary with environment for the range of overdensities probed, suggesting that there are more bright galaxies in denser regions than in voids. The variation of both the normalisation, ϕ^*, and the characteristic absolute magnitude, M^*, with overdensity, δ are found to be well described by simple relations. Using GAMA data, tighter constraints can be placed on the faint end slope, α, than has previously been possible. There is no measurable variation in the faint end slope with environment.

The clear difference in the shape of the luminosity function for red and blue galaxies confirms that red galaxies dominate overdense environments and are predominantly bright, while blue galaxies dominate underdense environments and are predominantly faint. These results are quantatively constrained here, by parameterising the environmental dependence of the luminosity function for red and blue galaxies.

While the galaxy luminosity function in the lightcone mock shows remarkably good agreement with the environmental trends seen in the GAMA survey, the GAL-FORM model predicts more bright blue galaxies in underdense environments, and more faint red galaxies in overdense environments than is observed. These discrepencies could possibly be explained by the treatment of AGN feedback in haloes, and the over efficiency of hot gas stripping in the model when a galaxy becomes a satellite of a larger halo.

The dependence of the luminosity function on environment is further investigated in Chapter 5, where a larger scale definition of environment is adopted, providing a characterisation of the structure of the cosmic web. The shape of the luminosity

function is inferred using the trends with overdensity and no further environmental dependence is found, suggesting that galaxy luminosity is influenced solely by local environment, and that the larger scale environment has little additional impact on galaxies luminosities.

8.2   Distribution of galaxies within the dark matter environment

Groups of galaxies in GAMA (Robotham et al., 2011) allow the distribution of dark matter haloes in the Universe to be mapped. To understand how the properties of galaxy groups relate to their underlying dark matter environment, it is important to first understand the properties of dark matter haloes in the lightcone mocks which are used to constrain the parameters of the group finder.

The pipeline for calculating halo properties, such as radius and mass estimates, the halo density profile, the circular velocity profile and velocity dispersion, is described in Chapter 6. For the GAMA lightcone mocks, the density profile of dark matter haloes closely follows an NFW profile, with a concentration-mass relation in good agreement with Klypin et al. (2014). The extrapolation from M_{200} to an alternative mass estimate, such as M_{500} (useful for studies of x-ray emission from hot gas in the centre of haloes), is shown to work particularly well assuming an NFW profile, estimating M_{500} to within 7% of the measured value.

Although results presented from this pipeline are specific to the GAMA lightcone mock catalogues used in this thesis, the pipeline can be used to determine the properties of haloes in any halo catalogue where the dark matter particle membership is known.

The galaxy density profile of groups in GAMA describes how galaxies are distributed within dark matter haloes in the Universe. Group luminosity is found to be a good indicator of the underlying halo mass (as estimated by M_{200}). Typically the number of satellite galaxies observed per halo is small, and so haloes are stacked by their luminosity inferred mass.

In the lightcone mock catalogues, the galaxy density profile in haloes appears to

be generally consistent with an NFW profile, although the galaxy density profile is more centrally concentrated than that of dark matter. The galaxy density profile of galaxy groups in GAMA is less centrally concentrated, suggesting the model predicts the clustering of galaxies inside haloes to be higher than is observed in galaxy groups. This agrees with the results found from the clustering studies of GAMA and the lightcone mocks by Farrow et al. (2015). Additionally, for a given mass bin at a fixed redshift, the shape of the galaxy density profile in GAMA groups is largely consistent with the shape of the dark matter density profile in haloes in the simulations, suggesting that galaxies are unbiased tracers of the distribution of dark matter in haloes.

8.3   Future work

The results outlined above provide motivation for further investigations of the role that environment plays on the physical processes which define the observed properties of galaxies. In particular the following studies naturally lead on from those presented in this thesis.

- An overabundance of faint red galaxies in overdense regions is predicted by the models, as was seen in Chapter 4. A prescription for the treatment of the hot gas in satellites falling into haloes is discussed in Font et al. (2008). Rather than instantly losing their hot gas halo on infall, quenching star formation, a model for ram pressure stripping allows satellites to retain some of their hot gas, depending on a satellite's orbit and the ram pressure it encounters. This process allows the fuelling further star formaton, thus reducing the number of red satellite galaxies. Implementing this prescription in the GALFORM model may account for the discrepency seen in the faint end of the red luminosity function in clusters.

- Clear trends between the r-band luminosity function and local environment are shown in Chapter 4. Performing the same analysis for different photometric bands provides insight into how the luminosity function for different galaxy

populations depends on environment. For example galaxies with strong ultra-violet emission are likely to be young, star forming galaxies, whereas K-band luminosity traces galaxies containing old stars and is a good indicator of stellar mass (Drory et al., 2004). Such an investigation can be done by utilising the multi-wavelength aspect of the GAMA survey. The GALFORM model also predicts luminosities in a range of photometric bands, allowing comparisons to theoretical predictions for various galaxy populations.

Likewise, while the galaxy r-band luminosity function is shown to be independent of the environment within the cosmic web, as investigated in Chapter 5, it is unclear whether or not the cosmic web has any influence on a more fundamental galaxy property such as the stellar mass, which depends on the star formation history and stellar metalicity of a galaxy. In addition to measuring the K-band luminosity function (indicating stellar mass) dependence on local and large-scale environment, stellar mass estimates for GAMA galaxies (Taylor et al., 2011) can be utilised to measure the local and large-scale environmental dependence of the stellar mass function.

- Further analysis of the galaxy density profile measured for groups in the GAMA survey in order to allow a theoretical interpretation to be made. In particular, in order to measure any evolution in density profile, the selection function which causes the typical number of galaxies residing a group to vary with redshift must be taken into account. Groups in the observable Universe are dominated by low multiplicity systems. The group finder calibrated by Robotham et al. (2011) artificially links together unrelated galaxies. It is important to take into account the impact that these spurious groups have on the shape of the measured galaxy density profile when interpreting any trends seen in the shape. These further constraints on the shape of the galaxy density profile are required to test whether it is well described by an NFW profile or if another functional form would be more appropriate.

- Once the shape of the galaxy density profile has been well constrained and parameterised, the variation in the shape with various halo properties, such as

halo mass and the evolution with redshift, can be investigated. Previous studies suggest that the shape of the profile around isolated primaries is dependent on the properties of the central galaxy such as luminosity (e.g. Prada et al., 2003) and colour (e.g. Guo et al., 2012). Such dependencies could be measured for the galaxy density profiles in groups in both the GAMA survey and in the lightcones to find out which physical processes influence the distribution of galaxies in haloes or if the galaxy density profile is entirely driven by the mass of the host dark matter halo.

Upcoming galaxy reshift surveys will provide a significantly larger volume than the GAMA survey, and in some cases probing much fainter magnitudes. For example the DESI BGS will sample a volume ~50 times larger than GAMA, while probing down to a similar magnitude limit to GAMA. 4MOST WAVES-Wide will observe an area ~5 times larger than GAMA but probing down to much fainter magnitudes, allowing more thorough studies of galaxy groups, while constraining the evolution of these groups will be possible using 4MOST WAVES-Deep. With these numerous spectroscopic surveys providing the tools to tackle new investigations, the future is bright for studies of galaxy formation.

Bibliography

Abazajian K. N. et al., 2009, ApJS, 182, 543

Abell G. O., 1958, Astrophys. J. Supplement Series, 3, 211

Alonso D., Eardley E., Peacock J. a., 2015, MNRAS, 13, 13

Alpaslan M. et al., 2015, MNRAS, 451, 3249

Alpaslan M. et al., 2014, MNRAS, 438, 177

Arnett W. D., 1969, Astrophys. Space Sci., 5, 180

Baldry I. K. et al., 2014, MNRAS, 441, 2440

Baldry I. K., Balogh M. L., Bower R. G., Glazebrook K., Nichol R. C., Bamford S. P., Budavari
    T., 2006, MNRAS, 373, 469

Baldry I. K. et al., 2012, MNRAS, 421, 621

Baldry I. K. et al., 2010, MNRAS, 404, 86

Bamford S. P. et al., 2009, MNRAS, 393, 1324

Bartelmann M., 1996, A&A, 313, 697

Beers T. C., Flynn K., Gebhardt K., 1990, Astron. J., 100, 32

Behroozi P. S., Wechsler R. H., Wu H.-Y., 2012, Astrophys. J., 762, 109

Benson A. J., 2012, New Astronomy, 17, 175

Benson A. J., Bower R. G., Frenk C. S., Lacey C. G., Baugh C. M., Cole S., 2003a, ApJ, 599, 38

Benson A. J., Frenk C. S., Baugh C. M., Cole S., Lacey C. G., 2003b, MNRAS, 343, 679

Benson A. J., Hoyle F., Torres F., Vogeley M. S., 2003c, MNRAS, 340, 160

Berlind A. a., Weinberg D. H., 2002, The Astrophysical Journal, 575, 587

Blanton M. R., Berlind A. A., 2007, ApJ, 664, 791

Blanton M. R. et al., 2003a, AJ, 125, 2348

Blanton M. R. et al., 2003b, ApJ, 592, 819

Blanton M. R., Roweis S., 2007, AJ, 133, 734

Blanton M. R. et al., 2005, Astron. J., 129, 2562

Bosma A., 1981, AJ, 86, 1825

Bower R. G., Benson a. J., Malbon R., Helly J. C., Frenk C. S., Baugh C. M., Cole S., Lacey
    C. G., 2006, MNRAS, 370, 645

Boylan-Kolchin M., Springel V., White S. D. M., Jenkins A., Lemson G., 2009, MNRAS, 398, 1150

Bromley B. C., Press W. H., Lin H., Kirshner R. P., 1998, ApJ, 505, 25

Brough S. et al., 2013, MNRAS, 435, 2903

Bryan G. L., Norman M. L., 1998, Astrophys. J., 495, 80

Bullock J. S., Kolatt T. S., Sigad Y., Somerville R. S., Kravtsov a. V., Klypin a. a., Primack J. R.,
    Dekel a., 2001, MNRAS, 321, 559

Cautun M., Weygaert R. V. D., Jones B. J. T., 2013, MNRAS, 429, 1286

Cluver M. E. et al., 2014, ApJ, 782, 90

Cole S., 2011, MNRAS, 416, 739

Cole S., Lacey C., 1996, MNRAS, 281, 716

Cole S., Lacey C., Baugh C., Frenk C., 2000, MNRAS, 319, 168

Colless M. et al., 2001, MNRAS, 328, 1039

Colless M. et al., 2003, preprint arXiv:astro-ph/0306581

Croton D. J. et al., 2005, MNRAS, 356, 1155

Croton D. J. et al., 2006, MNRAS, 365, 11

Dalton G. B., Efstathiou G., Maddox S. J., Sutherland W. J., 1992, ApJL, 390, L1

Davis M., Efstathiou G., Frenk C. S., White S. D. M., 1985, Astrophys. J., 292, 371

Davis M., Huchra J., 1982, ApJ, 254, 437

De Lucia G., Weinmann S., Poggianti B. M., Aragón-Salamanca A., Zaritsky D., 2012, MNRAS, 423, 1277

De Propris R. et al., 2003, MNRAS, 342, 725

De Propris R., Phillipps S., Bremer M. N., 2013, MNRAS, 434, 3469

Diaz E., Zandivarez A., Merchan M., Muriel H., 2005, Astrophys. J., 629, 158

Dressler A., 1980, ApJ, 236, 351

Driver S. P., 2015, ArXiv e-prints

Driver S. P., Davies L. J., Meyer M., Power C., Robotham A. S. G., Baldry I. K., Liske J., Norberg P., 2015, ArXiv e-prints

Driver S. P., Fernández-Soto A., Couch W. J., Odewahn S. C., Windhorst R. A., Phillipps S., Lanzetta K., Yahil A., 1998, ApJL, 496, L93

Driver S. P. et al., 2011, MNRAS, 413, 971

Drory N., Bender R., Feulner G., Hopp U., Maraston C., Snigula J., Hill G. J., 2004, ApJ, 608, 742

Duffy A. R., Schaye J., Kay S. T., Dalla Vecchia C., 2008, MNRAS, 390, L64

Eales S., 1993, ApJ, 404, 51

Eales S. et al., 2010, PASP, 122, 499

Eardley E. et al., 2015, MNRAS, 448, 3665

Efstathiou G., Ellis R. S., Peterson B. a., 1988, MNRAS, 232, 431

Efstathiou G., Fall S. M., 1984, MNRAS, 206, 453

Einasto M., Suhhonenko I., Hein P., 2005, Astronomy & Astrophysics, 436, 17

Eke V. R. et al., 2004, MNRAS, 348, 866

Ettori S., Donnarumma A., Pointecouteau E., Reiprich T. H., Giodini S., Lovisari L., Schmidt R. W., 2013, Mass profiles of galaxy clusters from X-ray analysis

Falco E. E. et al., 1999, PASP, 111, 438

Farrow D. J. et al., 2015, ArXiv e-prints

Ferguson H. C., Dickinson M., Williams R., 2000, ARA&A, 38, 667

Font A. S. et al., 2008, MNRAS, 389, 1619

Gerke B. F. et al., 2012, ApJ, 751, 50

Gillis B. R. et al., 2013, MNRAS, 431, 1439

Gonzalez-Perez V., Lacey C. G., Campbell D. J. R., Mitchell P. D., Baugh C. M., Lagos C. D. P.,
    Helly J., 2014, MNRAS, 439, 264

Gunawardhana M. L. P. et al., 2013, MNRAS, 433, 2764

Guo Q., Cole S., Eke V., Frenk C., 2012, MNRAS, 427, 428

Guo Q., White S., Angulo R. E., Henriques B., Lemson G., Boylan-Kolchin M., Thomas P., Short
    C., 2013, MNRAS, 428, 1351

Hahn O., Porciani C., Carollo C. M., Dekel A., 2007, MNRAS, 375, 489

Hamilton A. J. S., 1988, ApJ, 331, L59

Han J. et al., 2015, MNRAS, 446, 1356

Han J., Jing Y. P., Wang H., Wang W., 2012, MNRAS, 427, 2437

Hill D. T. et al., 2011, MNRAS, 412, 765

Hogg D. W., Baldry I. K., Blanton M. R., Eisenstein D. J., 2002, ArXiv Astrophysics e-prints, 1

Hopkins A. M. et al., 2013, MNRAS, 430, 2047

Hopkins a. M., McClure-Griffiths N. M., Gaensler B. M., 2008, Astrophys. J., 682, L13

Hoyle F., Rojas R. R., Vogeley M. S., Brinkmann J., 2005, ApJ, 620, 618

Hubble E., 1929, Proceedings of the National Academy of Sciences of the United States of America,
    15, 168

Huchra J., Davis M., Latham D., Tonry J., 1983, ApJS, 52, 89

Huchra J. P., Geller M. J., 1982, ApJ, 257, 423

Hütsi G., Einasto J., Tucker D. L., Saar E., Einasto M., Müller V., Heinämäki P., Allam S. S., 2002, preprint arXiv:astro-ph/0212327

Jiang L., Helly J. C., Cole S., Frenk C. S., 2014, MNRAS, 440, 2115

Kennicutt, R. C. J., 1983, Astrophys. J., 272, 54

Kimm T. et al., 2009, MNRAS, 394, 1131

King I., 1962, AJ, 67, 471

Klypin A., Yepes G., Gottlober S., Prada F., Hess S., 2014, ArXiv Astrophysics e-prints, 17, 1

Knebe A. et al., 2011, MNRAS, 415, 2293

Knobel C. et al., 2012, ApJ, 753, 121

Knollmann S. R., Knebe A., 2009, Astrophys. J. Supplement Series, 182, 608

Lagos C. P., Bayet E., Baugh C. M., Lacey C. G., Tom A., Fanidakis N., Geach J. E., 2012, MNRAS, 426, 2142

Laureijs R. et al., 2011, ArXiv e-prints

Lawrence A. et al., 2007, MNRAS, 379, 1599

Levi M. et al., 2013, ArXiv e-prints

Lilly S. J. et al., 2009, ApJS, 184, 218

Lilly S. J., Le Fevre O., Crampton D., Hammer F., Tresse L., 1995, ApJ, 455, 50

Lilly S. J. et al., 2007, ApJS, 172, 70

Lin H., Kirshner R. P., Shectman S. A., Landy S. D., Oemler A., Tucker D. L., Schechter P. L., 1996, ApJ, 464, 60

Lin H., Yee H. K. C., Carlberg R. G., Morris S. L., Sawicki M., Patton D. R., Wirth G., Shepherd C. W., 1999, ApJ, 518, 533

Liske J. et al., 2015, MNRAS, 452, 2087

Loveday J. et al., 2015, MNRAS, 451, 1540

Loveday J. et al., 2012, MNRAS, 420, 1239

Lu Y., Yang X., Shen S., 2015, Astrophys. J., 804, 17

Lukić Z., Reed D., Habib S., Heitmann K., 2009, ApJ, 692, 217

Madgwick D. S. et al., 2002, MNRAS, 333, 133

Mahajan S., Raychaudhury S., 2009, MNRAS, 400, 687

Maller A. H., Berlind A. A., Blanton M. R., Hogg D. W., 2009, ApJ, 691, 394

Martin D. C. et al., 2005, ApJL, 619, L1

Mathis H., White S. D. M., 2002, MNRAS, 337, 1193

McBride J., Fakhouri O., Ma C.-P., 2009, MNRAS, 398, 1858

McCarthy I. G., Frenk C. S., Font a. S., Lacey C. G., Bower R. G., Mitchell N. L., Balogh M. L.,
   Theuns T., 2008, MNRAS, 383, 593

McKay T. A. et al., 2002, ApJL, 571, L85

McNaught-Roberts T., Norberg P., Baugh C., Lacey C., Loveday J., Peacock J., Baldry I., Brough
   S., 2014, MNRAS, 445, 2125

Merson A. I. et al., 2013, MNRAS, 429, 556

Metuki O., Libeskind N. I., Hoffman Y., Crain R. a., Theuns T., 2015, MNRAS, 446, 1458

Mo H. J., Yang X., van den Bosch F. C., Jing Y. P., 2004, MNRAS, 349, 205

Muldrew S. I. et al., 2012, MNRAS, 419, 2670

Muldrew S. I., Pearce F. R., Power C., 2011, MNRAS, 410, 2617

Navarro J. F., Frenk C. S., White S. D. M., 1997, Astrophys. J., 490, 493

Neto A. F. et al., 2007, MNRAS, 381, 1450

Newman J. A. et al., 2013, ApJS, 208, 5

Norberg P. et al., 2002a, MNRAS, 332, 827

Norberg P. et al., 2002b, MNRAS, 336, 907

Orsi A., Baugh C. M., Lacey C. G., Cimatti A., Wang Y., Zamorani G., 2010, MNRAS, 405, 1006

Pearson R. J., Ponman T. J., Norberg P., Robotham a. S. G., Farr W. M., 2015, MNRAS, 449,
   3082

Peebles P. J. E., 2001, ApJ, 557, 495

Perlmutter S. et al., 1999, The Astrophysical Journal, 517, 565

Persic M., Salucci P., Stel F., Astronomico O., Tiepolo G. B., Trieste I., 1996, MNRAS, 281, 27

Petrosian V., 1976, ApJL, 209, L1

Planck Collaboration et al., 2014, Astronomy & Astrophysics, 571, 48

Power C., Navarro J. F., Jenkins A., Frenk C. S., White S. D. M., Springel V., Stadel J., Quinn
    T., 2003, MNRAS, 338, 14

Prada F., Klypin A. a., Cuesta A. J., Betancort-rijo J. E., Primack J., 2012, MNRAS, 423, 3018

Prada F. et al., 2003, ApJ, 598, 260

Press W. H., Schechter P., 1974, Formation of Galaxies and Clusters of Galaxies by Self-Similar
    Gravitational Condensation

Riess A. G. et al., 1998, Astron. J., 116, 1009

Roberts M. S., Rots A. H., 1973, A&A, 26, 483

Robotham A. et al., 2010, PASA, 27, 76

Robotham A., Phillipps S., De Propris R., 2010, MNRAS, 403, 1812

Robotham A., Wallace C., Phillipps S., De Propris R., 2006, Astrophys. J., 652, 1077

Robotham A. S. G. et al., 2011, MNRAS, 416, 2640

Rubin V. C., Ford, Jr. W. K., 1970, ApJ, 159, 379

Sales L., Lambas D. G., 2004, MNRAS, 348, 1236

Sandage A., Tammann G., 1982, Astrophys. J., 256, 339

Schaye J. et al., 2015, MNRAS, 446, 521

Schechter P., 1976, ApJ, 203, 297

Schlegel D. J., Finkbeiner D. P., Davis M., 1998, ApJ, 500, 525

Schmidt M., 1968, ApJ, 151, 393

Sharp R. et al., 2006, in Society of Photo-Optical Instrumentation Engineers (SPIE) Conference
    Series, Vol. 6269, Society of Photo-Optical Instrumentation Engineers (SPIE) Conference Series,
    p. 0

Smail I., Ellis R. S., Fitchett M. J., 1994, MNRAS, 270, 245

Spergel D. N. et al., 2003, Astrophys. J. Supplement Series, 148, 175

Springel V., White S., Tormen G., Kauffmann G., 2001, MNRAS, 328, 726

Springel V. et al., 2005, Nature, 435, 629

Taylor E. N. et al., 2011, MNRAS, 418, 1587

Tempel E., Saar E., Liivamägi L. J., Tamm A., Einasto J., Einasto M., Müller V., 2011, A&A, 529, A53

Tinker J., Wetzel A., Conroy C., 2011, ArXiv Astrophysics e-prints, 21, 21

Tonry J. L., Blakeslee J. P., Ajhar E. A., Dressler A., 2000, ApJ, 530, 625

Tully R. B., 2015, AJ, 149, 171

Verdes-Montenegro L., Sulentic J., Lisenfeld U., Al. E., 2005, Astronomy & Astrophysics, 436, 443

Viola M. et al., 2015, MNRAS, 452, 3529

Weinmann S. M., Bosch F. C. V. D., Yang X., Mo H. J., Croton D. J., Moore B., 2006, MNRAS, 372, 1161

Wetzel A. R., Tinker J. L., Conroy C., 2012, MNRAS, 424, 232

Wetzel A. R., Tinker J. L., Conroy C., van den Bosch F. C., 2013, MNRAS, 432, 336

Wheeler C., Phillips J. I., Cooper M. C., Boylan-Kolchin M., Bullock J. S., 2014, MNRAS, 442, 1396

Wijesinghe D. B. et al., 2012, MNRAS, 423, 3679

Yan H., Fan Z., White S. D. M., 2013, MNRAS, 430, 3432

Yang X., Mo H. J., Bosch F. C. V. D., Pasquali A., Li C., Barden M., 2007, Astrophys. J., 671, 153

Yang X., Mo H. J., van den Bosch F. C., 2009, ApJ, 695, 900

Yang X., Mo H. J., Van Den Bosch F. C., Jing Y. P., 2005, MNRAS, 356, 1293

York D. G. et al., 2000, AJ, 120, 1579

Zandivarez A., Martínez H. J., Merchán M. E., 2006, ApJ, 650, 137

Zaritsky D., White S. D. M., 1994, ApJ, 435, 599

Zehavi I. et al., 2011, Astrophys. J., 736, 59

Zhao C., Kitaura F.-s., Chuang C.-h., Prada F., Yepes G., Tao C., 2015, 000, 1

Zwicky F., 1933, Helvetica Physica Acta, 6, 110